Numerical Analysis and Simulation of Stiff Reaction-Diffusion Systems and Nonlinear Wave Equations with Damping Effects

Thesis submitted in partial fulfilment
for the Award of Degree
Doctor of Philosophy

by

JYOTI

DEPARTMENT OF MATHEMATICAL SCIENCES
RAJIV GANDHI INSTITUTE OF PETROLEUM TECHNOLOGY
JAIS, INDIA-229304

20BS0007 **2025**

CERTIFICATE

It is to certify that the work contained in the thesis titled ***"Numerical Analysis and Simulation of Stiff Reaction-Diffusion Systems and Nonlinear Wave Equations with Damping Effects"*** by **Jyoti** has been carried out under my supervision and that this work has not been submitted elsewhere for a degree. It is further certified that the student has fulfilled all the requirements of comprehensive, candidacy and state of the art.

Dr. Manoj K. Rajpoot
Thesis Advisor

DECLARATION BY THE CANDIDATE

I, **Jyoti**, certify that the work embodied in this thesis is my own bonafide work and carried out by me under the supervision of **Dr. Manoj K. Rajpoot** from **August 2020** to **July 2025** at Rajiv Gandhi Institute of Petroleum Technology, Jais, India. The matter embodied in this thesis has not been submitted for the award of any other degree. I declare that I have faithfully acknowledged and given credits to all the sources wherever their works have been cited in this thesis. I further declare that I have not wilfully copied any others' work, paragraphs, text, data and results reported in journals, books, magazines, reports, dissertations, thesis or available at websites and have not included them in this thesis and have not cited as my own work.

Date:
Place: Jyoti

CERTIFICATE BY THE THESIS SUPERVISOR

It is certified that the above statement made by the student is correct to the best of our knowledge.

Dr. Manoj K. Rajpoot
Thesis Advisor

Head of Department
Mathematical Sciences

CERTIFICATE

It is certified that the work contained in the thesis titled ***"Numerical Analysis and Simulation of Stiff Reaction-Diffusion Systems and Nonlinear Wave Equations with Damping Effects"*** by **Ms. Jyoti** has been carried out under my supervision. It is also certified that she fulfilled the mandatory requirement of two quality publications arose out of her thesis work. It is further certified that the two publications (copies enclosed) of the aforesaid **Ms. Jyoti** have been published in the Journals indexed by:

(a) SCI

(b) SCI Extended

(c) SCOPUS

(d) Non-indexed journals

Dr. Manoj K. Rajpoot
Thesis Advisor

Dr. Sudeep Kundu
Convener, DPGC

COPYRIGHT TRANSFER CERTIFICATE

Title of the Thesis: *Numerical Analysis and Simulation of Stiff Reaction-Diffusion Systems and Nonlinear Wave Equations with Damping Effects*
Name of the Student: Jyoti

Copyright Transfer

The undersigned hereby assigns to the Rajiv Gandhi Institute of Petroleum Technology, Jais, Amethi, all rights under copyright that may exist in and for the above thesis submitted for the award of the **"Doctor of Philosophy "**.

Date:
Place: Jyoti

Note: However, the author may reproduce or authorize others to reproduce material extracted verbatim from the thesis or derivative of the thesis for author's personal use provided that the source and the Institute's copyright notice are indicated.

Acknowledgments

I express my heartfelt gratitude to God for His grace and blessings, which have strengthened my determination to pursue my academic journey and explore the beauty of Mathematics through research. Throughout this journey, I have received invaluable support from many individuals to whom I extend my sincere gratitude.

First and foremost, I would like to express my heartfelt gratitude to my thesis advisor, **Dr. Manoj K. Rajpoot**, for his invaluable guidance, insightful suggestions, and unwavering support throughout my research. His vast knowledge, patience, and motivation have played a crucial role in shaping my academic growth and strengthening my research abilities. Conducting academic studies on such a difficult topic could not be as simple as he made it for me. His guidance has been invaluable in navigating complex research challenges while allowing me the independence to explore new ideas. I am also grateful for the assistance and insightful discussions of my labmates, Vivek, Ankit, and Vikas, as our collaborative efforts have resulted in the publication of a couple of research papers.

Apart from my advisor, I extend my sincere gratitude to the RPEC members, Prof. Chanchal Kundu and Dr. Rohit Bansal, for their encouragement and insightful suggestions. Furthermore, I sincerely acknowledge my course instructors, Prof. Chanchal Kundu and Dr. Alpesh Kumar, for teaching me the essential mathematical fundamentals during my Ph.D. course work. I would also like to thank the teaching and non-teaching staff of RGIPT for their kind cooperation throughout my Ph.D. journey.

In addition, I wish to express my thanks to Dr. Sonia Dhama for her unwavering belief, support, and encouragement. I would also like to express my sincere appreciation to my seniors, colleagues, juniors, and friends for their unconditional love and unlimited support.

Last but not least, I am deeply thankful to my mother, who stood by me in pursuit of my dreams and education, encouraging and inspiring me throughout this journey. This would not have been possible without her support. I am grateful to my father, brother, and friends, who keep me in their prayers and wish for my success. Their moral support and motivation have been invaluable in helping me accomplish my goals. Friends, whose

support and kindness have always uplifted me and reminded me of my worth. Their constant encouragement, companionship, and unwavering belief in me have made this journey more meaningful and enjoyable. I would not have made it this far without them. Finally, I gratefully acknowledge the Department of Science and Technology (DST), Govt. of India, New Delhi, for the financial support provided for my research.

Jyoti

Contents

List of Abbreviations

The following list describes the abbreviations used in this thesis, along with the page numbers where each term first appears. Abbreviations that are commonly used or accepted are excluded.

PDEs	Partial Differential Equations	xxx
SSP	Strong Stability Preserving	xxx
FDM	Finite Difference Method	2
ODEs	Ordinary Differential Equations	7
CFD	Computational Fluid Dynamics	9
IMEX	Implicit-Explicit Method	10
RK	Runge-Kutta Method	10
CEMRK	Computationally Explicit Multiderivative Runge-Kutta	10
RKN	Runge-Kutta-Nyström Method	14
AVF	Average Vector Field	15
EDRP	Energy and Dispersion Relation Preserving	17
EDPM	Energy-Dispersion Preserving Method	17
GSA	Globally Stiffly Accurate	21
2D	Two-Dimensional	27
CD2	Second-Order Centered Difference Scheme	28
TVD	Total Variation Diminishing Method	30
RK3	Third-Order Runge-Kutta Method	30
CN-MG	Crank-Nicolson/Multi-Grid Method	30

IIF	Implicit Integrating Factor	30
ERC	Estimated Rate of Convergence	31
NC	Non Convergent	32
ETD	Exponential Time Differencing Method	35
GSRD	Gray-Scott Reaction-Diffusion	36
C4	Fourth-Order Compact Scheme	57
1D	One-Dimensional	58
ROC	Rate of Convergence	60
ADI	Alternating Direction-Implicit	78
LF2	Second-Order Leapfrog Method	107
RE	Relative Energy Error	144
AE	Absolute Energy Error	144

List of Figures

List of Tables

Preface

Partial Differential Equations (PDEs) are crucial in modeling various physical phenomena in many disciplines such as mathematical biology, environmental engineering, fluid dynamics, and wave propagation in electromagnetics and acoustics. Due to the inherent complexity of these equations, analytical solutions are often infeasible, necessitating the use of numerical methods for accurate approximations. A significant challenge in solving these PDEs is stiffness, which arises from interactions between processes occurring at multiple spatial and temporal scales. Higher-order accurate methods are essential to resolve such problems efficiently. It is well known that the explicit methods often suffer from severe stability constraints when dealing with stiffness, while fully or partially implicit schemes provide better stability but introduce higher computational costs. Thus for efficient simulations of stiff dynamical systems we need numerical methods that balance stability, accuracy, and computational efficiency while preserving key physical properties.

Chapter 1 presents an introduction and a brief literature review of such PDEs. In Chapter 2, a class of unconditionally strong stability preserving (SSP) multi-derivative methods for the numerical simulation of stiff reaction-diffusion systems is introduced. The unconditional SSP property ensures that these methods remain stable without restrictive time-step constraints, making them highly efficient for solving reaction-diffusion problems in the stiff regime. Unlike traditional implicit methods, the proposed approach does not require inversion of the coefficient matrix, significantly reducing computational complexity while maintaining accuracy across a wide range of parameters. The theoretical proof of the SSP property is established, ensuring the efficiency of the method. The accuracy of these methods is evaluated using L^∞-error analysis, and comparisons with existing literature demonstrate superior performance, even for larger time steps.

In Chapter 3, the concept of high-order accurate methods with strong stability properties is extended for convection-diffusion systems. A novel class of computationally explicit multiderivative methods has been developed for the numerical solution of convection-dominated diffusion equations, where the dominance of the convection term poses computational challenges. The proposed methods have been designed to preserve strong stability, ensuring efficient simulation of convection-dominated diffusion equations without imposing restrictive time-step constraints. To enhance accuracy, a fourth-order compact finite difference scheme is employed for spatial discretization.

Chapter 4, deals with an energy-preserving, partially implicit method for the simulation of undamped acoustic and soliton wave propagation in homogeneous and heterogeneous mediums. The derived method is second-order accurate in time and preserves the physical properties of the wave propagation problems. The numerical properties of the methods are evaluated using Fourier analysis for one- and two-dimensional linear wave equations. Energy-preserving properties of the fully discrete scheme are validated through theoretical analysis and numerical experiments. Convergence analysis is also performed to assess the rate of convergence of the developed scheme.

In Chapter 5, the concept of energy-preserving space-time discretization methods is extended for damped wave equations. The developed methods are implemented with a fourth-order compact finite difference scheme for the numerical simulation of damped linear and nonlinear wave equations. The damped wave equation is an extension of the classical wave equation that includes a damping term to model energy dissipation over time. Theoretical convergence analysis is established, and discrete energy errors for the developed method are computed for wave propagation in the homogeneous and inhomogeneous mediums by considering the relative errors. The theoretical convergence rate is also validated numerically using the discrete L^2-norm. The accuracy of the developed method is validated through various cases of wave and soliton propagation.

Finally, Chapter 6 deals with the summary of the thesis, drawn conclusions based on our findings, and provided recommendations for future research directions.

Chapter 1

Introduction

The advancement of scientific computing and mathematical modeling has revolutionized our ability to understand, simulate, and predict complex physical phenomena. Among the most powerful mathematical tools for modeling such systems are partial differential equations (PDEs), which model both temporal and spatial changes in state variables, allowing for a detailed understanding of dynamic processes [1]. In modern contexts, PDEs serve as essential tools in science and engineering. PDEs are used to model fluid flow, stress distribution, and thermal conduction in structures and machines to name a few. In biological systems, PDEs describe the spread of diseases, neural activity, and ecological interactions. Financial models also rely on PDEs to evaluate derivatives and manage risk, while in image processing and artificial intelligence, they contribute to edge detection, noise reduction, and shape modeling. Moreover, the increasing reliance on computational power has transformed the way PDEs are solved, making numerical approximation and simulation indispensable where analytical solutions are either too complex or entirely unattainable. Thus, the importance of PDEs is not merely theoretical but deeply practical. As they bridge the abstract world of mathematics with the tangible, ever-changing systems of the real world, enabling us to analyze, predict, and innovate across disciplines. Reaction-diffusion systems and wave equations represent two foundational classes of partial differential equations that model fundamentally different, yet widely occurring, dynamic phenomena.

Nature often displays strikingly beautiful and complex patterns, from the stripes on a zebra and the spots on a leopard to the ripples in sand dunes and the distribution of vegetation in arid climates. These patterns, while visually fascinating, are not merely surface-level structures but often emerge due to chemical, biological, or ecological processes governed by PDEs. One of the most powerful models used to understand and simulate such natural phenomena is the reaction-diffusion model. Reaction-diffusion equations describe processes in which substances undergo both local chemical reactions and spatial diffusion, making them crucial for understanding pattern formation in biological systems, such as animal coat markings, morphogenesis, tumor growth, and ecological interactions.

In contrast, wave equations govern the propagation of disturbances through a medium and are central to modeling mechanical vibrations, acoustic and electromagnetic waves. They appear in domains ranging from engineering and geophysics to relativity and quantum mechanics. Together, these equations not only provide insight into natural processes but also offer a mathematical tool for designing and controlling systems in science and engineering. This thesis focuses on the development and analysis of finite difference methods (FDM) for solving different classes of PDEs, especially parabolic and hyperbolic type, such as stiff reaction-diffusion systems, convection-diffusion equations, and wave equations with or without damping effects. These systems are inherently complex and pose a variety of challenges, including stiffness, sharp gradients, and conservation of physical properties such as mass, momentum, and energy, over long time scales. Developing robust numerical methods for such equations is essential for the accurate and efficient simulation of governing systems [2]. Considerable efforts have been made in developing numerical integration methods for stiff problems [3], and the problem of stiffness has been discussed in details in [4]. A comprehensive discussion related to stiffness is given in [5].

Stiff dynamics commonly arise in systems of differential equations that involve processes occurring at widely different timescales. These systems are characterized by the coexistence of both rapidly and slowly changing solution components, leading to significant numerical challenges when simulating their behavior. Specifically, explicit numerical methods become inefficient or even unstable because they are constrained to take extremely small time-steps to maintain stability, even when the overall solution varies slowly

[6, 7]. In 1966, Robertson described stiffness as a phenomenon where fast and slow reactions make forward time integration difficult [4]. Later, in 1991, Lambert [8] explained that if a numerical method with limited stability needs to take very small time-steps, despite the solution being smooth, then the system is considered stiff in that region. Mathematically, stiffness is often related to large negative eigenvalues in the system's Jacobian matrix. A high stiffness ratio (that is the difference between the largest and smallest eigenvalues in magnitude) usually signals a stiff system [8]. Stiff dynamics are frequently encountered in chemical kinetics, combustion, electrical circuits, and biological regulatory networks, where fast transients are embedded within slower processes [9].

Stiff systems are especially challenging to simulate because standard explicit methods require very small time-steps to maintain stability, rendering them inefficient for long-term integration. The interplay between rapid local reactions and slower spatial diffusion leads to complex dynamical behavior, making stiff reaction-diffusion systems a critical subject of study. Combination of reaction and diffusion processes could spontaneously generate spatial patterns in chemical concentrations, providing a foundational explanation for morphogenesis, the biological process that causes an organism to develop its shape [10]. Classical work of Alan Turing [10] catalyzed decades of research into pattern formation, leading to the development of numerous reaction-diffusion models such as the Gray-Scott model [6], the Brusselator model [11], and the Schnakenberg model [12]. These models help researchers understand how nonlinearity and diffusion interact to produce spatiotemporal phenomena, including oscillations, traveling waves, and stationary patterns. Due to presence of stiffness, more advanced numerical methods are needed to solve them accurately and efficiently, making them a central focus in computational studies of pattern formation and nonlinear dynamics [13]. In this thesis, three fundamental reaction-diffusion models: the Gray-Scott model, the Brusselator model, and the Schnakenberg model are considered.

1.1 Reaction-diffusion systems

Reaction-diffusion models play a pivotal role across a wide spectrum of disciplines due to their ability to model complex spatiotemporal patterns arising from local interactions and transport processes. In biology and morphogenesis, these models help explain how patterns form during the development of organisms, such as animal skin pigmentation, limb formation, or tissue differentiation. For instance, Turing's original work was aimed at understanding the development of fingers and digits in embryos. Turing patterns have been applied to various phenomena, from explaining the shell markings of aquatic mollusks to offering insights into human settlement patterns and inspiring water filtration designs. Reaction-diffusion systems have also helped scientists understand the evenly spaced transverse ridges found on the mammalian palate [14]. The studies have expanded on highlighting their applicability to various proteins and RNAs in multicellular organisms. In neuroscience modeling brain activity, wave propagation, and pattern formation in neural circuits, reaction-diffusion systems are used to study processes like epilepsy and cortical patterning. Recent research has utilized reaction-diffusion models to simulate the propagation of dynamic concentration patterns in both healthy and damaged brain connectomes, providing insights into neurological disorders [15, 16]. In chemical engineering, these models are used to simulate reactions in catalytic surfaces and reactors, helping in the design of efficient chemical processes and materials with self-organizing properties. The advancements include the development of nanomaterial based smart coatings capable of real-time monitoring and applications in flexible electronics [17, 18, 19]. In ecology and environmental science, reaction-diffusion systems are used to model spatial patterns in ecosystems, such as vegetation clustering, predator-prey dynamics, and species dispersion in changing environments. The studies have explored the emergence of spatial patterns in predator-prey models influenced by habitat loss, and incorporating the effects of linear diffusion to understand ecosystem dynamics [20, 21]. Recent surveys have highlighted the role of diffusion-based models in visual art creation, emphasizing their potential in generating intricate and realistic patterns for digital media.

In this thesis, following reaction-diffusion systems are considered.

1.2 The Gray-Scott model

The Gray-Scott model [22] is a well-established reaction-diffusion system that describes how two interacting chemical species, typically denoted as X and Y, evolve over time due to both reaction kinetics and diffusion, helping us to understand self-organization in nature and materials. It was developed by P. Gray and S. K. Scott [22] in the 1980s as an extension of earlier autocatalytic reaction models, particularly to study nonlinear chemical dynamics. Autocatalysis is the process by which a chemical is involved in its own production [6]. The model is particularly known for its ability to produce a variety of spatial patterns, such as spots, stripes, and wave-like structures, through relatively simple equations. The process involves two reactions as described in [22]: the first is the trimolecular autocatalytic step $X + 2Y \to 3Y$, and the second reaction is $Y \to P$. Since both reactions are irreversible, P behaves as an inert product. The system is kept out of equilibrium through a feed term applied to X, while both X and Y are simultaneously extracted via feed process [23]. The specific reaction-diffusion system that describes the process is

$$\begin{aligned} \frac{\partial u}{\partial t} &= D_1 \nabla^2 u - uv^2 + R_1(1-u) \\ \frac{\partial v}{\partial t} &= D_2 \nabla^2 v + uv^2 - (R_1 + R_2)v \end{aligned} \tag{1.2.1}$$

where u and v are concentrations of chemical species X and Y, D_1 and D_2 are their respective diffusion coefficients, R_1 is the feed rate of X, R_2 is the removal (kill) rate of Y.

1.3 The Brusselator model

The Brusselator model [24] is a theoretical reaction-diffusion system that describes the behavior of autocatalytic oscillating chemical reactions far from equilibrium. It was proposed by Ilya Prigogine [24] and his colleagues at the Free University of Brussels as a simplified system to study oscillatory and pattern-forming reactions [11]. Like the Gray-Scott model, it helps illustrate how simple nonlinear chemical rules can lead to complex dynamic behavior, including stable oscillations, waves, and Turing patterns. The model is based on an abstract set of reactions [25] which are given as $P \to X$, $Q + X \to Y + D$ (bimolecular reaction), $2X + Y \to 3X$ (autocatalytic trimolecular reaction), $X \to E$.

Here, P and Q are input (feed) chemicals, and D and E are final products which remain constant, whereas the two intermediate components (X and Y) may have concentrations that change in time. The key autocatalytic step $2X+Y \to 3X$ drives nonlinear feedback. When extended with diffusion terms, the system is described by the following PDEs, given as

$$\begin{aligned} \frac{\partial u}{\partial t} &= D_1 \nabla^2 u + R_1 + u^2 v - (R_2 + 1)u \\ \frac{\partial v}{\partial t} &= D_2 \nabla^2 v - u^2 v + R_2 u \end{aligned} \tag{1.3.1}$$

where u and v are concentrations of intermediate species X and Y, D_1 and D_2 are their respective diffusion coefficients, R_1 and R_2 are the feed parameters. The Brusselator model is especially useful in studying chemical oscillations, biological rhythms, and pattern formation in morphology, making it a foundational tool in both theoretical chemistry and mathematical biology.

1.4 The Schnakenberg model

The Schnakenberg model, introduced by Jürgen Schnakenberg in 1979 [12], is a reaction-diffusion system employed to explore how activator–inhibitor interactions can lead to both spatial patterns and temporal oscillations. It originates from a simple set of chemical reactions given as

$$\begin{aligned} X &\rightleftharpoons P \\ Y &\to Q \\ 2P + Q &\to 3P \end{aligned}$$

where X acts as the activator and Y as the inhibitor play key roles in driving complex dynamical behavior. The Schnakenberg model captures the essential features of Turing instability and Hopf bifurcation, making it particularly important for modeling pattern formation in biological systems, such as eggshell pigmentation, limb development, and cellular differentiation. Expressed as a reaction-diffusion system, the model is governed by the system of PDEs, given as

$$\begin{aligned} \frac{\partial u}{\partial t} &= D_1 \nabla^2 u - R_1 + u^2 v - u \\ \frac{\partial v}{\partial t} &= D_2 \nabla^2 v - u^2 v + R_2 \end{aligned} \tag{1.4.1}$$

where u and v are concentrations of intermediate species X and Y, D_1 and D_2 are their respective diffusion coefficients, R_1 and R_2 are the feed parameters [26, 27]. The simplicity of this system allows it to exhibit dynamical phenomena, including stationary Turing patterns and oscillatory wave-like behaviors, depending on parameter values. Beyond its biological applications, the Schnakenberg model is widely used as a benchmark test case for numerical methods, such as finite difference, finite elements, spectral methods, and Galerkin approximations, especially when extended to fractional or time-delayed variants [28]. Use of numerical methods help researchers to accurately track the onset of Turing and Hopf bifurcations, analyze stability, and understand how parameter changes lead to qualitatively different pattern regimes.

Numerical simulation of time-dependent stiff reaction-diffusion system of PDEs requires efficient and accurate numerical methods. A widely used method for solving time-dependent PDEs involves initially discretizing the spatial variable, resulting in semi-discrete system of ordinary differential equations (ODEs). The resultant semi-discrete system can then be solved using standard time-integration methods. In [29], the authors developed a general method for higher-order semi-implicit linear multistep methods, analyzing their stability properties under strong stability preserving (SSP) schemes using a model linear advection-diffusion equation. A set of examples involving convection-diffusion and nonlinear reaction-diffusion problems was presented in [29]. Solving time-dependent PDEs naturally raise concerns about stability, and the appropriate assessment depends on the characteristics of the solution. Linear stability analysis is generally sufficient for smooth solutions. However, in cases where a solution involving discontinuities, a more robust stability approach becomes necessary. SSP methods, initially proposed in [30, 31] and later extended in [32]. In this thesis, we have assumed that the discretized system of ODEs obtained by applying a forward Euler time integration method of first-order maintains SSP under a given norm, provided that the time-step satisfies certain conditions. The main goal here is to develop and investigate time integration methods that have higher-order accuracy while preserving the SSP property with respect to the same norm, subject to altered time-step restrictions.

Widely used methods for solving time-dependent PDEs are discussed in [30, 31], as they maintain the convex functional properties of the forward Euler scheme while providing higher-order accuracy. Such ODE systems frequently result from discretizing the spatial terms of partial differential equations, which are often represented in the following form:

$$u_t = \mathcal{H}(u) \tag{1.4.2}$$

Here, the combined reaction and diffusion operators are represented by $\mathcal{H}$. The system described in Eq. (1.4.2) satisfies a condition of forward Euler stability of the following form, given as

$$\|u + \Delta t \mathcal{H}(u)\| \leq \|u\|$$

for all time-steps $\Delta t \leq \Delta t_{FE}$, where the norm $\|\cdot\|$ is a convex functional. Although the forward Euler method satisfies this stability criterion, its limited accuracy makes it less desirable in practical computations. Therefore, higher-order schemes that preserve this condition are preferred. This can be ensured by enforcing a modified restriction on time-step, provided as $\Delta t \leq K \Delta t_{FE}$ where $K > 0$. Such higher-order schemes, which are developed as convex combinations of forward Euler steps, are called SSP methods and maintain the same stability structure. The convex combination approach was employed to develop higher-order explicit Runge-Kutta methods [31] that preserve SSP properties. Additionally, the convex combination approach also ensures that all intermediate stages maintain the same stability property. The value of the SSP coefficient K determines how much the time-step can be scaled. To alleviate restrictions on time-step from linear stability requirements, implicit-explicit or implicit schemes are commonly used. However, achieving the SSP property even with implicit schemes can still impose significant limitations on the time-step size [33].

The authors in [34, 35] investigated the behavior of multiderivative Runge-Kutta schemes with SSP properties and showed that such schemes require not only the forward Euler condition but also an additional constraint, $\bar{\mathcal{H}} = d\mathcal{H}/dt$, on the second derivative. Initially explicit two-derivative methods with SSP properties were constructed to satisfy either both the forward Euler and second derivative conditions [34], or the forward Euler condition in conjunction with a Taylor series-based requirement [35]. As noted in [36, 37], the development of unconditional SSP schemes led to the introduction of a backward derivative condition, intended to replace the earlier second derivative and Taylor series requirements. In [37], the proposed implicit schemes involve numerical inversion of coefficient matrix, while the implicit-explicit formulations are subject to time-step constraints due to the explicit handling of the non-stiff terms. In contrast, the present work introduces multiderivative Runge-Kutta methods that avoid the need for coefficient matrix inversion and satisfy unconditionally SSP properties altogether.

The SSP methods for reaction-diffusion systems has been also extended to the convection-diffusion equations. The convection-diffusion equation can describe the convection and diffusion of various physical quantities such as mass, momentum, and energy. Accurate numerical solutions to the convection-diffusion equations are crucial in computational fluid dynamics (CFD) for simulating fluid flow and heat transfer problems. Consequently, developing stable and accurate numerical approximations of convection-diffusion equations is essential. Over the years, a variety of numerical methods have been developed for approximating convection-diffusion problems, including finite difference, finite volume, and finite element methods [38, 39, 40, 41, 42]. The finite difference method is widely used for solving problems in CFD [43, 44, 45, 46, 47, 48, 49].

Present work focuses on convection-dominated problems, characterized by $|D| << |\gamma|$, which pose significant computational challenges (see [50] for a comprehensive review). Here, D represents the diffusion coefficient, and γ denotes the convection coefficient. Due to the highly hyperbolic nature of these problems, solutions tend to form steep fronts resembling shocks. Traditional numerical methods, such as central difference methods or Galerkin methods, often struggle with stability and convergence issues. These methods lead to non-physical oscillations or excessive numerical dissipation at sharp gradients if the mesh and time-steps are not sufficiently refined [51, 52]. Therefore, it is important to develop robust methods that effectively handle these issues. Common approaches, such as upwinding in finite difference or finite volume methods, as well as SSP methods [53], are frequently employed to improve stability.

To improve accuracy and stability, authors in [34] analyzed the SSP characteristics of multiderivative Runge Kutta (RK) methods and revealed that these methods necessitate an extra requirement on the second derivative, given by $\bar{\mathcal{H}} = d\mathcal{H}/dt$, in addition to the forward Euler condition. In this work, the additional condition is considered as the second derivative condition. While implicit methods are computationally expensive, they introduce complexities in implementation and require matrix inversions. Implicit-explicit (IMEX) methods are limited by time-step restrictions due to explicit treatment of convection or diffusion terms, whereas the proposed computationally explicit multiderivative Runge Kutta (CEMRK) methods, which are SSP without time-step restriction, eliminate the need for coefficient matrix inversion.

For spatial discretization, we have used compact finite difference methods [54], as traditional finite difference methods, often fail to provide accurate solutions for convection-dominated problems. Compact finite difference schemes, particularly higher-order compact methods, offer a computationally efficient alternative to discretization techniques like central and upwind schemes, especially for convection-dominated flows. Unlike standard higher-order methods that rely on wide stencils and lead to increased computational cost, compact schemes achieve higher accuracy using only neighboring grid points, enabling accurate solutions. The foundational work by Lax and Wendroff [55, 56] and authors in [57] initiated the development of compact schemes, with further extensions by authors in [58, 54, 59] for both incompressible and compressible Navier–Stokes equations. In this study, a fourth-order compact scheme is used to accurately approximate spatial derivatives.

1.5 Linear and non-linear hyperbolic systems: Wave equations

Wave equations, especially acoustic waves, damped waves, and solitons serve as fundamental tools in modeling a vast array of real-world phenomena. Acoustic waves are pressure disturbances that travel through gases, liquids, and solids. They provide the basis for technologies like architectural acoustics where room designs rely on accurate simulations of sound propagation and medical ultrasonography, where focused wave models reveal internal body structures.

Damped wave equations describe systems in which wave energy dissipates over time due to mechanisms like friction, material resistance, or absorption, play a critical role in modeling how wave amplitude decreases over time. These models are indispensable for vibration analysis in mechanical structures, where damping mechanisms prevent resonant failures. They also describe stress wave attenuation during pile-driving operations in geotechnical engineering, and simulate water-wave dissipation in coastal areas. Mathematically, damping in wave equations introduces stable numerical behavior and energy decay during simulations. Recent methods that preserve energy dissipation properties have been applied to attenuating acoustic waves via conformal symplectic integrators, ensuring accurate phase and amplitude behavior in simulations.

Solitons are waveforms that maintain their shape and energy through a balance of nonlinearity and dispersion. These are foundational to high-speed optical communications, where temporal solitons enable error-free data transmission over thousands of kilometers and soliton lasers used in ultrafast sensing and metrology. Soliton theory also plays a role in plasmonic waveguides, quantum optics, and biological nerve signal modeling, providing an approach for understanding stability and information transfer in complex systems. Wave models form an essential tool for tackling real-world challenges from improving sound quality and structural resilience to advancing communication systems and biological understanding. Their importance lies in accurately capturing wave behavior under diverse conditions and enabling the development of reliable, high-performance numerical solvers [60, 61].

Nonlinear wave equations such as sine-Gordon, Klein-Gordon, Korteweg-de Vries and the nonlinear Schrödinger equation are fundamental in describing complex wave phenomena where nonlinearity and dispersion not only coexist, but interact to create solitons and kinks. In this thesis, following models are considered.

1.6 The sine-Gordon equation

The sine-Gordon equation is the prototypical nonlinear PDE which has applications in modeling Josephson junctions in superconducting electronics, crystal dislocation dynamics, and nonlinear excitations in biological systems like DNA and neural structures [62]. In particular, the Josephson junction model [63], which consists of two layers of superconducting material separated by an isolating barrier [64]. In superconductivity, the sine-Gordon equation models the phase dynamics of fluxons in long Josephson junctions, crucial for superconducting electronics, often under applied currents or magnetic fields in its perturbed form. In condensed matter physics, it describes dislocations in crystals, domain walls in magnetic materials, and localized excitations in lattice systems. Notable applications extend to DNA and protein folding dynamics, neural signal modeling, and elastic excitations in microtubules, reflecting its adaptability to systems with nonlinear wave phenomena.

The two-dimensional damped sine-Gordon equation [65] with Josephson junction is given as

$$\frac{\partial^2 u}{\partial t^2} + a\frac{\partial u}{\partial t} - c^2(x,y)\left(\frac{\partial^2 u}{\partial x^2} + \frac{\partial^2 u}{\partial y^2}\right) = F(x,y)\sin u, \quad a \geq 0, \tag{1.6.1}$$

where a represents the coefficient of damping, which is considered to be a non-negative real number, $c(x,y)$ denotes the phase speed, and $F(x,y)$ stands for the Josephson density of the current. Due to its nonlinearity and the presence of damping, numerical schemes to simulate this model accurately are discussed in [64, 65].

1.7 The Klein-Gordon equation

The Klein-Gordon equation is a fundamental relativistic wave equation originally formulated to describe scalar or pseudoscalar particles in quantum field theory. It represents the quantum version of the relativistic energy-momentum relation and is particularly applicable to spin-0 particles such as mesons. The Klein-Gordon equation [66] is given as

$$\frac{\partial^2 u}{\partial t^2} - c^2(x, y) \left(\frac{\partial^2 u}{\partial x^2} + \frac{\partial^2 u}{\partial y^2} \right) + u + u^3 = 0 \tag{1.7.1}$$

where $c(x, y)$ is the phase speed. The equation serves as a stepping stone to more complex models in quantum field theory and underpins the behavior of scalar fields in both flat and curved space times. While the original formulation is linear, the nonlinear Klein-Gordon equation, including terms such as λu^3, is used extensively in condensed matter physics, nonlinear optics, and cosmology to study soliton interactions, phase transitions, and defect dynamics in scalar field theories [67]. Numerical simulation of the damped Klein-Gordon systems has led to the development of robust methods, including finite difference time domain, spectral, and energy-conserving schemes [68]. Such studies often investigated the long-time behavior of solutions, stability of solitary waves, and energy dissipation in nonlinear media. These attributes underline the Klein-Gordon equation's significance not only in theoretical physics but also in applied mathematics requiring wave modeling under relativistic or nonlinear constraints.

1.8 The corner-edge model

The corner-edge model [69] refers to a class of nonlinear wave systems that describe how waves behave in domains with geometrical singularities, such as sharp corners or edges. These kind of models are especially relevant in situations where standard wave propagation is altered due to complex boundary interactions. Physically, they appear in fields like optics, acoustics, and quantum fluids, particularly when waves or solitons interact with corners of a medium or a confined geometry. Examples include nonlinear waveguides with sharp bends, polygonal traps in Bose-Einstein condensates, or diffraction of sound waves near architectural features.

Mathematically, such models are often governed by nonlinear partial differential equations like the nonlinear Schrödinger, sine-Gordon, or Klein-Gordon equations, but are frequently studied in angular or cornered domains. The presence of corners modifies the solution behavior significantly, sometimes giving rise to trapped or scattered soliton-like structures. A typical approach to studying these models is through boundary-adapted coordinates or employing numerical methods that respect the geometric singularity. When posed on a domain with a corner, the solution's behavior at the corner is influenced not only by nonlinearity but also by the angular geometry. Simulating these systems requires special attention to the boundary conditions and possibly singular behavior near the vertex of the corner. Applications of such models include corner-soliton localization, wave scattering, and energy concentration phenomena in confined nonlinear media.

The undamped wave equation in two dimensions is given as

$$\frac{\partial^2 u}{\partial t^2} = c^2(x,y)\left(\frac{\partial^2 u}{\partial x^2} + \frac{\partial^2 u}{\partial x^2}\right) + f(u) \tag{1.8.1}$$

where $c(x, y)$ denotes the phase speed and $f(u)$ represents a source or forcing term, which may be linear or nonlinear depending on the application. Numerical computations of acoustic wave propagation in two-dimensional heterogeneous media has been extensively investigated in [70, 71, 72, 73]. For systems governed by second-order time derivatives, it is a common strategy to reformulate them into equivalent first-order ODE systems, which are then advanced in time using methods such as Runge-Kutta or linear multistep schemes [74]. Nevertheless, classical Runge-Kutta-Nyström (RKN) methods offer a more direct approach for integrating second-order time derivatives by handling second-order systems without the need for such transformation. Various modifications and extensions of the RKN methods have been studied in [75, 76]. Stable numerical schemes for time-dependent diffusion problems have also been proposed by the authors in [77], who introduced a technique combining the hopscotch spatial arrangement with leapfrog-type temporal integration. Further developments involving odd-even hopscotch strategies can be found in [78, 79]. For spatial discretization, compact schemes are often preferred, as they provide higher accuracy using smaller stencils and better accommodate boundary conditions [54, 80, 81, 82, 83].

Energy preserving average vector field (AVF) methods have been effectively employed for solving Hamiltonian PDEs, as reported in [84, 85, 86, 87]. In [88], a compact higher-order finite difference scheme that conserves energy was proposed, achieving fourth-order spatial accuracy and second-order temporal accuracy for two-dimensional hyperbolic fractional systems. Additionally, the authors in [89] explored numerical simulations for the fractional Klein-Gordon-Zakharov equations from plasma physics, employing a second-order energy-preserving scheme. To solve such dynamical systems and to provide accurately solution it is required physical properties such as mass, momentum, and energy of the system to be satisfied as well.

In this study, we have developed an energy preserving partially implicit method for undamped acoustic and soliton wave equations in homogeneous and heterogeneous mediums, for which energy of the system will be conserved. Next, we have extended this idea of partially implicit methods which satisfies physical properties also for damped wave equations which is the extension of the classical wave equation. In case of damping, the total energy of the system decay with respect to time due to damping in the systems. So we have developed energy dissipation preserving method to study the stability properties and to simulate damped wave equation next.

The present work focuses on the development and analysis of space-time discretizing methods for solving linear and nonlinear homogeneous and inhomogeneous damped wave equations. The damped wave equation is given as

$$\frac{\partial^2 u}{\partial t^2} + a\frac{\partial u}{\partial t} = c^2(x,y)\left(\frac{\partial^2 u}{\partial x^2} + \frac{\partial^2 u}{\partial x^2}\right) + f(u) \tag{1.8.2}$$

where a is the damping coefficient and $f(u)$ is the forcing term. Numerical solutions of the nonlinear sine-Gordon and Klein-Gordon wave equations are discussed in [90, 91, 92, 93]. Simulation and analysis of the wave propagation with variable coefficients, such as non-constant permittivity or refractive index, are discussed in [94, 95, 96, 97, 98, 99]. Numerical simulation of the wave equations with variable coefficients are discussed in [100, 101, 102, 103, 104]. Higher-order AVF compact schemes for the solution of nonlinear wave equations are given in [105, 106, 66]. Numerical simulations of models admitting solitons, such as sine-Gordon and Klein-Gordon models are discussed in [63, 93]. Implicit approaches for solving PDEs are computationally expensive, as they require matrix inversions. The primary goal here is to establish and evaluate an energy dissipation-preserving method with enhanced stability, ensuring that computational costs are in line with those of explicit schemes for solving damped wave equations.

1.9 Thesis Outlines

The present thesis is structured as follows:

1. Chapter 2 focuses on the development of strong stability preserving multiderivative time integration methods for stiff reaction-diffusion systems. The proposed schemes are constructed to handle stiffness efficiently while ensuring numerical stability. The first-order multiderivative Runge-Kutta time-marching method is derived and tested on a range of nonlinear reaction-diffusion models, including the Gray-Scott, Schnakenberg, and the Brusselator models with or without cross-diffusion. Numerical experiments are used to validate the accuracy and stability of the methods, with error analysis based on maximum norm and comparison with established schemes. Stability analysis is performed to asses the numerical properties of the developed method.

2. Chapter 3 extends the multiderivative schemes to convection-diffusion problems. The emphasis is on designing computationally explicit schemes that retain SSP properties in the presence of sharp gradients and dominant convection effects. The developed computationally explicit multiderivative Runge-Kutta (CEMRK) method is used for time-integration, which provides second-order accuracy in time. Stability characteristics are also studied using Fourier analysis. The proposed schemes are applied to a series of convection-diffusion problems with a different combination of convection and diffusion coefficients. The methods demonstrate both robustness and improved accuracy in capturing essential features of the solution.

3. In Chapter 4, we have introduced a fully discrete, partially implicit energy-preserving scheme for undamped wave propagation in different media. For time discretization,

the proposed energy and dispersion relation preserving (EDRP) method is applied. The methods are tailored for both homogeneous and heterogeneous mediums and are analyzed for their dispersion-preserving properties. Fourier stability analysis is performed to asses the numerical properties of the developed method. For spatial discretization, we have used fourth-order compact scheme for the better accuracy in spatial direction. Theoretical convergence analysis and energy analysis is performed and also validated numerically. Numerical test cases include the sine-Gordon and Klein-Gordon equations, where soliton dynamics and acoustic wave propagation are accurately captured. The ability of the method to conserve energy over long simulation times is confirmed through various test cases.

4. Chapter 5 extends the energy-preserving approach to handle damped wave equations which is an extension of classical wave equation, where energy dissipation plays a critical role. A space-time discretization strategy is developed to retain dispersion accuracy while capturing the decay in wave energy due to damping. The formulated energy-dispersion preserving methods (EDPM) are partially implicit in nature and provide first- and second-order accuracy in time. Fourier analysis is used to assess the stability properties, and numerical simulations for both linear and nonlinear damped wave equations are presented.

5. Chapter 6 presents an overall summary of the key findings from the previous chapters and offers concluding remarks. It also outlines several directions for future research, including the extension of the proposed methods to three-dimensional and unbounded domains, adaptive meshing, and integration with machine learning models. These recommendations aim to broaden the applicability and performance of the developed numerical schemes in scientific and engineering applications.

All figures and tables are arranged chapter-wise and appear sequentially based on their first mention within the text.

Chapter 2

Multiderivative strong stability preserving methods for stiff reaction-diffusion systems [1]

In this chapter, strong stability preserving (SSP) multiderivative Runge-Kutta methods are developed to solve stiff reaction-diffusion systems introduced in Chapter 1. Spatial discretization of the governing PDEs results in a system of ODEs of the form as given in Eq. (1.4.2). Originally, the SSP methods are developed by the authors in [30, 31] and further extended in [32]. SSP methods are based on the principle that the obtained ODE system, after time discretization by applying a first-order Euler scheme, maintains strong stability properties under a given norm.

The SSP methods described in [30, 31] retain the convex functional characteristics of the forward Euler method and are able to produce higher-order accurate solutions. Generally, the system in Eq. (1.4.2) satisfy two conditions, the first is forward Euler condition and second is backward derivative conditions [37]. This chapter focuses on formulating two-derivative Runge-Kutta methods that are unconditionally SSP and computationally explicit. Moreover, as the developed methods satisfy the SSP condition, they also maintain positivity property.

---

[1] This work has been published in the *Mathematics and Computers in Simulation*, 225, (2024), 267–282.

While the methods proposed in [37] require numerical inversion of the coefficient matrix due to their implicit nature, and impose time-step restrictions in their implicit-explicit (IMEX) variants due to the explicit handling of non-stiff components. The developed methods do not require numerical inversion of the coefficient matrix. In this work, we have developed a class of multiderivative Runge-Kutta methods that are both computationally explicit and satisfy unconditionally SSP property. The structure of the Chapter 2 is as follows. Section 2.1 outlines the formulation of the proposed two-derivative Runge-Kutta methods and demonstrates that the developed methods satisfy the SSP condition without time-step restriction. A linear stability using Fourier analysis is also presented in Section 2.2. Finally, Section 2.3, a series of numerical simulations were conducted on several reaction-diffusion systems, such as the Brusselator model with and without cross-diffusion, the Gray-Scott model, and the Schnakenberg system to validate the accuracy of the developed methods.

2.1 Formulation of SSP methods

The following section presents the development of multiderivative Runge-Kutta methods that are computationally explicit and possess strong stability properties for solving reaction-diffusion systems, given as

$$\begin{aligned}\frac{\partial u}{\partial t} &= \mathcal{F}(u) + \mathcal{G}(u), \quad x \in \Omega, \quad t > 0 && (2.1.1)\\ u|_{t=0} &= f_1(x), \quad x \in \Omega && (2.1.2)\\ u|_{x\in\partial\Omega} &= f_2(t), \quad t > 0 && (2.1.3)\end{aligned}$$

Here, the diffusion operator is denoted by $\mathcal{F}$, and the stiff reaction operator is represented by $\mathcal{G}$. The initial and boundary conditions are specified by the functions f_1 and f_2, respectively, where the boundary of the spatial domain $\Omega \subset \mathbb{R}^n$ (with $n = 1$ or 2) is denoted as $\partial\Omega$. The methods in [37] are differ from those we proposed, as the SSP multiderivative schemes developed here apply an implicit strategy to the terms $\mathcal{F}$, $\mathcal{G}$, and $\dot{\mathcal{G}}$. Despite this implicit treatment, the methods are formulated to be computationally explicit, thus avoid the requirement for coefficient matrices inversion. In an s-stage multiderivative Runge-

Kutta method, the intermediate stage solutions u^*, are computed through an implicit relation involving the unknown u, as highlighted in [107], and are defined as

$$\begin{aligned} u^{(1)} &= u^n \\ u_1^{*(i)} &= \Delta t \sum_{j=1}^{i-1} a_{ij} \mathcal{F}(u^{(j)}) - \Delta t \hat{a}_{ii} u_1^{*(i)} \\ u_2^{*(i)} &= \Delta t \sum_{j=1}^{i-1} b_{ij} \mathcal{G}(u^{(j)}) - \Delta t \hat{b}_{ii} u_2^{*(i)} \\ u_3^{*(i)} &= \Delta t^2 \sum_{j=1}^{i-1} c_{ij} \dot{\mathcal{G}}(u^{(j)}) - \Delta t \hat{c}_{ii} u_3^{*(i)} \\ u^{(i)} &= u^n + u_1^{*(i)} + u_2^{*(i)} + u_3^{*(i)}, \quad i = 2, 3, ..., s+1 \\ u^{n+1} &= u^{(s+1)} \end{aligned} \tag{2.1.4}$$

where $\dot{\mathcal{G}} = \frac{d\mathcal{G}}{dt}$. Here, the method's coefficients a_{ij}, b_{ij}, c_{ij} are defined as in the Butcher tableau (see [107]). The terms $\hat{a}_{ii}$, $\hat{b}_{ii}$, and $\hat{c}_{ii}$ are considered as the free-parameters [108]. When the condition $u^{n+1} = u^{(s+1)}$ holds true, a method is referred to as globally stiffly accurate (GSA) [109]. In matrix form, Eq. (2.1.4) can be expressed as

$$u = eu^n + \Delta t \hat{A} \mathcal{F}(u) + \Delta t \hat{B} \mathcal{G}(u) + \Delta t^2 \hat{C} \dot{\mathcal{G}}(u) \tag{2.1.5}$$

here $u = [u^{(1)}, u^{(2)}, ..., u^{(s+1)}]^T$, $e = [1, 1, 1, ..., 1]^T$, $\mathcal{F}(u) = [\mathcal{F}(u^{(1)}), \mathcal{F}(u^{(2)}), ..., \mathcal{F}(u^{(s+1)})]^T$, $\mathcal{G}(u) = [\mathcal{G}(u^{(1)}), \mathcal{G}(u^{(2)}), ..., \mathcal{G}(u^{(s+1)})]^T$, and $\dot{\mathcal{G}}(u) = [\dot{\mathcal{G}}(u^{(1)}), \dot{\mathcal{G}}(u^{(2)}), ..., \dot{\mathcal{G}}(u^{(s+1)})]^T$. Denoting $a_{ii} = \Delta t \hat{a}_{ii}$, $b_{ii} = \Delta t \hat{b}_{ii}$, and $c_{ii} = \Delta t \hat{c}_{ii}$, $(s+1) \times (s+1)$ matrices $\hat{A}$, $\hat{B}$, $\hat{C}$ are given as $\hat{A} = diag\left(0, \frac{1}{1+a_{22}}, \frac{1}{1+a_{33}}, ..., \frac{1}{1+a_{(s+1)(s+1)}}\right) A$, $\hat{B} = diag\left(0, \frac{1}{1+b_{22}}, \frac{1}{1+b_{33}}, ..., \frac{1}{1+b_{(s+1)(s+1)}}\right) B$, and $\hat{C} = diag\left(0, \frac{1}{1+c_{22}}, \frac{1}{1+c_{33}}, ..., \frac{1}{1+c_{(s+1)(s+1)}}\right) C$, where

$$A = \begin{bmatrix} 0 & 0 & 0 & ... & 0 \\ a_{21} & 0 & 0 & ... & 0 \\ a_{31} & a_{32} & 0 & ... & 0 \\ \vdots & \vdots & \ddots & \ddots & \vdots \\ a_{(s+1)1} & a_{(s+1)2} & ... & a_{(s+1)s} & 0 \end{bmatrix}, \quad B = \begin{bmatrix} 0 & 0 & 0 & ... & 0 \\ b_{21} & 0 & 0 & ... & 0 \\ b_{31} & b_{32} & 0 & ... & 0 \\ \vdots & \vdots & \ddots & \ddots & \vdots \\ b_{(s+1)1} & b_{(s+1)2} & ... & b_{(s+1)s} & 0 \end{bmatrix},$$

$$C = \begin{bmatrix} 0 & 0 & 0 & \dots & 0 \\ c_{21} & 0 & 0 & \dots & 0 \\ c_{31} & c_{32} & 0 & \dots & 0 \\ \vdots & \vdots & \ddots & \ddots & \vdots \\ c_{(s+1)1} & c_{(s+1)2} & \cdots & c_{(s+1)s} & 0 \end{bmatrix}$$

In the case of single-stage method ($s = 1$), Eq. (2.1.4) takes the form

$$\begin{aligned} u^{(1)} &= u^n \\ u^{(2)} &= u^n + \frac{\Delta t}{(1+a_{22})} a_{21} \mathcal{F}(u^{(1)}) + \frac{\Delta t}{(1+b_{22})} b_{21} \mathcal{G}(u^{(1)}) + \frac{\Delta t^2}{(1+c_{22})} c_{21} \dot{\mathcal{G}}(u^{(1)}) \\ u^{n+1} &= u^{(2)} \end{aligned} \tag{2.1.6}$$

Here single-stage method's coefficients are denoted as a_{21}, b_{21}, c_{21} with ($a_{21} = 1.0$, $b_{21} = 1.0$, $c_{21} = -1.0$), and a_{22}, b_{22}, and c_{22} are the free-parameters. Next, in subsection 2.1.1, consistency analysis is performed which confirms that the scheme presented in Eq. (2.1.6) is first-order accurate. Furthermore, it has been established in subsection 2.1.2 that the proposed schemes retain SSP properties without time-step limitations and, as a result, preserve positivity.

2.1.1 Consistency analysis

To determine the order of accuracy of the developed method, we performed consistency analysis. For this, we considered Eq. (2.1.1) given as

$$u_t = \mathcal{F}(u) + \mathcal{G}(u)$$

Eq. (2.1.6) can be expressed as follows

$$\frac{u^{n+1} - u^n}{\Delta t} = \frac{1}{(1+\Delta t \hat{a}_{22})} \mathcal{F}(u^n) + \frac{1}{(1+\Delta t \hat{b}_{22})} \mathcal{G}(u^n) - \frac{\Delta t}{(1+\Delta t \hat{c}_{22})} \dot{\mathcal{G}}(u^n) \tag{2.1.7}$$

Now, proceeding with a Taylor series expansion leads to

$$u^{n+1} = u^n + \Delta t u_t^n + \frac{\Delta t^2}{2!} u_{tt}^n + \mathcal{O}(\Delta t^3) \tag{2.1.8}$$

Substituting Eq. (2.1.8) into Eq. (2.1.7), the local truncation error T_n is given as

$$\begin{aligned} T_n &= \frac{1}{\Delta t}\left\{\left(u^n + \Delta t u_t^n + \frac{\Delta t^2}{2!}u_{tt}^n + \mathcal{O}(\Delta t^3)\right) - u^n\right\} - (1+\Delta t\hat{a}_{22})^{-1}\mathcal{F}(u^n)r \\ &\quad - (1+\Delta t\hat{b}_{22})^{-1}\mathcal{G}(u^n) + \Delta t(1+\Delta t\hat{c}_{22})^{-1}\dot{\mathcal{G}}(u^n) \\ &= (u_t - \mathcal{F}(u) - \mathcal{G}(u))^n + \mathcal{O}(\Delta t) \end{aligned} \tag{2.1.9}$$

Using $u_t - \mathcal{F}(u) - \mathcal{G}(u) = 0$, we have

$$T_n = \mathcal{O}(\Delta t)$$

It follows that this method is accurate to first order.

2.1.2 Multiderivative SSP Runge-Kutta methods

To establish the SSP property of the proposed multiderivative Runge-Kutta methods, we assume that the operators $\mathcal{F}$, $\mathcal{G}$ and $\dot{\mathcal{G}}$ maintain specific nonlinear stability properties with respect to a convex functional $\|.\|$. For this, it is require that the operators $\mathcal{F}$ and $\mathcal{G}$ given in Eq. (2.1.1) satisfy the forward Euler condition, expressed as

$$\|u + \Delta t\mathcal{F}(u)\| \leq \|u\| \qquad \forall\ \Delta t \leq k_1'\Delta t_{FE} \tag{2.1.10}$$

$$\|u + \Delta t\mathcal{G}(u)\| \leq \|u\| \qquad \forall\ \Delta t \leq k_2'\Delta t_{FE} \tag{2.1.11}$$

for some $\Delta t_{FE} > 0$, $k_1' > 0$ and $k_2' > 0$. Furthermore, the backward derivative condition for $\dot{\mathcal{G}}$, as outlined in [37], is expressed as

$$\left\|u - \Delta t^2\dot{\mathcal{G}}(u)\right\| \leq \|u\| \qquad \forall\ \Delta t^2 \leq k_3'\Delta t_{FE}^2 \tag{2.1.12}$$

for some $k_3' > 0$. The following result establishes the SSP property of the proposed multiderivative Runge–Kutta method.

Theorem 2.1.1. *Assume that the operators $\mathcal{F}$ and $\mathcal{G}$ satisfy the forward Euler conditions given in Ineqs. (2.1.10)-(2.1.11), and $\dot{\mathcal{G}}$ satisfy the backward derivative condition given in Ineq. (2.1.12) with respect to some convex functional $\|.\|$. Moreover, if the method given in Eq. (2.1.5) satisfies the following componentwise conditions*

$$A \geq 0, \quad B \geq 0, \quad C \leq 0, \tag{2.1.13}$$

then the given method preserves the strong stability property

$$\left\|u^{n+1}\right\| \leq \|u^n\| \tag{2.1.14}$$

under the time-step condition $\Delta t \leq J'_s \Delta t_{FE}$ *and* $\Delta t^2 \leq K'_s \Delta t^2_{FE}$*, where* $J'_s > 0,\ K'_s > 0.$

Proof. Eq. (2.1.4) defines the i^{th} stage of the developed s-stage, can be expressed as

$$u^{(i)} = u^n + \frac{\Delta t}{(1+a_{ii})}\sum_{j=1}^{i-1} a_{ij}\mathcal{F}(u^{(j)}) + \frac{\Delta t}{(1+b_{ii})}\sum_{j=1}^{i-1} b_{ij}\mathcal{G}(u^{(j)}) + \frac{\Delta t^2}{(1+c_{ii})}\sum_{j=1}^{i-1} c_{ij}\dot{\mathcal{G}}(u^{(j)}) \tag{2.1.15}$$

In the case of a single-stage method ($s = 1$), the expression becomes

$$\begin{aligned} u^{(1)} &= u^n \\ u^{(2)} &= u^n + \frac{\Delta t}{(1+a_{22})}a_{21}\mathcal{F}(u^{(1)}) + \frac{\Delta t}{(1+b_{22})}b_{21}\mathcal{G}(u^{(1)}) + \frac{\Delta t^2}{(1+c_{22})}c_{21}\dot{\mathcal{G}}(u^{(1)}) \\ u^{n+1} &= u^{(2)} \end{aligned} \tag{2.1.16}$$

Assuming $(1 + a_{22}) > 0,\ (1 + b_{22}) > 0, (1 + c_{22}) > 0$ and taking the norm on both sides, we have

$$\begin{aligned} \left\|u^{(2)}\right\| &= \left\|u^n + \frac{\Delta t}{(1+a_{22})}a_{21}\mathcal{F}(u^n) + \frac{\Delta t}{(1+b_{22})}b_{21}\mathcal{G}(u^n) + \frac{\Delta t^2}{(1+c_{22})}c_{21}\dot{\mathcal{G}}(u^n)\right\| \\ \left\|u^{(2)}\right\| &\leq \left\|\alpha_1 u^n + \Delta t\left\{\frac{a_{21}}{(1+a_{22})}\mathcal{F}(u^n) + \frac{b_{21}}{(1+b_{22})}\mathcal{G}(u^n)\right\}\right\| \\ &\quad + \left\|(1-\alpha_1)u^n - \Delta t^2\frac{|c_{21}|}{(1+c_{22})}\dot{\mathcal{G}}(u^n)\right\| \end{aligned}$$

where $0 \leq \alpha_1 \leq 1$, therefore

$$\begin{aligned} \left\|u^{(2)}\right\| &\leq \alpha_1\left\|\beta_{11}u^n + \Delta t\frac{a_{21}}{\alpha_1(1+a_{22})}\mathcal{F}(u^n) + (1-\beta_{11})u^n + \Delta t\frac{b_{21}}{\alpha_1(1+b_{22})}\mathcal{G}(u^n)\right\| \\ &\quad + (1-\alpha_1)\left\|u^n - \Delta t^2\frac{|c_{21}|}{(1-\alpha_1)(1+c_{22})}\dot{\mathcal{G}}(u^n)\right\| \end{aligned}$$

where $0 \leq \beta_{11} \leq 1$. Using the condition given in Ineq. (2.1.12), we have

$$\begin{aligned} \left\|u^{(2)}\right\| &\leq \alpha_1\beta_{11}\left\|u^n + \Delta t\frac{a_{21}}{\beta_{11}\alpha_1(1+a_{22})}\mathcal{F}(u^n)\right\| \\ &\quad + \alpha_1(1-\beta_{11})\left\|u^n + \Delta t\frac{b_{21}}{\alpha_1(1-\beta_{11})(1+b_{22})}\mathcal{G}(u^n)\right\| + (1-\alpha_1)\|u^n\| \end{aligned}$$

Using conditions given in Ineqs. (2.1.10) and (2.1.11), we have

$$\left\|u^{(2)}\right\| \leq \alpha_1 \left\{\beta_{11}\|u^n\| + (1-\beta_{11})\|u^n\|\right\} + (1-\alpha_1)\|u^n\|$$

for all $\Delta t \leq \dfrac{k_1'\beta_{11}\alpha_1(1+a_{22})}{a_{21}}\Delta t_{FE}$, $\Delta t \leq \dfrac{k_2'\alpha_1(1-\beta_{11})(1+b_{22})}{b_{21}}\Delta t_{FE}$ and $\Delta t^2 \leq \dfrac{k_3'(1-\alpha_1)(1+c_{22})}{|c_{21}|}\Delta t_{FE}^2$. Therefore, we have

$$\left\|u^{(2)}\right\| \leq \|u^n\| \tag{2.1.17}$$

for all $\Delta t \leq J_1 \Delta t_{FE}$ and $\Delta t^2 \leq K_1 \Delta t_{FE}^2$, where

$J_1 = \min\left\{\frac{k_1'\beta_{11}\alpha_1(1+a_{22})}{a_{21}}, \frac{k_2'\alpha_1(1-\beta_{11})(1+b_{22})}{b_{21}}\right\}$ and $K_1 = \left\{\frac{k_3'(1-\alpha_1)(1+c_{22})}{|c_{21}|}\right\}$. As α_1, β_{11}, a_{22}, b_{22} and c_{22} are the free-parameters, thus Ineq. (2.1.17) hold for any Δt.

Next, assume that for the i^{th} stage of s-stage method, $(i-1)$ stages satisfy $\left\|u^{(i)}\right\| \leq \|u^n\|$ for all $\Delta t \leq J_{s-1}'\Delta t_{FE}$ and $\Delta t^2 \leq K_{s-1}'\Delta t_{FE}^2$, where $J_{s-1}' > 0$, $K_{s-1}' > 0$ and $J_{s-1}' = \min\{J_1,\ J_2, ..., J_p\}$, $J_p = \min\left\{\Gamma^a_{\beta_{ij}}, \Gamma^a_{\alpha\beta_{ij}}, \Gamma^b_{\beta_{ij}}, \Gamma^b_{\alpha\beta_{ij}}\right\}$, $K_{s-1}' = \min\{K_1, K_2, ..., K_p\}$, $K_p = \min\left\{\Omega^c_{ij}, \Omega^c_{\alpha_{ij}}\right\}$, $\Gamma^a_{\beta_{ij}} = \frac{k_1'\beta_{pq}(1+a_{ii})(1+a_{i-1i-1})}{a_{ij}(1+a_{i-1i-1})-a_{i-1j}(1+a_{ii})}$, $\Gamma^b_{\beta_{ij}} = \frac{k_2'(1-\beta_{pq})(1+b_{ii})(1+b_{i-1i-1})}{b_{ij}(1+b_{i-1i-1})-b_{i-1j}(1+b_{ii})}$, $\Omega^c_{ij} = \frac{k_3'(1+c_{ii})(1+c_{i-1i-1})}{|c_{i-1j}|(1+c_{ii})-|c_{ij}|(1+c_{i-1i-1})}$, when $j < i-1$, $q < p$, and $\Gamma^a_{\alpha\beta_{ij}} = \frac{k_1'\beta_{pq}\alpha_p(1+a_{ii})}{a_{ij}}$, $\Gamma^b_{\alpha\beta_{ij}} = \frac{k_2'(1-\beta_{pq})\alpha_p(1+b_{ii})}{b_{ij}}$, $\Omega^c_{\alpha_{ij}} = \frac{k_3'(1-\alpha_p)(1+c_{ii})}{|c_{ij}|}$, when $j = i-1$, $q = p$. Where $p \in \{1, 2, \ldots, s-1\}$, $q = 1, 2, \ldots, p$, $i = 2, ..., s$, $j = 1, ..., i-1$.

To conclude, now focus on the last stage ($i = s+1$), which depends on all prior $(i-1)$ stages

$$\begin{aligned} u^{(i-1)} &= u^n + \frac{\Delta t}{(1+a_{i-1i-1})}\sum_{j=1}^{i-2} a_{i-1j}\mathcal{F}(u^{(j)}) + \frac{\Delta t}{(1+b_{i-1i-1})}\sum_{j=1}^{i-2} b_{i-1j}\mathcal{G}(u^{(j)}) \\ &\quad - \frac{\Delta t^2}{(1+c_{i-1i-1})}\sum_{j=1}^{i-2} |c_{i-1j}|\dot{\mathcal{G}}(u^{(j)}) \qquad (2.1.18) \\ u^{(i)} &= u^n + \frac{\Delta t}{(1+a_{ii})}\sum_{j=1}^{i-1} a_{ij}\mathcal{F}(u^{(j)}) + \frac{\Delta t}{(1+b_{ii})}\sum_{j=1}^{i-1} b_{ij}\mathcal{G}(u^{(j)}) \\ &\quad - \frac{\Delta t^2}{(1+c_{ii})}\sum_{j=1}^{i-1} |c_{ij}|\dot{\mathcal{G}}(u^{(j)}) \qquad (2.1.19) \end{aligned}$$

$$\begin{aligned} u^{(i)} &= u^n + \frac{\Delta t}{(1+a_{ii})}\left(\sum_{j=1}^{i-2} a_{ij}\mathcal{F}(u^{(j)}) + a_{ii-1}\mathcal{F}(u^{(i-1)})\right) \\ &\quad + \frac{\Delta t}{(1+b_{ii})}\left(\sum_{j=1}^{i-2} b_{ij}\mathcal{G}(u^{(j)}) + b_{ii-1}\mathcal{G}(u^{(i-1)})\right) \\ &\quad - \frac{\Delta t^2}{(1+c_{ii})}\left(\sum_{j=1}^{i-2} |c_{ij}|\dot{\mathcal{G}}(u^{(j)}) + |c_{ii-1}|\dot{\mathcal{G}}(u^{(i-1)})\right) \end{aligned} \tag{2.1.20}$$

From Eqs. (2.1.18) and (2.1.20), we obtain

$$\begin{aligned} u^{(i)} &= \Bigg\{ u^{(i-1)} - \frac{\Delta t}{(1+a_{i-1i-1})}\sum_{j=1}^{i-2} a_{i-1j}\mathcal{F}(u^{(j)}) - \frac{\Delta t}{(1+b_{i-1i-1})}\sum_{j=1}^{i-2} b_{i-1j}\mathcal{G}(u^{(j)}) \\ &\quad + \frac{\Delta t^2}{(1+c_{i-1i-1})}\sum_{j=1}^{i-2} |c_{i-1j}|\dot{\mathcal{G}}(u^{(j)}) \Bigg\} \\ &\quad + \frac{\Delta t}{(1+a_{ii})}\sum_{j=1}^{i-2} a_{ij}\mathcal{F}(u^{(j)}) + \frac{\Delta t}{(1+a_{ii})} a_{ii-1}\mathcal{F}(u^{(i-1)}) \\ &\quad + \frac{\Delta t}{(1+b_{ii})}\sum_{j=1}^{i-2} b_{ij}\mathcal{G}(u^{(j)}) + \frac{\Delta t}{(1+b_{ii})} b_{ii-1}\mathcal{G}(u^{(i-1)}) \\ &\quad - \frac{\Delta t^2}{(1+c_{ii})}\sum_{j=1}^{i-2} |c_{ij}|\dot{\mathcal{G}}(u^{(j)}) - \frac{\Delta t^2}{(1+c_{ii})} |c_{ii-1}|\dot{\mathcal{G}}(u^{(i-1)}) \end{aligned}$$

$$\begin{aligned} \left\|u^{(i)}\right\| &\leq \left\| \beta_{ss-1}u^{(j)} + \Delta t \sum_{j=1}^{i-2}\left(\frac{a_{ij}}{(1+a_{ii})} - \frac{a_{i-1j}}{(1+a_{i-1i-1})}\right)\mathcal{F}(u^{(j)}) \right\| \\ &\quad + \left\| (1-\beta_{ss-1})u^{(j)} + \Delta t \sum_{j=1}^{i-2}\left(\frac{b_{ij}}{(1+b_{ii})} - \frac{b_{i-1j}}{(1+b_{i-1i-1})}\right)\mathcal{G}(u^{(j)}) \right\| \\ &\quad + \left\| -\left(u^{(j)} - \Delta t^2 \sum_{j=1}^{i-2}\left(\frac{|c_{i-1j}|}{(1+c_{i-1i-1})} - \frac{|c_{ij}|}{(1+c_{ii})}\right)\dot{\mathcal{G}}(u^{(j)}) \right) \right\| \\ &\quad + \left\| \alpha_s u^{(i-1)} + \Delta t \frac{a_{ii-1}}{(1+a_{ii})}\mathcal{F}(u^{(i-1)}) + \Delta t \frac{b_{ii-1}}{(1+b_{ii})}\mathcal{G}(u^{(i-1)}) \right\| \\ &\quad + \left\| (1-\alpha_s)u^{(i-1)} - \Delta t^2 \frac{|c_{ii-1}|}{(1+c_{ii})}\dot{\mathcal{G}}(u^{(i-1)}) \right\| \end{aligned}$$

$$\left\|u^{(i)}\right\| \leq \beta_{ss-1}\left\| u^{(j)} + \Delta t \sum_{j=1}^{i-2}\left(\frac{a_{ij}}{\beta_{ss-1}(1+a_{ii})} - \frac{a_{i-1j}}{\beta_{ss-1}(1+a_{i-1i-1})}\right)\mathcal{F}(u^{(j)}) \right\|$$

$$\begin{aligned}
&+(1-\beta_{ss-1})\left\| u^{(j)} + \Delta t \sum_{j=1}^{i-2}\left(\frac{b_{ij}}{(1-\beta_{ss-1})(1+b_{ii})} - \frac{b_{i-1j}}{(1-\beta_{ss-1})(1+b_{i-1i-1})}\right)\mathcal{G}(u^{(j)})\right\| \\
&+\left\| -\left(u^{(j)} - \Delta t^2 \sum_{j=1}^{i-2}\left(\frac{|c_{i-1j}|}{(1+c_{i-1i-1})} - \frac{|c_{ij}|}{(1+c_{ii})}\right)\dot{\mathcal{G}}(u^{(j)})\right)\right\| \\
&+\alpha_s\beta_{ss}\left\| u^{(i-1)} + \Delta t\frac{a_{ii-1}}{\beta_{ss}\alpha_s(1+a_{ii})}\mathcal{F}(u^{(i-1)})\right\| \\
&+\alpha_s(1-\beta_{ss})\left\| u^{(i-1)} + \Delta t\frac{b_{ii-1}}{(1-\beta_{ss})\alpha_s(1+b_{ii})}\mathcal{G}(u^{(i-1)})\right\| \\
&+(1-\alpha_s)\left\| u^{(i-1)} - \Delta t^2\frac{|c_{ii-1}|}{(1-\alpha_s)(1+c_{ii})}\dot{\mathcal{G}}(u^{(i-1)})\right\|
\end{aligned}$$

where $0 \leq \alpha_s \leq 1$, $0 \leq \beta_{ss-1} \leq 1$, $0 \leq \beta_{ss} \leq 1$.

Taking into account that $\left\|u^{(i)}\right\| \leq \|u^n\|$ holds for earlier $(i-1)$ stages, together with the conditions in Ineqs. (2.1.10) - (2.1.12), we conclude

$$\begin{aligned}
\left\|u^{(i)}\right\| \leq \beta_{ss-1}\|u^n\| + (1-\beta_{ss-1})\|u^n\| + \|u^n\| + \alpha_{ss}(\beta_{ss}\|u^n\| + (1-\beta_{ss})\|u^n\|) \\
+ (1-\alpha_s)\|u^n\|
\end{aligned}$$

which provides, $\left\|u^{(i)}\right\| \leq \|u^n\|$ for all $\Delta t \leq J_s'\Delta t_{FE}$ and $\Delta t^2 \leq K_s'\Delta t_{FE}^2$, where $J_s' > 0$, $K_s' > 0$ and $J_s' = \min\{J_1, J_2, \ldots, J_p\}$, $K_s' = \min\{K_1, K_2, \ldots, K_p\}$, $p \in \{1, 2, \ldots, s\}$. This completes the proof. $\square$

Remark: As methods that preserve strong stability also preserve positivity, the presented multiderivative Runge-Kutta SSP methods will inherit this property.

2.2 Fourier stability analysis

To perform the Fourier analysis, we consider a two-dimensional (2D) linear reaction-diffusion equation subject to periodic boundary conditions, expressed as

$$\begin{aligned}
&\frac{\partial u}{\partial t} = D\left(\frac{\partial^2 u}{\partial x^2} + \frac{\partial^2 u}{\partial y^2}\right) - Ru, \quad (x,y) \in [0,\pi]^2, \quad t > 0 \\
&u|_{t=0} = g(x,y), \quad (x,y) \in [0,\pi]^2
\end{aligned} \tag{2.2.1}$$

where the diffusion and reaction coefficients are represented by D and R, respectively. Using the Fourier transform, the unknown u can be expressed as

$$u(x, y, t) = \int_{-\infty}^{\infty} \int_{-\infty}^{\infty} \hat{u}(k_x, k_y, t) e^{i(k_x x + k_y y)} dk_x dk_y$$

where $\hat{u}$ is the Fourier transform of u, and k_x, k_y are the wavenumbers in x and y directions, respectively. Using Fourier transform, Eq. (2.2.1) can be expressed as

$$\begin{aligned} \frac{\partial \hat{u}}{\partial t} &= -[D(k_x^2 + k_y^2) + R]\hat{u} \\ \hat{u}|_{t=0} &= \hat{g}(k_x, k_y) \end{aligned} \tag{2.2.2}$$

By applying discrete Fourier transform, the unknown u and its spatial derivatives can be expressed as [110]

$$\begin{aligned} u(x, y, t)|_N &= \int_{-k_x^*}^{k_x^*} \int_{-k_y^*}^{k_y^*} \breve{u}(k_x, k_y, t) e^{i(k_x x + k_y y)} dk_x dk_y \\ u_{zz}(x, y, t)|_N &= \int_{-k_x^*}^{k_x^*} \int_{-k_y^*}^{k_y^*} -k_{z_{md}}^2 \breve{u}(k_x, k_y, t) e^{i(k_x x + k_y y)} dk_x dk_y \end{aligned} \tag{2.2.3}$$

where $z = x, y$, $k_{z_{md}}^2$ is the modified wavenumber, and $k_x^* = \pi/\Delta x$ and $k_y^* = \pi/\Delta y$. By applying discrete Fourier transform as in Eq. (2.2.3), semi-discrete system is given as

$$\begin{aligned} \frac{\partial \breve{u}^n}{\partial t} &= -[D(k_{x_{md}}^2 + k_{y_{md}}^2) + R]\breve{u}^n \\ \breve{u}|_{t=0} &= \breve{g}(k_x, k_y) \end{aligned} \tag{2.2.4}$$

where n is the time level. For the second-order centered difference (CD2) scheme, the modified wavenumber is obtained as, $k_{z_{md}}^2 = \frac{-2(cos(k_z \Delta z) - 1)}{\Delta z^2}$. Using Eq. (2.2.4), the amplification factor ($\lambda_N = \frac{\breve{u}^{n+1}}{\breve{u}^n}$) [110, 83] for the developed method with CD2 for spatial discretization scheme is expressed as

$$\lambda_N = 1 - \frac{R_o}{(1 + \hat{b}_{22} R_o)} - \frac{R_o^2}{(1 + \hat{c}_{22} R_o)} + 2(\cos k_x h + \cos k_y h - 2) \left[\frac{F_o}{(1 + \hat{a}_{22} F_o)} + \frac{R_o F_o}{(1 + \hat{c}_{22} R_o)} \right]$$

Here $F_o = D\Delta t/h^2$ express the grid Fourier (diffusion) number and $R_o = R\Delta t$ the reaction number [111], where uniform spatial step-size is denoted by $h = \Delta x = \Delta y$. The stability criterion is defined as $|\lambda_N| \leq 1$. Since $|\lambda_N|$ depends on certain free parameters, any unstable regions (where ($|\lambda_N| > 1$)) for specified diffusion and reaction numbers can be excluded by appropriately selecting the parameters $\hat{a}_{22}$, $\hat{b}_{22}$, and $\hat{c}_{22}$. This is achieved by minimizing the L^2 norm of the amplification error $\big(\big||\lambda_N| - 1\big|\big)$ [83].

2.3 Simulations of reaction-diffusion systems

Numerical simulations are conducted for a range of test problems in both one and two spatial dimensions, and the results are compared with those obtained using established reference methods. The numerical computations are performed on a PC that is equipped with six Intel cores (i5-10500 CPU @ 3.10GHz, x86_64) having 16GB of memory. Moreover, all simulations are performed using Fortran 90 (serial) codes with gfortran compiler (7.4.0). For spatial discretization, a second-order centered difference scheme is employed to approximate the Laplacian operator.

2.3.1 Linear reaction-diffusion system

To begin, we assess the performance of the proposed method on a one-dimensional reaction-diffusion system for which analytical solutions are available [112]. The governing equations are given as

$$\begin{aligned} \frac{\partial u}{\partial t} &= D\frac{\partial^2 u}{\partial x^2} - R_1 u + v, \quad x \in [0, \pi/2],\ t \in [0, T], \\ \frac{\partial v}{\partial t} &= D\frac{\partial^2 v}{\partial x^2} - R_2 v, \quad x \in [0, \pi/2],\ t \in [0, T] \end{aligned} \tag{2.3.1}$$

where R_1, R_2 represent the rates of reaction, and D denotes the diffusion coefficient. Boundary conditions are specified as

$$\frac{\partial u}{\partial x}(0, t) = \frac{\partial v}{\partial x}(0, t) = 0, \quad u(\pi/2, t) = v(\pi/2, t) = 0 \tag{2.3.2}$$

The exact solution of the system in Eqs. (2.3.1)-(2.3.2) is given as

$$\begin{aligned} u(x, t) &= \big(e^{-(R_1+D)t} + e^{-(R_2+D)t}\big)\cos(x), \\ v(x, t) &= (R_1 - R_2)e^{-(R_2+D)t}\cos(x) \end{aligned} \tag{2.3.3}$$

Initial conditions for solutions u and v are taken from the analytical solution. For discretizing in spatial direction, a second-order central difference scheme is employed, incorporating a consistent treatment of the homogeneous Neumann (no-flux) boundary condition at the left boundary ($x = 0$) and zero Dirichlet boundary condition at the right ($x = \pi/2$) boundary. In all numerical simulations, the spatial mesh is chosen to be sufficiently fine such that temporal errors dominate. All computations are carried out up to the final time $T = 1$, using 512 uniform spaced mesh points in the spatial domain, as in [112]. Furthermore, the proposed methods are tested under various conditions for the system (2.3.1–2.3.2) and compared with existing approaches to assess the performance.

2.3.1.1 Reaction-dominated systems with or without stiff reactions

To begin, we consider a reaction-dominated system with coefficients $(R_1, R_2, D) = (2, 1, 0.001)$, as outlined in [112]. In this case, numerical errors are primarily caused by approximation from the treatment of the reaction term. The performance of constructed scheme is compared with the explicit third-order total variation diminishing (TVD) Runge-Kutta (RK3) [32]. Table 2.1 summarizes the results in terms of the L^∞-error norm and CPU execution time.

From Table 2.1 it is evident that the present scheme allows a much larger time-step (8 times) as compared to the RK3-CD2 method. It is also evident from Table 2.1 that the errors for the present method are almost of the same order of magnitude as for CN-MG-CD2 and IIF2-CD2 methods [112] (Table 3.2, p. 521). Furthermore, since both CN-MG-CD2 and IIF2-CD2 methods are implicit in nature, they demonstrate convergence rates consistent with their theoretical orders, as reported in Table 3.2, [112]. Next, we investigate the case involving stiff reactions in a reaction-dominated regime, defined by the coefficients $(R_1, R_2, D) = (100, 1, 0.001)$ [112]. Table 2.2 compares the performance of the proposed scheme with that of the RK3-CD2 method [32], based on both the L^∞-error and CPU time. Consistent with observations for the reaction-dominated case without stiff reaction (see Table 2.1), the results in Table 2.2 indicate that the present scheme permits a significantly larger time-step (up to eight times) greater than the RK3-CD2 method. Moreover, the errors obtained by the proposed method are found to be of similar

Table 2.1: Numerical results comparing L^{∞}-error and CPU time (in seconds) for indicated methods applied to a reaction-dominated case without stiff reaction: $(R_1, R_2, D) = (2, 1, 0.001)$. For the constructed scheme, the values assigned to the free parameters are $a_{22} = 3.0582, b_{22} = -5.9000 \times 10^{-4}, c_{22} = 1.0064$. NC represents that the method does not converge.

	Present Method - CD2			RK3 - CD2		
Δt	$L^{\infty} - error$	ERC	CPU time	$L^{\infty} - error$	ERC	CPU time
4.00×10^{-2}	3.38×10^{-4}	–	0.0015	–	–	NC
2.00×10^{-2}	6.40×10^{-5}	2.4009	0.0027	–	–	NC
1.00×10^{-2}	8.24×10^{-6}	2.9573	0.0034	–	–	NC
5.00×10^{-3}	8.41×10^{-7}	3.2925	0.0070	1.29×10^{-8}	–	0.0100
2.50×10^{-3}	6.49×10^{-7}	0.3739	0.0136	1.26×10^{-9}	3.3559	0.0200
1.25×10^{-3}	4.31×10^{-7}	0.5905	0.0272	1.88×10^{-10}	2.7446	0.0400

magnitude to those reported for CN-MG-CD2 and IIF2-CD2 methods in [112] (Table 3.3, p. 522). As in the reaction-dominated case without stiff reaction, both CN-MG-CD2 and IIF2-CD2 exhibit convergence rates consistent with their theoretical accuracy for the stiff reactions in reaction-dominated case as well (Table 3.3, [112]).

From Tables 2.1 and 2.2, we observe that the expected theoretical order of convergence is not achieved for the tested methods when the diffusion coefficient is $D = 0.001$. This behavior arises because the numerical errors are primarily dominated by the diffusion process, rather than the numerical accuracy of the time integration scheme. As a result, further reduction in the time-step does not lead to significant improvements in accuracy, leading to error stagnation. The diffusion term tends to smooth the solution, making it difficult for the numerical methods to capture sharp spatial features. Consequently, the dominant source of error is associated with diffusion-induced smoothing rather than the numerical method itself. Therefore, due to the dominant error arises from diffusion-induced smoothing, the stagnation of error is observed with smaller time-steps.

Next, to highlight the influence of reaction parameters (R_1, R_2) on the approximated solutions, Tables 2.1 and 2.2 compare the obtained results, both corresponding to the same

Table 2.2: Numerical results comparing L^{∞}-error and CPU time (in seconds) for indicated methods applied to a reaction-dominated case with stiffness: $(R_1, R_2, D) = (100, 1, 0.001)$. For the constructed scheme, the values assigned to the free parameters are $a_{22} = 2.5800, b_{22} = 1.1200 \times 10^{-3}, c_{22} = 6.3690$. NC represents that the method does not converge.

	Present Method - CD2			RK3 - CD2		
Δt	$L^{\infty} - error$	ERC	CPU time	$L^{\infty} - error$	ERC	CPU time
4.00×10^{-2}	1.86×10^{-2}	–	0.0017	–	–	NC
2.00×10^{-2}	2.02×10^{-3}	3.2028	0.0030	–	–	NC
1.00×10^{-2}	6.66×10^{-4}	1.6008	0.0035	–	–	NC
5.00×10^{-3}	6.57×10^{-6}	6.6635	0.0091	1.96×10^{-1}	–	0.0100
2.50×10^{-3}	3.42×10^{-4}	-5.7019	0.0178	4.75×10^{-11}	31.9422	0.0200
1.25×10^{-3}	5.09×10^{-4}	-0.5737	0.0310	2.58×10^{-10}	-2.4414	0.0400

diffusion coefficient ($D = 0.001$). From these tables, it is evident that when the diffusion parameter is fixed, the reaction-dominated case without stiff reaction (involving smaller values of reaction parameters) leads to more consistent convergence rates. In contrast, in the stiff reaction case (where the reaction parameters are large), the convergence rates tend to fluctuate more significantly due to the formation of steep gradients. Moreover, in the case where diffusion coefficient is further reduced and the reaction parameters remain small (as in reaction dominated case without stiff reaction), such as if we choose $(R_1, R_2, D) = (2, 1, 0.0001)$, the computed convergence rates for both numerical methods agree well with their theoretical order of convergence, as displayed in Table 2.3.

2.3.1.2 Diffusion-dominated case

Next, we analyze the performance of the proposed method for a diffusion-dominated case defined by $(R_1, R_2, D) = (0.1, 0.01, 1)$ [112]. Table 2.4 compares the numerical L^{∞} error and CPU time obtained applying the proposed scheme and the RK3-CD2 method. It is evident from the Table 2.4 that the proposed method remains effective even with significantly larger time-steps, whereas the RK3-CD2 method fails for $\Delta t > 5 \times 10^{-6}$.

Table 2.3: Numerical results comparing L^∞-error and CPU time (in seconds) for indicated methods applied to a reaction-dominated case with reduced diffusion: $(R_1, R_2, D) = (2, 1, 0.0001)$. For the constructed scheme, the values assigned to the free parameters are $a_{22} = 7.5000$, $b_{22} = -1.0000 \times 10^{-4}$, $c_{22} = 8.0000 \times 10^{-1}$.

	Present method - CD2			RK3 - CD2		
Δt	$L^\infty - error$	ERC	CPU time	$L^\infty - error$	ERC	CPU time
4.00×10^{-2}	2.55×10^{-3}	–	0.0017	7.17×10^{-6}	–	0.0030
2.00×10^{-2}	1.12×10^{-3}	1.1869	0.0030	8.70×10^{-7}	3.0430	0.0049
1.00×10^{-2}	5.18×10^{-4}	1.1125	0.0035	1.07×10^{-7}	3.0219	0.0071
5.00×10^{-3}	2.41×10^{-4}	1.1039	0.0070	1.33×10^{-8}	3.0145	0.0114
2.50×10^{-3}	1.09×10^{-4}	1.1447	0.0140	1.62×10^{-9}	3.0358	0.0201

Furthermore, comparing Table 2.4 with Table 3.1 (p. 520) in [112] shows that CN-MG-CD2 and IIF2-CD2 schemes achieve lower errors than the present method. This improved accuracy of IIF2 is because of its exact treatment of linear diffusion terms, which enables it to provide more accurate results at relatively larger time-steps in diffusion-dominated case (Table 3.1, [112]).

Table 2.4 corresponds to the diffusion-dominated case characterized by the parameter set $(R_1, R_2, D) = (0.1, 0.01, 1)$, where the diffusion coefficient is significantly larger than the reaction parameters. Due to the smoothing nature of diffusion, the numerical method faces difficulty in resolving sharp gradients over time, even when temporal accuracy is maintained. Consequently, the observed numerical error arises primarily from diffusion-induced smoothing rather than the numerical method itself. Since the solution evolves slowly due to the dominant diffusion effect, this leads to stagnation in error reduction with respect to time-step refinement, as reflected in Table 2.4.

2.3.2 The Brusselator model

This section focuses on the two-dimensional reaction-diffusion Brusselator model [24] discussed in Chapter 1. Detailed discussion about its suitability for a hypothetical tri-

Table 2.4: Numerical results comparing L^∞-error and CPU time (in seconds) for indicated methods applied to a diffusion-dominated case: $(R_1, R_2, D) = (0.1, 0.01, 1)$. For the constructed scheme, the values assigned to the free parameters are $a_{22} = 1.1411 \times 10^4$, $b_{22} = -9.7437 \times 10^{-1}$, $c_{22} = 3.0000 \times 10^2$. NC indicates that the method does not converge.

	Present method - CD2		RK3 - CD2	
Δt	$L^\infty - error$	CPU time	$L^\infty - error$	CPU time
4.00×10^{-2}	7.91×10^{-3}	0.0029	–	NC
2.00×10^{-2}	4.03×10^{-3}	0.0017	–	NC
1.00×10^{-2}	2.03×10^{-3}	0.0034	–	NC
5.00×10^{-3}	1.02×10^{-3}	0.0069	–	NC
5.00×10^{-6}	9.04×10^{-7}	6.6439	5.4677×10^{-7}	8.0187
2.50×10^{-6}	3.91×10^{-7}	13.2687	5.4676×10^{-7}	16.0880
1.25×10^{-6}	3.55×10^{-7}	26.5305	5.4673×10^{-7}	32.0087
6.25×10^{-7}	2.38×10^{-7}	53.0294	5.4669×10^{-7}	64.1695

molecular reaction is given in [25]. Numerical simulation of this model poses significant challenges due to higher dimensionality, stiffness of both reaction and diffusion terms, and the nonlinear nature of the reaction term. The Brusselator model [113] in two dimensions is given in Eq. (1.3.1) in spatial domain Ω with the boundary conditions as follows

$$\frac{\partial u}{\partial n} = \frac{\partial v}{\partial n} = 0, \quad (x, y) \in \partial\Omega, \quad t \in [0, T] \tag{2.3.4}$$

considering the following initial conditions

$$u(x, y, t)|_{t=0} = 0.5 + y, \quad v(x, y, t)|_{t=0} = 1 + 5x \tag{2.3.5}$$

Here n represents the outward normal unit vector. For numerical simulations, we have chosen the following parameters $R_1 = 3.4$, $R_2 = 1$, $D_1 = D_2 = 0.002$ as given in [113, 114]. The spatial computational domain is defined as $\Omega = [0, 1]^2$. We specified the values of the method's free-parameters as $a_{22} = 3.9000 \times 10^2$, $b_{22} = 9.9950 \times 10^3$, $c_{22} = 9.9900 \times 10^3$. Simulations are performed using fixed uniform spatial mesh-width $h = 0.0125$, while

Table 2.5: Numerical results comparing L^∞-error and CPU time (in seconds) for indicated methods applied to Eq. (1.3.1) with initial conditions provided in Eq. (2.3.5). For the constructed scheme, the values assigned to the free parameters are $a_{22} = 3.9000 \times 10^2$, $b_{22} = 9.9950 \times 10^3$, $c_{22} = 9.9900 \times 10^3$. NC indicates that the method does not converge.

	Present method - CD2			RK3 - CD2		
Δt	$L^\infty - error$	ERC	CPU time	$L^\infty - error$	ERC	CPU time
1.0000×10^{-1}	1.65×10^{-3}	–	0.0231	–	–	NC
5.0000×10^{-2}	8.23×10^{-4}	1.0059	0.0319	–	–	NC
2.5000×10^{-2}	4.08×10^{-4}	1.0103	0.0341	–	–	NC
1.2500×10^{-2}	2.01×10^{-4}	1.0199	0.0678	1.07×10^{-4}	–	0.1169
6.2500×10^{-3}	9.79×10^{-5}	1.0402	0.1499	1.35×10^{-5}	2.9835	0.2431
3.1250×10^{-3}	4.62×10^{-5}	1.0837	0.2835	1.70×10^{-6}	2.9933	0.4738
1.5625×10^{-3}	2.03×10^{-5}	1.1835	0.5354	2.11×10^{-7}	3.0083	0.9148
7.8125×10^{-4}	7.41×10^{-6}	1.4564	1.0687	2.46×10^{-8}	3.1008	1.8174

varying Δt to compute the L^∞-error and estimated rate of convergence (ERC). The ERC is computed as $\log\big(E_{\Delta t}/E_{\Delta t/2}\big)/\log(2)$ for the final time $T = 2$.

Table 2.5 compares the numerical results obtained using the proposed method and the RK3 scheme in terms of maixmum norm L^∞-error, ERC, and CPU time (in seconds). The data presented in Table 2.5 clearly demonstrate that the proposed method supports significantly larger time-steps than the RK3-CD2 method, while both approaches exhibit their expected theoretical convergence rates.

Moreover, Table 2.5 shows that for a relatively higher error tolerance (say 1.0×10^{-3}), the proposed method requires less CPU time than the RK3-CD2 scheme. However, at a lower error tolerance (say 1.0×10^{-5}), RK3-CD2 outperforms the proposed method in terms of computational efficiency. This behavior can be attributed to the higher-order accuracy of RK3-CD2, when stable (i.e. when it converges, $\Delta t \leq 1.25 \times 10^{-2}$), its error decreases more rapidly with time-step refinement. Additionally, Section 8.2 of [113] presents simulations of this system using a second-order exponential time-differencing (ETD) method combined with CD2 scheme for spatial discretization and the same model parameters. Comparing

Table 2.5 with Table 3 in [113] (p. 12) reveals that the proposed method achieves lower error and requires less CPU time than the ETD approach.

2.3.3 The Gray-Scott model

Reaction-diffusion systems are fundamental tools for modeling the dynamics of chemical species and are known for their ability to generate a wide range of natural-like patterns. A widely studied example of such a system is the Gray–Scott model [22], which has been extensively applied for pattern formation studies. Experimental investigations involving stationary lamellar structures arising from the Gray–Scott dynamics in the ferrocyanide-iodate-sulphite reaction are reported in [23]. Furthermore, numerical simulations of the Gray–Scott system using a high-order compact discretization technique, which reformulates the problem as a pure diffusion equation, can be found in [115]. Motivated by these experimental findings [23], the present work conducts numerical simulations of the Gray–Scott system to explore stationary lamellar patterns. The Nonlinear Gray–Scott reaction–diffusion (GSRD) system is defined by Eq. (1.2.1) over the two-dimensional spatial domain $(x, y) \in \Omega$ and time interval $t \in [0, T]$.

The details have been presented in earlier findings discussed by Zegeling and Kok [25]. Additionally, we have specified the initial conditions for the system by utilizing two block functions within the domain $\Omega = [0, 1]^2$, as

$$\begin{aligned} u(x,y,t)|_{t=0} &= \begin{cases} 0.5, & 0.3 \leq x,\ y \leq 0.7 \\ 1, & \text{otherwise} \end{cases} \\ v(x,y,t)|_{t=0} &= \begin{cases} 0.25, & 0.3 \leq x,\ y \leq 0.7 \\ 0, & \text{otherwise} \end{cases} \end{aligned} \tag{2.3.6}$$

To numerically solve the GSRD system, we have discretized the domain using a uniform grid of 51 × 51 points in spatial directions, with Dirichlet boundary conditions imposed along the boundaries. The free-parameters of the chosen numerical method have been set to $a_{22} = 4.0000 \times 10^{-2}$, $b_{22} = -2.6000 \times 10^{-1}$, and $c_{22} = 1.0000$, with a time-

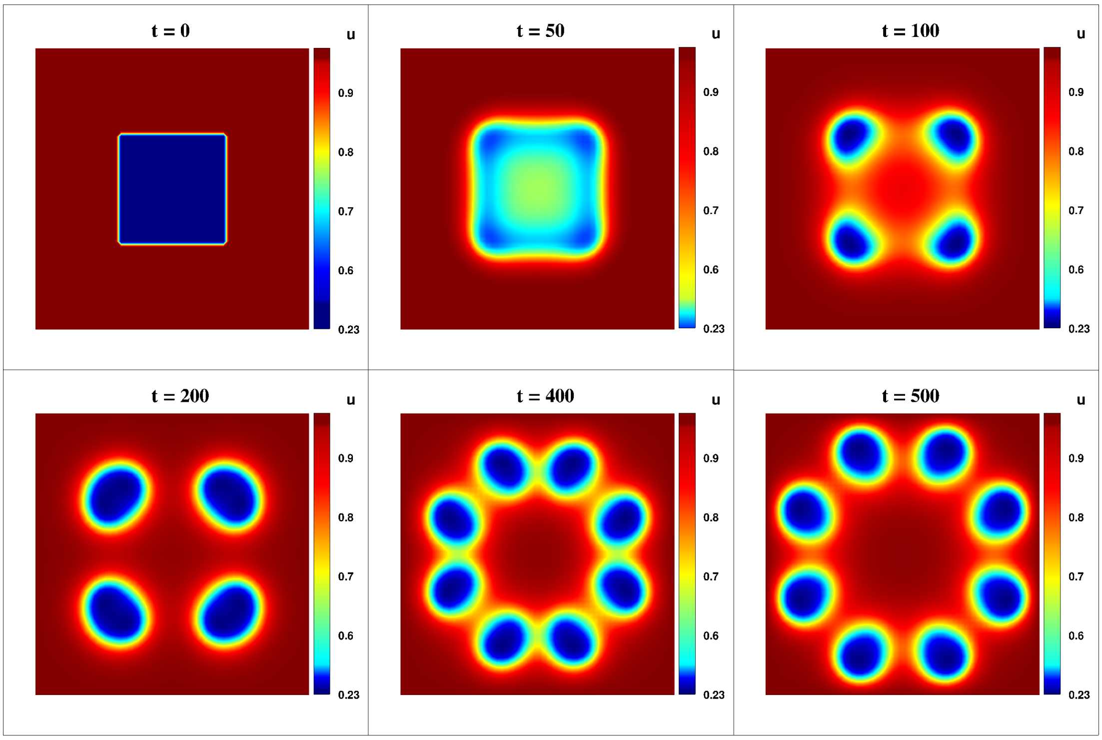

Figure 2.1(a): The spatiotemporal evolution of the solution component u of the system (1.2.1) is illustrated at indicated instants with initial data given in (2.3.6) and the method's free-parameters $a_{22} = 4.0000 \times 10^{-2}$, $b_{22} = -2.6000 \times 10^{-1}$, and $c_{22} = 1.0000$, while the model parameters D_1, D_2, R_1 and R_2 are set to 8×10^{-5}, 4×10^{-5}, 0.024, and 0.06, respectively.

step of $\Delta t = 1.0$. Moreover, the coefficients for simulation have been chosen as $D_1 = 8 \times 10^{-5}$, $D_2 = 4 \times 10^{-5}$, $R_1 = 0.024$, $R_2 = 0.06$. Figures 2.1(a)-2.1(b) display the spatiotemporal evolution of the concentration profiles u and v, respectively, at selected instants ($t = 0, 50, 100, 200, 400, 500$) up to $T = 500$. The simulation begins with an initial block function, which evolves into patterns characterized by four and eight distinct spots in two dimensions corresponding to the first and second concentration components, respectively. These results reveal the dynamic behavior of u and v over time. The generated spatiotemporal patterns closely align with those reported in [25], validating that the current approach is able to accurately reproduce the behavior of the GSRD system.

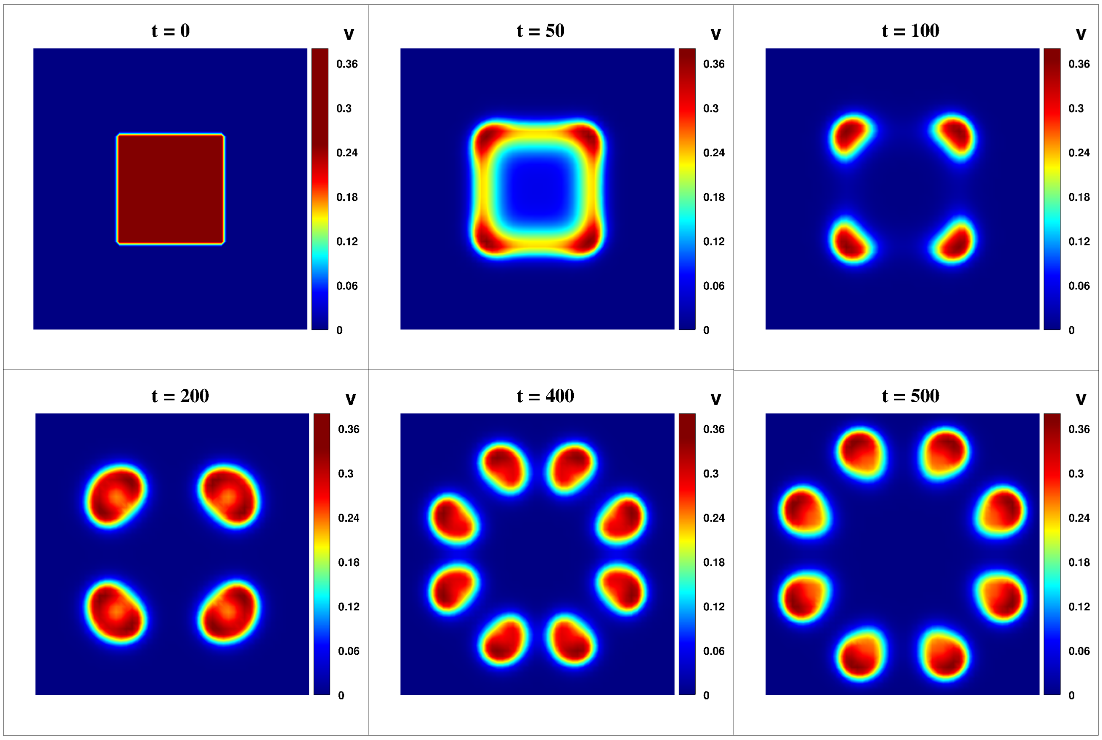

Figure 2.1(b): The spatiotemporal evolution of the solution component v of the system (1.2.1) is illustrated at indicated instants using initial data given in (2.3.6). The simulation was performed with the model parameters $D_1 = 8 \times 10^{-5}$, $D_2 = 4 \times 10^{-5}$, $R_1 = 0.024$, $R_2 = 0.06$, and method's free-parameters $a_{22} = 4.0000 \times 10^{-2}$, $b_{22} = -2.6000 \times 10^{-1}$, $c_{22} = 1.0000$.

2.3.4 The Brusselator model with cross-diffusion

2.3.4.1 Spotted patterns on a square

In this section, we focus on the inhomogeneous Brusselator model with cross-diffusion [116, 117] in two dimensions for spotted patterns in the domain $(x, y) \in \Omega$ and time $t \in [0, T]$, is given as

$$\begin{aligned} \frac{\partial u}{\partial t} &= \Delta\left(D_{11}u + D_{12}v\right) + u^2 v - (1 + R_2)u + R_1, \\ \frac{\partial v}{\partial t} &= \Delta(D_{21}u + D_{22}v) - u^2 v + R_2 u, \\ \frac{\partial u}{\partial n} &= \frac{\partial v}{\partial n} = 0, \quad (x, y) \in \partial\Omega \end{aligned} \tag{2.3.7}$$

considering the following initial conditions

$$u(x,y,t)|_{t=0} = 5.8 + \frac{1}{3}rand(), \quad v(x,y,t)|_{t=0} = 0.13 + \frac{1}{10}rand() \tag{2.3.8}$$

where $rand()$ is a random number generating library function which returns a real number between 0 and 1. To perform numerical simulations, we have used the following parameters: $R_1 = 6$, $R_2 = 1$, $D_{11} = 0.4$, $D_{22} = 2$, $D_{21} = 0.02$, $D_{12} = 24$. The spatial computational domain $\Omega = [0, 20]^2$ have partitioned using a grid consisting of 61×61 points, and the time-step size is $\Delta t = 0.001$. In addition, we have chosen the values of the method's free-parameters as $a_{22} = -5.0000 \times 10^{-1}$, $b_{22} = -6.0000 \times 10^{-2}$, $c_{22} = 3.0000$. The solutions computed for the concentration u and concentration v at different time levels ($t = 1, 10, 25$) up to $T = 25$ are illustrated in Figure 2.2. We have observed that the computed results are consistent with the numerical findings of [117].

2.3.4.2 Mixed patterns on a square

In order to investigate the mixed patterns that emerge on a square, we use a two-dimensional inhomogeneous Brusselator model with cross-diffusion [116, 117] in the spatial domain $(x, y) \in \Omega$ and time $t \in [0, T]$, given in Eq. (2.3.7). The boundary conditions for this case are provided in Eq. (2.3.7) and the initial conditions are considered as in Eq. (2.3.8).

Numerical simulations are performed using a two-dimensional Brusselator model with cross-diffusion, with the aim of observing mixed patterns on a square. In order to perform the simulations over the spatial computational domain $\Omega = [0, 20]^2$, we partitioned the domain using a grid consisting of 121×121 points with a time-step of $\Delta t = 0.001$. In the case of mixed pattern, we set the parameters to $R_1 = 6$, $R_2 = 1$, $D_{11} = 0.4$, $D_{22} = 2$, $D_{21} = 0.02$, and $D_{12} = 22.2665$. Additionally, we selected the method's free-parameters to be $a_{22} = 5.0000, b_{22} = 2.0000$, $c_{22} = 1.0000$. Figure 2.3 displays the computed results for u and v at different instants ($t = 1, 10, 25$) with $T = 20$. The results obtained in this study are consistent with the numerical findings reported in [117].

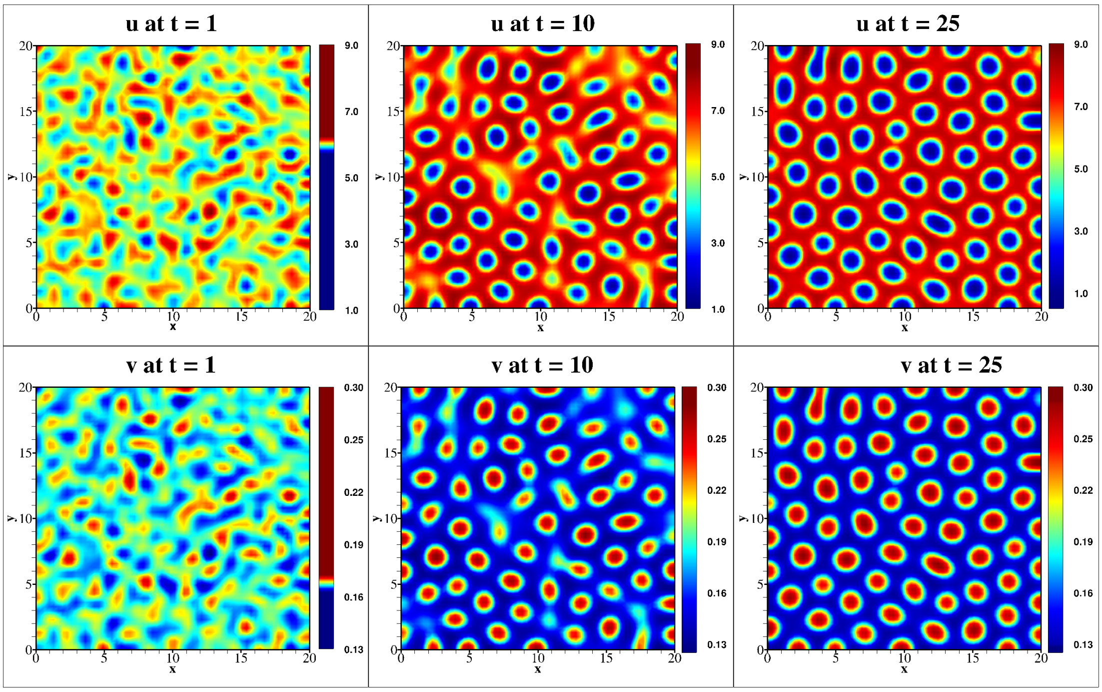

Figure 2.2: The solution profiles for approximated u (at the top) and v (at the bottom) of the system (2.3.7) are illustrated at varying final time, using initial data given in (2.3.8) with method's free-parameters as $a_{22} = -5.0000 \times 10^{-1}$, $b_{22} = -6.0000 \times 10^{-2}$, $c_{22} = 3.0000$.

2.3.5 The Schnakenberg model

The Schnakenberg system, introduced in 1979 [12], serves as a crucial mathematical model for describing autocatalytic chemical reactions capable of exhibiting oscillatory dynamics. It has been widely employed to study the emergence of spatiotemporal patterns in various reaction–diffusion systems [26]. The underlying reaction mechanism involves three molecules: two chemical products P and Q, and two chemical sources X and Y. This mechanism is mathematically formulated as shown in Eq. (1.4.1).

By applying the mass conservation principle, a set of nonlinear equations describing the concentration u of chemical product P and concentration v of chemical product Q can be obtained. The Schnakenberg system in dimensionless form over the domain $x \in \Omega =$

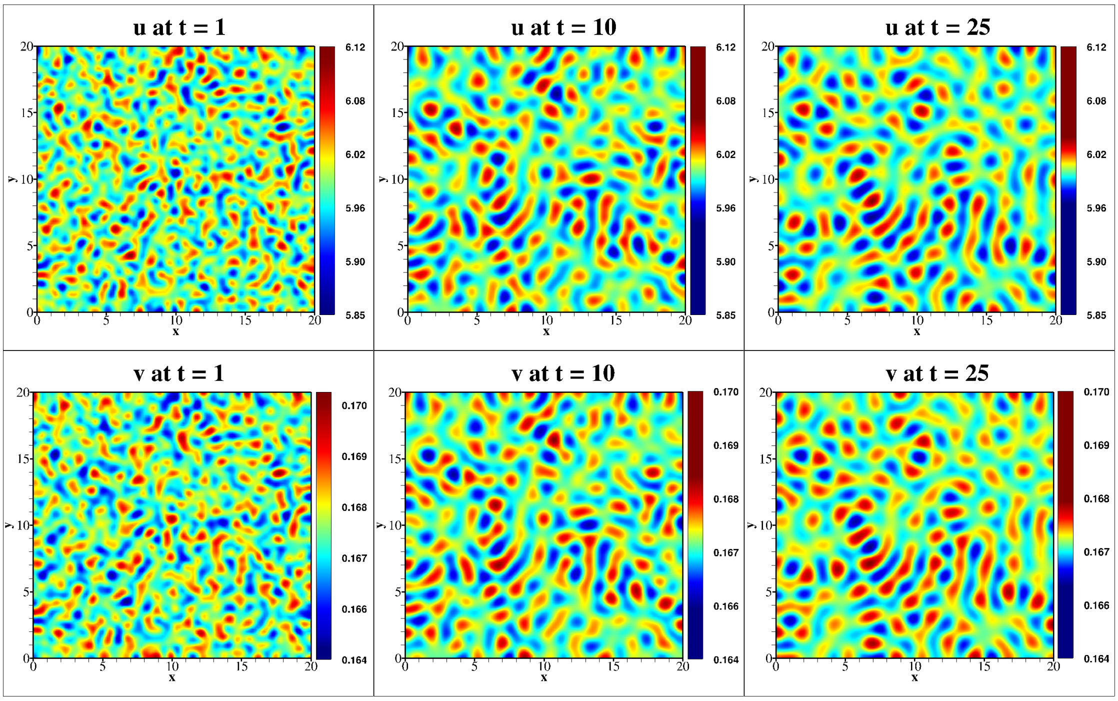

Figure 2.3: The solution profiles for approximated u (at the top) and v (at the bottom) of the system (2.3.7) are illustrated at varying final time, using initial data given in (2.3.8) with method's free-parameters as $a_{22} = 5.0000, b_{22} = 2.0000,\ c_{22} = 1.0000$.

$[0, 3\pi]$ and time $t \in [0, T]$ is given as in Eq. (1.4.1) with the boundary conditions

$$\begin{aligned} \frac{\partial u}{\partial x}(0,t) &= \frac{\partial u}{\partial x}(3\pi,t) = 0, \quad t \in [0,T], \\ \frac{\partial v}{\partial x}(0,t) &= \frac{\partial v}{\partial x}(3\pi,t) = 0, \quad t \in [0,T] \end{aligned} \tag{2.3.9}$$

considering the following initial conditions

$$(i) \begin{cases} u(x,t)|_{t=0} = 0.8 + 0.1\cos(x) \\ v(x,t)_{t=0} = 1.03 + 0.1\cos(x) \end{cases} \qquad (ii) \begin{cases} u(x,t)_{t=0} = 0.3 + 0.001\sin(3x) \\ v(x,t)_{t=0} = 1.778 + 0.001\cos(2x) \end{cases} \tag{2.3.10}$$

For numerical simulations with initial condition (i), we have taken the following parameters: $R_1 = 0.14$, $R_2 = 0.66$, $D_1 = 0.2$, $D_2 = 0.1$, and the values of method's free-parameters are chosen as $a_{22} = 7.0000 \times 10^{-3}$, $b_{22} = 1.0000 \times 10^{-3}$, $c_{22} = 1.0000 \times 10^{-2}$. For initial conditions (ii), we have chosen $R_1 = 0.14$, $R_2 = 0.16$, $D_1 = 0.01$, $D_2 = 1.0$ with the values of method's free-parameters chosen as $a_{22} = 5.0000 \times 10^{-1}$, $b_{22} = 1.0000 \times 10^{-3}$,

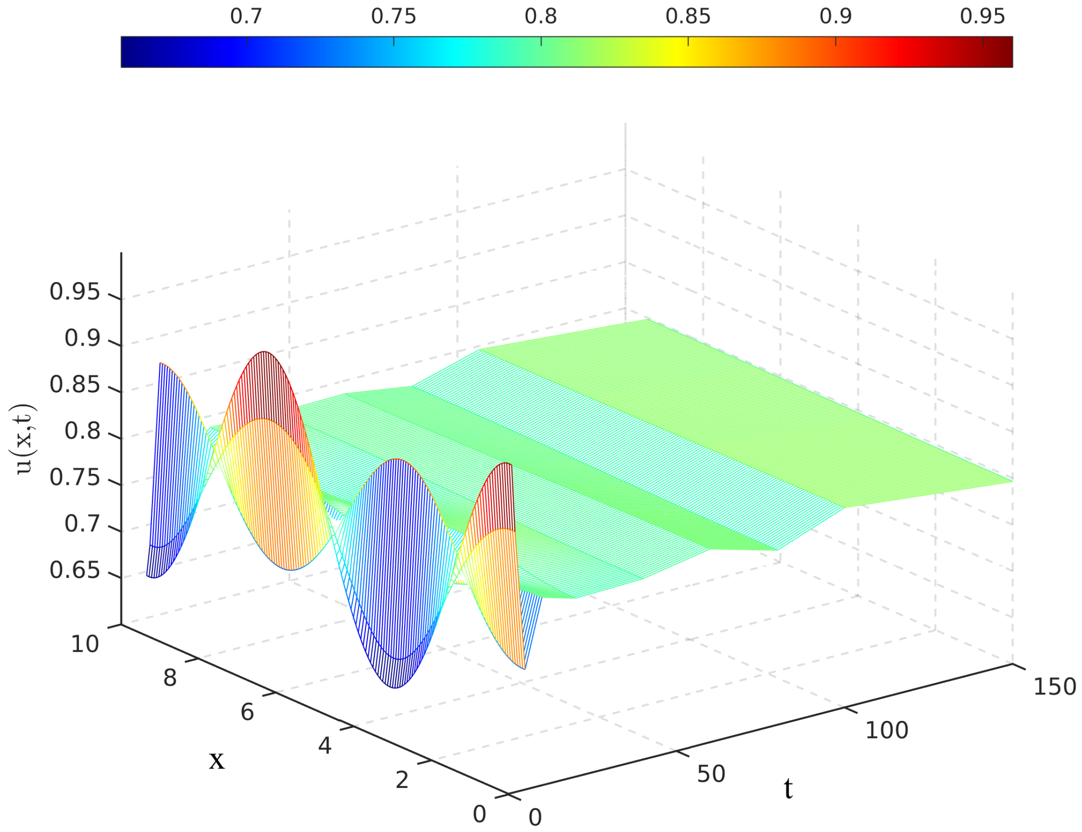

Figure 2.4(a): Surface plot of spatiotemporal evolution of the traveling wave for the solution profile u of the Schnakenberg model (1.4.1) is presented. The simulation is performed with parameters $D_1 = 0.2$, $D_2 = 0.1$, $R_1 = 0.14$, $R_2 = 0.66$, and method's free-parameters $a_{22} = 7.0000 \times 10^{-3}$, $b_{22} = 1.0000 \times 10^{-3}$, $c_{22} = 1.0000 \times 10^{-2}$.

$c_{22} = 1.0000 \times 10^{-2}$. With a time-step size of $\Delta t = 0.001$, numerical simulations are run over the domain $\Omega = [0, 3\pi]$ with 151 grid points.

Numerical simulations of one-dimensional Schnakenberg model is performed and the findings are presented in Figures 2.4(a) - 2.4(f) up to time $T = 200$. These results reveal that the system's behavior is highly dependent on the choice of initial conditions and parameters of the model. In particular, the system converges to a spatially homogeneous periodic orbit with the first initial condition. The solution, however, exhibits a spatially periodic spatiotemporal pattern with a wavelength of π for the second initial condition. To further investigate how these patterns behave physically, we have generated space-time

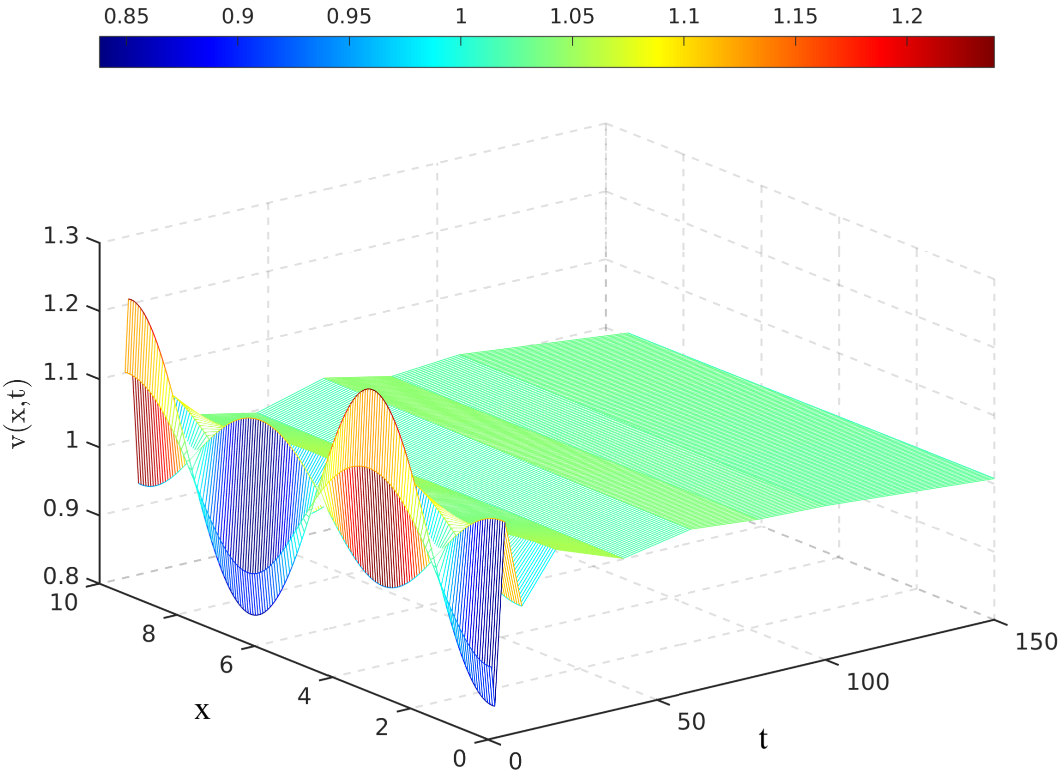

Figure 2.4(b): Surface plot of spatiotemporal evolution of the traveling wave for the solution profile v of the Schnakenberg model (1.4.1) is presented. The simulation is performed with parameters $D_1 = 0.2$, $D_2 = 0.1$, $R_1 = 0.14$, $R_2 = 0.66$, and method's free-parameters $a_{22} = 7.0000 \times 10^{-3}$, $b_{22} = 1.0000 \times 10^{-3}$, $c_{22} = 1.0000 \times 10^{-2}$.

plots displayed in Figures 2.4(a) - 2.4(b). The plots illustrate that the spatiotemporal patterns produced by the numerical simulations using the proposed method closely resemble those reported in [118]. Moreover, Figures 2.4(c), 2.4(d) (as well as 2.4(e), 2.4(f)) clearly show that the evolution of these patterns is highly sensitive to both the initial conditions and the selected model parameters.

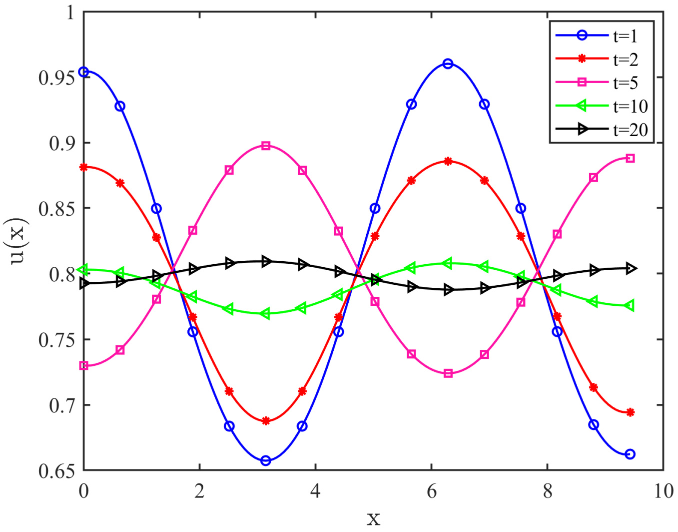

Figure 2.4(c): Traveling wave evolution of the solution profile u for the Schnakenberg model (1.4.1) is illustrated at indicated instants. The simulation uses initial data (i) given in (2.3.10) with the model parameters $D_1 = 0.2, D_2 = 0.1, R_1 = 0.14, R_2 = 0.66$, and method's free-parameters $a_{22} = 7.0000 \times 10^{-3}$, $b_{22} = 1.0000 \times 10^{-3}$, $c_{22} = 1.0000 \times 10^{-2}$.

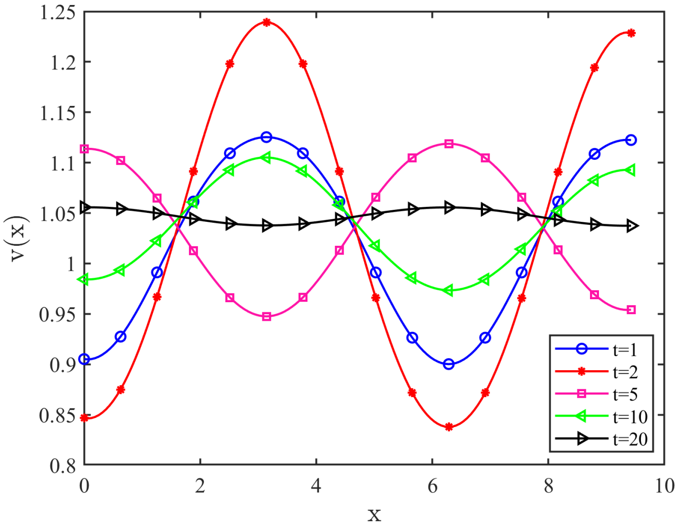

Figure 2.4(d): Traveling wave evolution of the solution profile v for the Schnakenberg model (1.4.1) is illustrated at indicated instants. The simulation uses initial data (i) given in (2.3.10) with the model parameters $D_1 = 0.2, D_2 = 0.1, R_1 = 0.14, R_2 = 0.66$, and method's free-parameters $a_{22} = 7.0000 \times 10^{-3}$, $b_{22} = 1.0000 \times 10^{-3}$, $c_{22} = 1.0000 \times 10^{-2}$.

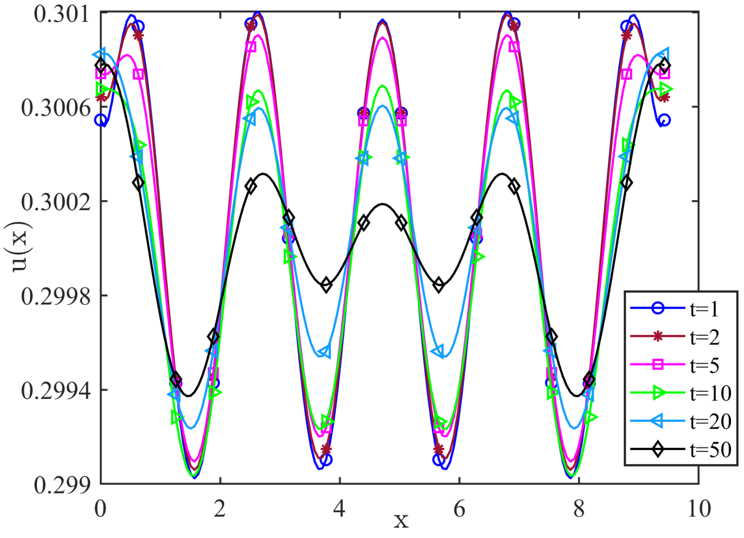

Figure 2.4(e): Traveling wave evolution of the solution profile u for the Schnakenberg model (1.4.1) is illustrated at indicated instants. The simulation uses using initial data (ii) given in (2.3.10) with $D_1 = 0.01$, $D_2 = 1.0$, $R_1 = 0.14$, $R_2 = 0.16$, and with method's free-parameters $a_{22} = 5.0000 \times 10^{-1}$, $b_{22} = 1.0000 \times 10^{-3}$, $c_{22} = 1.0000 \times 10^{-2}$.

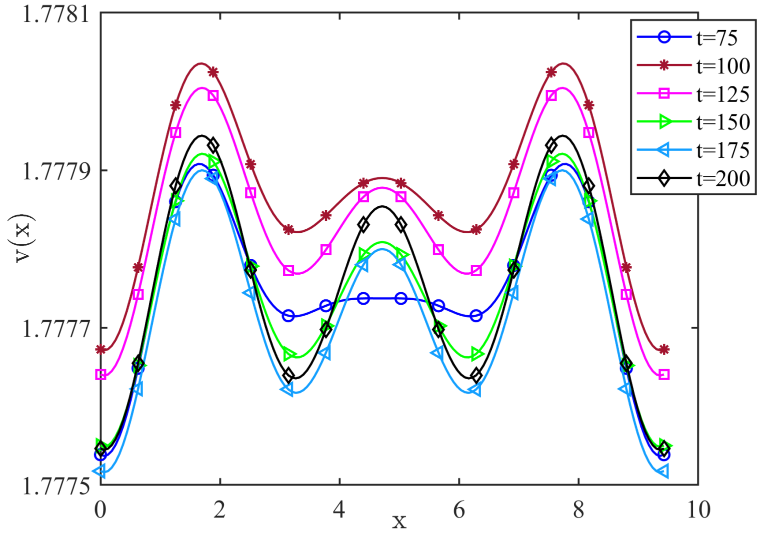

Figure 2.4(f): Traveling wave evolution of the solution profile v for the Schnakenberg model (1.4.1) is illustrated at indicated instants. The simulation uses initial data (ii) given in (2.3.10) with $D_1 = 0.01$, $D_2 = 1.0$, $R_1 = 0.14$, $R_2 = 0.16$, and with method's free-parameters $a_{22} = 5.0000 \times 10^{-1}$, $b_{22} = 1.0000 \times 10^{-3}$, $c_{22} = 1.0000 \times 10^{-2}$.

Chapter 3

Multiderivative strong stability preserving methods for stiff convection-diffusion problems [1]

Effectively modeling the interaction between convective and diffusive processes remains a fundamental and complex task in the numerical approximation of PDEs. The convection-diffusion equation draws continuous research interest, both for its theoretical importance and its broad applications, particularly in atmospheric sciences for weather prediction. In fluid dynamics, convection-diffusion equation describes the fluid flow and heat transfer. These systems describe the convection and diffusion of various physical quantities such as mass, momentum, and energy. Obtaining an accurate solution to the convection-diffusion equation requires the development of stable numerical approximations. Over the years, a wide range of numerical techniques have been developed for approximating convection-diffusion problems, including finite difference, finite volume, and finite element methods [38, 39, 40, 41, 42, 43, 44, 45, 46, 47, 48, 49].

The SSP methods, originally developed in [30, 31, 32], are constructed to retain the stability properties of the forward Euler scheme while enabling higher-order temporal accuracy. Authors in [29] used semi-implicit multistep schemes to solve convection-diffusion

---

[1] This work is under review, 2025.

equations.

To solve time-dependent PDEs, a common strategy is to first discretizing the derivatives in the spatial directions, resulting in a semi-discrete formulation. This transforms time-dependent PDEs into a system of ODEs. Finally, the resultant system of ODEs, when integrated using a first-order forward Euler scheme, show strong stability with respect to a particular norm. The focus then shifts to investigate the potential stability under different time-step constraints. The schemes proposed in [30, 31] preserve the convex functional properties of the forward Euler scheme while delivering high-order accuracy. The semi-discrete system can be expressed as

$$v_t = \mathcal{F}(v) \tag{3.0.1}$$

where $\mathcal{F}$ includes both diffusion and convection operators. The system described in Eq. (3.0.1) satisfies the stability criterion of the forward Euler scheme, expressed as, $||v + \Delta t\mathcal{F}(v)|| \leq ||v|| \ \ \forall\, \Delta t \leq \Delta t_{FE}$, where $||.||$ represents a convex functional. Implicit and semi-implicit methods are commonly used to reduce time-step constraints for stability. However, implicit methods generally contend with stringent time-step limitations to preserve the SSP properties [33]. In computations, a higher-order method that maintains the forward Euler condition is sought, and stability is maintained by modifying the time-step constraint to $\Delta t \leq K\Delta t_{FE}$ with $K > 0$, where K is the SSP coefficient.

The authors in [34] analyzed the SSP properties of the multi-derivative Runge-Kutta methods and revealed that these methods necessitate an extra requirement on the second derivative, given by $\bar{\mathcal{F}} = \frac{d\mathcal{F}}{dt}$, in addition to the forward Euler condition to improve accuracy and stability. In this chapter, the second-order time derivative of the convection term is considered, and the additional condition is imposed as a second derivative condition. In this thesis, explicit two-derivative SSP Runge–Kutta schemes is developed, which is able to achieve improved stability and efficiency while ensuring the preservation of positivity. These methods are described in Section 3.1. It is also demonstrated that the developed method satisfy unconditional SSP conditions.

Conventional finite-difference schemes often fail to capture the behavior of convection-dominated flows unless the grid is sufficiently fine, resulting in increased computational cost. To address this, we adopt compact finite difference schemes [54] for spatial discretization, which offer high accuracy with reduced stencil width and storage requirements.

Although implicit methods relax time-step constraints, they introduce complexity due to matrix inversion. Implicit-explicit schemes mitigate this, but still often suffer from step-size limitations due to the explicit treatment of certain terms. The proposed CEMRK methods eliminate this drawback by being fully explicit and avoiding matrix inversion while maintaining unconditional SSP properties.

The remainder of the chapter is structured as follows: Section 3.1 presents the derivation of the proposed computationally explicit two-derivative Runge–Kutta schemes and verifies their SSP characteristics. Section 3.3 provides a linear Fourier stability analysis. Section 3.4 reports numerical simulations for one- and two-dimensional problems.

3.1 Formulation

The following section discusses the development of CEMRK schemes for convection-dominated diffusion equations. The convection-diffusion equation is given as

$$\frac{\partial v}{\partial t} = D\frac{\partial^2 v}{\partial x^2} - \gamma\frac{\partial v}{\partial x} = \mathcal{F}_1(v) + \mathcal{F}_2(v), \quad x \in \Omega, \quad t > 0 \tag{3.1.1}$$

$$v|_{t=0} = g_1(x), \quad x \in \Omega \tag{3.1.2}$$

$$v|_{x\in\partial\Omega} = g_2(t), \quad t > 0 \tag{3.1.3}$$

where $\mathcal{F}_1$ denotes the diffusion operator and $\mathcal{F}_2$ the convection operator. The terms g_1 and g_2 correspond to the initial and boundary conditions, respectively. The boundary of the domain $\Omega \in \mathbb{R}^d$, where $d = 1, 2$, is represented by $\partial\Omega$. The SSP methods based on multiderivatives presented here are different from those proposed in [34] due to the implicit handling of $\mathcal{F}_1$, $\mathcal{F}_2$, and $\mathcal{G}(= \frac{\partial \mathcal{F}_2}{\partial t})$. Furthermore, the proposed methods are computationally explicit, which eliminates the requirement for matrix inversion in the numerical process. As outlined in [107], the intermediate values v^* at each stage in an s-stage CEMRK scheme for the unknown variable v are computed implicitly in the following manner

$$
\begin{aligned}
v^{(1)} &= v^n \\
v_1^{*(i)} &= \Delta t \sum_{j=1}^{i-1} a_{ij} \mathcal{F}_1(v^{(j)}) - \Delta t a_{ii} D v_1^{*(i)} \\
v_2^{*(i)} &= \Delta t \sum_{j=1}^{i-1} b_{ij} \mathcal{F}_2(v^{(j)}) - \Delta t b_{ii} \gamma v_2^{*(i)} \\
v_3^{*(i)} &= \Delta t^2 \sum_{j=1}^{i-1} c_{ij} \mathcal{G}(v^{(j)}) - \Delta t c_{ii} \gamma v_3^{*(i)} \\
v^{(i)} &= v^n + v_1^{*(i)} + v_2^{*(i)} + v_3^{*(i)}, \quad i = 2, 3, ..., s+1 \\
v^{n+1} &= v^{(s+1)}
\end{aligned}
\tag{3.1.4}
$$

where a_{ij}, b_{ij} and c_{ij} denote the method's coefficients derived using the Butcher tableau [107]. The free parameters in this case are a_{ii}, b_{ii} and c_{ii}. A scheme is considered globally stiffly accurate if $v^{n+1} = v^{(s+1)}$ [109]. A matrix representation of Eq. (3.1.4) is expressed as

$$
v = ev^n + \Delta t \mathcal{P} \mathcal{F}_1(v) + \Delta t \mathcal{Q} \mathcal{F}_2(v) + \Delta t^2 \mathcal{R} \mathcal{G}(v) \tag{3.1.5}
$$

where $v = [v^{(1)}, v^{(2)}, ..., v^{(s+1)}]^T$, $e = [1, 1, 1, ..., 1]^T$, $\mathcal{F}_1(v) = [\mathcal{F}_1(v^{(1)}), \mathcal{F}_1(v^{(2)}), ..., \mathcal{F}_1(v^{(s+1)})]^T$, $\mathcal{F}_2(v) = [\mathcal{F}_2(v^{(1)}), \mathcal{F}_2(v^{(2)}), ..., \mathcal{F}_2(v^{(s+1)})]^T$, $\mathcal{G}(v) = [\mathcal{G}(v^{(1)}), \mathcal{G}(v^{(2)}), ..., \mathcal{G}(v^{(s+1)})]^T$. Representing $\hat{a}_{ii} = \Delta t D a_{ii}$, $\hat{b}_{ii} = \Delta t \gamma b_{ii}$, and $\hat{c}_{ii} = \Delta t \gamma c_{ii}$, $(s+1) \times (s+1)$ matrices P, Q, and R are given as $P = diag\left(0, \frac{1}{1+\hat{a}_{22}}, \frac{1}{1+\hat{a}_{33}}, ..., \frac{1}{1+\hat{a}_{(s+1)(s+1)}}\right) \hat{P}$, $Q = diag\left(0, \frac{1}{1+\hat{b}_{22}}, \frac{1}{1+\hat{b}_{33}}, ..., \frac{1}{1+\hat{b}_{(s+1)(s+1)}}\right) \hat{Q}$, and $R = diag\left(0, \frac{1}{1+\hat{c}_{22}}, \frac{1}{1+\hat{c}_{33}}, ..., \frac{1}{1+\hat{c}_{(s+1)(s+1)}}\right) \hat{R}$, where

$$
\hat{P} = \begin{bmatrix} 0 & 0 & 0 & ... & 0 \\ a_{21} & 0 & 0 & ... & 0 \\ a_{31} & a_{32} & 0 & ... & 0 \\ \vdots & \vdots & \ddots & \ddots & \vdots \\ a_{(s+1)1} & a_{(s+1)2} & ... & a_{(s+1)s} & 0 \end{bmatrix}, \quad \hat{Q} = \begin{bmatrix} 0 & 0 & 0 & ... & 0 \\ b_{21} & 0 & 0 & ... & 0 \\ b_{31} & b_{32} & 0 & ... & 0 \\ \vdots & \vdots & \ddots & \ddots & \vdots \\ b_{(s+1)1} & b_{(s+1)2} & ... & b_{(s+1)s} & 0 \end{bmatrix},
$$

$$\hat{R} = \begin{bmatrix} 0 & 0 & 0 & ... & 0 \\ c_{21} & 0 & 0 & ... & 0 \\ c_{31} & c_{32} & 0 & ... & 0 \\ \vdots & \vdots & \ddots & \ddots & \vdots \\ c_{(s+1)1} & c_{(s+1)2} & \cdots & c_{(s+1)s} & 0 \end{bmatrix}$$

The single-stage ($s = 1$) CEMRK1 method can be expressed as

$$\begin{aligned} v^{(1)} &= v^n \\ v^{(2)} &= v^n + \frac{\Delta t}{(1+\hat{a}_{22})} a_{21}\mathcal{F}_1(v^{(1)}) + \frac{\Delta t}{(1+\hat{b}_{22})} b_{21}\mathcal{F}_2(v^{(1)}) + \frac{\Delta t^2}{(1+\hat{c}_{22})} c_{21}\mathcal{G}(v^{(1)}) \\ v^{n+1} &= v^{(2)} \end{aligned} \tag{3.1.6}$$

Two-stage ($s = 2$) CEMRK2 method is expressed as

$$\begin{aligned} v^{(1)} &= v^n \\ v^{(2)} &= v^n + \frac{\Delta t}{(1+\hat{a}_{22})} a_{21}\mathcal{F}_1(v^{(1)}) + \frac{\Delta t}{(1+\hat{b}_{22})} b_{21}\mathcal{F}_2(v^{(1)}) + \frac{\Delta t^2}{(1+\hat{c}_{22})} c_{21}\mathcal{G}(v^{(1)}) \\ v^{(3)} &= v^n + \frac{\Delta t}{(1+\hat{a}_{33})} \left[a_{31}\mathcal{F}_1(v^{(1)}) + a_{32}\mathcal{F}_1(v^{(2)})\right] + \frac{\Delta t}{(1+\hat{b}_{33})} \left[b_{31}\mathcal{F}_2(v^{(1)}) \right. \\ &\quad \left. + \, b_{32}\mathcal{F}_2(v^{(2)})\right] + \frac{\Delta t^2}{(1+\hat{c}_{33})} \left[c_{31}\mathcal{G}(v^{(1)}) + c_{32}\mathcal{G}(v^{(2)})\right] \\ v^{n+1} &= v^{(3)} \end{aligned} \tag{3.1.7}$$

where a_{21}, b_{21} and c_{21} represent the coefficients of the single-stage method ($a_{21} = 1.0$, $b_{21} = 1.0$, $c_{21} = 0.5$), and the free parameters are denoted as $\hat{a}_{22}$, $\hat{b}_{22}$ and $\hat{c}_{22}$. Section 3.2 provides consistency analysis, which validates the first-order accuracy of the method given in Eq. (3.1.6). For two-stage method a_{21}, a_{31}, a_{32}, b_{21}, b_{31}, b_{32}, and c_{21}, c_{31}, c_{32} are the coefficients of the method and $\hat{a}_{22}, \hat{a}_{33}$, $\hat{b}_{22}, \hat{b}_{33}$, and $\hat{c}_{22}, \hat{c}_{33}$ are the free parameters. Next, it is discussed that the present methods are SSP and also capable of maintaining the positivity property.

3.2 Consistency analysis

To analyze consistency, Eq. (3.1.1) is used and stated as

$$v_t = \mathcal{F}_1(v) + \mathcal{F}_2(v)$$

The method described in Eq. (3.1.6) can be rewritten as

$$\frac{v^{n+1} - v^n}{\Delta t} = \frac{1}{(1 + \Delta t D a_{22})}\mathcal{F}_1(v^n) + \frac{1}{(1 + \Delta t \gamma b_{22})}\mathcal{F}_2(v^n) + \frac{\Delta t}{(1 + \Delta t \gamma c_{22})}\mathcal{G}(v^n) \quad (3.2.1)$$

Applying the Taylor expansion, we obtain

$$v^{n+1} = v^n + \Delta t v_t^n + \frac{\Delta t^2}{2!}v_{tt}^n + \mathcal{O}(\Delta t^3) \quad (3.2.2)$$

The local truncation error, $\mathcal{T}_n$, is determined by using Eq. (3.2.2) within Eq. (3.2.1), and is expressed as

$$\begin{aligned} \mathcal{T}_n &= \frac{1}{\Delta t}\left\{\left(v^n + \Delta t v_t^n + \frac{\Delta t^2}{2!}v_{tt}^n + \mathcal{O}(\Delta t^3)\right) - v^n\right\} - (1 + \Delta t D a_{22})^{-1}\mathcal{F}_1(v^n) \\ &\quad -(1 + \Delta t \gamma b_{22})^{-1}\mathcal{F}_2(v^n) - \Delta t(1 + \Delta t \gamma c_{22})^{-1}\mathcal{G}(v^n) \\ &= (v_t - \mathcal{F}_1(v) - \mathcal{F}_2(v))^n + \mathcal{O}(\Delta t) \quad (3.2.3) \end{aligned}$$

By using $v_t - \mathcal{F}_1(v) - \mathcal{F}_2(v) = 0$, we have

$$\mathcal{T}_n = \mathcal{O}(\Delta t)$$

Therefore, the current first-stage CEMRK1 method achieves first-order accuracy.

3.2.1 Multiderivative Runge-Kutta methods with strong stability properties

For illustrating the strong stability preserving properties of the proposed CEMRK methods, we assume the given operators $\mathcal{F}_1$, $\mathcal{F}_2$, and $\mathcal{G}$ possess particular nonlinear stability characteristics related to a convex functional $\|.\|$. In particular, it is presumed the given operators $\mathcal{F}_1$ and $\mathcal{F}_2$, as defined in Eq. (3.1.1), comply with the stability criterion of the forward Euler scheme, expressed as

$$\|v + \Delta t \mathcal{F}_1(v)\| \leq \|v\| \qquad \forall \ \Delta t \leq k_1' \Delta t_{FE} \tag{3.2.4}$$

$$\|v + \Delta t \mathcal{F}_2(v)\| \leq \|v\| \qquad \forall \ \Delta t \leq k_2' \Delta t_{FE} \tag{3.2.5}$$

for some $\Delta t_{FE} > 0$, $k_1', k_2' > 0$. Furthermore, $\mathcal{G}$ fulfills the second derivative condition, outlined in [34], specified by

$$\left\|v + \Delta t^2 \mathcal{G}(v)\right\| \leq \|v\| \qquad \forall \ \Delta t \leq k_3' \Delta t_{FE} \tag{3.2.6}$$

for some $k_3' > 0$. The following result demonstrates that the proposed CEMRK scheme maintains the SSP property.

Theorem 3.2.1. *Let the operators $\mathcal{F}_1$ and $\mathcal{F}_2$ fulfill the stability criteria of the forward Euler scheme specified in Ineqs. (3.2.4)-(3.2.5), and let $\mathcal{G}$ satisfies the second derivative condition defined in Ineq. (3.2.6) about a convex functional $\|.\|$. Furthermore, suppose the coefficient matrices $\hat{P}$, $\hat{Q}$, $\hat{R}$ in Eq. (3.1.5) satisfy the component-wise conditions, given as*

$$\hat{P} \geq 0, \quad \hat{Q} \geq 0, \quad \hat{R} \geq 0, \tag{3.2.7}$$

Then the proposed scheme maintains the following SSP property

$$\left\|v^{n+1}\right\| \leq \|v^n\| \tag{3.2.8}$$

subject to the time-step condition $\Delta t \leq J_s' \Delta t_{FE}$, with $J_s' > 0$.

Proof. The expression for the i^{th} step in the s-stage method, as outlined in Eq. (3.1.4), is given by

$$v^{(i)} = v^n + \frac{\Delta t}{(1+\hat{a}_{ii})} \sum_{j=1}^{i-1} a_{ij} \mathcal{F}_1(v^{(j)}) + \frac{\Delta t}{(1+\hat{b}_{ii})} \sum_{j=1}^{i-1} b_{ij} \mathcal{F}_2(v^{(j)}) + \frac{\Delta t^2}{(1+\hat{c}_{ii})} \sum_{j=1}^{i-1} c_{ij} \mathcal{G}(v^{(j)}) \tag{3.2.9}$$

Specifically, the single-stage ($s = 1$) method is formulated as

$$\begin{aligned} v^{(1)} &= v^n \\ v^{(2)} &= v^n + \frac{\Delta t}{(1+\hat{a}_{22})} a_{21}\mathcal{F}_1(v^{(1)}) + \frac{\Delta t}{(1+\hat{b}_{22})} b_{21}\mathcal{F}_2(v^{(1)}) + \frac{\Delta t^2}{(1+\hat{c}_{22})} c_{21}\mathcal{G}(v^{(1)}) \\ v^{n+1} &= v^{(2)} \end{aligned} \tag{3.2.10}$$

Assuming $(1+\hat{a}_{22}) > 0$, $(1+\hat{b}_{22}) > 0, (1+\hat{c}_{22}) > 0$, and applying the norm to both sides, we obtain

$$\begin{aligned} \left\|v^{(2)}\right\| &= \left\| v^n + \frac{\Delta t}{(1+\hat{a}_{22})} a_{21}\mathcal{F}_1(v^n) + \frac{\Delta t}{(1+\hat{b}_{22})} b_{21}\mathcal{F}_2(v^n) + \frac{\Delta t^2}{(1+\hat{c}_{22})} c_{21}\mathcal{G}(v^n) \right\| \\ \left\|v^{(2)}\right\| &\leq \left\| \alpha_1 v^n + \Delta t \frac{a_{21}}{(1+\hat{a}_{22})}\mathcal{F}_1(v^n) + \Delta t \frac{b_{21}}{(1+\hat{b}_{22})}\mathcal{F}_2(v^n) \right\| \\ &\quad + \left\| (1-\alpha_1)v^n + \Delta t^2 \frac{c_{21}}{(1+\hat{c}_{22})}\mathcal{G}(v^n) \right\| \end{aligned}$$

with $0 \leq \alpha_1 \leq 1$, implying that

$$\begin{aligned} \left\|v^{(2)}\right\| &\leq \alpha_1 \left\| \beta_{11} v^n + \Delta t \frac{a_{21}}{\alpha_1(1+\hat{a}_{22})}\mathcal{F}_1(v^n) + (1-\beta_{11})v^n + \Delta t \frac{b_{21}}{\alpha_1(1+\hat{b}_{22})}\mathcal{F}_2(v^n) \right\| \\ &\quad + (1-\alpha_1) \left\| v^n + \Delta t^2 \frac{c_{21}}{(1-\alpha_1)(1+\hat{c}_{22})}\mathcal{G}(v^n) \right\| \end{aligned}$$

with $0 \leq \beta_{11} \leq 1$. By applying the condition provided in Ineq. (3.2.6), we obtain

$$\begin{aligned} \left\|v^{(2)}\right\| &\leq \alpha_1\beta_{11} \left\| v^n + \Delta t \frac{a_{21}}{\beta_{11}\alpha_1(1+\hat{a}_{22})}\mathcal{F}_1(v^n) \right\| \\ &\quad + \alpha_1(1-\beta_{11}) \left\| v^n + \Delta t \frac{b_{21}}{\alpha_1(1-\beta_{11})(1+\hat{b}_{22})}\mathcal{F}_2(v^n) \right\| + (1-\alpha_1)\|v^n\| \end{aligned}$$

By applying the conditions provided in Ineqs. (3.2.4) and (3.2.5), it follows that

$$\left\|v^{(2)}\right\| \leq \alpha_1 \left\{ \beta_{11}\|v^n\| + (1-\beta_{11})\|v^n\| \right\} + (1-\alpha_1)\|v^n\|$$

for all $\Delta t \leq \dfrac{k_1'\beta_{11}\alpha_1(1+\hat{a}_{22})}{a_{21}}\Delta t_{FE}$, $\Delta t \leq \dfrac{k_2'\alpha_1(1-\beta_{11})(1+\hat{b}_{22})}{b_{21}}\Delta t_{FE}$, and $\Delta t \leq \dfrac{k_3'(1-\alpha_1)(1+\hat{c}_{22})}{c_{21}}\Delta t_{FE}$. Therefore, we have

$$\left\|v^{(2)}\right\| \leq \|v^n\| \qquad \forall\ \Delta t \leq J_1 \Delta t_{FE} \tag{3.2.11}$$

where $J_1 = \min\left\{\frac{k_1'\beta_{11}\alpha_1(1+\hat{a}_{22})}{a_{21}}, \frac{k_2'\alpha_1(1-\beta_{11})(1+\hat{b}_{22})}{b_{21}}, \frac{k_3'(1-\alpha_1)(1+\hat{c}_{22})}{c_{21}}\right\}$. Since $\alpha_1,\ \beta_{11},\ \hat{a}_{22},\ \hat{b}_{22}$, and $\hat{c}_{22}$ are free parameters, Ineq. (3.2.11) holds for any value of Δt.

Now, suppose for the i^{th} step in the s-stage method, the first $(i-1)$ steps satisfy $\left\|v^{(i)}\right\| \leq \|v^n\| \ \ \forall\, \Delta t \leq J'_{s-1}\Delta t_{FE}$, where $J'_{s-1} > 0$ and $J'_{s-1} = \min\{J_1,\ J_2, ..., J_q\}$, $J_q = \min\left\{\Gamma^a_{\beta_{ij}}, \Gamma^a_{\alpha\beta_{ij}}, \Gamma^b_{\beta_{ij}}, \Gamma^b_{\alpha\beta_{ij}}, \Gamma^c_{ij}, \Gamma^c_{\alpha_{ij}}\right\}$, $\Gamma^a_{\beta_{ij}} = \frac{k_1'\beta_{qr}(1+\hat{a}_{ii})(1+\hat{a}_{i-1i-1})}{a_{ij}(1+\hat{a}_{i-1i-1})-a_{i-1j}(1+\hat{a}_{ii})}$, $\Gamma^b_{\beta_{ij}} = \frac{k_2'(1-\beta_{qr})(1+\hat{b}_{ii})(1+\hat{b}_{i-1i-1})}{b_{ij}(1+\hat{b}_{i-1i-1})-b_{i-1j}(1+\hat{b}_{ii})}$, $\Gamma^c_{ij} = \frac{k_3'(1+\hat{c}_{ii})(1+\hat{c}_{i-1i-1})}{c_{i-1j}(1+\hat{c}_{ii})-c_{ij}(1+\hat{c}_{i-1i-1})}$, when $j < i-1,\ r < q$, and $\Gamma^a_{\alpha\beta_{ij}} = \frac{k_1'\beta_{qr}\alpha_q(1+\hat{a}_{ii})}{a_{ij}}$, $\Gamma^b_{\alpha\beta_{ij}} = \frac{k_2'(1-\beta_{qr})\alpha_q(1+\hat{b}_{ii})}{b_{ij}}$, $\Gamma^c_{\alpha_{ij}} = \frac{k_3'(1-\alpha_q)(1+\hat{c}_{ii})}{c_{ij}}$, when $j = i-1,\ r = q$. Here $q \in \{1, 2, \ldots, s-1\}$, $r = 1, 2, \ldots, q$, $i = 2, ..., s,\ j = 1, ..., i-1$.

As a final step, consider the last stage $(i = s+1)$, along with the preceding $(i-1)$ stages

$$\begin{aligned} v^{(i-1)} &= v^n + \frac{\Delta t}{(1+\hat{a}_{i-1i-1})}\sum_{j=1}^{i-2} a_{i-1j}\mathcal{F}_1(v^{(j)}) + \frac{\Delta t}{(1+\hat{b}_{i-1i-1})}\sum_{j=1}^{i-2} b_{i-1j}\mathcal{F}_2(v^{(j)}) \\ &\quad + \frac{\Delta t^2}{(1+\hat{c}_{i-1i-1})}\sum_{j=1}^{i-2} c_{i-1j}\mathcal{G}(v^{(j)}) \qquad (3.2.12) \\ v^{(i)} &= v^n + \frac{\Delta t}{(1+\hat{a}_{ii})}\sum_{j=1}^{i-1} a_{ij}\mathcal{F}_1(v^{(j)}) + \frac{\Delta t}{(1+\hat{b}_{ii})}\sum_{j=1}^{i-1} b_{ij}\mathcal{F}_2(v^{(j)}) \\ &\quad + \frac{\Delta t^2}{(1+\hat{c}_{ii})}\sum_{j=1}^{i-1} c_{ij}\mathcal{G}(v^{(j)}) \qquad (3.2.13) \\ v^{(i)} &= v^n + \frac{\Delta t}{(1+\hat{a}_{ii})}\left(\sum_{j=1}^{i-2} a_{ij}\mathcal{F}_1(v^{(j)}) + a_{ii-1}\mathcal{F}_1(v^{(i-1)})\right) \\ &\quad + \frac{\Delta t}{(1+\hat{b}_{ii})}\left(\sum_{j=1}^{i-2} b_{ij}\mathcal{F}_2(v^{(j)}) + b_{ii-1}\mathcal{F}_2(v^{(i-1)})\right) \\ &\quad + \frac{\Delta t^2}{(1+\hat{c}_{ii})}\left(\sum_{j=1}^{i-2} c_{ij}\mathcal{G}(v^{(j)}) + c_{ii-1}\mathcal{G}(v^{(i-1)})\right) \qquad (3.2.14) \end{aligned}$$

By referring to Eqs. (3.2.12) and (3.2.14), it follows that

$$v^{(i)} = \left\{v^{(i-1)} - \frac{\Delta t}{(1+\hat{a}_{i-1i-1})}\sum_{j=1}^{i-2} a_{i-1j}\mathcal{F}_1(v^{(j)}) - \frac{\Delta t}{(1+\hat{b}_{i-1i-1})}\sum_{j=1}^{i-2} b_{i-1j}\mathcal{F}_2(v^{(j)})\right.$$

$$
\begin{aligned}
&- \frac{\Delta t^2}{(1+\hat{c}_{i-1i-1})} \sum_{j=1}^{i-2} c_{i-1j}\mathcal{G}(v^{(j)}) \Bigg\} \\
&+\frac{\Delta t}{(1+\hat{a}_{ii})}\sum_{j=1}^{i-2} a_{ij}\mathcal{F}_1(v^{(j)}) + \frac{\Delta t}{(1+\hat{a}_{ii})} a_{ii-1}\mathcal{F}_1(v^{(i-1)}) \\
&+\frac{\Delta t}{(1+\hat{b}_{ii})}\sum_{j=1}^{i-2} b_{ij}\mathcal{F}_2(v^{(j)}) + \frac{\Delta t}{(1+\hat{b}_{ii})} b_{ii-1}\mathcal{F}_2(v^{(i-1)}) \\
&+\frac{\Delta t^2}{(1+\hat{c}_{ii})}\sum_{j=1}^{i-2} c_{ij}\mathcal{G}(v^{(j)}) + \frac{\Delta t^2}{(1+\hat{c}_{ii})} c_{ii-1}\mathcal{G}(v^{(i-1)})
\end{aligned}
$$

$$
\begin{aligned}
\|v^{(i)}\| \;\leq\; & \left\| \beta_{ss-1} v^{(j)} + \Delta t \sum_{j=1}^{i-2} \left(\frac{a_{ij}}{(1+\hat{a}_{ii})} - \frac{a_{i-1j}}{(1+\hat{a}_{i-1i-1})} \right) \mathcal{F}_1(v^{(j)}) \right\| \\
& + \left\| (1-\beta_{ss-1}) v^{(j)} + \Delta t \sum_{j=1}^{i-2} \left(\frac{b_{ij}}{(1+\hat{b}_{ii})} - \frac{b_{i-1j}}{(1+\hat{b}_{i-1i-1})} \right) \mathcal{F}_2(v^{(j)}) \right\| \\
& + \left\| - \left(v^{(j)} + \Delta t^2 \sum_{j=1}^{i-2} \left(\frac{c_{i-1j}}{(1+\hat{c}_{i-1i-1})} - \frac{c_{ij}}{(1+\hat{c}_{ii})} \right) \mathcal{G}(v^{(j)}) \right) \right\| \\
& + \left\| \alpha_s v^{(i-1)} + \Delta t \frac{a_{ii-1}}{(1+\hat{a}_{ii})} \mathcal{F}_1(v^{(i-1)}) + \Delta t \frac{b_{ii-1}}{(1+\hat{b}_{ii})} \mathcal{F}_2(v^{(i-1)}) \right\| \\
& + \left\| (1-\alpha_s) v^{(i-1)} + \Delta t^2 \frac{c_{ii-1}}{(1+\hat{c}_{ii})} \mathcal{G}(v^{(i-1)}) \right\|
\end{aligned}
$$

$$
\begin{aligned}
\|v^{(i)}\| \;\leq\; & \beta_{ss-1} \left\| v^{(j)} + \frac{\Delta t}{\beta_{ss-1}} \sum_{j=1}^{i-2} \left(\frac{a_{ij}}{(1+\hat{a}_{ii})} - \frac{a_{i-1j}}{(1+\hat{a}_{i-1i-1})} \right) \mathcal{F}_1(v^{(j)}) \right\| \\
& + (1-\beta_{ss-1}) \left\| v^{(j)} + \frac{\Delta t}{(1-\beta_{ss-1})} \sum_{j=1}^{i-2} \left(\frac{b_{ij}}{(1+\hat{b}_{ii})} - \frac{b_{i-1j}}{(1+\hat{b}_{i-1i-1})} \right) \mathcal{F}_2(v^{(j)}) \right\| \\
& + \left\| v^{(j)} + \Delta t^2 \sum_{j=1}^{i-2} \left(\frac{c_{i-1j}}{(1+\hat{c}_{i-1i-1})} - \frac{c_{ij}}{(1+\hat{c}_{ii})} \mathcal{G}(v^{(j)}) \right) \right\| \\
& + \alpha_s \beta_{ss} \left\| v^{(i-1)} + \Delta t \frac{a_{ii-1}}{\beta_{ss}\alpha_s(1+\hat{a}_{ii})} \mathcal{F}_1(v^{(i-1)}) \right\| \\
& + \alpha_s (1-\beta_{ss}) \left\| v^{(i-1)} + \Delta t \frac{b_{ii-1}}{(1-\beta_{ss})\alpha_s(1+\hat{b}_{ii})} \mathcal{F}_2(v^{(i-1)}) \right\| \\
& + (1-\alpha_s) \left\| v^{(i-1)} + \Delta t^2 \frac{c_{ii-1}}{(1-\alpha_s)(1+\hat{c}_{ii})} \mathcal{G}(v^{(i-1)}) \right\|
\end{aligned}
$$

where $0 \leq \alpha_s \leq 1$, $0 \leq \beta_{ss-1} \leq 1$, $0 \leq \beta_{ss} \leq 1$.

By utilizing the inequality $\left\|v^{(i)}\right\| \leq \|v^n\|$ for the preceding $(i-1)$ steps and applying the Ineqs. (3.2.4) - (3.2.6), we derive

$$\begin{aligned}\left\|v^{(i)}\right\| &\leq \beta_{ss-1}\|v^n\| + (1-\beta_{ss-1})\|v^n\| + \|v^n\| + \alpha_{ss}(\beta_{ss}\|v^n\| + (1-\beta_{ss})\|v^n\|) \\ &\quad + (1-\alpha_s)\|v^n\|\end{aligned}$$

this results in, $\left\|v^{(i)}\right\| \leq \|v^n\| \;\; \forall\ \Delta t \leq J'_s \Delta t_{FE}$, with $J'_s > 0$ and $J'_s = \min\{J_1, J_2, \ldots, J_q\}$, $q \in \{1, 2, \ldots, s\}$. Thus, the proof is complete. □

Remark: Strong stability preserving schemes maintain positivity; the derived CEMRK schemes will also uphold the property of positivity.

3.2.2 Spatial discretization

For spatial discretization, consider a finite difference in the (x,t) plane. Let $1 \leq i \leq M+1, 0 \leq n \leq N$, $x \in [a,b]$ and $t \in [0,T]$ with uniform step size $\Delta x = (b-a)/M$ and $\Delta t = T/N$ when grid points are given as $x_i = a + (i-1)\Delta x, t_n = n\Delta t$. For a smooth function $v(x,t)$ and its semi-discrete solution $v_i = v(x_i, t)$, the central difference operator for first and second-order derivatives can be defined as follows

$$\delta_x v_i = \frac{v_{i+1} - v_{i-1}}{2\Delta x}, \qquad \delta_x^2 v_i = \frac{v_{i+1} - 2v_i + v_{i-1}}{\Delta x^2}$$

We have used the fourth-order compact (C4) scheme for first- and second-order spatial derivatives given in [54] as

$$\frac{1}{4}F_{i-1} + F_i + \frac{1}{4}F_{i+1} = \frac{3}{2}\delta_x v_i \tag{3.2.15}$$

$$\frac{1}{10}S_{i-1} + S_i + \frac{1}{10}S_{i+1} = \frac{12}{10}\delta_x^2 v_i \tag{3.2.16}$$

where F_i and S_i represent the approximations of the first and second-order derivatives, respectively. For Dirichlet boundary conditions, the boundary conditions for the compact methods for the first and second-order derivatives are taken from [44]. The third-order derivative is now approximated explicitly as

$$T_i = 2\delta_x^2 F_i - \delta_x S_i = \partial_x^3 v_i + \mathcal{O}(\Delta x^4)$$

which is fourth-order accurate (for more details, see [119], [44]).

Remark: For two-dimensional problems, the implementation of the two-derivative method requires the calculation of mixed derivatives in space, which is evaluated explicitly [44].

3.3 Fourier stability analysis of the convection-diffusion equation

To perform the stability analysis, a one-dimensional (1D) linear convection-diffusion equation defined on the domain $[0, \pi]$ is considered and expressed as

$$\begin{aligned} \frac{\partial v}{\partial t} &= -\gamma \frac{\partial v}{\partial x} + D\frac{\partial^2 v}{\partial x^2}, \quad t > 0 \\ v|_{t=0} &= g(x) \end{aligned} \tag{3.3.1}$$

here γ denotes the convection coefficient, and D denotes the diffusion coefficient. Considering periodic boundary conditions, the unknown v is expressed by applying the Fourier transform as

$$v(x,t) = \int_{-\infty}^{\infty} \check{v}(k,t)e^{ikx}dk$$

where $\check{v}$ is the Fourier transform of v, and k is the wavenumber. The discrete Fourier transform is applied to express the function v and its derivatives in the spatial direction [110]

$$\begin{aligned} v(x,t)|_N &= \int_{-k_{max}}^{k_{max}} \check{v}(k,t)e^{ikx}dk \\ v_x(x,t)|_N &= \int_{-k_{max}}^{k_{max}} ik_m\check{v}(k,t)e^{ikx}dk \\ v_{xx}(x,t)|_N &= \int_{-k_{max}}^{k_{max}} -k_m^2\check{v}(k,t)e^{ikx}dk \\ v_{xxx}(x,t)|_N &= \int_{-k_{max}}^{k_{max}} -ik_m^3\check{v}(k,t)e^{ikx}dk \end{aligned} \tag{3.3.2}$$

The modified wavenumber is represented by k_m, with $k_{max} = \pi/\Delta x$. By applying the discrete Fourier transform, Eq. (3.3.1) can be expressed as

$$\begin{aligned} \frac{\partial \breve{v}^n}{\partial t} &= -[\gamma i k_m + D k_m^2]\breve{v}^n \\ \hat{v}|_{t=0} &= \breve{g}(k_m) \end{aligned} \tag{3.3.3}$$

here n corresponds to the time level. Using Eq. (3.3.3), the amplification factor ($\lambda_N = \frac{\breve{v}^{n+1}}{\breve{v}^n}$) [110, 83] for the developed first-order CEMRK1 method with the C4 scheme for spatial discretization is expressed as

$$\lambda_{N_1} = 1 - \frac{F_o}{(1 + a_{22}F_o)}k_m^{[2]} - \frac{C_r^2}{2(1 + c_{22}C_r)}k_m^{[2]} + i\left(\frac{C_r F_o}{2(1 + c_{22}C_r)}k_m^{[3]} - \frac{C_r}{(1 + b_{22}C_r)}k_m^{[1]}\right)$$

Here, $F_o = D\Delta t/\Delta x^2$ represents the grid Fourier number, and $C_r = \gamma\Delta t/\Delta x$ denotes the Courant number [111]. Moreover, we have also analyzed the Fourier stability property of the developed second-order CEMRK2 method given in Eq. (3.1.7), for which the numerical amplification factor with the C4 scheme is expressed as

$$\begin{aligned} \lambda_{N_2} \;=\;& 1 - \frac{F_o}{(1 + a_{33}F_o)}k_m^{[2]} - \frac{C_r^2}{6(1 + c_{33}C_r)}k_m^{[2]} + \frac{1}{3(1 + c_{33}C_r)}\left[\frac{C_r^2 F_o}{2(1 + a_{22}F_o)}k_m^{[2]^2}\right. \\ & \left. -C_r^2 k_m^{[2]} + \frac{C_r^2}{8(1 + c_{22}C_r)}\left(-F_o^2 k_m^{[3]^2} + C_r^2 k_m^{[2]^2}\right) + \frac{C_r^2 F_o}{2(1 + b_{22}C_r)}k_m^{[1]}k_m^{[3]}\right] \\ & +i\left[\frac{C_r F_o}{6(1 + c_{33}C_r)}k_m^{[3]} - \frac{C_r}{(1 + b_{33}C_r)}k_m^{[1]} + \frac{1}{3(1 + c_{33}C_r)}\left\{C_r F_o k_m^{[3]}\right.\right. \\ & \left.\left. - \frac{C_r F_o^2}{2(1 + a_{22}F_o)}k_m^{[2]}k_m^{[3]} - \frac{C_r^3 F_o}{4(1 + c_{22}C_r)}k_m^{[2]}k_m^{[3]} + \frac{C_r^3}{2(1 + b_{22}C_r)}k_m^{[2]}k_m^{[1]}\right\}\right] \end{aligned}$$

where $k_m^{[1]} = k_m\Delta x = \dfrac{3\sin\alpha}{(2 + \cos\alpha)}$, $k_m^{[2]} = k_m^2\Delta x^2 = \dfrac{12(1 - \cos\alpha)}{(5 + \cos\alpha)}$, $k_m^{[3]} = k_m^3\Delta x^3 = \dfrac{36\sin\alpha(1 - \cos\alpha)}{(2 + \cos\alpha)(5 + \cos\alpha)}$, $\alpha = k\Delta x$. The stability condition is expressed as $|\lambda_{N_{1,2}}| \leq 1$. Since $|\lambda_{N_{1,2}}|$ is dependent on free parameters, the unstable region ($|\lambda_{N_{1,2}}| > 1$) can be eliminated (if present) by optimally selecting the method's free parameters a_{22}, a_{33}, b_{22}, b_{33}, and c_{22}, c_{33}. This is achieved by minimizing the error in the L^2- norm of the amplification factor $\left(\big||\lambda_{N_{1,2}}| - 1\big|\right)$ [83, 120].

Contour plots showing absolute values of the numerical amplification factor ($|\lambda_{N_1}|$) for the first-order CEMRK1 method are shown in Fig. 3.1(a). The values of free parameters for CEMRK1 are $a_{22} = 20$, $b_{22} = 1.9$, $c_{22} = 5.1$ for $F_o = 0.001$, for $F_o = 0.1$, $a_{22} = 20$,

$b_{22} = 1.6$, $c_{22} = 5.2$, and for $F_o = 1$, $a_{22} = 20$, $b_{22} = 1.5$, $c_{22} = 5.18$. The numerical properties are compared with the properties of the IMEX-SSP2 [121] method, which are shown in Fig. 3.1(a) with different values of F_o. For the second-order CEMRK2 method, the absolute value of the numerical amplification factor ($|\lambda_{N_2}|$) is shown in Fig. 3.1(b). The free parameters for CEMRK2 are $a_{22} = 40$, $a_{33} = 1$, $b_{22} = 1$, $b_{33} = 3.5$, $c_{22} = 5$, $c_{33} = 11$ for $F_o = 0.001$, for $F_o = 0.1$, $a_{22} = 30$, $a_{33} = 1$, $b_{22} = 1$, $b_{33} = 1.2$, $c_{22} = 12$, $c_{33} = 11$, and for $F_o = 1$, $a_{22} = 10$, $a_{33} = 3$, $b_{22} = 1$, $b_{33} = 1$, $c_{22} = 5$, $c_{33} = 10$. As observed from Figs. 3.1(a)-3.1(b), the IMEX-SSP2 method exhibits an unstable region highlighted by shaded region, whereas the developed method remains stable across all values of C_r, even for larger values.

3.4 Numerical simulations

In the following section, computational findings of the proposed methods for the model test problem are compared with those obtained using similar methods. The rate of convergence (ROC) can then be determined using the formula.

$$ROC = \log\left(\frac{Err_{\Delta x_1}}{Err_{\Delta x_2}}\right) / \log\left(\frac{\Delta x_1}{\Delta x_2}\right)$$

where, $Err_{\Delta x_1}$ and $Err_{\Delta x_2}$ denote the errors calculated using the L^2-norm for grid sizes Δx_1 and Δx_2, respectively.

3.4.1 One-dimensional convection-diffusion model problem

Computations of 1D convection-diffusion equations with different choices of reaction and diffusion parameters are discussed next.

3.4.1.1 Problem-1

The 1D convection-diffusion model test problem considered here is given as

$$\frac{\partial v}{\partial t} + \gamma\frac{\partial v}{\partial x} - D\frac{\partial^2 v}{\partial x^2} = 0, \quad x \in [0, 2] \tag{3.4.1}$$

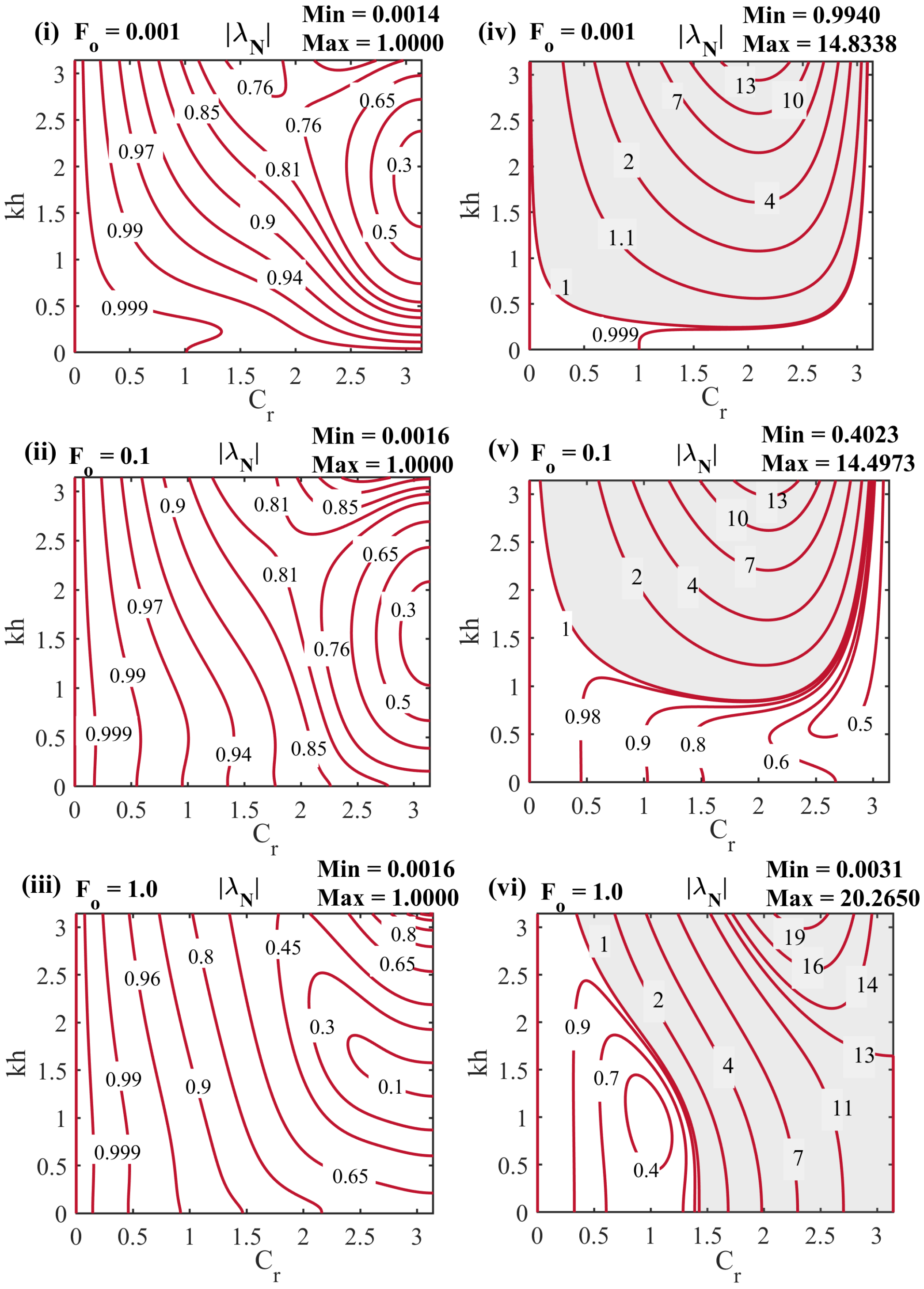

Figure 3.1(a): Contour plots showing the absolute values of λ_{N_1} given in Eq. (3.3.1) using the CEMRK1-C4 (in left frames $(i) - (iii)$) and using the IMEX-SSP2 - C4 (in right frames $(iv) - (vi)$) with the various values of F_o.

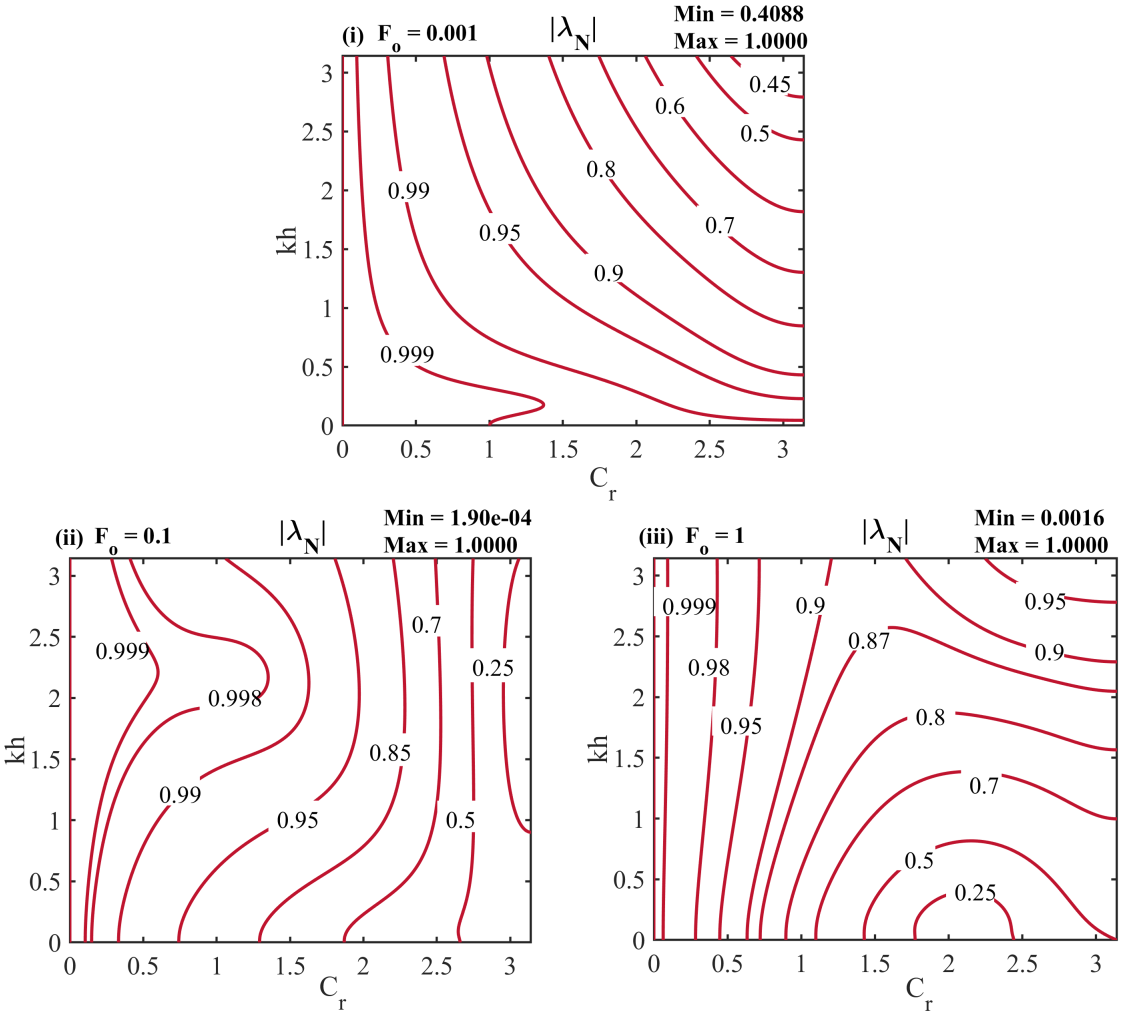

Figure 3.1(b): Contour plots showing the absolute values of the computed amplification factor λ_{N_2} for Eq. (3.3.1) using CEMRK2-C4 scheme with the various values of F_o.

The exact solution of Eq. (3.4.1) is given as [122]

$$v(x,t) = 1 + \exp\bigl(-\pi^2 Dt\bigr)\sin(\pi x - \pi\gamma t) \tag{3.4.2}$$

To evaluate the accuracy of the proposed method, the L^2-error norm have been computed. Initial data is chosen from the exact solution given in Eq. (3.4.2), and periodic boundary conditions are used for the numerical simulations. Numerical solutions are computed up to the final time $T = 1$ using the CEMRK2 method with the C4 scheme. For computational, $D = 10^{-5}$ and $\gamma = 1, 10$ have been fixed. In all numerical experiments, the time-step is set to $\Delta t = \Delta x^2$. For $\gamma = 1$, the values of free parameters are $a_{22} = 100$, $a_{33} = 20$, $b_{22} = 1.0 \times 10^{-2}$, $b_{33} = 5.0 \times 10^{-5}$, $c_{22} = 1$, $c_{33} = 1.0 \times 10^{-1}$. For $\gamma = 10$ the free parameters are chosen as $a_{22} = 10$, $a_{33} = 100$, $b_{22} = 1.0 \times 10^{-4}$, $b_{33} = 1.0 \times 10^{-5}$, $c_{22} = 1.0 \times 10^{-3}$, $c_{33} = 1.1 \times 10^{-2}$.

The L^2-error norm and the corresponding convergence in space and time at $T = 1$ are provided in Tables 3.1 - 3.2 for $\gamma = 1$, $\gamma = 10$, respectively. It is evident from Tables 3.1 and 3.2 that the CEMRK2-C4 scheme exhibits a convergence of fourth-order in space and second-order in time. Figure 3.2(a) - 3.2(b) present the numerical solutions at $T = 1$ with the exact solution for $\gamma = 1$ and $\gamma = 10$. Additionally, Figs. 3.2(c) - 3.2(d) compares the L^∞-errors for $\gamma = 1$ and $\gamma = 10$, demonstrating that the presented scheme produces less error as compared to the IMEX-SSP2 [121] method for the case of convection-dominated problems.

Table 3.1: Convergence rate and L^2-error for Problem (3.4.1.1) corresponding to Eq. (3.4.1) using the CEMRK2-C4 scheme, considering $\gamma = 1$, $D = 10^{-5}$ and final time $T = 1$.

M	Δt	L^2-error	ROC (space)	ROC (time)
60	1.1111×10^{-3}	1.5610×10^{-6}	–	–
80	6.2500×10^{-4}	4.9297×10^{-7}	4.0067	2.0033
100	4.0000×10^{-4}	2.0182×10^{-7}	4.0022	2.0011
120	2.7778×10^{-4}	9.7357×10^{-8}	3.9984	1.9992

Table 3.2: Convergence and L^2-error for Problem (3.4.1.1) corresponding to Eq. (3.4.1) using the CEMRK2-C4 scheme, considering $\gamma = 10$, $D = 10^{-5}$ and final time $T = 1$.

M	Δt	L^2-error	ROC (space)	ROC (time)
60	1.1111×10^{-3}	4.9806×10^{-5}	–	–
80	6.2500×10^{-4}	1.5865×10^{-5}	3.9768	1.9884
100	4.0000×10^{-4}	6.5588×10^{-6}	3.9584	1.9792
120	2.7778×10^{-4}	3.2004×10^{-6}	3.9355	1.9677

3.4.1.2 Problem-2

Next, convection-diffusion problem given in Eq. (3.4.1) is considered with higher value of diffusion coefficient. The parameters are set to $\gamma = 1$ and $D = 0.1$ with the domain $[0, 1]$ and a final time of $T = 1$. The initial and boundary conditions are derived from the exact solution at $t = 0$ and at the boundaries $x = 0$ and $x = 1$, respectively.

Table 3.3: Convergence and L^2-error for Problem (3.4.1.2) corresponding to Eq. (3.4.1) solved through the CEMRK2-C4 scheme, considering $\gamma = 1$ and $D = 0.1$.

M	Δt	L^2-error	ROC (space)	ROC (time)
10	1.0000×10^{-2}	1.3639×10^{-3}	–	–
20	2.5000×10^{-3}	9.9758×10^{-5}	3.7731	1.8866
40	6.2500×10^{-4}	5.7839×10^{-6}	4.1083	2.0542
80	1.5625×10^{-4}	3.4685×10^{-7}	4.0596	2.0298

Table 3.3 shows the L^2-error and the corresponding convergence rates in space and time, using the computed solutions at $T = 1$. For the free parameters, the selected values are $a_{22} = 5.0 \times 10^3$, $a_{33} = 5.0$, $b_{22} = 4.0 \times 10^2$, $b_{33} = 5.0 \times 10^{-1}$, $c_{22} = 5.0 \times 10^1$, $c_{33} = 3.2 \times 10^1$. As seen in Table 3.3, the CEMRK2-C4 scheme exhibits a convergence of order four in space and order two in time. The numerical solution is presented alongside the exact solution in Figs. 3.3(a) - 3.3(b). The surface plot of the absolute difference

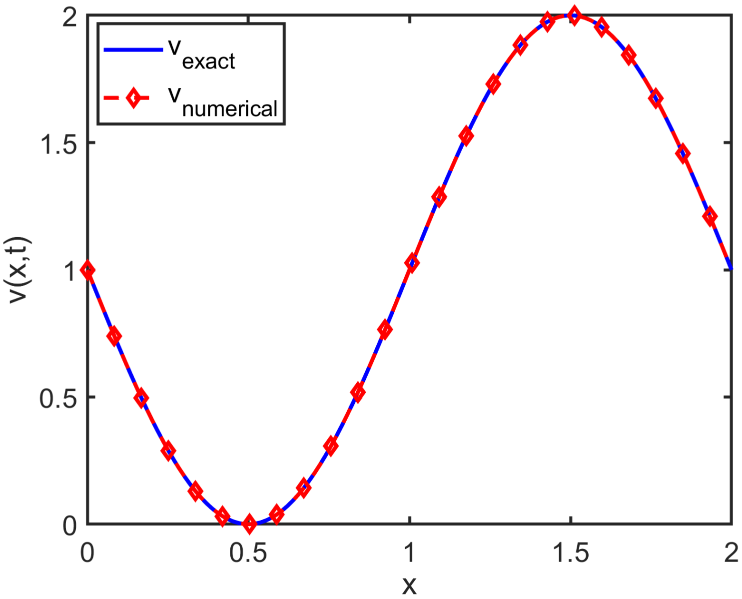

Figure 3.2(a): Plot of exact and numerical solutions at final time $T = 1$ for Problem (3.4.1.1), using CEMRK2-C4 method for Eq. (3.4.1) with $\gamma = 1$, $D = 10^{-5}$, $\Delta x = 1.6667 \times 10^{-2}$ and $\Delta t = \Delta x^2$.

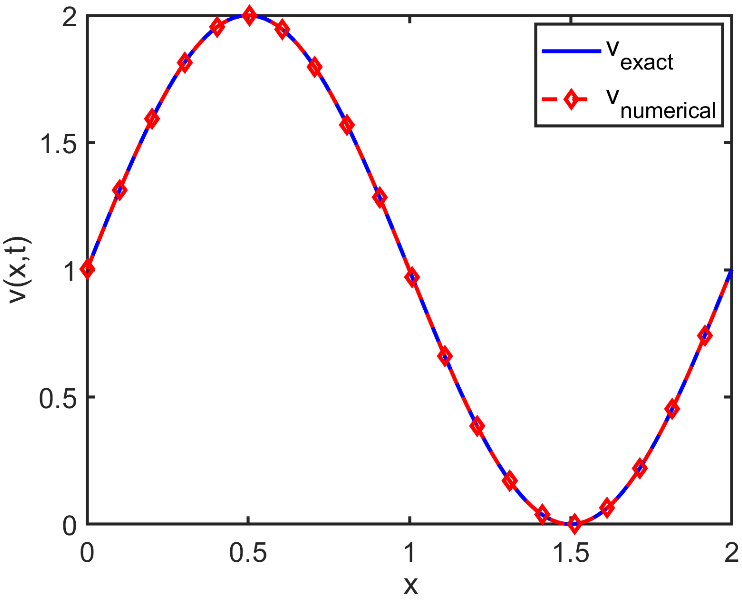

Figure 3.2(b): Plot of exact and numerical solutions at final time $T = 1$ for Problem (3.4.1.1), using CEMRK2-C4 method for Eq. (3.4.1) with $\gamma = 10$, $D = 10^{-5}$, $\Delta x = 1.6667 \times 10^{-2}$ and $\Delta t = \Delta x^2$.

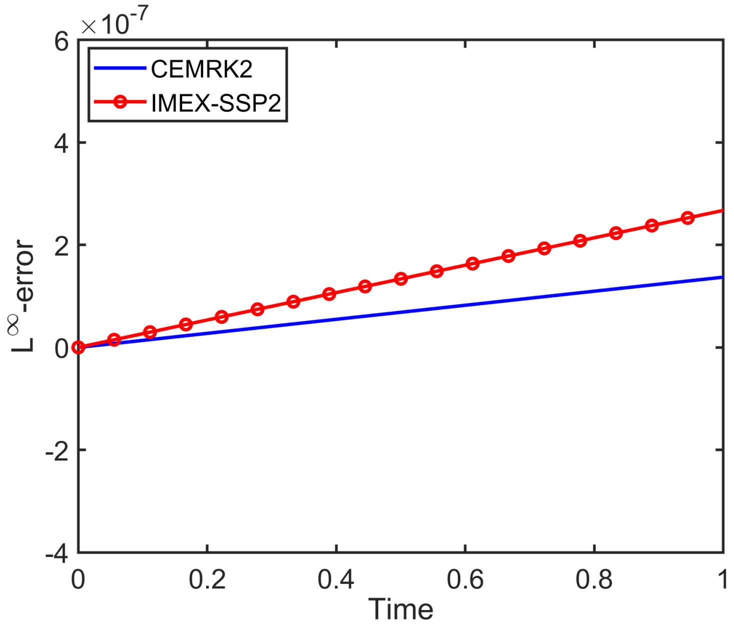

Figure 3.2(c): Comparison of the L^{∞}-error at final time $T = 1$ for Problem (3.4.1.1) using the indicated numerical methods for Eq. (3.4.1) with $\gamma = 1$, $D = 10^{-5}$, $\Delta x = 1.6667 \times 10^{-2}$ and $\Delta t = \Delta x^2$.

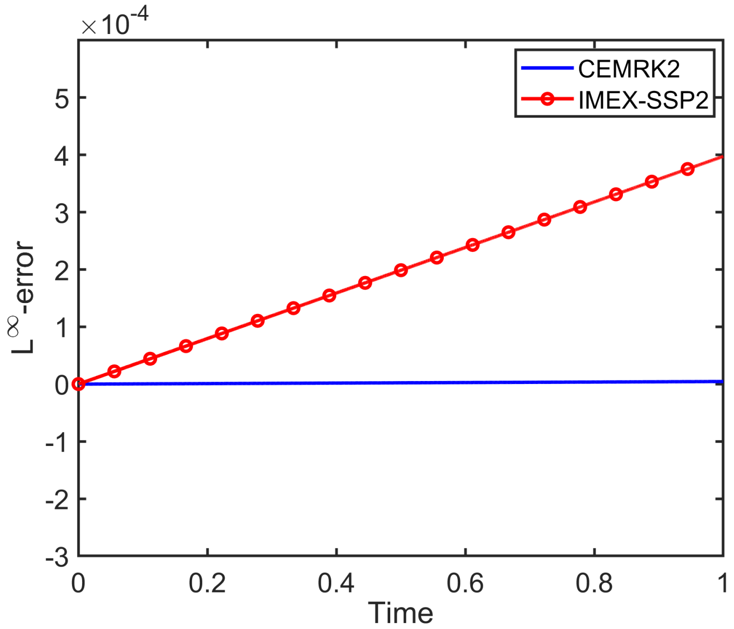

Figure 3.2(d): Comparison of the L^{∞}-error at final time $T = 1$ for Problem (3.4.1.1) using the indicated numerical methods for Eq. (3.4.1) with $\gamma = 10$, $D = 10^{-5}$, $\Delta x = 1.6667 \times 10^{-2}$ and $\Delta t = \Delta x^2$.

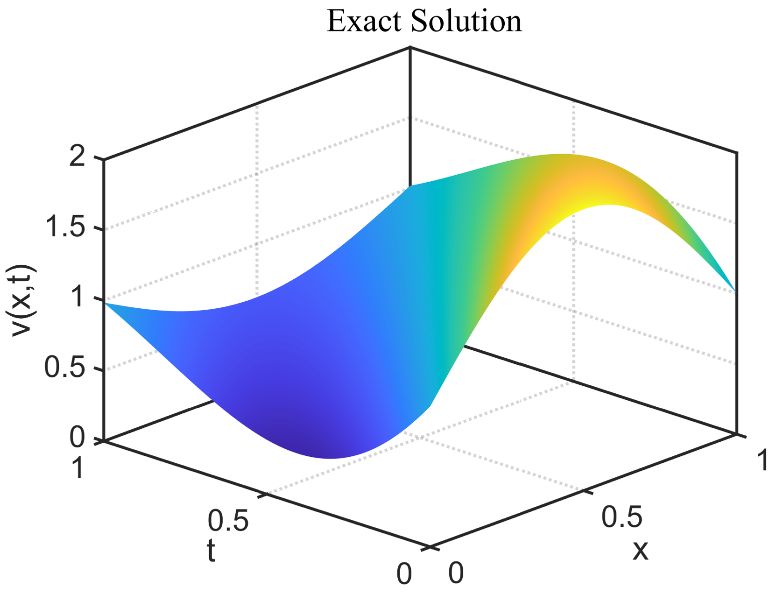

Figure 3.3(a): Surface plot of exact solution for Problem (3.4.1.2) using the CEMRK2-C4 scheme with $\gamma = 1$ and $D = 0.1$, $\Delta x = 1.2500 \times 10^{-2}, \Delta t = \Delta x^2$.

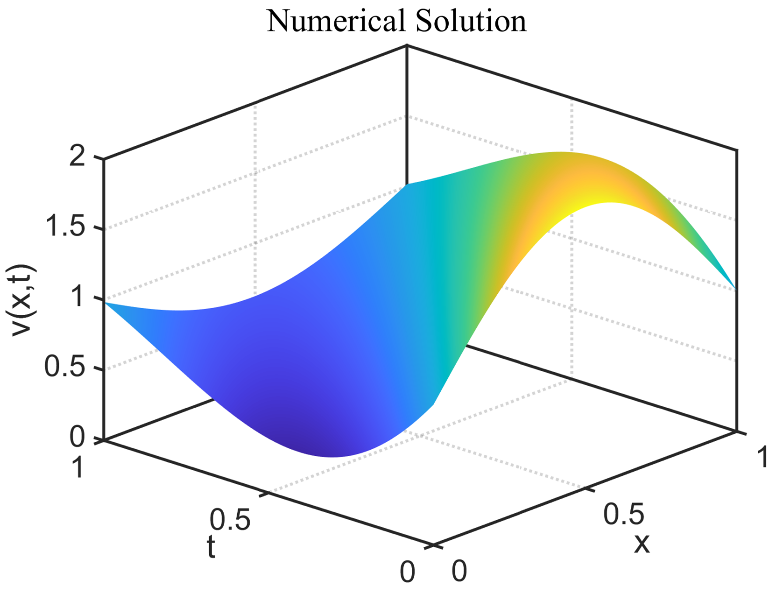

Figure 3.3(b): Surface plot of exact solution for Problem (3.4.1.2) using the CEMRK2-C4 scheme with $\gamma = 1$ and $D = 0.1$, $\Delta x = 1.2500 \times 10^{-2}, \Delta t = \Delta x^2$.

between the exact and computed solutions is shown in Fig. 3.3(c). Furthermore, the L^∞-error using the developed method, along with the error computed using IMEX-SSP2 [121] method, is displayed in Fig. 3.3(d).

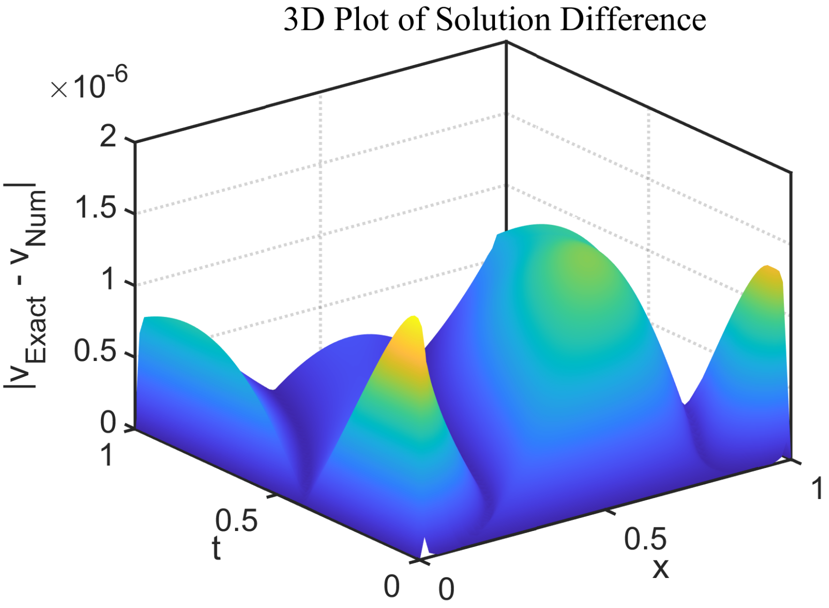

Figure 3.3(c): Surface plot of absolute error for Problem (3.4.1.2) using the CEMRK2-C4 scheme with $\gamma = 1$ and $D = 0.1$, $\Delta x = 1.2500 \times 10^{-2}, \Delta t = \Delta x^2$.

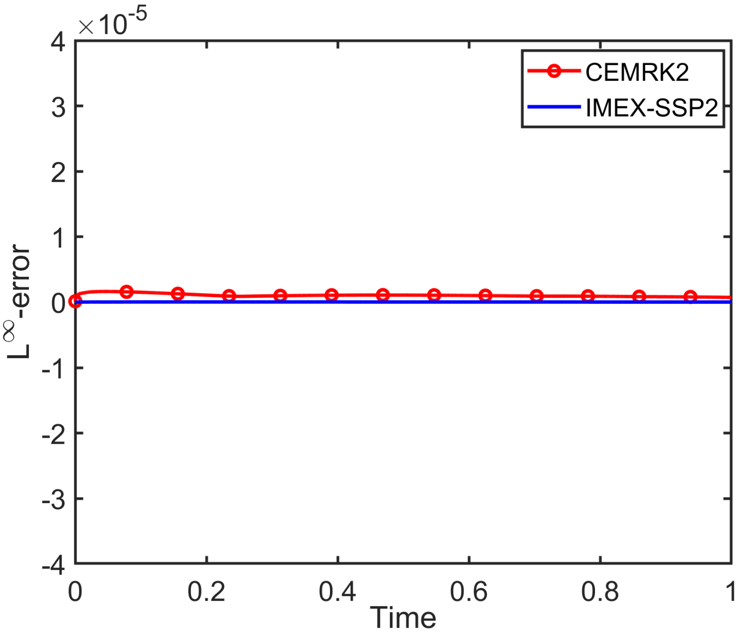

Figure 3.3(d): Comparison of the L^∞-error for Problem (3.4.1.2) using specified schemes for Eq. (3.4.1) at final time $T = 1$ with $\Delta x = 1.2500 \times 10^{-2}$ and $\Delta t = \Delta x^2$. Here, $\gamma = 1$ and $D = 0.1$.

3.4.2 Two-dimensional convection-diffusion model problem

Computations of 2D convection-diffusion equations with different choices of reaction and diffusion parameters are discussed next.

3.4.2.1 Problem-3

To assess the performance and accuracy of the proposed scheme, simulations of the 2D convection-diffusion equation have been performed. The governing equation is given as [43]

$$\frac{\partial v}{\partial t} + \gamma_1 \frac{\partial v}{\partial x} + \gamma_2 \frac{\partial v}{\partial y} - D_1 \frac{\partial^2 v}{\partial x^2} - D_2 \frac{\partial^2 v}{\partial y^2} = 0, \quad (x, y) \in [0, 2]^2 \tag{3.4.3}$$

For numerical computations, the parameters have been set to $\gamma_1 = 1$, $\gamma_2 = 1$, and $D_1 = D_2 = 0$, with periodic boundary conditions applied over the domain $(x, y) \in [0, 2]^2$. The exact solution is given as

$$v(x, y, t) = \sin(\pi(x + y - 2t)) \tag{3.4.4}$$

The initial data is derived from the exact solution provided in Eq. (3.4.4).

To validate the accuracy of results obtained from the developed scheme, the L^2-norm and L^∞-norm of the error have been computed. The numerical solution is advanced to the final time $T = 1$ using the CEMRK2 method for time integration and the C4 scheme for spatial discretization. For the free parameters, values are $a_{22} = 1.0 \times 10^1$, $a_{33} = 1.0$, $b_{22} = 7.0 \times 10^{-1}$, $b_{33} = -1.0 \times 10^{-4}$, $c_{22} = 3.0 \times 10^{-1}$, $c_{33} = 1.0 \times 10^{-1}$. For the two-dimensional case, we use uniform spatial grids of size $M_x \times M_y$, where M_x and M_y represent the number of grid points in the $x-$ and $y-$ directions, respectively. Table 3.4 shows the L^2-error norm and the corresponding convergence in space and time at final time. The results demonstrate that the CEMRK2-C4 scheme achieves fourth-order accuracy in space and second-order accuracy in time. Numerical solutions at $t = 0.4, 0.8,$ and 1.0 are illustrated alongside the initial solution in Figs. 3.4(a) - 3.4(d). Figure 3.5 presents a comparison of the L^∞-error between the developed second-order method and the IMEX-SSP2 [121] method. As seen in the Fig. 3.5, the presented scheme produces less error as compared to the IMEX-SSP2 method.

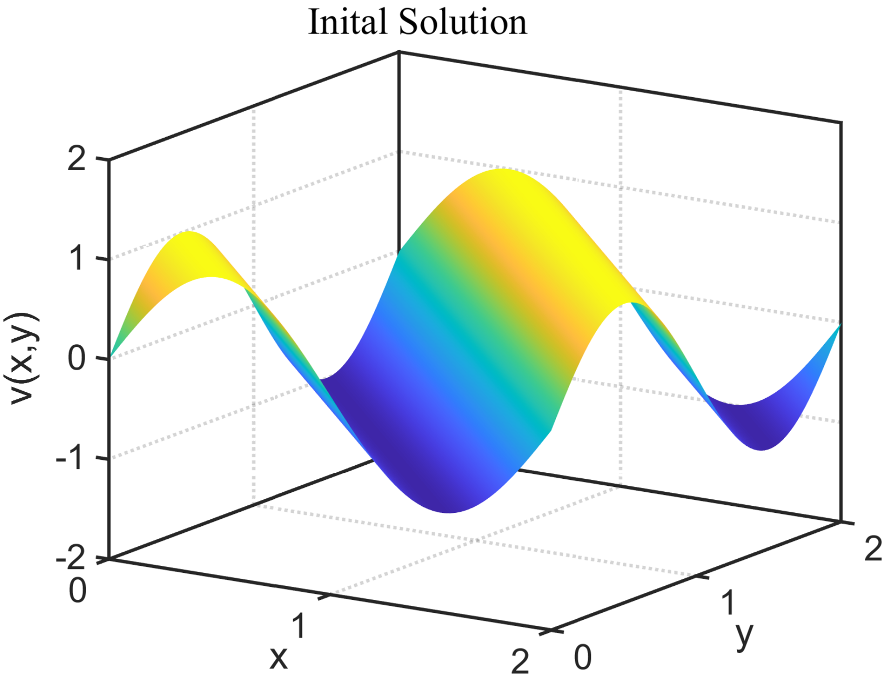

Figure 3.4(a): Numerical solution plot for Problem (3.4.2.1) using the CEMRK2-C4 with $\gamma_1 = \gamma_2 = 1$ and $D_1 = D_2 = 0$, $\Delta x = \Delta y = 2.5000 \times 10^{-2}$, and $\Delta t = \Delta x^2$ at $t = 0$.

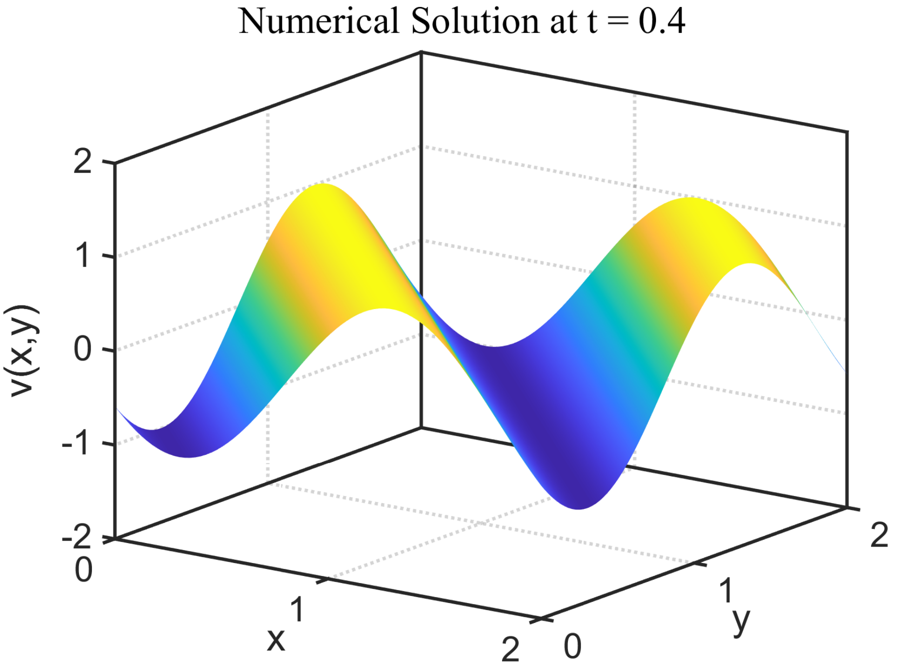

Figure 3.4(b): Numerical solution plot for Problem (3.4.2.1) using the CEMRK2-C4 with $\gamma_1 = \gamma_2 = 1$ and $D_1 = D_2 = 0$, $\Delta x = \Delta y = 2.5000 \times 10^{-2}$, and $\Delta t = \Delta x^2$ at $t = 0.4$.

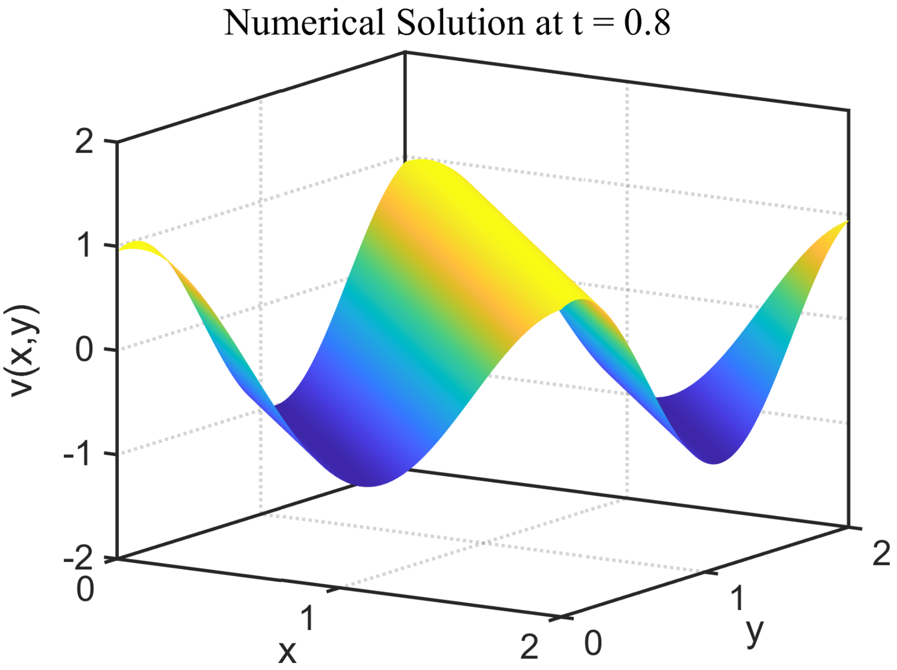

Figure 3.4(c): Numerical solution plot for Problem (3.4.2.1) using the CEMRK2-C4 with $\gamma_1 = \gamma_2 = 1$ and $D_1 = D_2 = 0$, , $\Delta x = \Delta y = 2.5000 \times 10^{-2}$, and $\Delta t = \Delta x^2$ at $t = 0.8$.

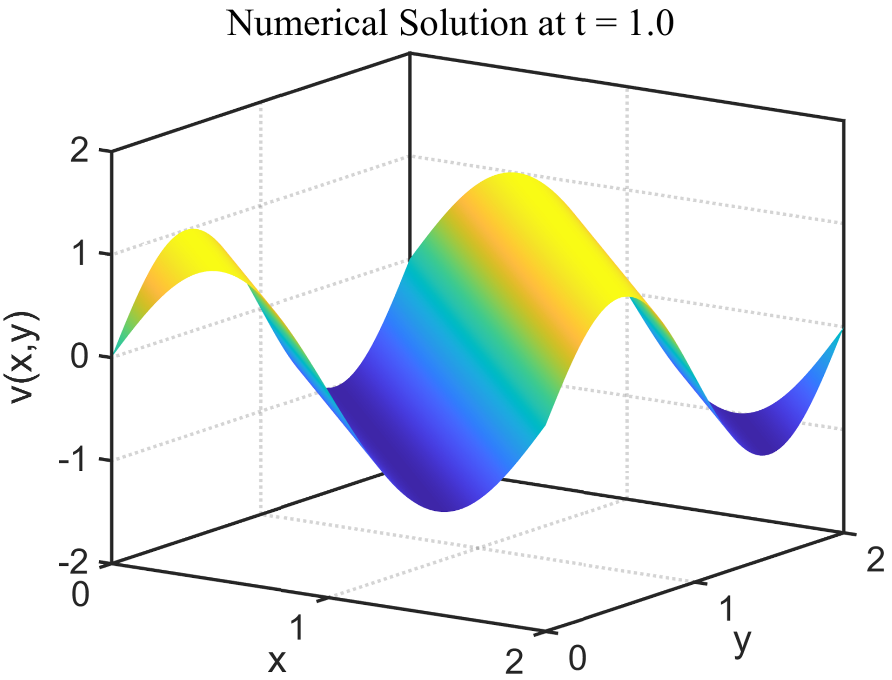

Figure 3.4(d): Numerical solution plot for Problem (3.4.2.1) using the CEMRK2-C4 with $\gamma_1 = \gamma_2 = 1$ and $D_1 = D_2 = 0$, $\Delta x = \Delta y = 2.5000 \times 10^{-2}$, and $\Delta t = \Delta x^2$ at $t = 1$.

Table 3.4: Convergence rate and L^2-error for Problem (3.4.2.1) corresponding to Eq. (3.4.3) using the CEMRK2-C4 scheme with $\gamma_1 = 1$, $\gamma_2 = 1$, and $D_1 = D_2 = 0$.

$M_x = M_y$	Δt	L^2-error	ROC (space)	ROC (time)
10	4.0000×10^{-2}	2.7710×10^{-3}	–	–
20	1.0000×10^{-2}	1.7280×10^{-4}	4.0033	2.0016
40	2.5000×10^{-3}	1.0797×10^{-5}	4.0003	2.0002
80	6.2500×10^{-4}	5.7640×10^{-7}	4.2275	2.1137

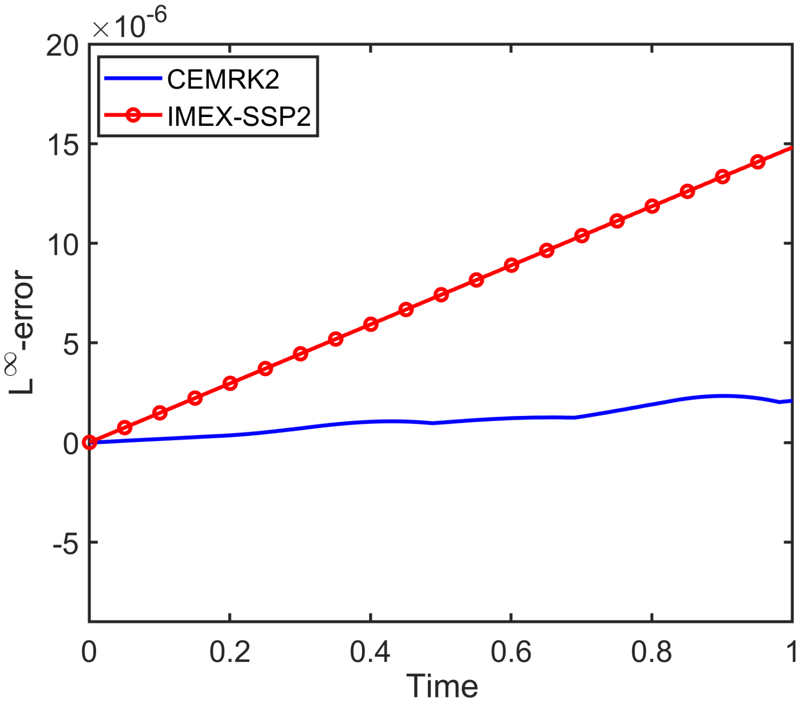

Figure 3.5: Comparison of L^∞-error for specified computational schemes applied to Problem (3.4.2.1) with parameters $\gamma_1 = \gamma_2 = 1$ and $D_1 = D_2 = 0$, $\Delta x = \Delta y = 2.5000 \times 10^{-2}$, and $\Delta t = \Delta x^2$.

3.4.2.2 Problem-4

Finally, we have considered a convection-diffusion problem, governed by Eq. (3.4.3), with a non-zero diffusion coefficient in the domain $[0, 2]^2$. The exact solution [39], is given by

$$v(x,y,t) = \frac{1}{4t+1}\exp\left[-\frac{(x-\gamma_1 t-0.5)^2}{D_1(4t+1)} - \frac{(y-\gamma_2 t-0.5)^2}{D_2(4t+1)}\right] \tag{3.4.5}$$

For assessing the performance of the current method, the L^2-error norm has been computed. The initial and boundary conditions are taken from the exact solution provided in Eq. (3.4.5). For the numerical simulations, the parameters are considered as $\gamma_1 = \gamma_2 = 1$ and $D_1 = D_2 = 0.01$, with a final time of $T = 1$. The numerical solution is computed using the CEMRK2 method for time integration and the C4 scheme for spatial discretization. The L^2-error norm and the corresponding convergence in space and time at $T = 1$ are summarized in Table 3.5. For the free parameters, we have selected $a_{22} = 1.0$, $a_{33} = 1.0 \times 10^2$, $b_{22} = 4.09 \times 10^2$, $b_{33} = 1.5 \times 10^{-1}$, $c_{22} = 1.0$, $c_{33} = 1.8 \times 10^2$. From Table 3.5, it is clear that the CEMRK2-C4 scheme achieves fourth-order accuracy in space and second-order accuracy in time. Plots of the exact and numerical solutions are presented in Figs. 3.6(a) - 3.6(b). To assess the accuracy of the proposed method, we compare the L^∞-norm of the error obtained using our presented approach with the IMEX-SSP2 [121] method, as illustrated in Fig. 3.6(c).

Table 3.5: Convergence and L^2-error for Problem (3.4.2.2) corresponding to Eq. (3.4.3) using CEMRK2-C4 scheme with $\gamma_1 = 1$, $\gamma_2 = 1$, and $D_1 = 0.01$, $D_2 = 0.01$ at final time $T = 1$.

$M_x = M_y$	Δt	L^2-error	ROC (space)	ROC (time)
10	4.0000×10^{-2}	2.0229×10^{-1}	–	–
20	1.0000×10^{-2}	2.4571×10^{-2}	3.0413	1.5207
40	2.5000×10^{-3}	1.3054×10^{-3}	4.2344	2.1172
80	6.2500×10^{-4}	7.6987×10^{-5}	4.0837	2.0419

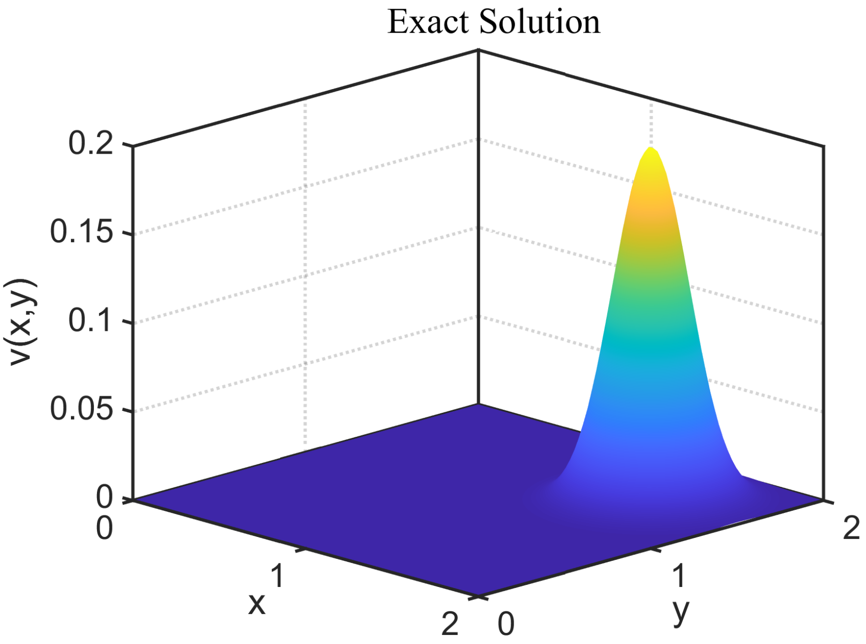

Figure 3.6(a): Exact solution plot for Problem (3.4.2.2) using the CEMRK2-C4 scheme with $\gamma_1 = 1$, $\gamma_2 = 1$, and $D_1 = 0.01$, $D_2 = 0.01$, $\Delta x = \Delta y = 2.5000 \times 10^{-2}, \Delta t = \Delta x^2$ at the final time $T = 1$.

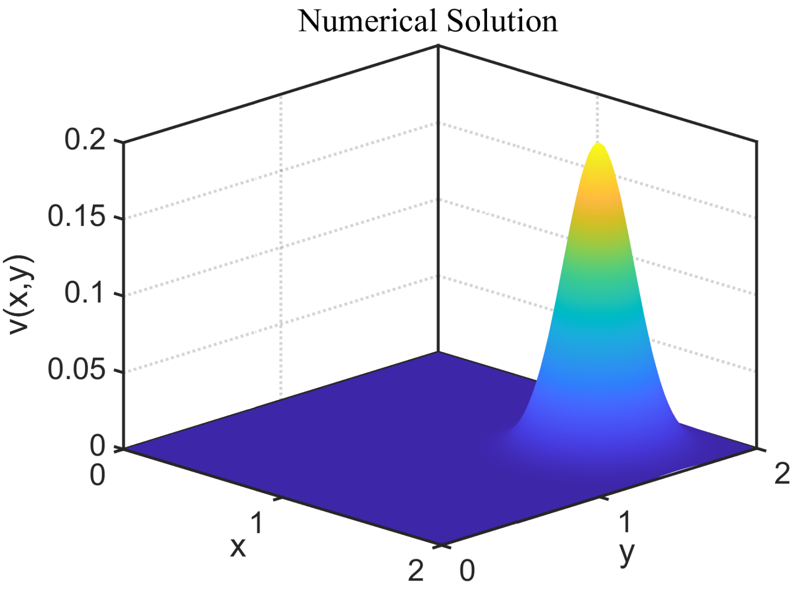

Figure 3.6(b): Numerical solution plot for Eq. (3.4.3) using the CEMRK2-C4 scheme with $\gamma_1 = 1$, $\gamma_2 = 1$, and $D_1 = 0.01$, $D_2 = 0.01$, $\Delta x = \Delta y = 2.5000 \times 10^{-2}, \Delta t = \Delta x^2$ at the final time $T = 1$.

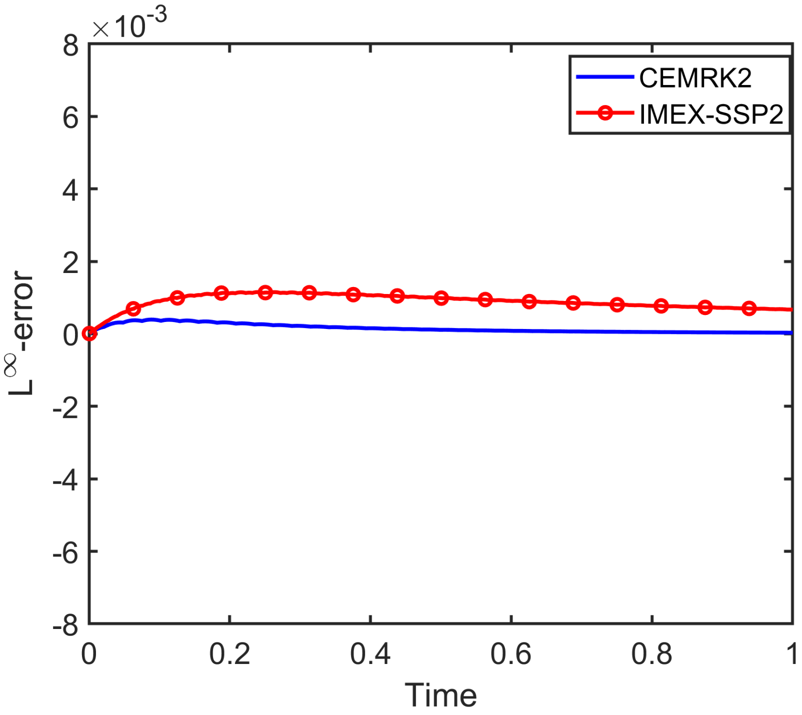

Figure 3.6(c): Comparison of L^∞-error for specified schemes for Problem (3.4.2.2) using $\Delta x = \Delta y = 2.5000 \times 10^{-2}$ and $\Delta t = \Delta x^2$ with parameter values $\gamma_1 = \gamma_2 = 1$ and $D_1 = D_2 = 0.01$.

Chapter 4

Energy-preserving fully-discrete methods for wave and soliton propagation in heterogeneous medium [1]

Many physical systems, such as wave propagation in acoustics and electromagnetism, crack propagation, and biological diffusion, are modeled by second-order wave equations [123, 124, 125, 100]. In two-dimensional heterogeneous domains, numerical modeling of acoustic waves has been explored in [70, 71, 72, 73]. Generally, systems with second-order time derivative are first reduced to first-order system before applying time integration [74]. Alternatively, Runge-Kutta-Nyström (RKN) methods can be employed directly to solve these systems, and variants of the RKN are studied in [75]. In [77], the authors presented a stable scheme for time-dependent diffusion problems by combining hopscotch spatial discretization with leapfrog time-stepping.

The energy-preserving AVF method introduced in [85] has been effectively applied to Hamiltonian PDEs. For spatial discretization, compact schemes offer higher accuracy

---

[1] The work has been published in the *Computers and Mathematics with Applications*, 174, (2024), 379–396.

as compared to the traditional finite difference methods with relatively smaller computational stencils. These compact stencils are the more precise to implement the corresponding boundary conditions [54, 80, 81]. To circumvent the challenges associated with applying compact schemes to wave equations with variable coefficients, the approach discussed in [126, 127] suggested shifting the variable coefficients with the time derivative term.

In [88], the authors developed a higher-order compact difference scheme that conserves energy, achieving fourth-order spatial accuracy and second-order temporal accuracy for two-dimensional hyperbolic systems. Furthermore, an energy-conserving Legendre-Galerkin spectral approach to solve the Higgs boson equation numerically was introduced in [128]. The authors in [105, 66] proposed an energy-preserving AVF-based compact scheme for simulating nonlinear two-dimensional wave equations. Soliton dynamics are often captured using nonlinear Klein-Gordon and sine-Gordon models [63, 129, 130, 131]. For one-dimensional nonlinear Klein-Gordon equations, the study in [93] developed a compact scheme combined with the diagonally implicit RKN method. Additionally, compact alternating direction-implicit (ADI) schemes for solving nonlinear wave equations were proposed in [132, 133].

For time-dependent PDEs, implicit methods are computationally expensive due to matrix inversions. This work proposes a partially implicit approach that does not require matrix inversion. The main goal in this chapter is to design and analyze a fully discrete, energy-preserving scheme that offers improved stability, while maintaining a computational cost comparable to that of explicit methods, for modeling wave and soliton propagation in both homogeneous and heterogeneous media.

Chapter 4 is structured as follows. Section 4.1 outlines the development of a second-order time integration scheme combined with a fourth-order compact spatial discretization method. In Section 4.2, Fourier analysis along with the formulation of an optimization problem to determine appropriate values for the free parameters is presented. Section 4.3 provides a theoretical proof that the proposed scheme conserves energy. Convergence results for the fully discrete scheme are detailed in Section 4.4. Finally, Section 4.5 presents numerical computations for various acoustic wave propagation test cases. Additional simulations involving the sine-Gordon and Klein-Gordon equations are included in Section 4.6.

4.1 Formulation of energy-preserving time integration method

The formulation of the new second-order time integration scheme is based on the two-dimensional undamped wave equation provided in Eq. (1.8.1) over the spatial domain Ω with boundary $\partial\Omega$, and T is the final time. The initial and boundary conditions are considered as follows

$$\begin{aligned} &u|_{t=0} = g_1(x,y), \quad \left.\frac{\partial u}{\partial t}\right|_{t=0} = g_2(x,y), \quad (x,y) \in \Omega \\ &u|_{\partial\Omega} = g_3(t), \quad t \in (0,T] \end{aligned} \tag{4.1.1}$$

Here, $c(x,y)$ is the phase speed, $g_1,\ g_2$ are the initial and g_3 represent the boundary data. The function $f(u)$ serves as a nonlinear forcing term and can take on specific forms to model different wave dynamics. For instance, Equation (1.8.1) corresponds to the sine-Gordon equation when $f(u) = -\sin u$, while $f(u) = -u - u^3$ corresponds to the Klein-Gordon equation.

Substituting, $z = \frac{1}{c^2(x,y)}\frac{\partial u}{\partial t}$, Eq. (1.8.1) can be rewritten as

$$\begin{aligned} \frac{\partial z}{\partial t} &= \left(\frac{\partial^2 u}{\partial x^2} + \frac{\partial^2 u}{\partial y^2}\right) + \frac{f(u)}{c^2(x,y)} \\ \frac{\partial u}{\partial t} &= c^2(x,y) z \end{aligned} \tag{4.1.2}$$

For time integration, second-order energy and dispersion relation preserving (EDRP2) method for the system (4.1.2) is derived following the optimized partially implicit procedure discussed in [134], as

$$\begin{aligned} z^{(1)} &= z^n + \Delta t \left[u^n_{xx} + u^n_{yy} + \frac{f(u^n)}{c^2(x,y)}\right] \\ u^{(1)} &= u^n + c^2(x,y)\Delta t((1-\alpha_1)z^n + \alpha_1 z^{(1)}) \end{aligned}$$

$$
\begin{aligned}
z^{n+1} &= \frac{1}{2}\left[z^{n} + z^{(1)} + \Delta t\left(u^{(1)}_{xx} + u^{(1)}_{yy} + \frac{f(u^{(1)})}{c^{2}(x,y)}\right)\right] \\
u^{n+1} &= u^{n} + c^{2}(x,y)\frac{\Delta t}{2}\left[z^{n} + 2\alpha_2 z^{(1)} + (1-2\alpha_2)z^{n+1}\right]
\end{aligned}
\tag{4.1.3}
$$

where α_1 and α_2 are the free-parameters. The C4 scheme is used for the spatial discretization. Spatial discretization of the Eq. (4.1.2) with zero forcing function ($f(u) = 0$), given as

$$
\begin{aligned}
\frac{\partial z}{\partial t} &= \left(\frac{\partial^2 u}{\partial x^2} + \frac{\partial^2 u}{\partial y^2}\right) \\
\frac{\partial u}{\partial t} &= c^2(x,y) z
\end{aligned}
\tag{4.1.4}
$$

is discussed next. Simulations for the nonhomogeneous linear and nonlinear wave equations with forcing term are given in Sections 4.5 and 4.6.

4.1.1 Spatial discretization

Spatial discretization of the second-order spatial derivatives is performed using the C4 scheme discussed in [135, 80]. For the C4 scheme mesh-widths are defined as, $\Delta x = (x_{Nx} - x_0)/Nx$, $\Delta y = (y_{Ny} - y_0)/Ny$, for positive integers Nx and Ny, respectively. The mesh-points are given as, $x_i = x_0 + i\Delta x$, for $i = 0, 1, ..., Nx$, $y_j = y_0 + j\Delta y$, for $j = 0, 1, ..., Ny$. The discrete mesh is defined as, $\Omega_h = \{(x_i, y_j)|i = 1, ..., Nx, j = 1, ...$ $, Ny\}$. Discrete periodic boundary conditions are given as, $x_{Nx+1} = x_0 +$ $(Nx + 1)\Delta x$, $y_{Ny+1} = y_0 + (Ny + 1)\Delta y$, and the mesh-points for the full-domain using periodic boundary conditions are given as, $\Omega^E_h = \{(x_i, y_j)|i = 0, ..., Nx + 1, j = 0, ..., Ny + 1\}$. For a given mesh function, $u = \left\{u_{i,j}|(x_i, y_j) \in \Omega^E_h\right\}$, the important difference operators are defined as

$$
\begin{gathered}
\delta^+_x u_{i,j} = \tfrac{u_{i+1,j} - u_{i,j}}{\Delta x},\quad \delta^-_x u_{i,j} = \tfrac{u_{i,j} - u_{i-1,j}}{\Delta x},\quad \delta^2_x u_{i,j} = \tfrac{u_{i-1,j} - 2u_{i,j} + u_{i+1,j}}{\Delta x^2} \\
\delta^+_y u_{i,j} = \tfrac{u_{i,j+1} - u_{i,j}}{\Delta y},\quad \delta^-_y u_{i,j} = \tfrac{u_{i,j} - u_{i,j-1}}{\Delta y},\quad \delta^2_y u_{i,j} = \tfrac{u_{i,j-1} - 2u_{i,j} + u_{i,j+1}}{\Delta y^2} \\
\delta^2_x u_{i,j} = \delta^+_x \delta^-_x u_{i,j},\quad \delta^2_y u_{i,j} = \delta^+_y \delta^-_y u_{i,j}
\end{gathered}
$$

By approximating the unknowns as, $U_{i,j}(t) \approx u(x_i, y_j, t)$ and $Z_{i,j}(t) \approx z(x_i, y_j, t)$, the C4 scheme is derived to discretize the second-order spatial derivatives using the following finite difference operators

$$\begin{aligned}\mathcal{P}_x u_{i,j} &= \Big(1+\frac{\Delta x^2}{12}\delta_x^2\Big)u_{i,j}, \;\; i=1,...,Nx, \;\; j=0,...,Ny+1,\\ \mathcal{P}_y u_{i,j} &= \Big(1+\frac{\Delta y^2}{12}\delta_y^2\Big)u_{i,j}, \;\; i=0,...,Nx+1, \;\; j=1,...,Ny.\end{aligned} \tag{4.1.5}$$

As discussed in [135, 80], fourth-order compact finite difference operators are obtained as

$$\begin{aligned}\mathcal{P}_x^{-1}\delta_x^2 u_{i,j} &= \frac{\partial^2 u}{\partial x^2}(x_i,y_j) - \frac{\Delta x^4}{240}\frac{\partial^6 u}{\partial x^6}(\zeta_1,y_j)\\ \mathcal{P}_y^{-1}\delta_y^2 u_{i,j} &= \frac{\partial^2 u}{\partial y^2}(x_i,y_j) - \frac{\Delta y^4}{240}\frac{\partial^6 u}{\partial y^6}(x_i,\zeta_2)\end{aligned} \tag{4.1.6}$$

where $\xi_1 \in (x_{i-1}, x_{i+1})$, $\xi_2 \in (y_{i-1}, y_{i+1})$. By neglecting the $\mathcal{O}(\Delta x^4)$ terms in Eq. (4.1.6), fourth-order compact finite difference approximation of the Laplacian operator given in Eq. (4.1.4) is obtained as

$$\mathcal{P}_x^{-1}\delta_x^2 u_{i,j} + \mathcal{P}_y^{-1}\delta_y^2 u_{i,j} \approx \left(\frac{\partial^2 u}{\partial x^2} + \frac{\partial^2 u}{\partial y^2}\right)\Bigg|_{(x_i,y_j)} \tag{4.1.7}$$

where, $\mathcal{P}_x^{-1}$ and $\mathcal{P}_y^{-1}$ are the inverse of the coefficient operators $\mathcal{P}_x$ and $\mathcal{P}_y$, respectively. It is observed that the matrices corresponding to the operators $\mathcal{P}_x$ and $\mathcal{P}_y$ take the form of periodic tridiagonal matrices, as shown in Eq. (4.1.12), which can be efficiently inverted using Thomas algorithm. By applying the C4 approximation of the Laplacian operator given in Eq. (4.1.7), the semi-discrete representation of the system given in Eq. (4.1.4) is obtained in vector notation as follows

$$\begin{aligned}\frac{dZ_{i,j}(t)}{dt} &= \mathcal{P}_x^{-1}\delta_x^2 U_{i,j} + \mathcal{P}_y^{-1}\delta_y^2 U_{i,j},\\ \frac{dU_{i,j}(t)}{dt} &= c_{i,j}^2 Z_{i,j}(t), \;\; i=1,...,Nx, \;\; j=1,...,Ny.\end{aligned} \tag{4.1.8}$$

with the periodic boundary conditions given as

$$\begin{aligned}U_{0,j} = U_{Nx,j}, \;\; U_{1,j} = U_{Nx+1,j}, \;\; j=0,...,Ny+1\\ U_{i,0} = U_{i,Ny}, \;\; U_{i,1} = U_{i,Ny+1}, \;\; i=0,...,Nx+1\end{aligned} \tag{4.1.9}$$

and the initial conditions

$$U_{i,j}(0) = \Phi_1(x_i,y_j), \;\; Z_{i,j}(0) = \Phi_2(x_i,y_j) \tag{4.1.10}$$

Using matrix notations, Eq. (4.1.8) can be represented as

$$\frac{dZ}{dt} = \mathscr{P}U, \quad \frac{dU}{dt} = C^2 Z \tag{4.1.11}$$

where $Z = \{Z_{i,j}\}$ and $U = \{U_{i,j}\}$. Here, C is the diagonal matrix given by $C = diag(c_{1,1}, c_{2,1}, \cdots, c_{Nx,1}, c_{1,2}, c_{2,2}, \cdots, c_{Nx,2}, \cdots, c_{1,Ny}, c_{2,Ny}, \cdots, c_{Nx,Ny})$ and matrix $\mathscr{P}$ corresponds to the operator $(\mathcal{P}_x^{-1}\delta_x^2 + \mathcal{P}_y^{-1}\delta_y^2)$, is given as

$$\begin{aligned}
&\mathscr{P} = Q_x\Gamma_x^+\Gamma_x^- + Q_y\Gamma_y^+\Gamma_y^- \\
&Q_x = I_{Ny} \otimes P_x^{-1}, \quad \Gamma_x^+ = I_{Ny} \otimes \bar{\Gamma}_x^+, \quad \Gamma_x^- = I_{Ny} \otimes \bar{\Gamma}_x^-, \\
&Q_y = P_y^{-1} \otimes I_{Nx}, \quad \Gamma_y^+ = \bar{\Gamma}_y^+ \otimes I_{Nx}, \quad \Gamma_y^- = \bar{\Gamma}_y^- \otimes I_{Nx}
\end{aligned}$$

where Q_x and Q_y are the symmetric positive definite matrices. Matrices P_x, P_y, $\bar{\Gamma}_x^+$, $\bar{\Gamma}_x^-$, $\bar{\Gamma}_y^+$, and $\bar{\Gamma}_y^-$ (corresponding to the operators $\mathcal{P}_x$, $\mathcal{P}_x$, δ_x^+, δ_x^-, δ_y^+, and δ_y^-, respectively) are given as

$$P_x = \begin{bmatrix} \frac{10}{12} & \frac{1}{12} & 0 & \cdots & 0 & \frac{1}{12} \\ \frac{1}{12} & \frac{10}{12} & \frac{1}{12} & \cdots & 0 & 0 \\ \vdots & \vdots & \vdots & & \vdots & \vdots \\ 0 & 0 & 0 & \cdots & \frac{10}{12} & \frac{1}{12} \\ \frac{1}{12} & 0 & 0 & \cdots & \frac{1}{12} & \frac{10}{12} \end{bmatrix}_{Nx\times Nx}, P_y = \begin{bmatrix} \frac{10}{12} & \frac{1}{12} & 0 & \cdots & 0 & \frac{1}{12} \\ \frac{1}{12} & \frac{10}{12} & \frac{1}{12} & \cdots & 0 & 0 \\ \vdots & \vdots & \vdots & & \vdots & \vdots \\ 0 & 0 & 0 & \cdots & \frac{10}{12} & \frac{1}{12} \\ \frac{1}{12} & 0 & 0 & \cdots & \frac{1}{12} & \frac{10}{12} \end{bmatrix}_{Ny\times Ny}$$

$$\bar{\Gamma}_x^+ = \frac{1}{\Delta x}\begin{bmatrix} -1 & 1 & 0 \cdots & 0 & 0 \\ 0 & -1 & 1 \cdots & 0 & 0 \\ \vdots & \vdots & \vdots & \vdots & \vdots \\ 0 & 0 & 0 \cdots & -1 & 1 \\ 1 & 0 & 0 \cdots & 0 & -1 \end{bmatrix}_{Nx\times Nx}, \bar{\Gamma}_y^+ = \frac{1}{\Delta y}\begin{bmatrix} -1 & 1 & 0 \cdots & 0 & 0 \\ 0 & -1 & 1 \cdots & 0 & 0 \\ \vdots & \vdots & \vdots & \vdots & \vdots \\ 0 & 0 & 0 \cdots & -1 & 1 \\ 1 & 0 & 0 \cdots & 0 & -1 \end{bmatrix}_{Ny\times Ny}$$

$$\bar{\Gamma}_x^- = \frac{1}{\Delta x}\begin{bmatrix} 1 & 0 & 0 & \cdots & 0 & -1 \\ -1 & 1 & 0 & \cdots & 0 & 0 \\ \vdots & \vdots & \vdots & & \vdots & \vdots \\ 0 & 0 & 0 & \cdots & 1 & 0 \\ 0 & 0 & 0 & \cdots & -1 & 1 \end{bmatrix}_{Nx\times Nx}, \bar{\Gamma}_y^- = \frac{1}{\Delta y}\begin{bmatrix} 1 & 0 & 0 & \cdots & 0 & -1 \\ -1 & 1 & 0 & \cdots & 0 & 0 \\ \vdots & \vdots & \vdots & & \vdots & \vdots \\ 0 & 0 & 0 & \cdots & 1 & 0 \\ 0 & 0 & 0 & \cdots & -1 & 1 \end{bmatrix}_{Ny\times Ny} \tag{4.1.12}$$

The fully discrete form of the system presented in Eq. (4.1.4) is derived as follows

$$
\begin{aligned}
Z_{i,j}^{n+1} &= Z_{i,j}^{n} + \frac{\Delta t}{2}\left(\mathcal{P}_x^{-1}\delta_x^2 + \mathcal{P}_y^{-1}\delta_y^2\right)U_{i,j}^{n} + \frac{\Delta t}{2}(\mathcal{P}_x^{-1}\delta_x^2 + \mathcal{P}_y^{-1}\delta_y^2) \\
&\qquad \left[U_{i,j}^{n} + \Delta t c_{i,j}^2\left\{(1-\alpha_1)Z_{i,j}^{n} + \alpha_1\left(Z_{i,j}^{n} + \Delta t(\mathcal{P}_x^{-1}\delta_x^2 + \mathcal{P}_y^{-1}\delta_y^2)U_{i,j}^{n}\right)\right\}\right] \\
U_{i,j}^{n+1} &= U_{i,j}^{n} + \frac{\Delta t}{2}c_{i,j}^2\left[Z_{i,j}^{n} + 2\alpha_2 Z_{i,j}^{n} + 2\alpha_2\Delta t\left(\mathcal{P}_x^{-1}\delta_x^2 + \mathcal{P}_y^{-1}\delta_y^2\right)U_{i,j}^{n}\right] \\
&\qquad + \frac{\Delta t}{2}c_{i,j}^2\left[(1-2\alpha_2)Z_{i,j}^{n+1}\right]
\end{aligned}
\tag{4.1.13}
$$

where $Z_{i,j}^n \approx z(x_i, y_j, t^n)$ and $U_{i,j}^n \approx u(x_i, y_j, t^n)$. The system presented in Eq. (4.1.13) can be equivalently expressed in matrix form by introducing $Z = \{Z_{i,j}\}$, $U = \{U_{i,j}\}$ and $C = \{c_{i,j}\}$, as follows

$$
\begin{aligned}
\frac{Z^{n+1} - Z^n}{\Delta t} &= \mathscr{P}U^n + \frac{\Delta t}{2}\mathscr{P}C^2 Z^n + \alpha_1\frac{\Delta t^2}{2}\mathscr{P}C^2\mathscr{P}U^n \\
\frac{U^{n+1} - U^n}{\Delta t} &= C^2\left(\frac{Z^n + Z^{n+1}}{2} - \alpha_2(Z^{n+1} - Z^n) + \alpha_2\Delta t\mathscr{P}U^n\right)
\end{aligned}
\tag{4.1.14}
$$

Equation (4.1.14) can also be represented as

$$
\begin{aligned}
\frac{Z^{n+1} - Z^n}{\Delta t} &= \mathscr{P}U^* \\
\frac{U^{n+1} - U^n}{\Delta t} &= C^2 Z^*
\end{aligned}
\tag{4.1.15}
$$

where $Z^* = \frac{Z^n + Z^{n+1}}{2} - \alpha_2(Z^{n+1} - Z^n) + \alpha_2\Delta t\mathscr{P}U^n$ and $U^* = U^n + \frac{\Delta t}{2}C^2 Z^n + \alpha_1\frac{\Delta t^2}{2}C^2\mathscr{P}U^n$. Fourier analysis is next performed to assess the behavior of the developed schemes for linear wave equations in one- and two- dimensions.

4.2 Fourier analysis of undamped wave equation

For accurate numerical simulations of dynamical systems, it is essential to use methods that not only resolve spatial and temporal scales but also preserve key physical properties. To ensure this, the chosen scheme must maintain neutral stability and satisfy the physical dispersion relation. For the purpose of stability and dispersion analysis, the following model equation with periodic boundary conditions is used, and it is expressed as

$$
\begin{aligned}
&\frac{\partial^2 u}{\partial t^2} = c^2\frac{\partial^2 u}{\partial x^2}, \quad x \in [0, \pi], \quad t > 0 \\
&u|_{t=0} = f(x), \quad \left.\frac{\partial u}{\partial t}\right|_{t=0} = g(x), \quad x \in [0, \pi]
\end{aligned}
\tag{4.2.1}
$$

using two-sided Fourier-Laplace transform [136], $u(x,t) = \int_{-\infty}^{\infty}\int_{-\infty}^{\infty} \hat{U}(k,\omega)e^{i(kx-\omega t)}\, dkd\omega$, dispersion relation for Eq. (4.2.1) is expressed as, $\omega^2 = c^2k^2$. In this expression, ω denotes the circular frequency and k is the wavenumber. Equation (4.2.1) can be reformulated as

$$\begin{aligned} \frac{\partial z}{\partial t} &= \frac{\partial^2 u}{\partial x^2}, \quad \frac{\partial u}{\partial t} = c^2 z, \quad x \in [0,\pi], \quad t > 0 \\ u|_{t=0} &= f(x), \quad z|_{t=0} = g_1(x), \quad x \in [0,\pi] \end{aligned} \tag{4.2.2}$$

where $g_1(x) = \frac{g(x)}{c^2}$. Applying discrete Fourier transform, the unknown u and its spatial derivatives can be represented as [110]

$$\begin{aligned} u(x,t)\big|_N &= \int_{-k_{max}}^{k_{max}} \check{u}(k,t)e^{ikx}dk \\ u_{xx}(x,t)\big|_N &= \int_{-k_{max}}^{k_{max}} -k_m^2\check{u}(k,t)e^{ikx}dk \end{aligned}$$

where k_m is the modified wavenumber and $k_{max} = \pi/\Delta x$. The semi-discretized version of Eq. (4.2.2) is derived using the discrete Fourier transform and is given by

$$\begin{aligned} \frac{d\check{z}^n}{dt} &= -k_m^2\check{u}^n, \quad \frac{d\check{u}^n}{dt} = c^2\check{z}^n \\ \check{u}|_{t=0} &= \check{f}(k), \quad \check{z}|_{t=0} = \check{g}_1(k) \end{aligned} \tag{4.2.3}$$

where $t = n\Delta t$. Equation (4.2.3) is discretized using EDRP2 method, resulting in

$$\begin{aligned} \check{z}^{(1)} &= \check{z}^n - \Delta t k_m^2 \check{u}^n \\ \check{u}^{(1)} &= \check{u}^n + c^2\Delta t\left[(1-\alpha_1)\check{z}^n + \alpha_1\check{z}^{(1)}\right] \\ \check{z}^{n+1} &= \frac{1}{2}\left[\check{z}^n + \check{z}^{(1)} - \Delta t k_m^2\check{u}^n\right] \\ \check{u}^{n+1} &= \check{u}^n + c^2\frac{\Delta t}{2}\left[\check{z}^n + 2\alpha_2\check{z}^{(1)} + (1-2\alpha_2)\check{z}^{n+1}\right] \end{aligned} \tag{4.2.4}$$

In the vector notation, Eq. (4.2.4) can be represented as, $P^{n+1} = MP^n$, where M is the 2×2 evolution matrix and $P = (\check{z},\check{u})^T$. Entries of the matrix M are given as,

$$\begin{aligned} m_{11} &= 1 - \frac{c^2\Delta t^2 k_m^2}{2}, \quad m_{12} = \frac{\alpha_1 c^2\Delta t^3(k_m^2)^2}{2} - \Delta t k_m^2 \\ m_{21} &= c^2\Delta t - \frac{c^4\Delta t^3 k_m^2}{4} + \frac{c^4\alpha_2\Delta t^3 k_m^2}{2} \\ m_{22} &= 1 + \frac{c^4\alpha_1\Delta t^4(k_m^2)^2}{4} - \frac{c^2\Delta t^2 k_m^2}{2} - \frac{c^4\alpha_1\alpha_2\Delta t^4(k_m^2)^2}{2} \end{aligned}$$

Numerical amplification factors (eigenvalues of the matrix M) for the EDRP2 method are expressed as, $\lambda = [\lambda_{N_1}, \lambda_{N_2}]^T$. Furthermore, by denoting $k_m^2 = \frac{\varphi(k\Delta x)}{\Delta x^2}$ the eigenvalues of M are obtained as

$$\lambda_{N_{1,2}} = e_1 \pm \frac{C_r}{8}\sqrt{e_2} \tag{4.2.5}$$

where $e_1 = 1 - (C_r^4\alpha_1\alpha_2\varphi^2(k\Delta x))/4 + (C_r^4\alpha_1\varphi^2(k\Delta x))/8 - (C_r^2\varphi^2(k\Delta x))/2$,
$e_2 = \varphi(k\Delta x)\Big(4C_r^6\alpha_2^2\alpha_1^2\varphi^3(k\Delta x) - 4C_r^6\alpha_2^2\alpha_1\varphi^3(k\Delta x) + C_r^6\alpha_1^2\varphi^3(k\Delta x) - 8C_r^4\alpha_1\varphi^2(k\Delta x) + 16C_r^4\alpha_2\alpha_1\varphi^2(k\Delta x) + 32C_r^2\alpha_1\varphi(k\Delta x) - 32C_r^2\alpha_2\varphi(k\Delta x) + 16C_r^2\varphi(k\Delta x) - 64\Big)$, and $C_r = \frac{c\Delta t}{\Delta x}$ is the Courant number.

It is evident from Eq. (4.2.5) that for the wave-like solutions $e_2 < 0$. Applying the Fourier transform, the nondimensional wavenumber for the CD2 scheme is obtained as

$$\int_{-k_{max}}^{k_{max}} -k_m^2\check{u}(k,t)e^{ikx}dk = \frac{1}{\Delta x^2}\int_{-k_{max}}^{k_{max}} \left(e^{ik\Delta x} - 2 + e^{-ik\Delta x}\right)\check{u}(k,t)e^{ikx}dk$$

$$k_m^2 = -\frac{1}{\Delta x^2}\left(e^{ik\Delta x} - 2 + e^{-ik\Delta x}\right) = \frac{2}{\Delta x^2}(1 - \cos(k\Delta x))$$

Thus, the nondimensional wavenumbers ($\varphi(k\Delta x)$) for the CD2 scheme is given by

$$\varphi(k\Delta x)_{\mathrm{CD2}} = k_m^2\Delta x^2 = 2\left(1 - \cos(k\Delta x)\right)$$

Similarly, the nondimensional wavenumbers ($\varphi(k\Delta x)$) for the C4 scheme is provided as

$$\varphi(k\Delta x)_{\mathrm{C4}} = \frac{12\left(1 - \cos(k\Delta x)\right)}{\cos(k\Delta x) + 5}$$

Moreover, nondimensional modified wavenumber for Eq. (4.1.4) is expressed as, $k_m^2 = \frac{\varphi(k_xh)+\varphi(k_yh)}{h^2}$, where $h = \Delta x = \Delta y$ denote the uniform spatial step-size. Numerical circular frequency ω_N is given as, $\omega_N = -\frac{1}{\Delta t}\tan^{-1}\left(\frac{\lambda_{Ni}}{\lambda_{Nr}}\right)$, where λ_{Ni} and λ_{Nr} represent the imaginary and real parts of the numerical amplification factor, respectively. The numerical phase speed and group velocity are defined as, $c_N = \frac{\omega_N}{k}$, $Vg_N = \frac{\partial\omega_N}{\partial k}$ [83, 137].

Contours showing absolute values of amplification factors ($|\lambda_N|$), normalized phase speed (c_N/c) and group velocity (Vg_N/c) for EDRP2-CD2 (left column frames) and EDRP2-C4 (middle column frames) schemes are presented in Fig. 4.1(a). Neutrally stable regions ($|\lambda| = 1$) are indicated by a vertical dash-dotted lines in Fig. 4.1(a) highlighting the critical values of C_r, up to which we have the neutrally stable region for all wavenumbers.

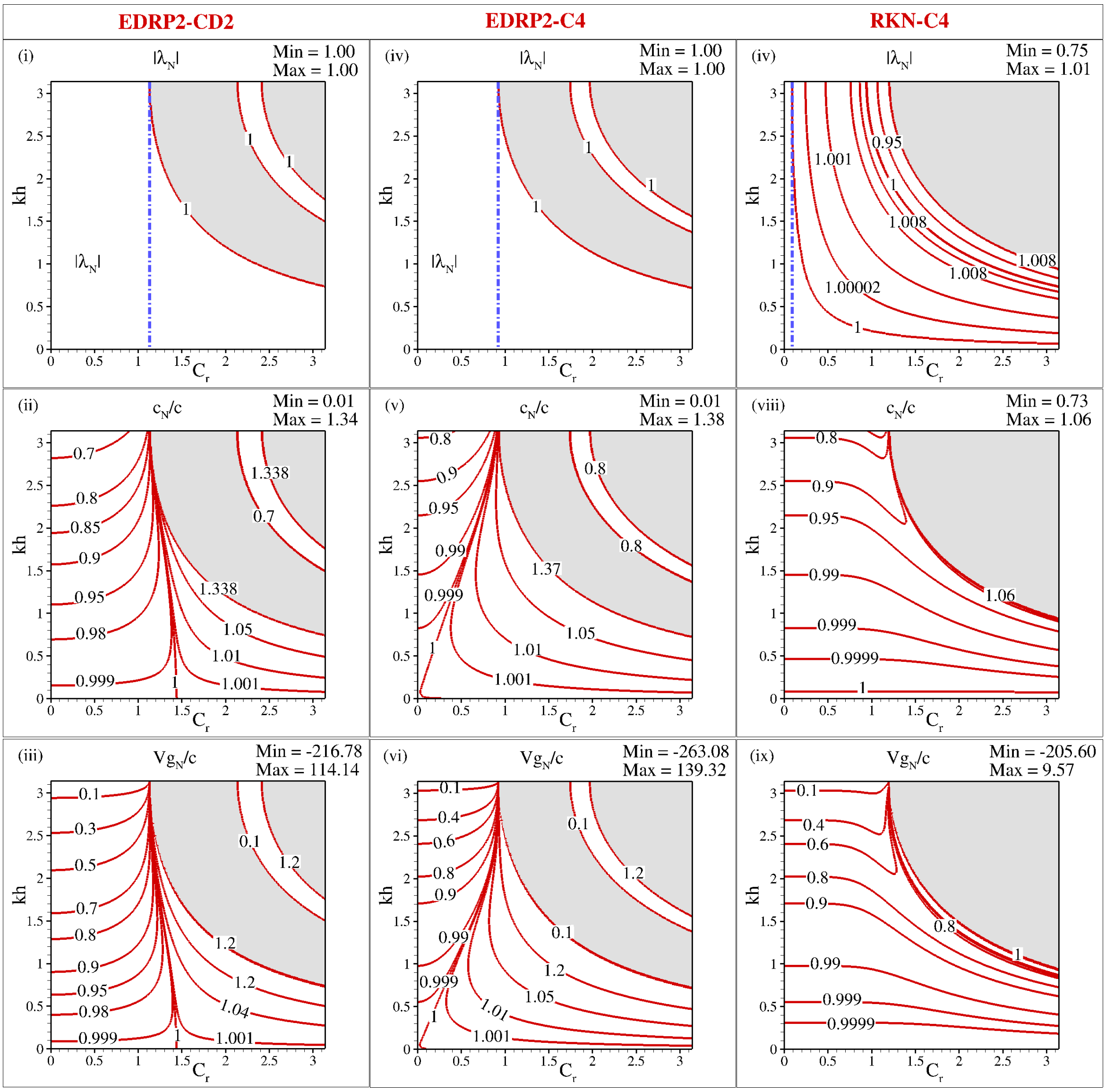

Figure 4.1(a): Contour plots of $|\lambda_N|$, c_N/c and Vg_N/c corresponding to one-dimensional Eq. (4.2.1) obtained using indicated schemes. Dash-dotted line represent the critical CFL number ($C_{r_{crit}}$) up to which neutrally stable ($|\lambda_N| = 1$) condition is satisfied. For the EDRP2 scheme, optimized values of free-parameters are $\alpha_1 = 0.29289$, $\alpha_2 = 0.20711$ (Table 4.1).

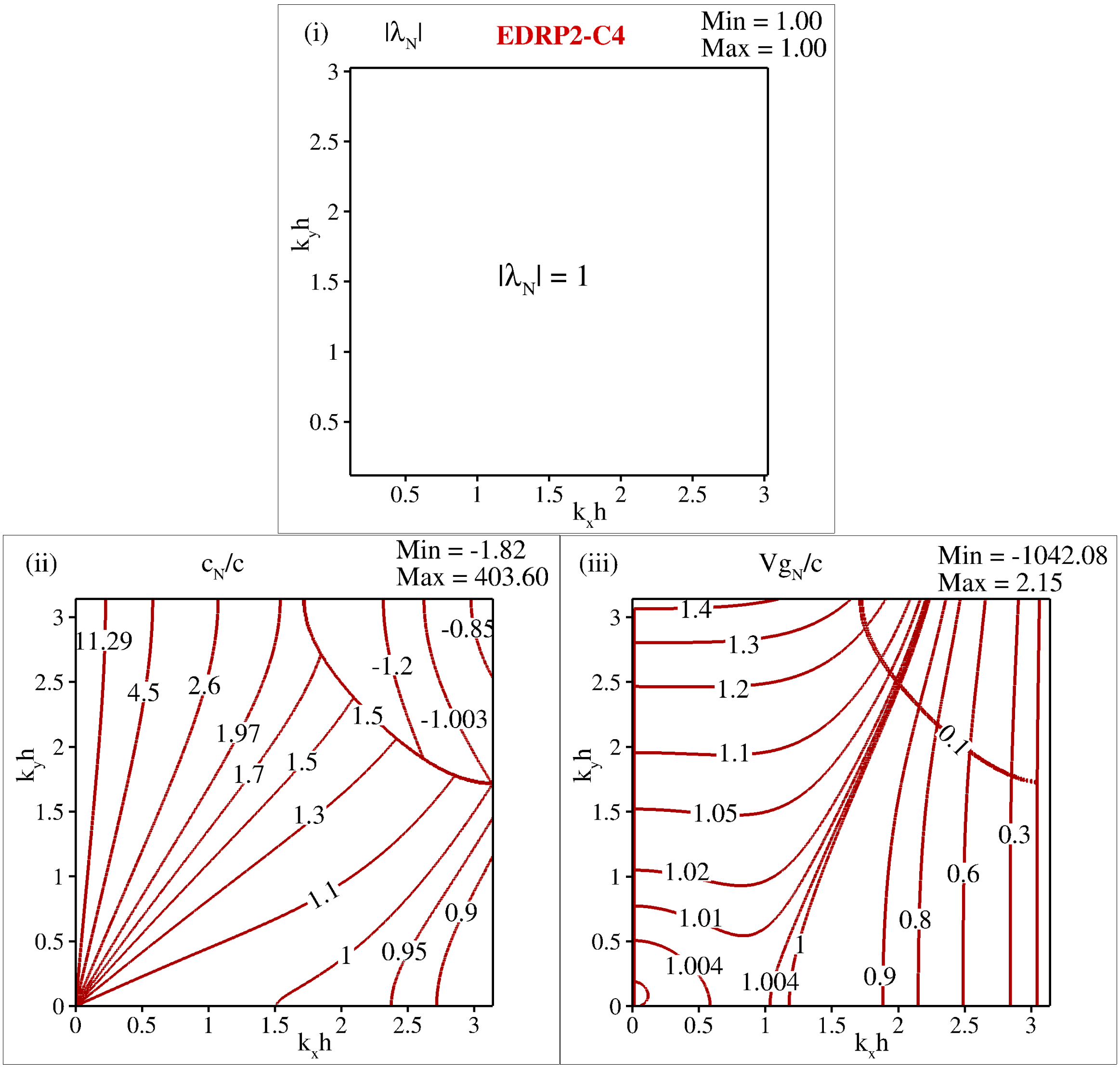

Figure 4.1(b): Contour plots of $|\lambda_N|$, c_N/c and Vg_N/c corresponding to two-dimensional Eq. (4.1.4) obtained using EDRP2-C4 scheme for $C_r = 0.5$. Here, optimized values of free-parameters are $\alpha_1 = 0.29289$, $\alpha_2 = 0.20711$ (Table 4.2).

Additionally, the right column in Fig. 4.1(a) compares the numerical characteristics of the EDRP2-CD2 and EDRP2-C4 schemes with the RKN-C4 method. It is evident from the Fig. 4.1(a) that the EDRP2 schemes offer a wider neutrally stable region and improved dispersion and stability characteristics compared to RKN.

Furthermore, Fig. 4.1(b) illustrates the numerical properties of the EDRP2-C4 scheme applied to the 2D Eq. (4.1.4) in terms of amplification factors magnitude, normalized group velocity, and normalized phase speed.

4.2.1 Optimization problem

To fix the optimized values of the free-parameters, an optimization problem as discussed in [138, 139, 83] is considered. We have taken the following objective functions, given as

$$f(\alpha_i, C_r) = \int_0^{\delta} |\lambda_N - \lambda_{\text{exact}}|^2 d(kh) \tag{4.2.6}$$

where λ_N represents the numerical amplification factor and $\lambda_{\text{exact}} = e^{iC_r k\Delta x}$ is the the exact amplification factor. The objective function defined by Eq. (4.2.6) is further subject to the following constraints [83], given as

$$\begin{aligned} g_1(\alpha_i, C_r) &= \int_0^{\delta_1} \big||\lambda_N| - 1\big| d(kh) \leq \zeta_1 \\ g_2(\alpha_i, C_r) &= \int_0^{\delta_2} \left|\left(\frac{Vg_N}{c}\right) - 1\right| d(kh) \leq \zeta_2 \\ g_3(\alpha_i, C_r) &= \int_0^{\delta_3} \left|\left(\frac{c_N}{c}\right) - 1\right| d(kh) \leq \zeta_3 \end{aligned} \tag{4.2.7}$$

here, δ_i and ζ_i are error tolerances. The specific values of ζ_i have been selected following the discussion given in [83]. To identify the feasible region for the optimized problem presented in Eq. (4.2.6) and Ineq. (4.2.7), a grid-search technique [83] is employed. The process of grid-search technique involves exploring the parameter space while keeping the value of C_r constant at an arbitrary but fixed value. The inclusion of constraints specified in Eq. (4.2.7) transforms the optimization problem described by Eq. (4.2.6) and Ineq. (4.2.7) into a Pareto front optimization problem. The resulting optimized values of the free-parameters α_i are given in Tables 4.1 and 4.2, corresponding to one- and two-dimensional wave equations, respectively.

4.3 Energy conservation analysis

In this section, we have performed the theoretical analysis to establish the energy conservation of the developed space-time discretization schemes for Eq. (4.1.4) [105, 106, 140].

Table 4.1: Values of the free-parameters α_1 and α_2 for the 1D wave equation in Eq. (4.2.2), optimized using EDRP2-CD2 and EDRP2-C4 schemes.

		EDRP2 - CD2			EDRP2 - C4		
α_1	α_2	Min($\lvert\lambda\rvert$)	Max($\lvert\lambda\rvert$)	$(C_r)_{crit}$	Min($\lvert\lambda\rvert$)	Max($\lvert\lambda\rvert$)	$(C_r)_{crit}$
0.30000	0.20000	0.93561	1.00000	1.11	0.93561	1.00000	0.91
0.30000	0.20711	0.96732	1.00000	1.12	0.96733	1.00000	0.92
0.29300	0.20711	0.99951	1.00000	1.13	0.99951	1.00000	0.92
0.29289	**0.20711**	**1.00000**	**1.00000**	**1.13**	**1.00000**	**1.00000**	**0.92**
0.29289	0.20700	0.99951	1.00000	1.13	0.99951	1.00000	0.92
0.29289	0.10000	0.58003	1.00000	1.02	0.57996	1.00000	0.83
0.29280	0.20711	1.00000	1.00044	1.13	1.00000	1.00044	0.92
0.25000	0.20711	1.00000	4.13379	2.85	1.00000	1.21128	0.96

Table 4.2: Values of the free-parameters α_1 and α_2 for the 2D wave equation in Eq. (4.1.4), optimized using EDRP2-CD2 and EDRP2-C4 schemes.

		EDRP2 - CD2			EDRP2 - C4		
α_1	α_2	Min($\lvert\lambda\rvert$)	Max($\lvert\lambda\rvert$)	$(C_r)_{crit}$	Min($\lvert\lambda\rvert$)	Max($\lvert\lambda\rvert$)	$(C_r)_{crit}$
0.30000	0.20000	0.93561	1.00000	0.79	0.93766	1.00000	0.64
0.30000	0.20711	0.96819	1.00000	0.79	0.96919	1.00000	0.64
0.29300	0.20711	0.99951	1.00000	0.80	0.99953	1.00000	0.65
0.29289	**0.20711**	**1.00000**	**1.00000**	**0.80**	**1.00000**	**1.00000**	**0.65**
0.29289	0.20700	0.99951	1.00000	0.80	0.99953	1.00000	0.65
0.29289	0.10000	0.59052	1.00000	0.72	0.58246	1.00000	0.59
0.29280	0.20711	1.00000	1.00044	0.80	1.00000	1.00043	0.65
0.25000	0.20711	1.00000	1.20857	0.83	1.00000	1.21179	0.68

For Eq. (4.1.4), the corresponding Hamiltonian function is given as

$$\mathcal{H}(z,u) = \frac{1}{2}\int_{\Omega} \big[c^2(x,y)z^2 + (u_x)^2 + (u_y)^2\big]dxdy \tag{4.3.1}$$

using the definition of the functional derivative, an equivalent infinite-dimensional Hamiltonian system for Eq. (4.1.4) with the periodic boundary conditions are given as

$$\frac{d\hat{w}}{dt} = L\frac{\delta\mathcal{H}}{\delta\hat{w}}, \quad \hat{w} = \begin{bmatrix} z \\ u \end{bmatrix}, \quad L = \begin{bmatrix} 0 & -1 \\ 1 & 0 \end{bmatrix} \tag{4.3.2}$$

where L is a skew-symmetric matrix.

Theorem 4.3.1. *The Hamiltonian system corresponding to wave propagation in a heterogeneous medium, given in Eq. (4.3.2), is energy conservative, that is,*

$$E(t) := \frac{1}{2}\int_{\Omega} \big[c^2(x,y)z^2 + (u_x)^2 + (u_y)^2\big]dxdy = E(0).$$

Proof. As given in [105], the proof for the continuous case is discussed next. Using functional derivative, the first-order derivative of Hamiltonian concerning time t is given as

$$\frac{d}{dt}\mathcal{H}(z,u) = \frac{d}{dt}\mathcal{H}(\hat{w}) = \int_{\Omega}\left(\frac{\delta\mathcal{H}}{\delta\hat{w}}\right)^{\tau}\frac{d\hat{w}}{dt}dxdy \tag{4.3.3}$$

from Eqs. (4.3.2)-(4.3.3) and using skew-adjoint property of matrix L, we

$$\int_{\Omega}\left(\frac{\delta\mathcal{H}}{\delta\hat{w}}\right)^{\tau}\frac{d\hat{w}}{dt}dxdy = \int_{\Omega}\left(\frac{\delta\mathcal{H}}{\delta\hat{w}}\right)^{\tau} L\left(\frac{\delta\mathcal{H}}{\delta\hat{w}}\right)dxdy = 0$$

Therefore, $\mathcal{H}(z,u)(t) = \mathcal{H}(z,u)(0)$, $t \in (0,T]$, which further implies that, $E(t) = E(0)$. □

The discrete Hamiltonian associated with the semi-discretized system (4.1.11) is expressed as

$$\mathcal{H}_d(Z,U) = \frac{1}{2}(CZ)^{\tau}CZ - \frac{1}{2}U^{\tau}(Q_x\Gamma_x^{+}\Gamma_x^{-} + Q_y\Gamma_y^{+}\Gamma_y^{-})U \tag{4.3.4}$$

Moreover, the following relation is satisfied by the discrete Hamiltonian

$$\nabla\mathcal{H}_d(Z,U) = \begin{bmatrix} \frac{\partial\mathcal{H}_d}{\partial Z} \\ \frac{\partial\mathcal{H}_d}{\partial U} \end{bmatrix} = \begin{bmatrix} C^2 Z \\ -\mathscr{P}U \end{bmatrix} \tag{4.3.5}$$

Finally, the finite-dimensional Hamiltonian system corresponding to Eq. (4.1.11) is given as

$$\frac{d}{dt}\begin{bmatrix} Z \\ U \end{bmatrix} = \bar{L}\nabla\mathcal{H}_d(Z,U), \quad \bar{L} = \begin{bmatrix} 0 & -I_{Nx}\otimes I_{Ny} \\ I_{Nx}\otimes I_{Ny} & 0 \end{bmatrix} \tag{4.3.6}$$

where $\bar{L}$ is a skew-symmetric matrix. Using the EDRP2 time integration method for the Hamiltonian system given in Eq. (4.3.6), it follows that

$$\frac{1}{\Delta t}\begin{bmatrix} Z^{n+1}-Z^n \\ U^{n+1}-U^n \end{bmatrix} = \bar{L}\nabla\mathcal{H}_d(Z^*,U^*)$$

substituting the expressions of Z^* and U^* given in Eq. (4.1.15), it follows that

$$\frac{1}{\Delta t}\begin{bmatrix} Z^{n+1}-Z^n \\ U^{n+1}-U^n \end{bmatrix} = \bar{L}\begin{bmatrix} C^2\left(\frac{Z^n+Z^{n+1}}{2} - \alpha_2(Z^{n+1}-Z^n) + \alpha_2\Delta t\mathscr{P}U^n\right) \\ -\mathscr{P}\left(U^n + \frac{\Delta t}{2}C^2Z^n + \alpha_1\frac{\Delta t^2}{2}C^2\mathscr{P}U^n\right) \end{bmatrix} \tag{4.3.7}$$

Energy conservation analysis for the fully-discretized system is discussed next.

4.3.1 Energy conservation of the fully-discretized system

Let $\Lambda_h^p = \{U|U = (U_{i,j}|(x_i,y_j)\in\Omega_h^E)\}$ represent the space of periodic grid functions on Ω_h^E. The discrete inner-product and norms for given mesh-functions, $Z,U\in\Lambda_h^p$, are defined as

$$\langle Z,U\rangle = \sum_{i=1}^{Nx}\sum_{j=1}^{Ny} Z_{i,j}U_{i,j}\Delta x\Delta y, \quad ||U||^2 = \langle U,U\rangle$$
$$||\Gamma_x^+U||^2 = \left\langle\Gamma_x^+U,\Gamma_x^+U\right\rangle, \quad ||\Gamma_y^+U||^2 = \left\langle\Gamma_y^+U,\Gamma_y^+U\right\rangle$$

Moreover, for symmetric positive definite matrices, Q_x and Q_y, the discrete norms are defined as

$$||U||_{Q_x}^2 = \langle Q_xU,U\rangle, \quad ||U||_{Q_y}^2 = \langle Q_yU,U\rangle \tag{4.3.8}$$

Lemma 4.3.2. *Matrices Q_x and Q_y satisfies the following inequalities*

$$1\le ||Q_x|| \le \frac{3}{2}, \quad 1\le ||Q_y|| \le \frac{3}{2}, \tag{4.3.9}$$

and

$$||U||^2 \le ||U||_{Q_x}^2 \le \frac{3}{2}||U||^2, \quad ||U||^2 \le ||U||_{Q_y}^2 \le \frac{3}{2}||U||^2 \tag{4.3.10}$$

moreover, matrix P_x satisfy the following inequality

$$\frac{2}{3} \leq ||P_x|| \leq 1. \tag{4.3.11}$$

Proof. The circulant matrix property states that the eigenvalues of P_x take the form of

$$\lambda_i = \frac{5}{6} + \frac{1}{6}cos\left(\frac{2i\pi}{N_x}\right), \quad i = 0, 1, 2, \ldots, N_x - 1. \tag{4.3.12}$$

Hence, we obtain $\frac{2}{3} \leq \lambda_i \leq 1$, which results in $\frac{2}{3} \leq ||P_x|| \leq 1$. The eigenvalues of Q_x satisfy $1 \leq \mu_j \leq \frac{3}{2}, j = 1, 2, \ldots, N_x \times N_y$, and as a result, $1 \leq ||Q_x|| \leq \frac{3}{2}$. This is evident from the properties of the inverse matrix and Kronecker product. Additionally, $||U||^2 \leq (Q_xU, U) \leq ||Q_x||||U||^2 \leq \frac{3}{2}||U||^2$. □

Lemma 4.3.3. *For given mesh-function $Z, U \in \Lambda_h^p$, it holds that*

$$(\Gamma_x^+\Gamma_x^- Z, U) = -(\Gamma_x^+ Z, \Gamma_x^+ U). \tag{4.3.13}$$

Lemma 4.3.4. *Matrices pairs Q_x and Γ_x^+, Q_x and Γ_x^-, Q_y and Γ_y^+, Q_y and Γ_y^- are commutative, that is*

$$\begin{aligned} Q_x\Gamma_x^+ &= \Gamma_x^+ Q_x, \quad Q_x\Gamma_x^- = \Gamma_x^- Q_x, \\ Q_y\Gamma_y^+ &= \Gamma_y^+ Q_y, \quad Q_y\Gamma_y^- = \Gamma_y^- Q_y. \end{aligned} \tag{4.3.14}$$

Lemma 4.3.5. *Let C be the diagonal matrix and $0 < c_1 = \min\limits_{(x,y)\in\Omega} |c(x, y)|$, $0 < c_2 = \max\limits_{(x,y)\in\Omega} |c(x, y)|$ then C satisfies $c_1 \leq ||C|| \leq c_2$.*

Remark 4.3.1. *Proofs of the above lemmas are given in [106].*

Theorem 4.3.6. *Solution (Z, U) of the fully-discretized system given in Eq. (4.3.7) is energy conservative, and satisfies the following relation*

$$E^{n+1} := \frac{1}{2}\left\|CZ^{n+1}\right\|^2 + \frac{1}{2}\Big(\left\|\Gamma_x^+ U^{n+1}\right\|_{Q_x}^2 + \left\|\Gamma_y^+ U^{n+1}\right\|_{Q_y}^2\Big) = E^n.$$

Proof. Using chain rule, $\frac{d\mathcal{H}_d}{dt} = [\frac{dz}{dt}, \frac{du}{dt}]\nabla\mathcal{H}_d(z, u)$. To establish our claim, the matrix form of the discretized first-order derivative of the discrete Hamiltonian function $\mathcal{H}_d$ concerning time has been considered, as

$$\begin{aligned} \frac{\mathcal{H}_d(Z^{n+1}, U^{n+1}) - \mathcal{H}_d(Z^n, U^n)}{\Delta t} &= \frac{Z^{n+1} - Z^n}{\Delta t}\frac{\partial}{\partial Z}\mathcal{H}_d(Z^*, U^*) \\ &+ \frac{U^{n+1} - U^n}{\Delta t}\frac{\partial}{\partial U}\mathcal{H}_d(Z^*, U^*) \end{aligned} \tag{4.3.15}$$

In matrix notations, Eq. (4.3.15) can be written as

$$\frac{\mathcal{H}_d(Z^{n+1},U^{n+1})-\mathcal{H}_d(Z^n,U^n)}{\Delta t}=\frac{1}{\Delta t}\begin{bmatrix}Z^{n+1}-Z^n\\ U^{n+1}-U^n\end{bmatrix}^{\tau}\nabla\mathcal{H}_d(Z^*,U^*) \tag{4.3.16}$$

Using Eqs. (4.3.5), (4.3.7), and skew-symmetric property of the matrix $\bar{L}$, it follows that

$$\begin{aligned}\frac{\mathcal{H}_d(Z^{n+1},U^{n+1})-\mathcal{H}_d(Z^n,U^n)}{\Delta t}&=\begin{bmatrix}C^2\left(\frac{Z^n+Z^{n+1}}{2}-\alpha_2(Z^{n+1}-Z^n)+\alpha_2\Delta t\mathscr{P}U^n\right)\\ -\mathscr{P}\left(U^n+\frac{\Delta t}{2}C^2Z^n+\alpha_1\frac{\Delta t^2}{2}C^2\mathscr{P}U^n\right)\end{bmatrix}^{\tau}\\ &\bar{L}^{\tau}\begin{bmatrix}C^2\left(\frac{Z^n+Z^{n+1}}{2}-\alpha_2(Z^{n+1}-Z^n)+\alpha_2\Delta t\mathscr{P}U^n\right)\\ -\mathscr{P}\left(U^n+\frac{\Delta t}{2}C^2Z^n+\alpha_1\frac{\Delta t^2}{2}C^2\mathscr{P}U^n\right)\end{bmatrix}=0\end{aligned}$$

as, $\mathcal{H}_d(Z(t),U(t))\Delta x\Delta y=E(t)$, which establishes that, $E^{n+1}=E^n$. □

4.4 Convergence analysis

In this section, the convergence results for the EDRP2-C4 scheme have been derived.

Lemma 4.4.1. *For any functions $f_1, f_2 \in C^1(\Omega)$, following inequalities hold*

$$\begin{aligned}||\Gamma_x^+(f_1f_2)|| &\le ||\Gamma_x^+(f_1)||\ ||f_2||+||f_1||\ ||\Gamma_x^+(f_2)||\\ ||\Gamma_y^+(f_1f_2)|| &\le ||\Gamma_y^+(f_1)||\ ||f_2||+||f_1||\ ||\Gamma_y^+(f_2)||\end{aligned} \tag{4.4.1}$$

Lemma 4.4.2. *For given $f_1 \in C^1(\Omega)$ and $f_2 \in C^2(\Omega)$, following inequalities hold*

$$||\Gamma_x^+f_1||\le K,\quad ||\Gamma_y^+f_1||\le K,\quad ||\Gamma_x^+\Gamma_x^-f_2||\le K,\quad ||\Gamma_y^+\Gamma_y^-f_2||\le K \tag{4.4.2}$$

To quantify the truncation errors, the fully-discretized system (in matrix form) given in Eq. (4.1.14) has been considered. Using the exact solution (z,u), Eq. (4.1.14) can be represented as

$$\begin{aligned}\frac{z^{n+1}-z^n}{\Delta t}&=\mathscr{P}u^n+\frac{\Delta t}{2}\mathscr{P}C^2z^n+\alpha_1\frac{\Delta t^2}{2}\mathscr{P}C^2\mathscr{P}u^n+\tilde{\mathbf{T}}_{\mathbf{e}}^{n+\frac{1}{2}}\\ \frac{u^{n+1}-u^n}{\Delta t}&=C^2\left(\frac{z^n+z^{n+1}}{2}+\alpha_2(z^n-z^{n+1})+\alpha_2\Delta t\mathscr{P}u^n\right)+\mathbf{T}_{\mathbf{e}}{}^{n+\frac{1}{2}}\end{aligned} \tag{4.4.3}$$

where $\tilde{\mathbf{T}}_{\mathbf{e}}^{n+\frac{1}{2}}$ and $\mathbf{T}_{\mathbf{e}}{}^{n+\frac{1}{2}}$ denote the truncation error vectors.

Lemma 4.4.3. *The truncation error vectors satisfy the following estimates for the sufficiently smooth exact solution (z,u) of Eq. (4.1.4)*

$$||\tilde{\mathbf{T}}_{\mathbf{e}}^{n+\frac{1}{2}}|| \leq K(\Delta t^2 + \Delta x^4 + \Delta y^4 + \Delta t^2(\Delta x^4 + \Delta y^4)), \tag{4.4.4}$$

$$||\mathbf{T_e}^{n+\frac{1}{2}}|| \leq K(\Delta t^2 + \Delta t^2(\Delta x^4 + \Delta y^4)) \tag{4.4.5}$$

and

$$||\Gamma_x^+ \mathbf{T_e}^{n+\frac{1}{2}}|| \leq K(\Delta t^2 + \Delta t^2 \Delta x^4 + \Delta t^2 \Delta y^4), \tag{4.4.6}$$

$$||\Gamma_y^+ \mathbf{T_e}^{n+\frac{1}{2}}|| \leq K(\Delta t^2 + \Delta t^2 \Delta x^4 + \Delta t^2 \Delta y^4) \tag{4.4.7}$$

where K is a positive constant independent of Δx, Δy and Δt.

Proof. Using the Taylor's series expansion at $t = t^{n+\frac{1}{2}}$, we have

$$\frac{u_{i,j}^{n+1} - u_{i,j}^n}{\Delta t} = \frac{\partial u_{i,j}}{\partial t}\left(t^{n+\frac{1}{2}}\right) + \frac{\Delta t^2}{24}\frac{\partial^3 u_{i,j}}{\partial t^3}\left(t^{\chi_1}\right), \tag{4.4.8}$$

$$\frac{z_{i,j}^{n+1} + z_{i,j}^n}{2} = z_{i,j}\left(t^{n+\frac{1}{2}}\right) + \frac{\Delta t^2}{8}\frac{\partial^2 z_{i,j}}{\partial t^2}\left(t^{\chi_2}\right), \tag{4.4.9}$$

$$z_{i,j}^{n+1} - z_{i,j}^n = \Delta t\frac{\partial z_{i,j}}{\partial t}\left(t^{n+\frac{1}{2}}\right) + \frac{\Delta t^3}{24}\frac{\partial^3 z_{i,j}}{\partial t^3}\left(t^{\chi_3}\right), \tag{4.4.10}$$

$$u_{i,j}^n = u_{i,j}\left(t^{n+\frac{1}{2}}\right) - \frac{\Delta t}{2}\frac{\partial u_{i,j}}{\partial t}\left(t^{n+\frac{1}{2}}\right) + \frac{\Delta t^2}{2^2}\frac{1}{2!}\frac{\partial^2 u_{i,j}}{\partial t^2}\left(t^{\chi_4}\right) \tag{4.4.11}$$

where $t^{\chi_1}, t^{\chi_2}, t^{\chi_3}, t^{\chi_4} \in (t^n, t^{n+1})$. Eqs. (4.4.8)-(4.4.11) can be represented in the vector form, as

$$\frac{u^{n+1} - u^n}{\Delta t} = \frac{\partial u}{\partial t}\left(t^{n+\frac{1}{2}}\right) + \frac{\Delta t^2}{24}s_1^{n+\frac{1}{2}}(u), \tag{4.4.12}$$

$$\frac{z^{n+1} + z^n}{2} = z\left(t^{n+\frac{1}{2}}\right) + \frac{\Delta t^2}{8}s_2^{n+\frac{1}{2}}(z), \tag{4.4.13}$$

$$z^{n+1} - z^n = \Delta t\frac{\partial z}{\partial t}\left(t^{n+\frac{1}{2}}\right) + \frac{\Delta t^3}{24}s_3^{n+\frac{1}{2}}(z), \tag{4.4.14}$$

$$u^n = u\left(t^{n+\frac{1}{2}}\right) - \frac{\Delta t}{2}\frac{\partial u}{\partial t}\left(t^{n+\frac{1}{2}}\right) + \frac{\Delta t^2}{2^2}\frac{1}{2!}s_4^{n+\frac{1}{2}}(u) \tag{4.4.15}$$

from Eq. (4.1.6), it follow that

$$\begin{aligned} \mathscr{P}u\left(t^{n+\frac{1}{2}}\right) &= \left(\frac{\partial^2 u}{\partial x^2} + \frac{\partial^2 u}{\partial y^2}\right)\left(t^{n+\frac{1}{2}}\right) - \frac{\Delta x^4}{240}s_5^{n+\frac{1}{2}}(u) - \frac{\Delta y^4}{240}s_6^{n+\frac{1}{2}}(u) \\ &= \frac{\partial z}{\partial t}\left(t^{n+\frac{1}{2}}\right) - \frac{\Delta x^4}{240}s_5^{n+\frac{1}{2}}(u) - \frac{\Delta y^4}{240}s_6^{n+\frac{1}{2}}(u) \end{aligned} \tag{4.4.16}$$

where

$$
\begin{aligned}
s_1^{n+\frac{1}{2}}(u) &= \left\{ \frac{\partial^3 u_{i,j}}{\partial t^3}\left(t^{\chi_1}\right) \right\}, \quad s_2^{n+\frac{1}{2}}(z) = \left\{ \frac{\partial^2 z_{i,j}}{\partial t^2}\left(t^{\chi_2}\right) \right\}, \\
s_3^{n+\frac{1}{2}}(z) &= \left\{ \frac{\partial^3 z_{i,j}}{\partial t^3}\left(t^{\chi_3}\right) \right\}, \quad s_4^{n+\frac{1}{2}}(u) = \left\{ \frac{\partial^2 u_{i,j}}{\partial t^2}\left(t^{\chi_4}\right) \right\}, \\
s_5^{n+\frac{1}{2}}(u) &= \left\{ \frac{\partial^6 u}{\partial x^6}\left(\zeta_1, y_j, t^{n+\frac{1}{2}}\right) \right\}, \quad s_6^{n+\frac{1}{2}}(u) = \left\{ \frac{\partial^6 u}{\partial y^6}\left(x_i, \zeta_2, t^{n+\frac{1}{2}}\right) \right\}.
\end{aligned}
$$

Thus, using Eqs. (4.4.12)-(4.4.15) in the first equation of (4.4.3), it follow that

$$
\begin{aligned}
\tilde{\mathbf{T}}_{\mathbf{e}}^{n+\frac{1}{2}} = {} & \left(\frac{\partial z}{\partial t}\left(t^{n+\frac{1}{2}}\right) + \frac{\Delta t^2}{24} s_1^{n+\frac{1}{2}}(z) \right) \\
& - \mathscr{P}\left(u\left(t^{n+\frac{1}{2}}\right) - \frac{\Delta t}{2}\frac{\partial u}{\partial t}\left(t^{n+\frac{1}{2}}\right) + \frac{\Delta t^2}{2^2}\frac{1}{2!} s_4^{n+\frac{1}{2}}(u) \right) \\
& - \frac{\Delta t}{2}\mathscr{P}C^2\left(z\left(t^{n+\frac{1}{2}}\right) - \frac{\Delta t}{2}\frac{\partial z}{\partial t}\left(t^{n+\frac{1}{2}}\right) + \frac{\Delta t^2}{2^2}\frac{1}{2!} s_4^{n+\frac{1}{2}}(z) \right) \\
& - \alpha_1 \frac{\Delta t^2}{2}\mathscr{P}C^2\mathscr{P}\left(u\left(t^{n+\frac{1}{2}}\right) - \frac{\Delta t}{2}\frac{\partial u}{\partial t}\left(t^{n+\frac{1}{2}}\right) + \frac{\Delta t^2}{2^2}\frac{1}{2!} s_4^{n+\frac{1}{2}}(u) \right) \qquad (4.4.17)
\end{aligned}
$$

from Eqs. (4.1.4) and (4.4.16), it follow that

$$
\begin{aligned}
\tilde{\mathbf{T}}_{\mathbf{e}}^{n+\frac{1}{2}} = {} & \frac{\Delta t^2}{24} s_1^{n+\frac{1}{2}}(z) + \left(\frac{\Delta x^4}{240} s_5^{n+\frac{1}{2}}(u) + \frac{\Delta y^4}{240} s_6^{n+\frac{1}{2}}(u) \right) - \frac{\Delta t^2}{2^2}\frac{1}{2!}\mathscr{P} s_4^{n+\frac{1}{2}}(u) \\
& - \alpha_1 \frac{\Delta t^2}{2}\mathscr{P}C^2\left(\frac{\partial z}{\partial t}\left(t^{n+\frac{1}{2}}\right) - \frac{\Delta x^4}{240} s_5^{n+\frac{1}{2}}(u) - \frac{\Delta y^4}{240} s_6^{n+\frac{1}{2}}(u) \right) \\
& + \frac{\Delta t^2}{4}\mathscr{P}C^2\frac{\partial z}{\partial t}\left(t^{n+\frac{1}{2}}\right) + \mathcal{O}(\Delta t^3) \qquad (4.4.18)
\end{aligned}
$$

using Eq. (4.1.6), components of $\mathscr{P} s_4^{n+\frac{1}{2}}(u)$ are given as

$$
\begin{aligned}
\left(\mathcal{P}_x^{-1}\delta_x^2 + \mathcal{P}_y^{-1}\delta_y^2\right)\left(s_4^{n+\frac{1}{2}}(u_{i,j})\right) = {} & \frac{\partial^2}{\partial x^2}\left(\frac{\partial^2 u}{\partial t^2}(x_i, y_j, t^{\chi_4})\right) + \frac{\partial^2}{\partial y^2}\left(\frac{\partial^2 u}{\partial t^2}(x_i, y_j, t^{\chi_4})\right) \\
& + K(\Delta x^4 + \Delta y^4) \qquad (4.4.19)
\end{aligned}
$$

which, further implies that

$$
||\mathscr{P} s_4^{n+\frac{1}{2}}(u)|| \leq K \qquad (4.4.20)
$$

similarly, it follow that

$$
||\mathscr{P}C^2\frac{\partial z}{\partial t}\left(t^{n+\frac{1}{2}}\right)|| \leq K, \quad ||\mathscr{P}C^2 s_5^{n+\frac{1}{2}}(u)|| \leq K, \quad ||\mathscr{P}C^2 s_6^{n+\frac{1}{2}}(u)|| \leq K \qquad (4.4.21)
$$

substituting Ineqs. (4.4.20) and (4.4.21) in Eq. (4.4.18), the following is obtained

$$||\tilde{\mathbf{T}}_{\mathbf{e}}^{n+\frac{1}{2}}|| \leq K(\Delta t^2 + \Delta x^4 + \Delta y^4 + \Delta t^2(\Delta x^4 + \Delta y^4)) \tag{4.4.22}$$

Next, using Eqs. (4.4.12)-(4.4.15) in Eq. (4.4.3), it follows that

$$\begin{aligned}\mathbf{T_e}^{n+\frac{1}{2}} = &\left(\frac{\partial u}{\partial t}\left(t^{n+\frac{1}{2}}\right) + \frac{\Delta t^2}{24} s_1^{n+\frac{1}{2}}(u)\right) - C^2\left(z\left(t^{n+\frac{1}{2}}\right) + \frac{\Delta t^2}{8} s_2^{n+\frac{1}{2}}(z)\right)\\ &+ \alpha_2 C^2\left(\Delta t \frac{\partial z}{\partial t}\left(t^{n+\frac{1}{2}}\right) + \frac{\Delta t^3}{24} s_3^{n+\frac{1}{2}}(z)\right)\\ &- \alpha_2 \Delta t C^2 \mathscr{P}\left(u\left(t^{n+\frac{1}{2}}\right) - \frac{\Delta t}{2}\frac{\partial u}{\partial t}\left(t^{n+\frac{1}{2}}\right) + \frac{\Delta t^2}{2^2}\frac{1}{2!} s_4^{n+\frac{1}{2}}(u)\right)\end{aligned} \tag{4.4.23}$$

from Eq. (4.1.4), it follows that

$$\begin{aligned}\mathbf{T_e}^{n+\frac{1}{2}} = &\frac{\Delta t^2}{24} s_1^{n+\frac{1}{2}}(u) - \frac{\Delta t^2}{8} C^2 s_2^{n+\frac{1}{2}}(z) + \alpha_2 \frac{\Delta t^3}{24} C^2 s_3^{n+\frac{1}{2}}(z)\\ &+ \alpha_2 \frac{\Delta t^2}{2} C^2 \mathscr{P} \frac{\partial u}{\partial t}\left(t^{n+\frac{1}{2}}\right) - \alpha_2 \frac{\Delta t^3}{2^2}\frac{1}{2!} C^2 \mathscr{P} s_4^{n+\frac{1}{2}}(u)\end{aligned} \tag{4.4.24}$$

from Eq. (4.4.16) and first equation of Eq. (4.1.4), the following is obtained

$$\begin{aligned}\mathscr{P}\frac{\partial u}{\partial t}\left(t^{n+\frac{1}{2}}\right) &= \left(\frac{\partial^2}{\partial x^2}\frac{\partial u}{\partial t} + \frac{\partial^2}{\partial y^2}\frac{\partial u}{\partial t}\right)\left(t^{n+\frac{1}{2}}\right) - \frac{\Delta x^4}{240} s_5^{n+\frac{1}{2}}\left(\frac{\partial u}{\partial t}\right) - \frac{\Delta y^4}{240} s_6^{n+\frac{1}{2}}\left(\frac{\partial u}{\partial t}\right)\\ &= \frac{\partial^2 z}{\partial t^2}\left(t^{n+\frac{1}{2}}\right) + K(\Delta x^4 + \Delta y^4)\end{aligned} \tag{4.4.25}$$

thus, using Eq. (4.4.25) and $s_2^{n+\frac{1}{2}}(z) = \frac{\partial^2 z}{\partial t^2}\left(t^{n+\frac{1}{2}}\right)$ it follows that

$$\begin{aligned}\mathbf{T_e}^{n+\frac{1}{2}} = &\frac{\Delta t^2}{24} s_1^{n+\frac{1}{2}}(u) - \frac{\Delta t^2}{8} C^2 s_2^{n+\frac{1}{2}}(z) + \alpha_2 \frac{\Delta t^2}{2} C^2 s_2^{n+\frac{1}{2}}(z)\\ &- \alpha_2 \frac{\Delta t^2}{2} C^2 K\left(\Delta x^4 + \Delta y^4\right) + \mathcal{O}(\Delta t^3)\end{aligned} \tag{4.4.26}$$

using Lemma 4.3.5, the following estimate is obtained as

$$||\mathbf{T_e}^{n+\frac{1}{2}}|| \leq K(\Delta t^2 + \Delta t^2(\Delta x^4 + \Delta y^4)) \tag{4.4.27}$$

Moreover, from Eq. (4.4.26), it follows that

$$\begin{aligned}\Gamma_x^+ \mathbf{T_e}^{n+\frac{1}{2}} = &\frac{\Delta t^2}{24}\Gamma_x^+ s_1^{n+\frac{1}{2}}(u) - \frac{\Delta t^2}{8} C^2 \Gamma_x^+ s_2^{n+\frac{1}{2}}(z) + \alpha_2 C^2 \frac{\Delta t^2}{2}\Gamma_x^+ \frac{\partial^2 z}{\partial t^2}\left(t^{n+\frac{1}{2}}\right)\\ &- \alpha_2 C^2 \frac{\Delta t^2}{2}\left(\frac{\Delta x^4}{240}\Gamma_x^+ s_5^{n+\frac{1}{2}}\left(\frac{\partial u}{\partial t}\right) + \frac{\Delta y^4}{240}\Gamma_x^+ s_6^{n+\frac{1}{2}}\left(\frac{\partial u}{\partial t}\right)\right)\end{aligned} \tag{4.4.28}$$

using Lemmas 4.3.5, 4.4.1, and 4.4.2, it follows that

$$||\Gamma_x^+ \mathbf{T_e}^{n+\frac{1}{2}}|| \leq K(\Delta t^2 + \Delta t^2 \Delta x^4 + \Delta t^2 \Delta y^4)$$

Similarly, we can also be obtained that

$$||\Gamma_y^+ \mathbf{T_e}^{n+\frac{1}{2}}|| \leq K(\Delta t^2 + \Delta t^2 \Delta x^4 + \Delta t^2 \Delta y^4)$$

□

Finally, the convergence result for the fully-discretized system using the EDRP2-C4 scheme is discussed next.

Theorem 4.4.4. *If* (z, u) *be the sufficiently smooth solution to the Eq. (4.1.4) and* (Z, U) *be the corresponding numerical solution obtained using EDRP2-C4 scheme. Then, there exists a positive constant* K *independent of* $\Delta t, \Delta x,$ *and* Δy *such that*

$$||z^n - Z^n|| + ||u^n - U^n|| + ||\Gamma_x^+(u^n - U^n)|| + ||\Gamma_y^+(u^n - U^n)|| \leq K(\Delta t^2 + \Delta x^4 + \Delta y^4) \tag{4.4.29}$$

Proof. Solution errors are represented as, $\psi_{i,j}^n = z_{i,j}^n - Z_{i,j}^n, \phi_{i,j}^n = u_{i,j}^n - U_{i,j}^n$. Subtracting Eq. (4.1.14) from Eq. (4.4.3), the following error equations are obtained

$$\frac{\psi^{n+1} - \psi^n}{\Delta t} = \mathscr{P}\phi^n + \frac{\Delta t}{2}\mathscr{P}C^2\psi^n + \alpha_1 \frac{\Delta t^2}{2}\mathscr{P}C^2\mathscr{P}\phi^n + \tilde{\mathbf{T}}_{\mathbf{e}}^{n+\frac{1}{2}} \tag{4.4.30}$$

$$\frac{\phi^{n+1} - \phi^n}{\Delta t} = C^2 \frac{\psi^{n+1} + \psi^n}{2} - \alpha_2 C^2(\psi^{n+1} - \psi^n) + \alpha_2 \Delta t C^2 \mathscr{P}\phi^n + \mathbf{T_e}^{n+\frac{1}{2}} \tag{4.4.31}$$

with $\psi|_{t=0} = 0, \phi|_{t=0} = 0$. Taking inner product of each term of Eq. (4.4.31) with $\frac{\phi^{n+1} + \phi^n}{2}$, it follows that

$$\begin{aligned}\left\langle \frac{\phi^{n+1} - \phi^n}{\Delta t}, \frac{\phi^{n+1} + \phi^n}{2} \right\rangle &= \left\langle C^2 \frac{\psi^{n+1} + \psi^n}{2}, \frac{\phi^{n+1} + \phi^n}{2} \right\rangle \\ &\quad - \left\langle \alpha_2 C^2(\psi^{n+1} - \psi^n), \frac{\phi^{n+1} + \phi^n}{2} \right\rangle \\ &\quad + \left\langle \alpha_2 \Delta t C^2 \mathscr{P}\phi^n, \frac{\phi^{n+1} + \phi^n}{2} \right\rangle + \left\langle \mathbf{T_e}^{n+\frac{1}{2}}, \frac{\phi^{n+1} + \phi^n}{2} \right\rangle \\ &= \Upsilon_1 + \Upsilon_2 + \Upsilon_3 + \Upsilon_4 \end{aligned} \tag{4.4.32}$$

where

$$\begin{aligned}\Upsilon_1 &= \left\langle C^2\frac{\psi^{n+1}+\psi^n}{2}, \frac{\phi^{n+1}+\phi^n}{2}\right\rangle \\ &\leq \frac{1}{4}\left(||C\psi^{n+1}||^2 + ||C\psi^n||^2 + ||C\phi^{n+1}||^2 + ||C\phi^n||^2\right)\end{aligned} \tag{4.4.33}$$

$$\begin{aligned}\Upsilon_2 &= \left\langle \alpha_2 C^2(\psi^n - \psi^{n+1}), \frac{\phi^{n+1}+\phi^n}{2}\right\rangle \\ &\leq \frac{\alpha_2}{2}\left(2(||C\psi^{n+1}||^2 + ||C\psi^n||^2) + ||C\phi^{n+1}||^2 + ||C\phi^n||^2\right)\end{aligned} \tag{4.4.34}$$

$$\begin{aligned}\Upsilon_3 &= \left\langle \alpha_2 \Delta t C^2 \mathscr{P}\phi^n, \frac{\phi^{n+1}+\phi^n}{2}\right\rangle = \frac{\alpha_2\Delta t}{2}\left\langle C^2\mathscr{P}\phi^n, \phi^{n+1}+\phi^n\right\rangle \\ &\leq \frac{\alpha_2\Delta t}{2}\left(\frac{1}{2}||C\mathscr{P}\phi^n||^2 + ||C\phi^{n+1}||^2 + ||C\phi^n||^2\right)\end{aligned} \tag{4.4.35}$$

and

$$\Upsilon_4 = \left\langle \mathbf{T_e}^{n+\frac{1}{2}}, \frac{\phi^{n+1}+\phi^n}{2}\right\rangle \leq \frac{1}{2}||\mathbf{T_e}^{n+\frac{1}{2}}||^2 + \frac{1}{4}(||\phi^{n+1}||^2 + ||\phi^n||^2) \tag{4.4.36}$$

from Ineqs. (4.4.33)-(4.4.36), and using Lemmas 4.3.2 and 4.3.5, the following estimate for Eq. (4.4.32) is obtained as

$$\begin{aligned}\frac{||\phi^{n+1}||^2 - ||\phi^n||^2}{2\Delta t} &\leq \frac{1}{4}(1 + c_2^2 + 2\alpha_2 c_2^2)\left(||\phi^{n+1}||^2 + ||\phi^n||^2\right) \\ &\quad + \frac{(1+4\alpha_2)}{4}\left(||C\psi^{n+1}||^2 + ||C\psi^n||^2\right) + \frac{1}{2}||\mathbf{T_e}^{n+\frac{1}{2}}||^2 \\ &\quad + \frac{\alpha_2\Delta t}{2}\left(\frac{1}{2}||C\mathscr{P}\phi^n||^2 + ||C\phi^{n+1}||^2 + ||C\phi^n||^2\right)\end{aligned} \tag{4.4.37}$$

Next, by taking the inner products of $C^2\frac{\psi^{n+1}+\psi^n}{2}$ with Eq. (4.4.30) and $\mathscr{P}(\phi^{n+1}+\phi^n)$ with Eq. (4.4.31), respectively, and then subtracting the resultant equations, it follows that

$$\begin{aligned}\left\langle \frac{\psi^{n+1}-\psi^n}{\Delta t}, C^2\frac{\psi^{n+1}+\psi^n}{2}\right\rangle &- \left\langle \frac{\phi^{n+1}-\phi^n}{\Delta t}, \mathscr{P}(\phi^{n+1}+\phi^n)\right\rangle \\ &= \left\langle \frac{\Delta t}{2}\mathscr{P}C^2\psi^n, C^2\frac{\psi^{n+1}+\psi^n}{2}\right\rangle \\ + \left\langle \alpha_1\frac{\Delta t^2}{2}\mathscr{P}C^2\mathscr{P}\phi^n, C^2\frac{\psi^{n+1}+\psi^n}{2}\right\rangle &+ \left\langle \tilde{\mathbf{T}}_{\mathbf{e}}^{n+\frac{1}{2}}, C^2\frac{\psi^{n+1}+\psi^n}{2}\right\rangle\end{aligned}$$

$$
\begin{aligned}
&-\left\langle C^2\frac{\psi^{n+1}+\psi^n}{2},\mathscr{P}\phi^{n+1}\right\rangle+\left\langle\alpha_2C^2(\psi^{n+1}-\psi^n),\mathscr{P}(\phi^{n+1}+\phi^n)\right\rangle\\
&\quad-\left\langle\alpha_2\Delta tC^2\mathscr{P}\phi^n,\mathscr{P}(\phi^{n+1}+\phi^n)\right\rangle-\left\langle\mathbf{T_e}^{n+\frac{1}{2}},\mathscr{P}(\phi^{n+1}+\phi^n)\right\rangle\\
&\qquad=\Theta_1+\Theta_2+\Theta_3+\Theta_4+\Theta_5+\Theta_6+\Theta_7
\end{aligned}
\tag{4.4.38}
$$

Next, the estimates of the left-hand side terms of Eq. (4.4.38) have been evaluated. The first term is obtained as

$$
\left\langle\frac{\psi^{n+1}-\psi^n}{\Delta t},C^2\frac{\psi^{n+1}+\psi^n}{2}\right\rangle=\frac{1}{2\Delta t}(||C\psi^{n+1}||^2-||C\psi^n||^2)
\tag{4.4.39}
$$

and using Lemmas 4.3.3, 4.3.4 and matrix $\mathscr{P}$, the second term has been obtained as

$$
\begin{aligned}
-\left\langle\frac{\phi^{n+1}-\phi^n}{\Delta t},\mathscr{P}(\phi^{n+1}+\phi^n)\right\rangle=\frac{1}{\Delta t}\Big(&||\Gamma_x^+\phi^{n+1}||_{Q_x}^2-||\Gamma_x^+\phi^n||_{Q_x}^2\\
&+||\Gamma_y^+\phi^{n+1}||_{Q_y}^2-||\Gamma_y^+\phi^n||_{Q_y}^2\Big)
\end{aligned}
\tag{4.4.40}
$$

Next, the estimates for the right-hand side terms of Eq. (4.4.38) have been evaluated as

$$
\begin{aligned}
\Theta_1&=\left\langle\frac{\Delta t}{2}\mathscr{P}C^2\psi^n,C^2\frac{\psi^{n+1}+\psi^n}{2}\right\rangle\\
&\le\frac{\Delta t}{4}\left(\frac{1}{2}||\mathscr{P}C^2\psi^n||^2+||C^2\psi^{n+1}||^2+||C^2\psi^n||^2\right)
\end{aligned}
\tag{4.4.41}
$$

$$
\begin{aligned}
\Theta_2&=\left\langle\alpha_1\frac{\Delta t^2}{2}\mathscr{P}C^2\mathscr{P}\phi^n,C^2\frac{\psi^{n+1}+\psi^n}{2}\right\rangle=\alpha_1\frac{\Delta t^2}{4}\left\langle\mathscr{P}C^2\mathscr{P}\phi^n,C^2(\psi^{n+1}+\psi^n)\right\rangle\\
&\le\frac{\alpha_1\Delta t^2}{4}\left(\frac{1}{2}||\mathscr{P}C^2\mathscr{P}\phi^n||^2+||C^2\psi^{n+1}||^2+||C^2\psi^n||^2\right)
\end{aligned}
\tag{4.4.42}
$$

$$
\Theta_3=\left\langle\tilde{\mathbf{T}}_{\mathbf{e}}^{n+\frac{1}{2}},C^2\frac{\psi^{n+1}+\psi^n}{2}\right\rangle\le\frac{1}{2}||C\tilde{\mathbf{T}}_{\mathbf{e}}^{n+\frac{1}{2}}||^2+\frac{1}{4}\left(||C\psi^{n+1}||^2+||C\psi^n||^2\right)
\tag{4.4.43}
$$

from the definition of $\mathscr{P}$ and using Lemmas 4.3.3, 4.3.4, it can be derived that

$$
\begin{aligned}
\Theta_4&=-\left\langle C^2\frac{\psi^{n+1}+\psi^n}{2},\mathscr{P}\phi^{n+1}\right\rangle\\
&\le\frac{1}{2}\Big(||\Gamma_x^+C^2\psi^{n+1}||_{Q_x}^2+||\Gamma_x^+C^2\psi^n||_{Q_x}^2+||\Gamma_y^+C^2\psi^{n+1}||_{Q_y}^2\\
&\qquad+||\Gamma_y^+C^2\psi^n||_{Q_y}^2+||\Gamma_x^+\phi^{n+1}||_{Q_x}^2+||\Gamma_y^+\phi^{n+1}||_{Q_y}^2\Big)
\end{aligned}
$$

using Lemmas 4.3.2, 4.3.5, it follows that

$$\begin{aligned}\Theta_4 \leq{} & \frac{3c_2^4}{4}\left(||\Gamma_x^+\psi^{n+1}||^2 + ||\Gamma_x^+\psi^n||^2 + ||\Gamma_y^+\psi^{n+1}||^2 + ||\Gamma_y^+\psi^n||^2\right)\\ & + \frac{1}{2}\left(||\Gamma_x^+\phi^{n+1}||_{Q_x}^2 + ||\Gamma_y^+\phi^{n+1}||_{Q_y}^2\right)\end{aligned} \tag{4.4.44}$$

$$\begin{aligned}\Theta_5 ={} & \left\langle \alpha_2 C^2(\psi^{n+1} - \psi^n), \mathscr{P}(\phi^{n+1} + \phi^n)\right\rangle\\ \leq{} & \frac{3c_2^4\alpha_2}{2}\left(||\Gamma_x^+\psi^n||^2 - ||\Gamma_x^+\psi^{n+1}||^2 + ||\Gamma_y^+\psi^n||^2 - ||\Gamma_y^+\psi^{n+1}||^2\right)\\ & + \alpha_2\left(||\Gamma_x^+\phi^{n+1}||_{Q_x}^2 + ||\Gamma_y^+\phi^{n+1}||_{Q_y}^2 + ||\Gamma_x^+\phi^n||_{Q_x}^2 + ||\Gamma_y^+\phi^n||_{Q_y}^2\right)\end{aligned} \tag{4.4.45}$$

$$\begin{aligned}\Theta_6 ={} & -\left\langle \alpha_2 \Delta t C^2 \mathscr{P}\phi^n, \mathscr{P}(\phi^{n+1} + \phi^n)\right\rangle\\ \leq{} & \alpha_2\Delta t\left(\frac{1}{2}||C^2\mathscr{P}\phi^n||^2 + ||\mathscr{P}\phi^{n+1}||^2 + ||\mathscr{P}\phi^n||^2\right)\end{aligned} \tag{4.4.46}$$

by using Lemmas 4.3.3, 4.3.4 and matrix $\mathscr{P}$, it has been obtained that

$$\begin{aligned}\Theta_7 ={} & -\left\langle \mathbf{T_e}^{n+\frac{1}{2}}, \mathscr{P}(\phi^{n+1} + \phi^n)\right\rangle\\ \leq{} & \frac{1}{2}\left(||\Gamma_x^+\mathbf{T_e}^{n+\frac{1}{2}}||_{Q_x}^2 + ||\Gamma_y^+\mathbf{T_e}^{n+\frac{1}{2}}||_{Q_y}^2\right)\\ & + \frac{1}{2}\left(||\Gamma_x^+\phi^{n+1}||_{Q_x}^2 + ||\Gamma_y^+\phi^{n+1}||_{Q_y}^2 + ||\Gamma_x^+\phi^n||_{Q_x}^2 + ||\Gamma_y^+\phi^n||_{Q_y}^2\right)\end{aligned} \tag{4.4.47}$$

combining the above estimates for Eq. (4.4.38) and using Lemma 4.3.5, the following estimate is obtained as

$$\begin{aligned}& \frac{1}{2\Delta t}(||C\psi^{n+1}||^2 - ||C\psi^n||^2) + \frac{1}{\Delta t}\left(||\Gamma_x^+\phi^{n+1}||_{Q_x}^2 - ||\Gamma_x^+\phi^n||_{Q_x}^2\right)\\ & + \frac{1}{\Delta t}\left(||\Gamma_y^+\phi^{n+1}||_{Q_y}^2 - ||\Gamma_y^+\phi^n||_{Q_y}^2\right) \leq \frac{\Delta t}{4}\left(\frac{1}{2}||\mathscr{P}C^2\psi^n||^2 + ||C^2\psi^{n+1}||^2\right.\\ & \left. + ||C^2\psi^n||^2\right) + \frac{\alpha_1\Delta t^2}{4}\left(\frac{1}{2}||\mathscr{P}C^2\mathscr{P}\phi^n||^2 + ||C^2\psi^{n+1}||^2 + ||C^2\psi^n||^2\right)\\ & + \frac{c_2^2}{2}||\tilde{\mathbf{T}}_{\mathbf{e}}^{n+\frac{1}{2}}|| + \frac{1}{4}\left(||C\psi^{n+1}||^2 + ||C\psi^n||^2\right) + \frac{3c_2^2(1+2\alpha_2)}{4}\left(||\Gamma_x^+\psi^n||^2 + ||\Gamma_y^+\psi^n||^2\right)\\ & + \frac{3c_2^2(1-2\alpha_2)}{4}\left(||\Gamma_x^+\psi^{n+1}||^2 + ||\Gamma_y^+\psi^{n+1}||^2\right) + \frac{(1+\alpha_2)}{2}\left(2(||\Gamma_x^+\phi^{n+1}||_{Q_x}^2\right.\\ & \left. + ||\Gamma_y^+\phi^{n+1}||_{Q_y}^2) + ||\Gamma_x^+\phi^n||_{Q_x}^2 + ||\Gamma_y^+\phi^n||_{Q_y}^2\right) + \alpha_2\Delta t\left(\frac{1}{2}||C^2\mathscr{P}\phi^n||^2\right.\\ & \left. + ||\mathscr{P}\phi^{n+1}||^2 + ||\mathscr{P}\phi^n||^2\right) + \frac{1}{2}\left(||\Gamma_x^+\mathbf{T_e}^{n+\frac{1}{2}}||_{Q_x}^2 + |||\Gamma_y^+\mathbf{T_e}^{n+\frac{1}{2}}||_{Q_y}^2\right)\end{aligned} \tag{4.4.48}$$

adding Ineqs. (4.4.37) and (4.4.48), multiplying resulting expression by $2\Delta t$, and discarding $\mathcal{O}(\Delta t^2)$ terms, it follows that

$$\begin{aligned}
&(||\phi^{n+1}||^2 - ||\phi^n||^2) + (||C\psi^{n+1}||^2 - ||C\psi^n||^2) + 2\left(||\Gamma_x^+\phi^{n+1}||_{Q_x}^2 - ||\Gamma_x^+\phi^n||_{Q_x}^2\right) \\
&+ 2\left(||\Gamma_y^+\phi^{n+1}||_{Q_y}^2 - ||\Gamma_y^+\phi^n||_{Q_y}^2\right) \le \frac{\Delta t}{2}(1 + c_2^2 + 2\alpha_2 c_2^2)\left(||\phi^{n+1}||^2 + ||\phi^n||^2\right) \\
&+ \frac{\Delta t(1+4\alpha_2)}{2}\left(||C\psi^{n+1}||^2 + ||C\psi^n||^2\right) + \Delta t||\mathbf{T_e}^{n+\frac{1}{2}}||^2 + \Delta t c_2^2||\tilde{\mathbf{T}}_{\mathbf{e}}^{n+\frac{1}{2}}||^2 \\
&+ \frac{\Delta t}{2}\left(||C\psi^{n+1}||^2 + ||C\psi^n||^2\right) + \frac{3\Delta t c_2^2(1+2\alpha_2)}{2}\left(||\Gamma_x^+\psi^n||^2 + ||\Gamma_y^+\psi^n||^2\right) \\
&+ \frac{3\Delta t c_2^2(1-2\alpha_2)}{2}\left(||\Gamma_x^+\psi^{n+1}||^2 + ||\Gamma_y^+\psi^{n+1}||^2\right) + \Delta t\left(||\Gamma_x^+\mathbf{T_e}^{n+\frac{1}{2}}||_{Q_x}^2 + ||\Gamma_y^+\mathbf{T_e}^{n+\frac{1}{2}}||_{Q_y}^2\right) \\
&+ \Delta t(1+\alpha_2)\left(2(||\Gamma_x^+\phi^{n+1}||_{Q_x}^2 + ||\Gamma_y^+\phi^{n+1}||_{Q_y}^2) + ||\Gamma_x^+\phi^n||_{Q_x}^2 + ||\Gamma_y^+\phi^n||_{Q_y}^2\right) \qquad (4.4.49)
\end{aligned}$$

Considering discrete sum of Ineq. (4.4.49) from $n = 0, 1, ..., m-1$ and using $\psi^0 = 0$, $\phi^0 = 0$, it follows that

$$\begin{aligned}
||\phi^m||^2 + ||C\psi^m||^2 + 2\left(||\Gamma_x^+\phi^m||_{Q_x}^2 + ||\Gamma_y^+\phi^m||_{Q_y}^2\right) &\le K\Delta t\sum_{i=1}^{m}\left(||\phi^i||^2 + ||C\psi^i||^2\right) \\
&+ K\Delta t\sum_{i=1}^{m}\left(||\Gamma_x^+\phi^i||_{Q_x}^2 + ||\Gamma_y^+\phi^i||_{Q_y}^2 + ||\Gamma_x^+\psi^i||^2 + ||\Gamma_y^+\psi^i||^2\right) \\
&+ K\Delta t\sum_{i=0}^{m-1}\left(||\Gamma_x^+\mathbf{T_e}^{i+\frac{1}{2}}||_{Q_x}^2 + ||\Gamma_y^+\mathbf{T_e}^{i+\frac{1}{2}}||_{Q_y}^2 + ||\mathbf{T_e}^{i+\frac{1}{2}}||^2 + ||\tilde{\mathbf{T}}_{\mathbf{e}}^{i+\frac{1}{2}}||^2\right)
\end{aligned} \qquad (4.4.50)$$

Ultimately, by utilizing Lemmas 4.3.2, 4.3.5, 4.4.1, 4.4.2 in conjunction with the discrete Grönwall's inequality, the result given in Ineq. (4.4.29) is obtained. □

4.5 Simulation of acoustic wave equation

4.5.1 Acoustic wave equation with constant phase speed

To validate the accuracy and efficiency of the developed method, simulations of various test cases for the propagation of acoustic wave equations in homogeneous and heterogeneous mediums have been performed. The 2D wave equation is given as

$$\frac{\partial^2 u}{\partial t^2} - c^2\left(\frac{\partial^2 u}{\partial x^2} + \frac{\partial^2 u}{\partial y^2}\right) = 0, \quad (x,y,t) \in [0,2]^3 \qquad (4.5.1)$$

initial conditions are chosen as

$$u(x,y)|_{t=0} = \cos(-\pi x - \pi y), \quad \frac{\partial u}{\partial t}(x,y)\bigg|_{t=0} = -\sqrt{2}\pi \sin(-\pi x - \pi y) \tag{4.5.2}$$

To establish the accuracy of the present scheme, the L^2-norm of the error and the relative error in the discrete energy for the 2D wave equation have been computed. Boundary data are chosen so that the exact solution for Eqs. (4.5.1)-(4.5.2) is given as, $u(x,y,t) = \cos\big(\sqrt{2}\pi t - \pi x - \pi y\big)$. Time advancement is performed using the EDRP2 method and the C4 scheme is used for spatial discretization. For numerical computations, $c = 1$ and $\Delta t = \Delta x^2 = \Delta y^2$ have been fixed. Using computed solutions, L^2-norm of the error and rate of convergence at time $T = 2$ are given in Table 4.3. It is evident from Table 4.3 that the EDRP2-C4 scheme has a fourth-order spatial convergence rate and second-order temporal convergence rate. Relative errors (RE) in the discrete energy are defined as

$$RE = \frac{|E_{num} - E_0|}{|E_0|}$$

Relative errors in the discrete energy at indicated final time T are shown in Table 4.4. Table 4.4 confirms that the present scheme is energy conservative irrespective of final time T. Moreover, a comparison of maximum absolute error at $C_r = 0.5$ shown in Fig. 4.2 validates that the developed method has better accuracy as compared to the RKN method.

4.5.2 Acoustic wave equation with variable phase speed

The 2D wave equation with variable phase speed and source function is given as

$$\frac{\partial^2 u}{\partial t^2} - c^2(x,y)\left(\frac{\partial^2 u}{\partial x^2} + \frac{\partial^2 u}{\partial y^2}\right) = f(x,y,t), \quad (x,y,t) \in [0,2]^3 \tag{4.5.3}$$

where $f(x,y,t) = \pi^2 \cos\big(\sqrt{2}\pi t - \pi x - \pi y\big)\left(2 + 2\times 10^{-5}\left(\sin^2(\pi x) + \sin^2(\pi y)\right) - 1\right)$ is the source function and $c^2(x,y) = 2\left(1 + 10^{-5}\left(\sin^2(\pi x) + \sin^2(\pi y)\right)\right)$. Initial conditions are chosen as

$$u(x,y)|_{t=0} = \cos(-\pi x - \pi y), \quad \frac{\partial u}{\partial t}(x,y)\bigg|_{t=0} = -\sqrt{2}\pi \sin(-\pi x - \pi y) \tag{4.5.4}$$

Boundary data are taken such that the exact solution for Eqs. (4.5.3)-(4.5.4) is given as, $u(x,y,t) = \cos\big(\sqrt{2}\pi t - \pi x - \pi y\big)$. Using computed solutions, L^2-norm of the error and

Table 4.3: L^2-norm of the error and convergence rate using EDRP2-C4 scheme for Eq. (4.5.1) with initial conditions given in Eq. (4.5.2) for indicated values of Δx, Δy and Δt at time $T = 2$.

$\Delta x = \Delta y$	Δt	$L^2 - error$	Convergence Rate (space)	Convergence Rate (time)
1/2	$1/2^2$	4.8693×10^{-2}	–	–
1/4	$1/4^2$	7.2704×10^{-3}	2.7436	1.3718
1/8	$1/8^2$	5.2425×10^{-4}	3.7937	1.8969
1/16	$1/16^2$	3.3116×10^{-5}	3.9846	1.9923
1/32	$1/32^2$	2.0581×10^{-6}	4.0081	2.0041

Table 4.4: Relative error in discrete energy using EDRP2-C4 scheme for Eq. (4.5.1) with initial conditions given in Eq. (4.5.2) at indicated values of time T. Here, $\Delta x = \Delta y = 1/32$ and $\Delta t = \Delta x^2$.

Time (T)	Relative Energy Error
1/4	5.3075×10^{-9}
1/2	5.3076×10^{-9}
1	5.3075×10^{-9}
3/2	5.3078×10^{-9}
2	5.3077×10^{-9}

rate of convergence at final time $T = 2$ are given in Table 4.5. It is observed from Table 4.5 that the EDRP2-C4 scheme has a fourth-order spatial convergence rate and a second-order temporal convergence rate. Relative errors in the discrete energy at indicated final time T are given in Table 4.6. Similar to the constant phase speed case, Table 4.6 shows that the present scheme is energy conservative for the variable phase speed case also.

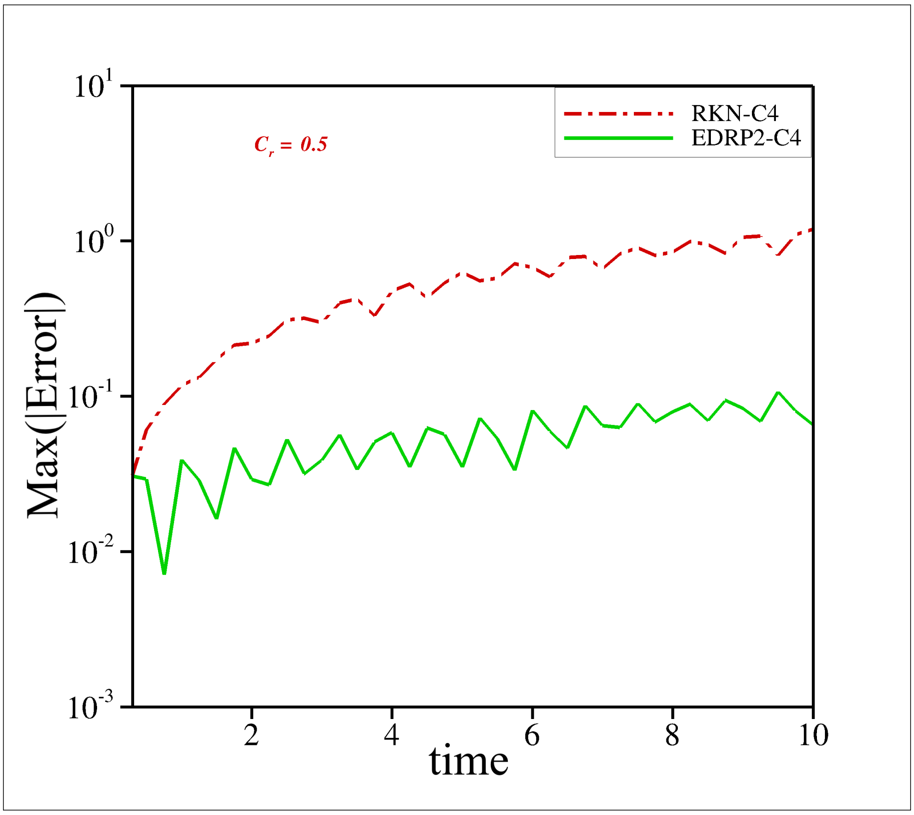

Figure 4.2: Comparison of maximum absolute error over time for the marked numerical methods at $C_r = 0.5$ for the 2D acoustic wave equation provided in Eq. (4.5.1) with $c = 1$ and initial data given in Eq. (4.5.2).

4.5.3 Acoustic waves in heterogeneous medium

For wave propagation in the heterogeneous medium, we have considered the nonhomogeneous acoustic wave equation given as

$$\frac{\partial^2 u}{\partial t^2} - c^2(x,y)\left(\frac{\partial^2 u}{\partial x^2} + \frac{\partial^2 u}{\partial y^2}\right) = f(x,y,t) \tag{4.5.5}$$

with a point source located inside the domain $[0, 5000]^2$ with zero Dirichlet boundary conditions. The source function is defined using Ricker's wavelet [71], given as

$$f(x,y,t) = \delta(x-x_0, y-y_0)\left[1 - 2\pi^2 {f_p}^2 (t-d_r)^2\right] e^{-\pi^2 {f_p}^2 (t-d_r)^2} \tag{4.5.6}$$

where $\delta(x-x_0, y-y_0)$ is the Dirac distribution, $f_p = 10Hz$ is the peak frequency and $d_r = 0.5/f_p$ is the time delay that is used to ensure zero initial conditions. In the present case,

Table 4.5: L^2-norm of the error and convergence rate using EDRP2-C4 scheme for Eq. (4.5.3) with initial conditions given in Eq. (4.5.4) for indicated values of Δx, Δy and Δt at time $T = 2$.

$\Delta x = \Delta y$	Δt	$L^2 - error$	Convergence Rate (space)	Convergence Rate (time)
1/2	$1/2^2$	4.8695×10^{-2}	–	–
1/4	$1/4^2$	7.2702×10^{-3}	2.7437	1.3718
1/8	$1/8^2$	5.2425×10^{-4}	3.7937	1.8968
1/16	$1/16^2$	3.3120×10^{-5}	3.9845	1.9922
1/32	$1/32^2$	2.0591×10^{-6}	4.0076	2.0038

Table 4.6: Relative error in discrete energy using EDRP2-C4 scheme for Eq. (4.5.3) with initial conditions given in Eq. (4.5.4) at indicated values of time T. Here, $\Delta x = \Delta y = 1/32$ and $\Delta t = \Delta x^2$.

Time (T)	Relative Energy Error
1/4	2.7976×10^{-7}
1/2	2.2082×10^{-7}
1	3.2991×10^{-7}
3/2	6.3225×10^{-8}
2	1.2390×10^{-7}

simulations of wave propagation in two- and three-layered mediums have been performed with $\Delta x = \Delta y = 12.5m$ and $\Delta t = 0.001s$. Schematic of a two-layered medium with the location of source function is shown in Fig. 4.3(a). As shown in Fig. 4.3(a), the upper half-layer has phase speed $c = 1500m/s$ and for the lower half-layer $c = 3000m/s$ with the source function located at $(x_0, y_0) = (2500m, 2000m)$. Computed wavefields for the two-layered medium are shown in Fig. 4.3(b) at marked instants. Due to the time delay,

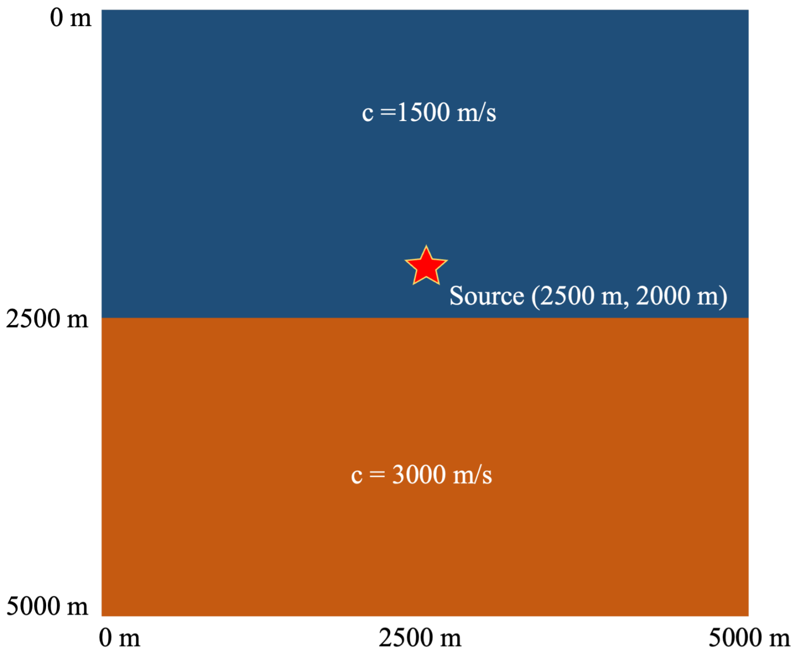

Figure 4.3(a): Schematic of the nonhomogeneous acoustic wave propagation given in Eqs. (4.5.5)-(4.5.6) in a two-layered heterogeneous medium.

the source gets activated approximately at $t = 0.05s$. Thus, solution at $t = 0.3s$ (left top frame of Fig. 4.3(b)) form a pure circle wavefront due to the constant phase speed in the upper-layer. Reflections from the layer's interface are visible from $t = 0.65s$ onward. Due to unequal phase speeds in both layers, reflected and refracted wavefronts retain the circular shape with different radii. At $t = 1.15s$, the wavefront (in the bottom layer) hits the left and right boundaries of the domain. However, no significant numerical dispersion is observed due to boundary reflections confirming that the developed method also has negligible dispersion error.

The schematic of the three-layered model is shown in Fig. 4.3(d). For three-layered medium, the upper layer has phase speed $c = 3000m/s$, for the middle layer $c = 1500m/s$, and $c = 3000m/s$ in the lower layer of the domain. The source function is located at $(2500m, 2500m)$. The computed wavefields in a three-layered medium are depicted in Fig. 4.3(e). The wave propagates only within the mid-layer till $t = 0.30s$ and at $t = 0.65s$ the wavefront strikes the upper and lower interfaces producing the reflections

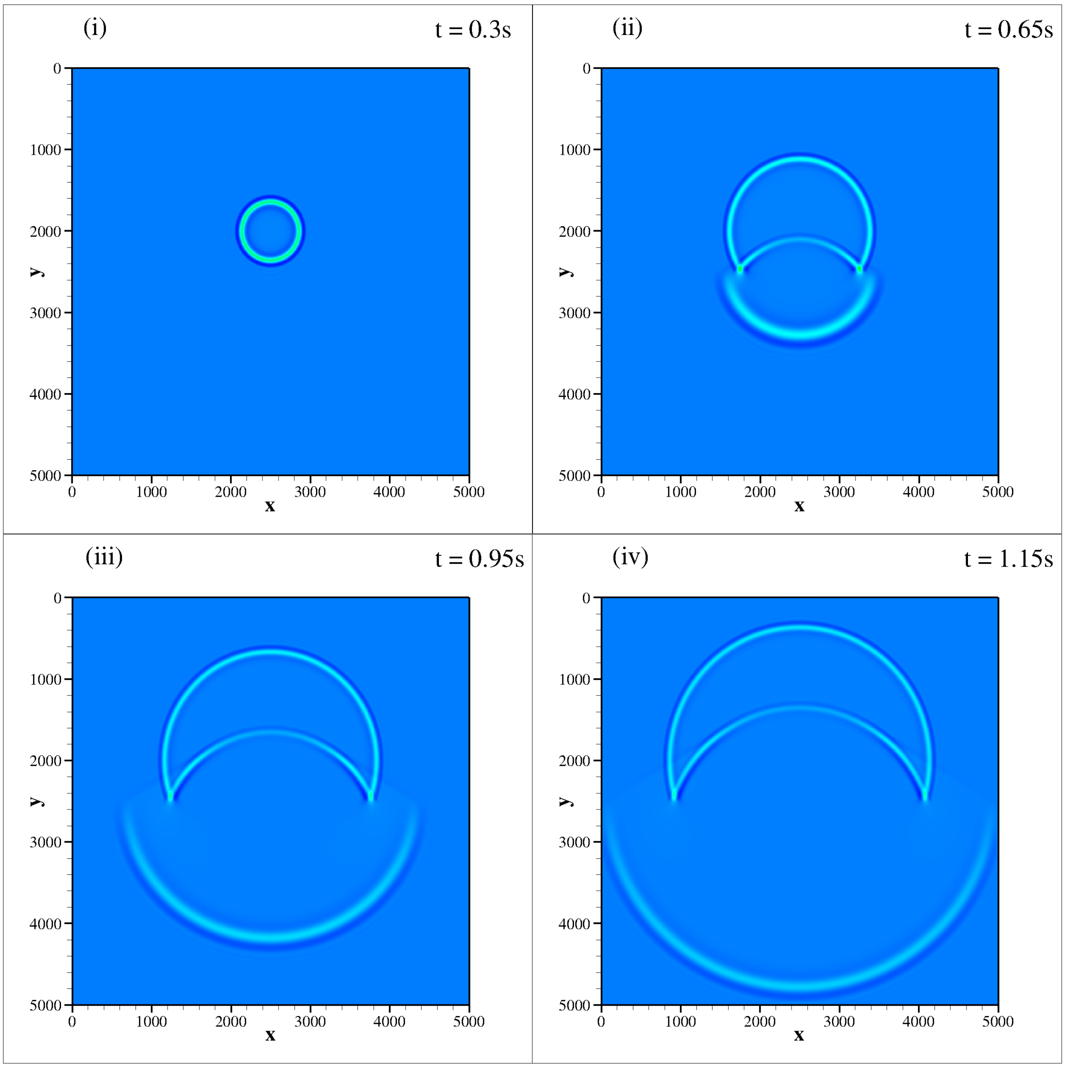

Figure 4.3(b): Wavefields contours for the nonhomogeneous acoustic wave propagation given in Eqs. (4.5.5)-(4.5.6) in a two-layered medium using the EDRP2-C4 scheme at indicated instants.

in the middle-layer. As time progresses, both reflected and refracted waves advance with circular wavefronts, as illustrated at $t = 0.95s$, while two reflected waves collide at $t = 1.15s$.

Moreover, to highlight the dispersion error, comparisons of the computed wavefields at marked instants using the EDRP2-C4 scheme and with the second-order leapfrog (LF2) time marching for the two-layered medium (shown in Fig. 4.3(a)) across the vertical line at $x = 2500m$ are presented in Fig. 4.3(c). From Fig. 4.3(c), it is evident that the present

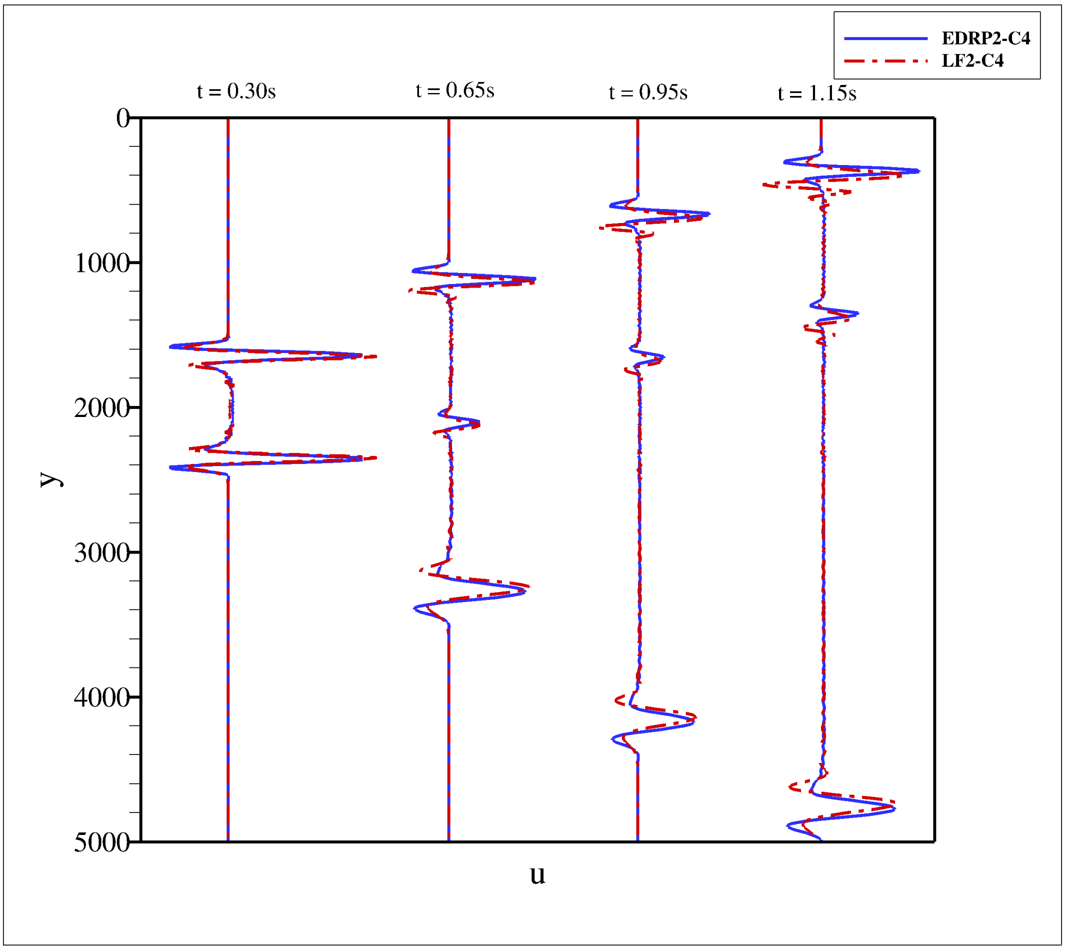

Figure 4.3(c): Comparison of the amplitudes of wavefields shown in Fig. 4.3(b) using EDRP2-C4 and LF2-C4 schemes across the vertical line at $x = 2500m$ in a two-layered heterogeneous medium at indicated instants.

method has negligible dispersion error as compared to the LF2 method.

4.5.4 The corner edge model

To further examine the accuracy of the developed method, the corner edge model [69] has been simulated following Eq. (4.5.5). The schematic of the corner edge model is given in Fig. 4.4(a). The phase speed in the region I is $2000m/s$, $3000m/s$ in the region II, and $4000m/s$ in the region III of the domain. For numerical simulation, a domain $[0, 12000]^2$

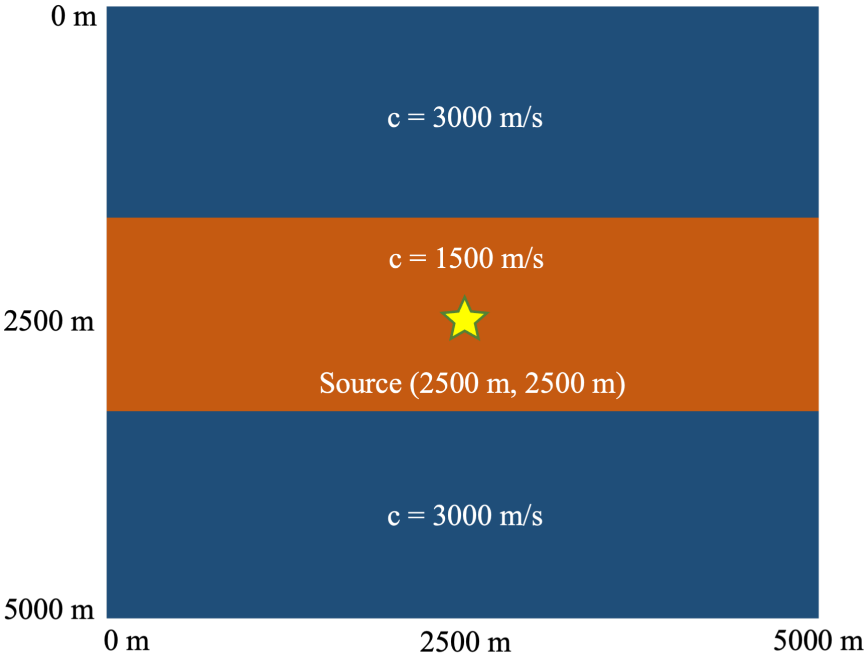

Figure 4.3(d): Schematic of the nonhomogeneous wave propagation given in Eqs. (4.5.5)-(4.5.6) in a three-layered heterogeneous medium.

has been considered. The source function is chosen as

$$f(t) = -5.76 f_0^2 \left[1 - 16(0.6 f_0 t - 1)^2\right] e^{-8(0.6 f_0 t - 1)^2} \tag{4.5.7}$$

The source function having a crest frequency of $f_0 = 20Hz$ is located at the domain's center. For numerical simulation, $\Delta t = 0.006s$ and $\Delta x = \Delta y = 40m$ have been chosen, with zero initial and Dirichlet boundary conditions. Fig. 4.4(b) shows the comparison of wavefield images produced by the EDRP2-C4 method with the LF2-C4 method at indicated instants. It is noticed that the acoustic wave propagation stays inside domain III, there is no reflected wave till time $t = 0.5s$. The reflected wave from vertical and horizontal interfaces can be seen at $t = 0.8s$ and as time advances more reflection and transmission of wave can be seen at $t = 1.2s$. Finally, Fig. 4.4(b) shows that the EDRP2-C4 scheme performs better than the LF2-C4 method, as the EDRP2-C4 scheme produces less numerical dispersion in comparison to the LF2-C4 method.

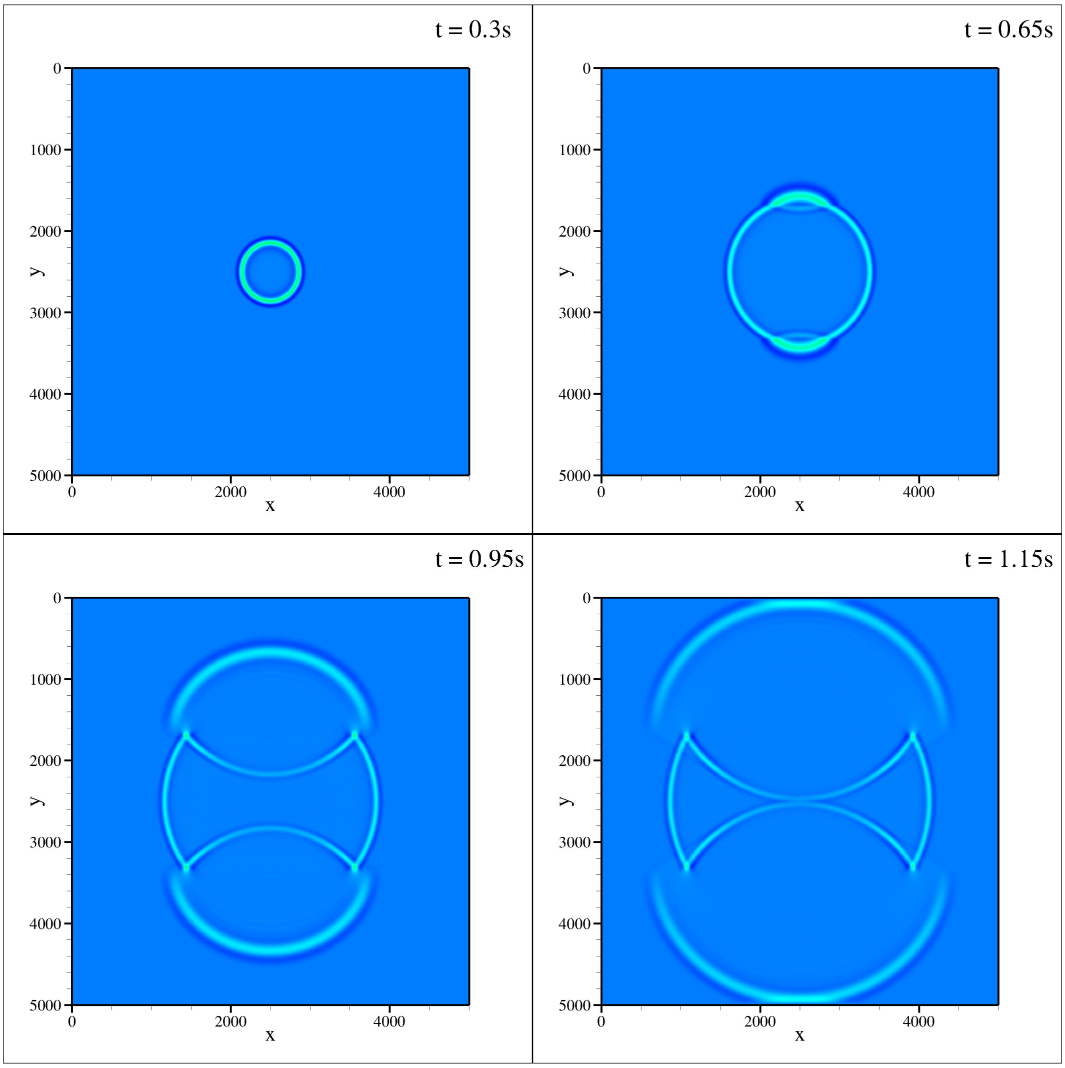

Figure 4.3(e): Wavefields contours for the nonhomogeneous acoustic wave propagation given in Eqs. (4.5.5)-(4.5.6) in a three-layered heterogeneous medium using the EDRP2-C4 scheme at indicated instants.

4.6 Simulation of nonlinear wave equations

For the numerical simulations of the nonlinear wave equations, the sine-Gordon and Klein-Gordon equations have been considered as the model systems.

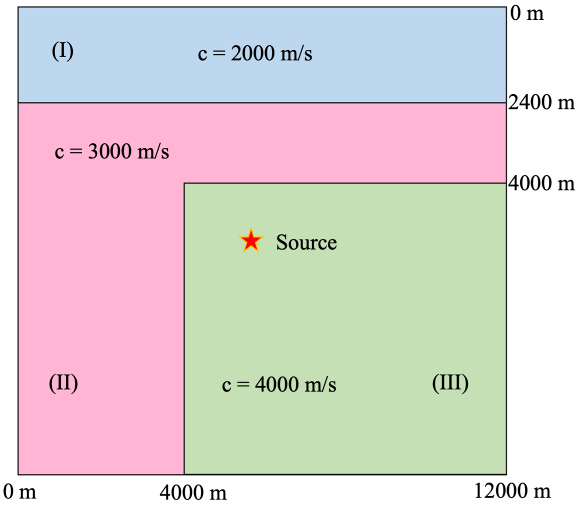

Figure 4.4(a): Schematic of the corner edge model for the nonhomogeneous acoustic wave propagation with the source function given in Eq. (4.5.7).

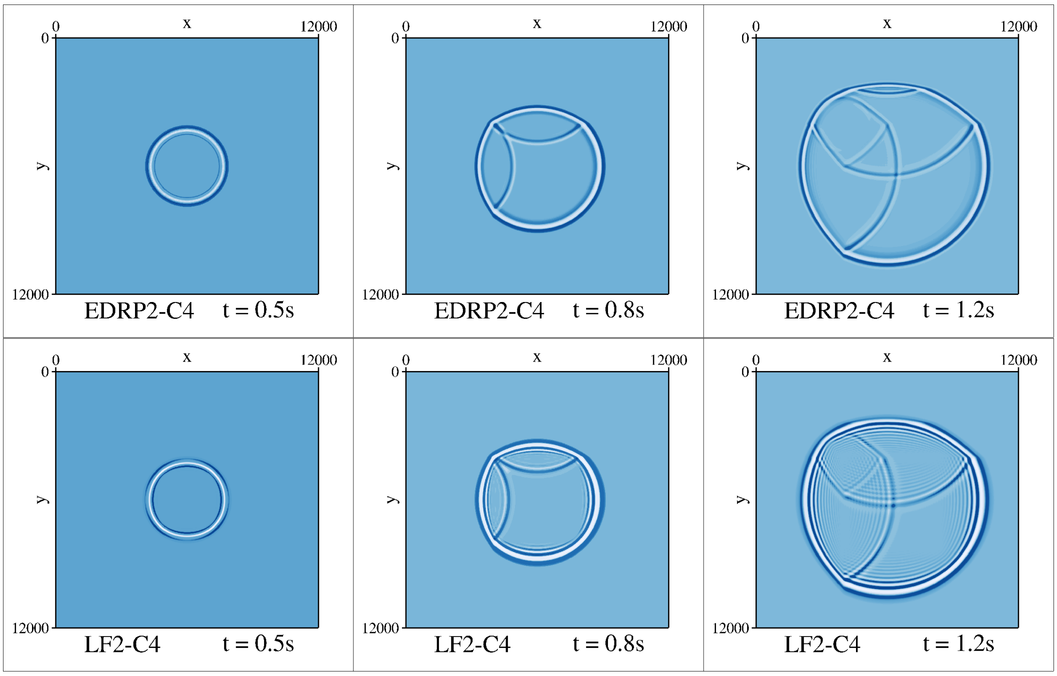

Figure 4.4(b): Comparison of the wavefield snapshots for the corner edge-model using EDRP2-C4 and LF2-C4 schemes at indicated instants for the nonhomogeneous acoustic wave propagation with the source function given in Eq. (4.5.7).

4.6.1 Propagation of orthogonal line-solitons

Two-dimensional damped sine-Gordon equation described in Eq. (1.6.1)[65] with Josephson junction is considered, where a represents the coefficient of damping and $F(x,y)$ stands for Josephson density of the current. Here, $\Omega = \{(x,y),\ a \le x \le b,\ a \le y \le b\}$ and $t > 0$ is chosen as the computational domain. Numerical simulations of the sine-Gordon equation are performed to investigate the combining of two perpendicular line-solitons in a superposed state with $F(x,y) = -1$. The initial and boundary conditions [141] are chosen as

$$\begin{aligned} u(x,y)\Big|_{t=0} &= 4\tan^{-1}(\exp(x)) + 4\tan^{-1}(\exp(y)), \quad (x,y) \in [-6,6]^2 \\ \frac{\partial u}{\partial t}(x,y)\Big|_{t=0} &= 0, \quad (x,y) \in [-6,6]^2 \end{aligned} \tag{4.6.1}$$

and

$$\frac{\partial u}{\partial x}(y,t)\Big|_{x=-6,6} = 0, \quad y \in [-6,6], \quad \frac{\partial u}{\partial y}(x,t)\Big|_{y=-6,6} = 0, \quad x \in [-6,6],\ t > 0 \tag{4.6.2}$$

respectively. Computations are performed for the undamped system ($a = 0$) with $\Delta x = \Delta y = 0.25m$ and $\Delta t = 0.001s$ using EDRP2-C4 scheme. The computed results, depicted in Fig. 4.5(a), illustrate that the line-solitons exhibit an outward motion along $y = x$ line.

Additionally, the energy for the Eq. (1.6.1) has been calculated using the initial and boundary data specified by Eqs. (4.6.1)-(4.6.2). The energy (E) for Eq. (1.6.1) is expressed as

$$\frac{\partial E}{\partial t} = -a \int\int_{\Omega} (u_t)^2 dxdy \tag{4.6.3}$$

where

$$E = \frac{1}{2} \int\int_{\Omega} \left(u_x^2 + u_y^2 + u_t^2 + 2(1 - \cos(u))\right) dxdy$$

Equation (4.6.3) confirms that in the absence of damping ($a = 0$), the energy (E) remain conserved. The initial energy $E(t = 0)$ is determined by substituting the initial data given in Eq. (4.6.1) into the energy expression (E), as

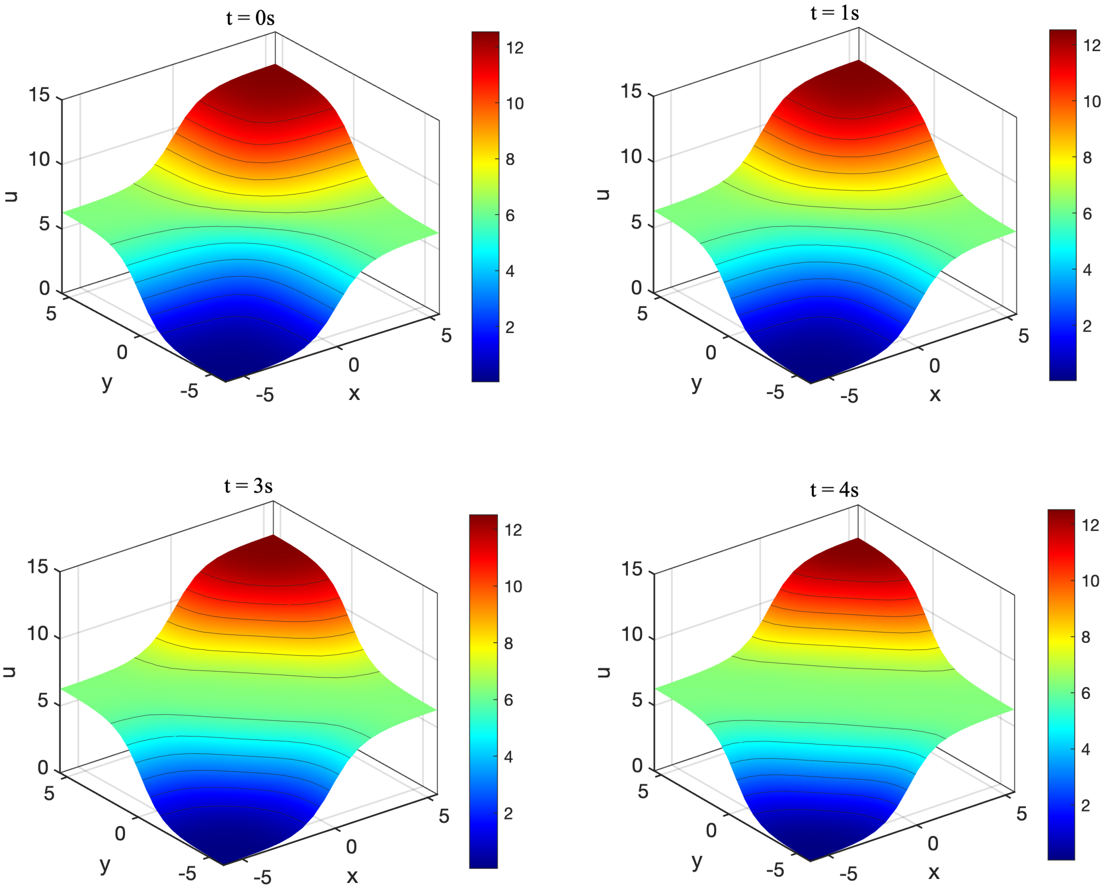

Figure 4.5(a): Interaction of two orthogonal line-solitons following undamped sine-Gordon equation with initial and boundary conditions given in Eqs. (4.6.1)-(4.6.2) at indicated instant using EDRP2-C4 scheme. Here, $a = 0$, $F(x, y) = -1$, $\Delta x = \Delta y = 0.25m$ and $\Delta t = 0.001s$.

$$E_0 = 8\left(\frac{b\left(e^a - e^{-a}\right)}{e^a + e^{-a}} + \frac{a\left(e^b - e^{-b}\right)}{e^b + e^{-b}}\right) + 8\left(\frac{1}{1+e^{-2a}} - \frac{1}{1+e^{2a}}\right)$$

$$\times\left(\frac{1}{1+e^{2b}} - \frac{1}{1+e^{-2b}} + b\right) + 8\left(\frac{1}{1+e^{-2b}} - \frac{1}{1+e^{2b}}\right) \times \left(\frac{1}{1+e^{2a}} - \frac{1}{1+e^{-2a}} + a\right)$$

$$+4\left(\sin 2(\tan^{-1}(e^a)) - \sin 2(\tan^{-1}(e^{-a}))\right) \times \left(\sin 2(\tan^{-1}(e^b)) - \sin 2(\tan^{-1}(e^{-b}))\right)$$

It is observed from Fig. 4.5(b) that the discrete energy for the undamped sine-Gordon system remains conserved with time.

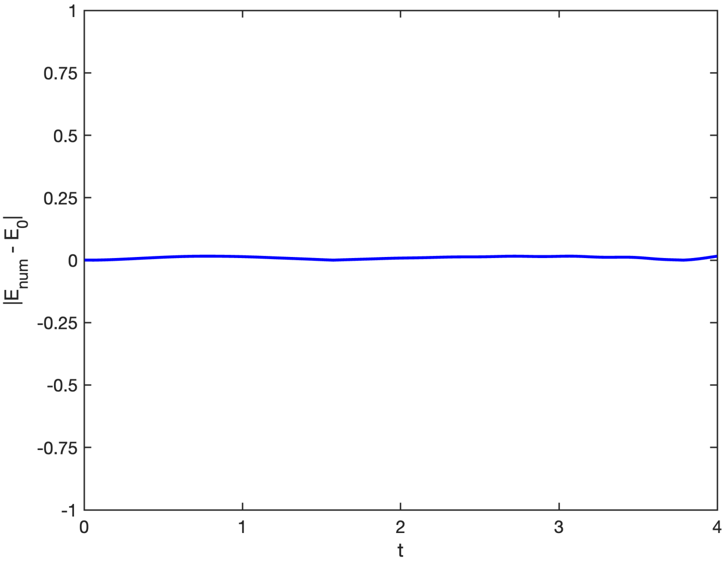

Figure 4.5(b): Variation of the absolute difference of initial and numerical energy ($|E_{num} - E_0|$) with time for the undamped sine-Gordon equation (1.6.1) with initial and boundary conditions given in Eqs. (4.6.1)-(4.6.2). Computations are performed with $F(x, y) = -1$, $\Delta x = \Delta y = 0.25m$ and $\Delta t = 0.001s$.

4.6.2 The sine-Gordon equation in a two-layered medium

In the present case, the undamped sine-Gordon equation has been simulated in a two-layered medium. The upper-layer of the domain has a phase speed $c = 1.0m/s$ and for the lower-layer $c = 1.5m/s$. Schematic for the simulation of undamped sine-Gordon equation in a two-layered medium is shown in Fig. 4.6(a). Numerical simulations of the collision of four expanding circular ring-solitons following sine-Gordon equation are performed to examine the accuracy and efficiency of the developed method. For computations, a domain $[-30, 10]^2$ is chosen with the initial conditions [66] given as

$$\begin{aligned} u(x,y)|_{t=0} &= 4\tan^{-1}\left[e^{\frac{1}{0.4360}\left(4-\sqrt{(x+3)^2+(y+3)^2}\right)}\right] \\ \frac{\partial u}{\partial t}(x,y)\Big|_{t=0} &= 4.1300/\cosh\left[\frac{1}{0.4360}\left(4-\sqrt{(x+3)^2+(y+3)^2}\right)\right] \end{aligned} \tag{4.6.4}$$

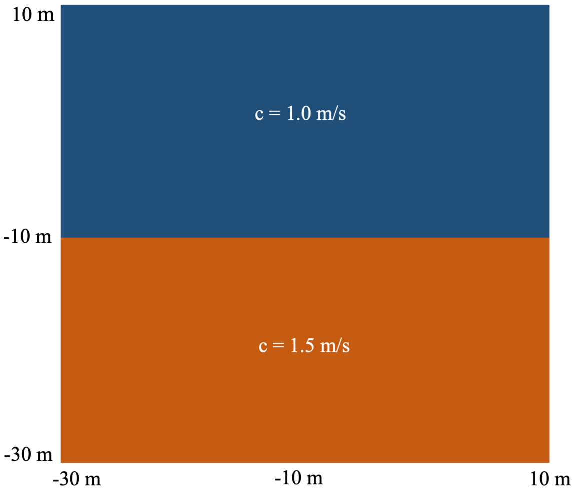

Figure 4.6(a): Schematic of the domain for the simulation of the collision of four ring-solitons following undamped sine-Gordon equation (1.6.1) in a two-layered heterogeneous medium.

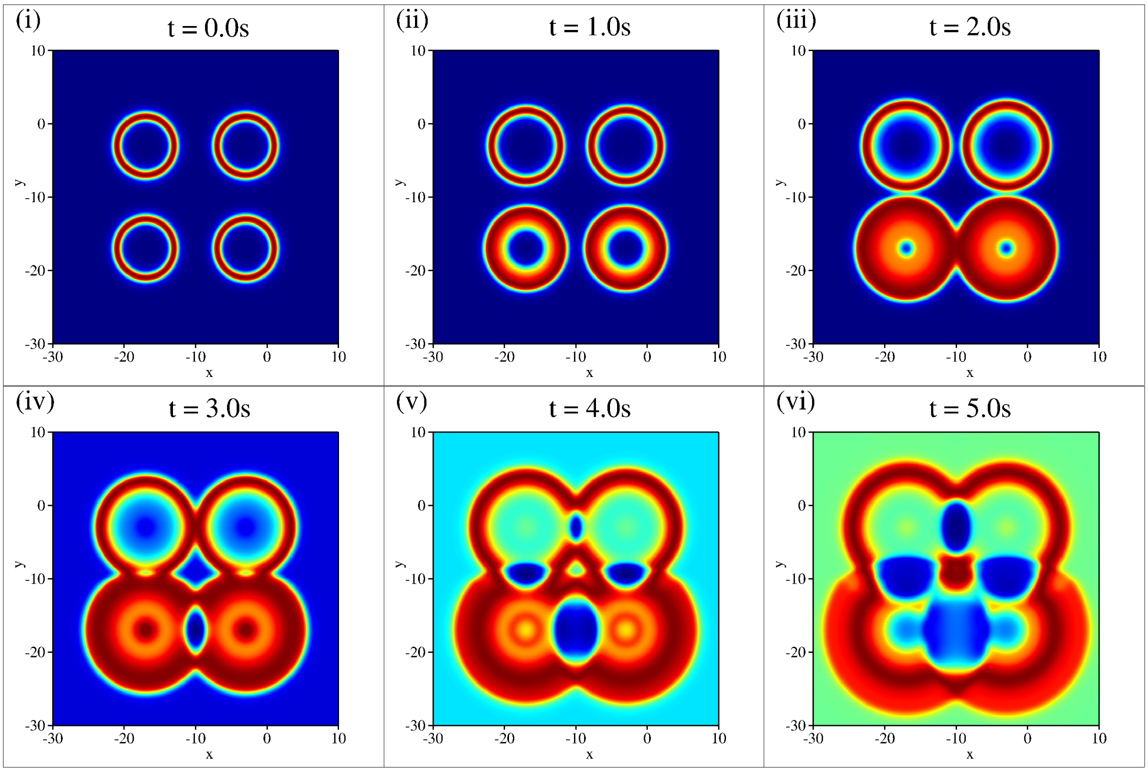

Figure 4.6(b): Computed solution of the collision of four ring-solitons with respect to $\sin(u/2)$ (instead of u) following sine-Gordon equation (1.6.1) with periodic boundary conditions and the initial data given in Eq. (4.6.4) at indicated instants using EDRP2-C4 scheme.

Computations are performed using periodic boundary conditions with $\Delta x = \Delta y = 1/8m$, $\Delta t = 1/64s$ and $a = 0$. Due to symmetry relations, computed results are expanded along vertical ($x = -10$) and horizontal ($y = -10$) lines. Figure 4.6(b) shows the propagation of solitons in terms of $\sin(u/2)$ in a two-layered medium up to time $t = 5s$. At $t = 0s$, all four solitons form a perfect circle due to their constant phase speed in their respective layer. As time advances, it is observed that the ring-solitons enclosing an annular region merge into a larger single ring soliton. As evident from Fig. 4.6(b) that the four ring-solitons interact in a very complex manner in the center of the domain and due to this, values of unknown u change very quickly. Moreover, due to the homogeneity of both layers, solitons in each layer maintain the similar shape. It is also noticed from Fig. 4.6(b) that the bottom layer experiences faster wave propagation than the top layer due to the higher phase speed in the bottom layer. Finally, numerical simulations of the nonlinear Klein-Gordon equation in the layered medium are discussed.

4.6.3 The Klein-Gordon equation in a two-layered medium

The two-dimensional nonlinear Klein-Gordon equation is given as

$$\frac{\partial^2 u}{\partial t^2} - c^2\left(\frac{\partial^2 u}{\partial x^2} + \frac{\partial^2 u}{\partial y^2}\right) + u + u^3 = 0, \quad (x, y) \in [-8, 8]^2 \tag{4.6.5}$$

with the following initial conditions [66], as

$$u(x, y)|_{t=0} = 2\exp\big[-(x+2)^2 - y^2\big], \quad \frac{\partial u}{\partial t}(x, y)\Big|_{t=0} = \exp\big(-x^2 - y^2\big) \tag{4.6.6}$$

Simulations are performed using the EDRP2-C4 scheme with the periodic boundary conditions. Here, $\Delta x = \Delta y = 1/8m$ and $\Delta t = 1/64s$ have been chosen. Schematic of the domain for the simulation of the Klein-Gordon equation is shown in Fig. 4.7(a), where phase speed for the left-layer is $c = 1.0m/s$ and for the phase speed for the right half-layer is $c = 0.5m/s$. Figure 4.7(b) shows the wave propagation for the Klein-Gordon equation at indicated instants in a two-layered medium. The computed solutions shown in Fig. 4.7(b) demonstrate the intricate interaction between the solitons includes shrink, radiation, and collision.

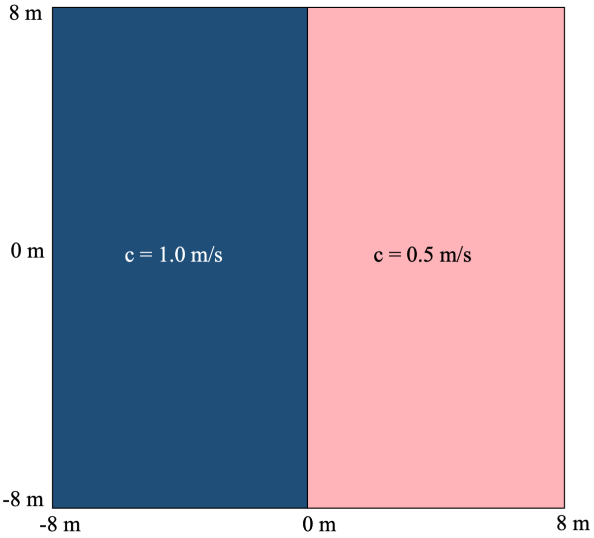

Figure 4.7(a): Schematic of the domain for the simulation of the Klein-Gordon equation (4.6.5) in a two-layered heterogeneous medium.

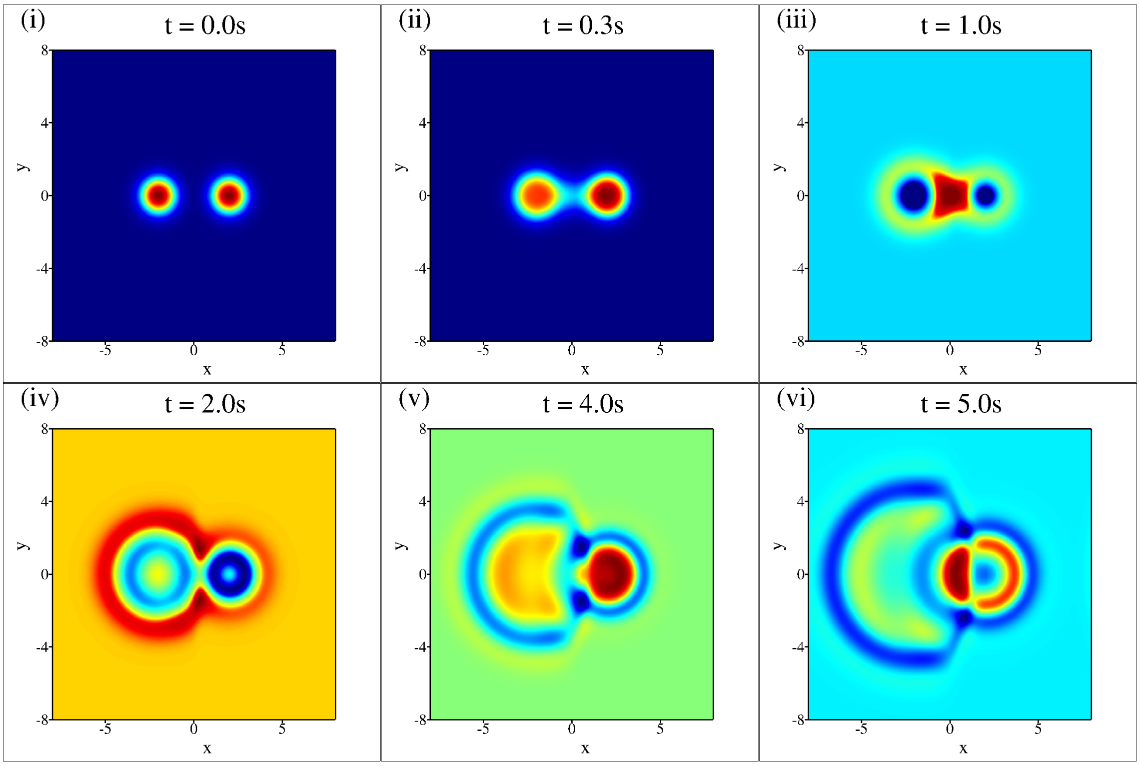

Figure 4.7(b): Simulation of the collision of two ring-solitons following Klein-Gordon equation (4.6.5) with periodic boundary conditions and the initial data given in Eq. (4.6.6) at indicated instants using EDRP2-C4 scheme.

It is also observed from Fig. 4.7(b) that after the collision of two ring-solitons, the wave in the left-layer propagates faster due to higher phase speed than the wave in the right-layer. Furthermore, at the collision between two solitons, the values of u fluctuate drastically.

It is emphasized that an energy preserving scheme for wave propagation simulation with variable coefficients has been developed. Our convergence analysis necessitates smoothness of coefficient functions and exact solutions. Nevertheless, numerical experiments in subsections 4.5.3, 4.5.4, 4.6.2, and 4.6.3 with layered mediums demonstrate how well the developed method performs when the coefficient functions are piecewise constants. The future study will address the convergence analysis and accuracy of solutions for problems with discontinuous coefficient functions with reduced regularity requirement of the solution.

Chapter 5

Dispersion-preserving fully discrete schemes for inhomogeneous damped waves equations [1]

The wave equation is a basic mathematical model that describes the propagation of waves through different mediums. Wave equations play a central role in the mathematical modeling of numerous physical processes, such as acoustic propagation, electromagnetic waves, crack propagation, and fluid dynamics [125, 142]. The damped wave equation is an extension of the classical wave equation that includes a damping term to model energy dissipation over time. Computations of acoustic wave equation are discussed in [71, 72, 70, 143, 144]. The wave propagation with variable coefficients, such as non-constant permittivity or refractive index, are discussed in [94, 95, 96, 97, 98, 99].

Systems characterized by second-order time derivatives are commonly converted into corresponding systems with first-order that can be integrated using methods such as linear multistep or Runge-Kutta methods [74]. The authors in [78, 79] formulated stable and explicit odd-even hopscotch methods for solving time-dependent diffusion equations. However, classical Runge-Kutta-Nyström (RKN) methods may be employed for the time integration of systems having time derivative of second-order. Dispersion analysis of

---

[1] The work is under review, 2025.

the RKN method for linear wave equations is discussed in [145]. For simulating wave equations, compact finite difference schemes have evolved as an effective tool which provide high accuracy and the use of smaller stencils enable the accurate implementation of boundary conditions [82, 83]. Moreover, to overcome the challenges associated with implementing a compact finite difference scheme, the authors in [127, 126] examined variable coefficients in conjunction with the time-derivative term.

Energy preserving methods for wave-like PDEs, based on AVF methods, are discussed in [84, 85, 86, 87, 105, 106, 66]. Moreover, compact ADI methods for solving two-dimensional nonlinear wave equations are given in [132, 133]. Implicit methods are computationally costly since they necessitate inversion of coefficient matrix. Here, the main objective is to develop and assess an energy-preserving method with improved stability while keeping computational costs comparable to explicit approaches for damped wave equations.

Chapter 5 focuses on the development and analysis of space-time discretizing methods for solving linear and nonlinear damped wave equations in different mediums. This chapter is structured as follows: Section 5.1 presents the derivation of time-integration methods for the 2D damped wave equation and discusses spatial discretization schemes. Fourier-spectral analysis of the developed method for the damped wave equation is discussed in Section 5.2. Convergence analysis of the developed space-time discretizing scheme is given in Section 5.3. Numerical experiments for the linear and nonlinear wave equations are discussed in Section 5.4 and Section 5.5, respectively.

5.1 Formulation

We have adopted the 2D inhomogeneous wave equation described in Eq. (1.8.2) as a reference model, where the initial and boundary conditions are expressed as

$$\begin{aligned} u(x,y,0) = g_1(x,y), \quad \frac{\partial u}{\partial t}(x,y,0) = g_2(x,y),\ (x,y)\in\Omega \\ u(x,y,t)|_{(x,y)\in\partial\Omega} = g_3(t), \quad t>0 \end{aligned} \tag{5.1.1}$$

defined over a finite computational domain $\Omega\subset\mathbb{R}^2$, with a phase speed $c(x,y)$, a final time

T, and a forcing term $f(u)$. Here, $g_1(x, y)$, $g_2(x, y)$ are the initial data and $g_3(t)$ represents the boundary data. It is assumed here that $f(u)$ satisfies the Lipschitz condition, given as

$$|f(u_1) - f(u_2)| \leq L|u_1 - u_2|, \quad \forall\, u_1, u_2 \tag{5.1.2}$$

where L is the Lipschitz constant. Substituting, $w = \frac{1}{c^2(x,y)}\left(\frac{\partial u}{\partial t} + au\right)$, Eq. (5.1.1) can be represented as

$$\begin{aligned} \frac{\partial w}{\partial t} &= L_1(u) \\ \frac{\partial u}{\partial t} &= L_2(w) + L_3(u) \end{aligned} \tag{5.1.3}$$

where $L_1(u) = \frac{\partial^2 u}{\partial x^2} + \frac{\partial^2 u}{\partial y^2} + \frac{1}{c^2(x,y)} f(x, y, u)$, $L_2(w) = c^2(x, y)w$, and $L_3(u) = -au$.

The first-order energy-dispersion preserving partially implicit time-advancement method (EDPM1) for the system in Eq. (5.1.3) is given as

$$\begin{aligned} w^{n+1} &= w^n + \Delta t L_1(u^n) \\ u^{n+1} &= u^n + \Delta t L_3(u^n) + \Delta t \left[\alpha L_2(w^n) + (1-\alpha) L_2(w^{n+1})\right] \end{aligned} \tag{5.1.4}$$

where, α is a free-parameter.

The second-order energy-dispersion preserving partially implicit time-advancement method (EDPM2) for the system in Eq. (5.1.3) is given as

$$\begin{aligned} w^{(1)} &= w^n + \Delta t L_1(u^n) \\ u^{(1)} &= u^n + \Delta t L_3(u^n) + \Delta t \left[\alpha_1 L_2(w^n) + (1-\alpha_1) L_2(w^{(1)})\right] \\ w^{n+1} &= 0.5 \left[w^n + w^{(1)} + \Delta t L_1(u^{(1)})\right] \\ u^{n+1} &= u^n + 0.5\Delta t \left[L_3(u^n) + L_3(u^{(1)})\right] + 0.5\Delta t \left[L_2(w^n) + 2\alpha_2 L_2(w^{(1)}) + (1-2\alpha_2) L_2(w^{n+1})\right] \end{aligned} \tag{5.1.5}$$

where, α_1 and α_2 are free parameters.

For spatial discretizations of Eq. (5.1.3), we have assumed that Ω is a rectangular domain. The domain Ω is discretized by considering $N_x \times N_y$ mesh-points with Δx and Δy representing the mesh step-sizes and Δt is the time-step. The conditions for boundaries are taken as periodic, represented as $x_{N_x+1} = x_0 + (N_x + 1)\Delta x$, $y_{N_y+1} = y_0 + (N_y + 1)\Delta y$. Mesh points satisfying these periodic conditions are denoted as, $\Omega_h^E =$

$\{(x_i, y_j)|0 \leq i \leq N_x+1, 0 \leq j \leq N_y+1\}$. For a mesh function, $u = \left\{u_{i,j}|(x_i, y_j) \in \Omega_h^E\right\}$, the corresponding difference operators are defined as

$$\begin{aligned}
\delta_x^+ u_{i,j} &= \frac{u_{i+1,j} - u_{i,j}}{\Delta x}, \;\; \delta_x^- u_{i,j} = \frac{u_{i,j} - u_{i-1,j}}{\Delta x}, \;\; \delta_x^2 u_{i,j} = \frac{u_{i-1,j} - 2u_{i,j} + u_{i+1,j}}{\Delta x^2} \\
\delta_y^+ u_{i,j} &= \frac{u_{i,j+1} - u_{i,j}}{\Delta y}, \;\; \delta_y^- u_{i,j} = \frac{u_{i,j} - u_{i,j-1}}{\Delta y}, \;\; \delta_y^2 u_{i,j} = \frac{u_{i,j-1} - 2u_{i,j} + u_{i,j+1}}{\Delta y^2} \\
\delta_x^2 u_{i,j} &= \delta_x^+ \delta_x^-, \;\; \delta_y^2 u_{i,j} = \delta_y^+ \delta_y^-
\end{aligned}$$

Using discrete approximations for the unknowns as, $W_{i,j}(t) \approx w(x_i, y_j, t)$, $U_{i,j}(t) \approx u(x_i, y_j, t)$, and $F_{i,j}(t) \approx f(u(x_i, y_j, t))$, the corresponding semi-discrete system for Eq. (5.1.1) with second-order centered difference (CD2) scheme is given as

$$\begin{aligned}
\frac{dW_{i,j}(t)}{dt} &= \delta_x^2 U_{i,j} + \delta_y^2 U_{i,j} + \frac{1}{c_{i,j}^2} F_{i,j}(t) \\
\frac{dU_{i,j}(t)}{dt} &= c_{i,j}^2 W_{i,j}(t) - aU_{i,j}(t)
\end{aligned} \tag{5.1.6}$$

The matrix-vector representation of Eq. (5.1.6) is given as

$$\begin{aligned}
\frac{dW}{dt} &= AU + Q^2 F \\
\frac{dU}{dt} &= C^2 W - aU
\end{aligned} \tag{5.1.7}$$

where, $W = \{W_{i,j}\}, U = \{U_{i,j}\}$, $F = \{F_{i,j}(t)\}$, $A = \Gamma_x^+\Gamma_x^- + \Gamma_y^+\Gamma_y^-$, $C = diag(c_{1,1}, c_{2,1}, \cdots, c_{N_x,1}, c_{1,2}, c_{2,2}, \cdots, c_{N_x,2}, \cdots, c_{1,N_y}, c_{2,N_y}, \cdots, c_{N_x,N_y})$, $Q = 1/C$. By denoting corresponding identity matrices with I_{N_x} and I_{N_y}, Γ_x^+, Γ_x^-, Γ_y^+, and Γ_y^- are given as

$$\begin{aligned}
\Gamma_x^+ &= I_{N_y} \otimes \bar{\Gamma}_x^+, \quad \Gamma_x^- = I_{N_y} \otimes \bar{\Gamma}_x^- \\
\Gamma_y^+ &= \bar{\Gamma}_y^+ \otimes I_{N_x}, \quad \Gamma_y^- = \bar{\Gamma}_y^- \otimes I_{N_x}
\end{aligned}$$

where

$$\bar{\Gamma}_x^+ = \frac{1}{\Delta x}\begin{bmatrix} -1 & 1 & 0 & \cdots & 0 & 0 \\ 0 & -1 & 1 & \cdots & 0 & 0 \\ \vdots & \vdots & \vdots & & \vdots & \vdots \\ 0 & 0 & 0 & \cdots & -1 & 1 \\ 1 & 0 & 0 & \cdots & 0 & -1 \end{bmatrix}_{N_x \times N_x}, \bar{\Gamma}_x^- = \frac{1}{\Delta x}\begin{bmatrix} 1 & 0 & 0 & \cdots & 0 & -1 \\ -1 & 1 & 0 & \cdots & 0 & 0 \\ \vdots & \vdots & \vdots & & \vdots & \vdots \\ 0 & 0 & 0 & \cdots & 1 & 0 \\ 0 & 0 & 0 & \cdots & -1 & 1 \end{bmatrix}_{N_x \times N_x}$$

$$\bar{\Gamma}_y^{+} = \frac{1}{\Delta y}\begin{bmatrix} -1 & 1 & 0 & \cdots & 0 & 0 \\ 0 & -1 & 1 & \cdots & 0 & 0 \\ \vdots & \vdots & \vdots & & \vdots & \vdots \\ 0 & 0 & 0 & \cdots & -1 & 1 \\ 1 & 0 & 0 & \cdots & 0 & -1 \end{bmatrix}_{N_y \times N_y}, \bar{\Gamma}_y^{-} = \frac{1}{\Delta y}\begin{bmatrix} 1 & 0 & 0 & \cdots & 0 & -1 \\ -1 & 1 & 0 & \cdots & 0 & 0 \\ \vdots & \vdots & \vdots & & \vdots & \vdots \\ 0 & 0 & 0 & \cdots & 1 & 0 \\ 0 & 0 & 0 & \cdots & -1 & 1 \end{bmatrix}_{N_y \times N_y}$$

Three-point fourth-order compact scheme (C4) for the spatial discretization of second-order derivatives [54, 80] can be obtained utilizing the difference operators described as

$$\begin{aligned} \mathcal{A}_x u_{i,j} &= \Big(1 + \frac{\Delta x^2}{12}\delta x^2\Big)u_{i,j}, \quad 1 \le i \le N_x, \quad 0 \le j \le N_y + 1 \\ \mathcal{A}_y u_{i,j} &= \Big(1 + \frac{\Delta y^2}{12}\delta y^2\Big)u_{i,j}, \quad 0 \le i \le N_x + 1, \quad 1 \le j \le N_y \end{aligned} \tag{5.1.8}$$

where

$$\mathcal{A}_x = \frac{1}{12}\begin{bmatrix} 10 & 1 & 0 & \cdots & 0 & 1 \\ 1 & 10 & 1 & \cdots & 0 & 0 \\ \vdots & \vdots & \vdots & & \vdots & \vdots \\ 0 & 0 & 0 & \cdots & 10 & 1 \\ 1 & 0 & 0 & \cdots & 1 & 10 \end{bmatrix}_{N_x \times N_x}, \mathcal{A}_y = \frac{1}{12}\begin{bmatrix} 10 & 1 & 0 & \cdots & 0 & 1 \\ 1 & 10 & 1 & \cdots & 0 & 0 \\ \vdots & \vdots & \vdots & & \vdots & \vdots \\ 0 & 0 & 0 & \cdots & 10 & 1 \\ 1 & 0 & 0 & \cdots & 1 & 10 \end{bmatrix}_{N_y \times N_y}$$

Following [80], the fourth-order compact finite difference scheme is given by

$$\begin{aligned} \frac{\partial^2 u}{\partial x^2}(x_i, y_j) &= \mathcal{A}_x^{-1}\delta_x^2 u_{i,j} + \frac{\Delta x^4}{240}\frac{\partial^6 u}{\partial x^6}(\varsigma_1, y_j) \\ \frac{\partial^2 u}{\partial y^2}(x_i, y_j) &= \mathcal{A}_y^{-1}\delta_y^2 u_{i,j} + \frac{\Delta y^4}{240}\frac{\partial^6 u}{\partial y^6}(x_i, \varsigma_2) \end{aligned} \tag{5.1.9}$$

where $\varsigma_1 \in (x_{i-1}, x_{i+1})$, $\varsigma_2 \in (y_{j-1}, y_{j+1})$. The semi-discrete system using the C4 scheme for Eq. (5.1.1) is given as

$$\begin{aligned} \frac{dW_{i,j}(t)}{dt} &= \mathcal{A}_x^{-1}\delta_x^2 U_{i,j} + \mathcal{A}_y^{-1}\delta_y^2 U_{i,j} + \frac{1}{c_{i,j}^2}F_{i,j}(t), i = 1, \cdots, N_x, j = 1, \cdots, N_y \\ \frac{dU_{i,j}(t)}{dt} &= c_{i,j}^2 W_{i,j}(t) - aU_{i,j}(t) \end{aligned} \tag{5.1.10}$$

with the initial and periodic boundary conditions, given as

$$\begin{aligned} U_{i,j}(0) = \Phi_1(x_i, y_j), &\;\; W_{i,j}(0) = \Phi_2(x_i, y_j) \\ U_{0,j} = U_{N_x,j}, \;\; U_{1,j} = U_{N_x+1,j}, &\;\; j = 0, \cdots, N_y + 1 \\ U_{i,0} = U_{i,N_y}, \;\; U_{i,1} = U_{i,N_y+1}, &\;\; i = 0, \cdots, N_x + 1 \end{aligned} \tag{5.1.11}$$

Using matrix representation, Eq. (5.1.10) can be rewritten as

$$\begin{aligned} \frac{dW}{dt} &= MU + Q^2 F \\ \frac{dU}{dt} &= C^2 W - aU \end{aligned} \tag{5.1.12}$$

where Q and C are the same matrices as given in Eq. (5.1.7). Moreover, the coefficient matrix M associated to operator $(\mathcal{A}_x^{-1}\delta_x^2 + \mathcal{A}_y^{-1}\delta_y^2)$ is given as, $M = P_x\Gamma_x^+\Gamma_x^- + P_y\Gamma_y^+\Gamma_y^-$ with $P_x = I_{N_y} \otimes \mathcal{A}_x^{-1}$ and $P_y = \mathcal{A}_y^{-1} \otimes I_{N_x}$. It is noted that the matrices P_x and P_y are symmetric and positive definite. The next section focuses on the stability analysis of the fully discretized system.

5.2 Fourier-stability analysis of damped wave equation

Fourier-spectral analysis [83, 146] of the fully discretized system for linear one - dimensional damped wave equation with periodic boundary conditions is discussed next. One - dimensional linear damped wave equation is taken as

$$\begin{aligned} \frac{\partial^2 u}{\partial t^2} = -a\frac{\partial u}{\partial t} + c^2\frac{\partial^2 u}{\partial x^2}, &\;\; x \in \Omega, t \in (0, T] \\ u(x, 0) = g_1(x), \;\; \frac{\partial u}{\partial t}(x, 0) = g_2(x) & \end{aligned} \tag{5.2.1}$$

where constant phase speed is represented by c. Using Fourier transform the unknown, $u(x, t)$, can be represented as

$$u(x, t) = \int \hat{U}(k, t)e^{ikx}dk \tag{5.2.2}$$

where $\hat{U}$ is the Fourier amplitude and k is the wavenumber. Substituting Eq. (5.2.2) in Eq. (5.2.1), the transformed equation is given by

$$\frac{\partial^2 \hat{U}}{\partial t^2} = -a\frac{\partial \hat{U}}{\partial t} - c^2k^2\hat{U} \tag{5.2.3}$$

Solving Eq. (5.2.3), it follows that

$$\hat{U}_{1,2}(k,t) = e^{\frac{t}{2}(-a\pm i\sqrt{4c^2k^2-a^2})} \tag{5.2.4}$$

Moreover, using bi-lateral Fourier-Laplace transform [83, 136] of the unknown $u(x,t)$ given as, $u(x,t) = \int\int \hat{U}(k,\omega)e^{i(kx-\omega t)}dkd\omega$, the dispersion relation for Eq. (5.2.1) is obtained as

$$\omega^2 + ia\omega - c^2k^2 = 0 \tag{5.2.5}$$

where, ω denotes the circular frequency. Roots of Eq. (5.2.5) are given by, $\omega_{1,2} = (-ai \pm \sqrt{4c^2k^2 - a^2})/2$. Using dispersion relation, physical phase speed and group velocity [147], can be expressed as

$$(c_{phy})_{1,2} = \frac{\omega_{1,2}}{k} \text{ and } (V_g)_{1,2} = \frac{\partial \omega_{1,2}}{\partial k} = \pm\frac{2c^2k}{\sqrt{4c^2k^2-a^2}}$$

The physical amplification factor λ_{phy} can be obtained from Eq. (5.2.4) as

$$(\lambda_{phy})_{1,2} = \frac{\hat{U}_{1,2}(k,t+\Delta t)}{\hat{U}_{1,2}(k,t)} = e^{-\frac{a\Delta t}{2}}e^{\pm\frac{i\Delta t\sqrt{4c^2k^2-a^2}}{2}} \tag{5.2.6}$$

In discrete computations, numerical dispersion relation [147, 148, 149] corresponding to the chosen space-time discretizing scheme is given as

$$\omega_N^2 + ia\omega_N - c_N^2k^2 = 0 \tag{5.2.7}$$

Numerical amplification factor is given as

$$\lambda_{N_{1,2}} = e^{-\frac{a\Delta t}{2}}e^{\pm\frac{i\Delta t\sqrt{4c_N^2k^2-a^2}}{2}} \tag{5.2.8}$$

Moreover, the numerical phase shift and normalized phase speed are defined as

$$\beta_{1,2} = -\arctan\left[\frac{(\lambda_{N_{1,2}})_{Im}}{(\lambda_{N_{1,2}})_{Re}}\right] = \pm\frac{\Delta t}{2}\sqrt{4c_N^2k^2-a^2}$$

$$\frac{c_{N_{1,2}}}{c} = \pm\frac{1}{2}\sqrt{\frac{4\beta_{1,2}^2+\tilde{\gamma}^2}{C_r^2(k\Delta x)^2}} \tag{5.2.9}$$

where $(\lambda_N)_{Im}$ and $(\lambda_N)_{Re}$ denote the real and the imaginary parts of λ_N, respectively. $C_r = \frac{c\Delta t}{\Delta x}$ is the CFL number and $\tilde{\gamma} = a\Delta t$. The numerical group velocity [147] using the numerical dispersion relation is given as $V_{g_{N_{1,2}}} = \frac{\partial}{\partial k}(\omega_N)_{1,2} = \frac{1}{\Delta t}\frac{d\beta_{1,2}}{dk}$. Thus, the expression for the normalized group velocity is obtained as

$$\frac{V_{g_{N_{1,2}}}}{V_g} = \pm\frac{\sqrt{4C_r^2(k\Delta x)^2 - \tilde{\gamma}^2}}{2C_r^2 k\Delta x}\frac{d\beta_{1,2}}{d(k\Delta x)} \tag{5.2.10}$$

Equation (5.2.1) can be rewritten as

$$\begin{aligned} \frac{\partial w}{\partial t} &= \frac{\partial^2 u}{\partial x^2} \\ \frac{\partial u}{\partial t} &= -au + c^2 w \end{aligned} \tag{5.2.11}$$

Using the EDPM1 method, the semi-discretized representation of Eq. (5.2.11) is given by

$$\begin{aligned} w^{n+1} &= w^n + \Delta t u_{xx}^n \\ u^{n+1} &= u^n - a\Delta t u^n + c^2\Delta t(\alpha w^n + (1-\alpha)w^{n+1}) \end{aligned} \tag{5.2.12}$$

Using Eq. (5.2.2), the first- and second-order derivatives in spatial direction are represented as, $u_x(x,t)|_{exact} = \int ik\hat{U}(k,t)e^{ikx}dk$ and $u_{xx}(x,t)|_{exact} = \int (ik)^2\hat{U}(k,t)e^{ikx}dk$. Numerically, the first- and second-order spatial derivatives are expressed as, $u_x(x,t)|_N = \int ik_{eq}\hat{U}(k,t)e^{ikx}dk$ and $u_{xx}(x,t)|_N = \int (ik_{eq})^2\hat{U}(k,t)e^{ikx}dk$, where k_{eq} is the equivalent wavenumber. Applying Fourier-Laplace transform to Eq. (5.2.12) gives

$$\begin{aligned} \hat{W}^{n+1} &= \hat{W}^n - \Delta t k_{eq}^2 \hat{U}^n \\ \hat{U}^{n+1} &= \hat{U}^n - a\Delta t\hat{U}^n + c^2\Delta t(\alpha\hat{W}^n + (1-\alpha)\hat{W}^{n+1}) \end{aligned} \tag{5.2.13}$$

where, $\hat{U}$ and $\hat{W}$ are the Fourier transforms of u and w, respectively. In terms of matrix representation, Eq. (5.2.13) is given as

$$\hat{\Theta}^{n+1} = \mathcal{M}\hat{\Theta}^n$$

where, $\hat{\Theta} = (\hat{W}, \hat{U})^T$ and $\mathcal{M} = \begin{bmatrix} 1 & -\Delta t k_{eq}^2 \\ c^2\Delta t & 1 - a\Delta t - c^2\Delta t^2(1-\alpha)k_{eq}^2 \end{bmatrix}$

Amplification factors representing the roots of the characteristic equation of the matrix $(\mathcal{M})$ are denoted by $\lambda = [\lambda_{N_1}, \lambda_{N_2}]^T$. Substituting $k_{eq}^2 = \frac{\hat{k}_{eq}}{\Delta x^2}$ gives the amplification factors as

$$\lambda_{N_{1,2}} = e_1 \pm \frac{1}{2}\sqrt{e_2} \tag{5.2.14}$$

where, $e_1 = \frac{-C_r^2\hat{k}_{eq}}{2} + \frac{C_r^2\hat{k}_{eq}\alpha}{2} - \frac{\tilde{\gamma}}{2} + 1$, $e_2 = (\hat{k}_{eq}^2 C_r^4\alpha^2 - 2\hat{k}_{eq}^2 C_r^4\alpha + \hat{k}_{eq}^2 C_r^4 - 2\hat{k}_{eq}C_r^2\tilde{\gamma}\alpha + 2\hat{k}_{eq}C_r^2\tilde{\gamma} - 4\hat{k}_{eq}C_r^2 + \tilde{\gamma}^2)$ and $\hat{k}_{eq} = \phi(k\Delta x)$. It follows directly from Eq. (5.2.14) that $e_2 < 0$, for a wave-like solution. For the spatial discretization of second-order derivative, we have used the CD2 and C4 schemes. Nondimensional equivalent wavenumbers for the CD2 and C4 schemes are obtained as

$$\phi(k\Delta x)_{\mathrm{CD2}} = 2(1-\cos(k\Delta x)), \quad \phi(k\Delta x)_{\mathrm{C4}} = \frac{12\,(1-\cos(k\Delta x))}{\cos(k\Delta x)+5} \tag{5.2.15}$$

Fourier-spectral analysis for the two-dimensional case is discussed next. Two-dimensional linear damped wave equation with periodic boundary conditions is given as

$$\frac{\partial^2 u}{\partial t^2} = -a\frac{\partial u}{\partial t} + c^2\left(\frac{\partial^2 u}{\partial x^2} + \frac{\partial^2 u}{\partial y^2}\right), \ (x,y)\in\Omega, t\in(0,T] \tag{5.2.16}$$

where c is constant and the initial conditions for Eq. (5.2.16) are given as

$$u(x,y,0) = g_1(x,y), \quad \frac{\partial u}{\partial t}(x,y,0) = g_2(x,y), \ (x,y)\in\Omega \tag{5.2.17}$$

Equation (5.2.16) can be rewritten as

$$\begin{aligned} \frac{\partial w}{\partial t} &= \frac{\partial^2 u}{\partial x^2} + \frac{\partial^2 u}{\partial y^2} \\ \frac{\partial u}{\partial t} &= -au + c^2 w \end{aligned} \tag{5.2.18}$$

Using the EDPM1 method, the semi-discretized representation of Eq. (5.2.18) is given by

$$\begin{aligned} w^{n+1} &= w^n + \Delta t\left(u_{xx}^n + u_{yy}^n\right) \\ u^{n+1} &= u^n - a\Delta t u^n + c^2\Delta t(\alpha w^n + (1-\alpha)w^{n+1}) \end{aligned} \tag{5.2.19}$$

Applying Fourier-Laplace transform to Eq. (5.2.19) gives

$$\begin{aligned} \hat{W}^{n+1} &= \hat{W}^n - \Delta t k_{eq}^2 \hat{U}^n \\ \hat{U}^{n+1} &= \hat{U}^n - a\Delta t\hat{U}^n + c^2\Delta t(\alpha\hat{W}^n + (1-\alpha)\hat{W}^{n+1}) \end{aligned} \tag{5.2.20}$$

where, $\hat{U}$ and $\hat{W}$ are the Fourier transforms of u and w, respectively. In terms of matrix representation, Eq. (5.2.20) is given as

$$\hat{\Theta}^{n+1} = \mathcal{M}\hat{\Theta}^{n}$$

where, $\hat{\Theta} = (\hat{W}, \hat{U})^T$ and $\mathcal{M} = \begin{bmatrix} 1 & -\Delta t^2 k_{eq}^2 \\ c^2\Delta t & 1 - a\Delta t - c^2\Delta t^2(1-\alpha)k_{eq}^2 \end{bmatrix}$

By substituting $k_{eq}^2 = \frac{\hat{k}_{eq}}{h^2}$, the amplification factors (characteristic values of $\mathcal{M}$) are obtained as

$$\lambda_{N_{1,2}} = e_1 \pm \frac{1}{2}\sqrt{e_2} \tag{5.2.21}$$

The expressions for e_1 and e_2 are the same as given in Eq. (5.2.14). For the two-dimensional case, the nondimensional equivalent wavenumber is given by $\hat{k}_{eq} = \phi(k_x h) + \phi(k_y h)$. Here, the spatial step-size is uniform, denoted by $\Delta x = \Delta y = h$. The numerical circular frequency (ω_N) is expressed as $(\omega_N)_{1,2} = \frac{-ai \pm \sqrt{4c_N^2(k_x^2+k_y^2)-a^2}}{2}$, where, $\vec{k} = \hat{i}k_x + \hat{j}k_y$. Similar to one-dimensional damped wave equation, expressions of numerical phase speed and group velocity for two-dimensional damped wave equation are defined as

$$\begin{aligned}
\frac{c_{Nx_{1,2}}}{c} &= \pm\frac{\sqrt{4\beta_{1,2}^2 + \tilde{\gamma}^2}}{2C_{r_x}\sqrt{(k_x h)^2 + (k_y h)^2}}, \quad \frac{c_{Ny_{1,2}}}{c} = \pm\frac{\sqrt{4\beta_{1,2}^2 + \tilde{\gamma}^2}}{2C_{r_y}\sqrt{(k_x h)^2 + (k_y h)^2}} \\
(V_g^x)_{1,2} &= \frac{\partial\omega_{1,2}}{\partial k_x} = \pm\frac{2c^2 k_x}{\sqrt{4c^2(k_x^2 + k_y^2) - a^2}}, \quad (V_g^y)_{1,2} = \frac{\partial\omega_{1,2}}{\partial k_y} = \pm\frac{2c^2 k_y}{\sqrt{4c^2(k_x^2 + k_y^2) - a^2}} \\
(V_{g_N}^x)_{1,2} &= \frac{\partial(\omega_N)_{1,2}}{\partial k_x}, \quad (V_{g_N}^y)_{1,2} = \frac{\partial(\omega_N)_{1,2}}{\partial k_y} \\
\frac{(V_{g_N}^x)_{1,2}}{V_g^x} &= \pm\frac{\sqrt{4C_{r_x}^2[(k_x h)^2 + (k_y h)^2] - \tilde{\gamma}^2}}{2C_{r_x}^2 k_x h}\frac{\partial\beta_{1,2}}{\partial(k_x h)} \\
\frac{(V_{g_N}^y)_{1,2}}{V_g^y} &= \pm\frac{\sqrt{4C_{r_y}^2[(k_x h)^2 + (k_y h)^2] - \tilde{\gamma}^2}}{2C_{r_y}^2 k_y h}\frac{\partial\beta_{1,2}}{\partial(k_y h)}
\end{aligned}$$

where $C_{r_x} = \dfrac{c\Delta t}{\Delta x}$, $C_{r_y} = \dfrac{c\Delta t}{\Delta y}$, and $\tilde{\gamma} = a\Delta t$.

Numerical properties for the undamped ($a = 0$) wave equation using the CD2 and C4 spatial discretization schemes are shown in Fig. 5.1(a). Figure 5.1(a) presents contours depicting the absolute values of amplification factors ($|\lambda_N|$), numerical phase speed

(c_N/c), numerical group velocity (V_{g_N}/V_g) for the EDPM1-CD2 and EDPM1-C4 schemes with the optimized value of free parameter $\alpha = 0.00015$. Numerical properties of the RKN-C4 scheme are also shown in the right column frames of Fig. 5.1(a). In Fig. 5.1(a), vertical dash-dotted line indicate the values of CFL numbers up to which methods are neutrally stable and the shaded area represents the corresponding non-hyperbolic region. Figure 5.1(a) demonstrates that the developed scheme exhibits a larger neutral stability ($|\lambda_N| = 1$) region as compared to the RKN method. Figure 5.1(b) shows the numerical properties of one-dimensional damped wave equation using the EDPM1-CD2 and EDPM1-C4 schemes with the optimized value of free parameter $\alpha = 0.00015$ and $\tilde{\gamma} = a\Delta t = 0.002$. Figures 5.1(c) and 5.1(d) present contours depicting the amplification factors ($|\lambda_N|$), the numerical phase speed (c_N/c), and the numerical group velocity (V_{g_N}/V_g) for the EDPM1-CD2 and EDPM1-C4 schemes with the optimized value of free parameter $\alpha = 0.00015$ for two-dimensional damped wave equation with $\tilde{\gamma} = 0.002$ and $C_r = 0.2, 0.4$, respectively. We would like mention here that Figs 5.1(a) - 5.1(d) show the numerical properties corresponding to the first mode λ_{N_1} only.

Furthermore, we have performed Fourier-spectral analysis for one-dimensional damped wave equation described in Eq. (5.2.1). Using EDPM2 method, the semi-discretized representation of the system given in Eq. (5.2.11) of Eq. (5.2.1) is obtained as

$$\begin{aligned}
w^{(1)} &= w^n + \Delta t u_{xx}^n \\
u^{(1)} &= u^n - a\Delta t u^n + c^2\Delta t \left[\alpha_1 w^n + (1-\alpha_1) w^{(1)}\right] \\
w^{n+1} &= 0.5\left[w^n + w^{(1)} + \Delta t u_{xx}^{(1)}\right] \\
u^{n+1} &= u^n - 0.5a\Delta t\left[u^n + u^{(1)}\right] + 0.5c^2\Delta t\left[w^n + 2\alpha_2 w^{(1)} + (1-2\alpha_2) w^{n+1}\right]
\end{aligned} \tag{5.2.22}$$

Applying Fourier-Laplace transform to Eq. (5.2.22) gives

$$\begin{aligned}
\hat{W}^{(1)} &= \hat{W}^n - \Delta t k_{eq}^2 \hat{U}^n \\
\hat{U}^{(1)} &= \hat{U}^n - a\Delta t\hat{U}^n + c^2\Delta t\left[\alpha_1 \hat{W}^n + (1-\alpha_1)\hat{W}^{(1)}\right] \\
\hat{W}^{n+1} &= 0.5\left[\hat{W}^n + \hat{W}^{(1)} - \Delta t k_{eq}^2 \hat{U}_{xx}^{(1)}\right] \\
\hat{U}^{n+1} &= \hat{U} - 0.5a\Delta t\left[\hat{U}^n + \hat{U}^{(1)}\right] + 0.5c^2\Delta t\left[\hat{W}^n + 2\alpha_2\hat{W}^{(1)} + (1-2\alpha_2)\hat{W}^{n+1}\right]
\end{aligned} \tag{5.2.23}$$

Here $\hat{U}$ and $\hat{W}$ represent the Fourier transforms of u and w, respectively. In terms of matrix representation, Eq. (5.2.23) is given as

$$\hat{\Theta}^{n+1} = \mathcal{M}_1 \hat{\Theta}^n$$

where, $\hat{\Theta} = (\hat{W}, \hat{U})^T$ and $\mathcal{M}_1 = \begin{bmatrix} m_{11} & m_{12} \\ m_{21} & m_{22} \end{bmatrix}$. Here, the entries of the matrix $\mathcal{M}_1$ are obtained as

$$\begin{aligned}
m_{11} &= 1 - 0.5\Delta t^2 c^2 k_{eq}^2, \qquad m_{12} = -\Delta t k_{eq}^2 + 0.5a\Delta t^2 k_{eq}^2 + 0.5(1-\alpha_1)\Delta t^3 c^2 k_{eq}^4, \\
m_{21} &= \Delta t c^2 - 0.5a\Delta t^2 c^2 - 0.25\Delta t^3 c^4 k_{eq}^2 + 0.5\Delta t^3 c^4 \alpha_2 k_{eq}^2, \\
m_{22} &= 1 + 0.5a^2\Delta t^2 + 0.5(1-\alpha_1)a\Delta t^3 c^2 k_{eq}^2 - 0.5\Delta t^2 c^2 k_{eq}^2 + 0.25(1-2\alpha_2)a\Delta t^3 c^2 k_{eq}^2 \\
&\quad - a\Delta t + 0.25(1-\alpha_1)(1-2\alpha_2)\Delta t^4 c^4 k_{eq}^4
\end{aligned}$$

By substituting $k_{eq}^2 = \frac{\hat{k}_{eq}}{\Delta x^2}$, the amplification factors (characteristic values of $\mathcal{M}_1$) are obtained as

$$\lambda_{N_{1,2}} = e_3 \pm \frac{1}{8}\sqrt{e_4} \tag{5.2.24}$$

Here, the expressions of e_3, e_4 are given as

$$\begin{aligned}
e_3 &= 1 - 0.5\gamma + 0.25\gamma^2 - 0.5C_r^2\hat{k}_{eq} + 0.125C_r^4\hat{k}_{eq}^2 - 0.125\alpha_1 C_r^4\hat{k}_{eq}^2 - 0.25\alpha_2 C_r^4\hat{k}_{eq}^2 \\
&\quad + 0.375\gamma C_r^2\hat{k}_{eq} - 0.25\gamma\alpha_1 C_r^2\hat{k}_{eq} - 0.25\gamma\alpha_2 C_r^2\hat{k}_{eq} + 0.25\alpha_1\alpha_2 C_r^4\hat{k}_{eq}^2,
\end{aligned}$$

$$\begin{aligned}
e_4 &= 4\alpha_1^2\alpha_2^2 C_r^8\hat{k}_{eq}^4 - 4\alpha_1^2\alpha_2 C_r^8\hat{k}_{eq}^4 + \alpha_1^2 C_r^8\hat{k}_{eq}^4 - 8\alpha_1\alpha_2^2 C_r^8\hat{k}_{eq}^4 + 8\alpha_1\alpha_2 C_r^8\hat{k}_{eq}^4 - 2\alpha_1 C_r^8\hat{k}_{eq}^4 \\
&\quad + 4\alpha_2^2 C_r^8\hat{k}_{eq}^4 - 4\alpha_2 C_r^8\hat{k}_{eq}^4 + C_r^8\hat{k}_{eq}^4 - 8\gamma\alpha_1^2\alpha_2 C_r^6\hat{k}_{eq}^3 + 4\gamma\alpha_1^2 C_r^6\hat{k}_{eq}^3 - 8\gamma\alpha_1\alpha_2^2 C_r^6\hat{k}_{eq}^3 \\
&\quad + 24\gamma\alpha_1\alpha_2 C_r^6\hat{k}_{eq}^3 - 10\gamma\alpha_1 C_r^6\hat{k}_{eq}^3 + 8\gamma\alpha_2^2 C_r^6\hat{k}_{eq}^3 - 16\gamma\alpha_2 C_r^6\hat{k}_{eq}^3 - 16\alpha_1\alpha_2 C_r^6\hat{k}_{eq}^3 \\
&\quad + 6\gamma C_r^6\hat{k}_{eq}^3 + 8\alpha_1 C_r^6\hat{k}_{eq}^3 + 16\alpha_2 C_r^6\hat{k}_{eq}^3 - 8C_r^6\hat{k}_{eq}^3 + 4\gamma^2\alpha_1^2 C_r^4\hat{k}_{eq}^2 - 16\gamma^2\alpha_1 C_r^4\hat{k}_{eq}^2 \\
&\quad + 16\gamma^2\alpha_1\alpha_2 C_r^4\hat{k}_{eq}^2 + 4\gamma^2\alpha_2^2 C_r^4\hat{k}_{eq}^2 - 20\gamma^2\alpha_2 C_r^4\hat{k}_{eq}^2 + 13\gamma^2 C_r^4\hat{k}_{eq}^2 - 16\gamma\alpha_1\alpha_2 C_r^4\hat{k}_{eq}^2 \\
&\quad + 24\gamma\alpha_1 C_r^4\hat{k}_{eq}^2 + 32\gamma\alpha_2 C_r^4\hat{k}_{eq}^2 - 32\gamma C_r^4\hat{k}_{eq}^2 - 32\alpha_1 C_r^4\hat{k}_{eq}^2 - 32\alpha_2 C_r^4\hat{k}_{eq}^2 + 48C_r^4\hat{k}_{eq}^2 \\
&\quad - 8\gamma^3\alpha_1 C_r^2\hat{k}_{eq} - 8\gamma^3\alpha_2 C_r^2\hat{k}_{eq} + 12\gamma^3 C_r^2\hat{k}_{eq} + 16\gamma^2\alpha_1 C_r^2\hat{k}_{eq} + 16\gamma^2\alpha_2 C_r^2\hat{k}_{eq} \\
&\quad - 40\gamma^2 C_r^2\hat{k}_{eq} + 64\gamma C_r^2\hat{k}_{eq} - 64C_r^2\hat{k}_{eq} + 4\gamma^4 - 16\gamma^3 + 16\gamma^2
\end{aligned}$$

where $\hat{k}_{eq} = \phi(k\Delta x)$ represents equivalent nondimensional wavenumber given as in Eq. (5.2.15) and for wave-like solution, it follows from Eq. (5.2.24) that $e_4 < 0$.

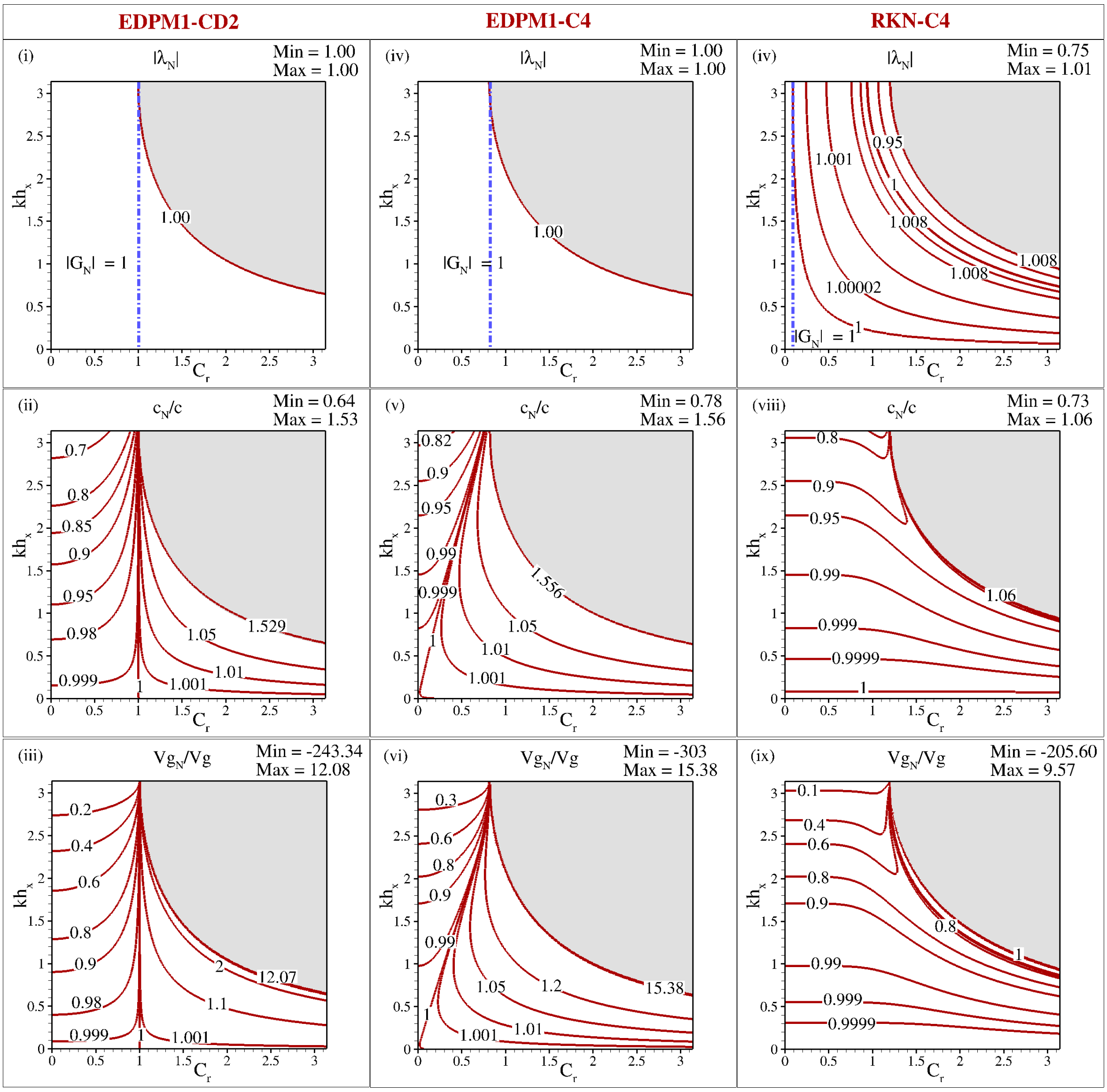

Figure 5.1(a): Contour plots showing $|\lambda_N|$, c_N/c, and V_{gN}/V_g for one-dimensional undamped wave equation given in Eq. (5.2.1) (with $a = 0$) using indicated schemes. In the top frames, vertical dash-dotted line indicate the values of CFL numbers up to which methods are (neutrally) stable and the shaded area represents the corresponding non-hyperbolic region. For the EDPM1 method, the value of free parameter is chosen as, $\alpha = 0.00015$.

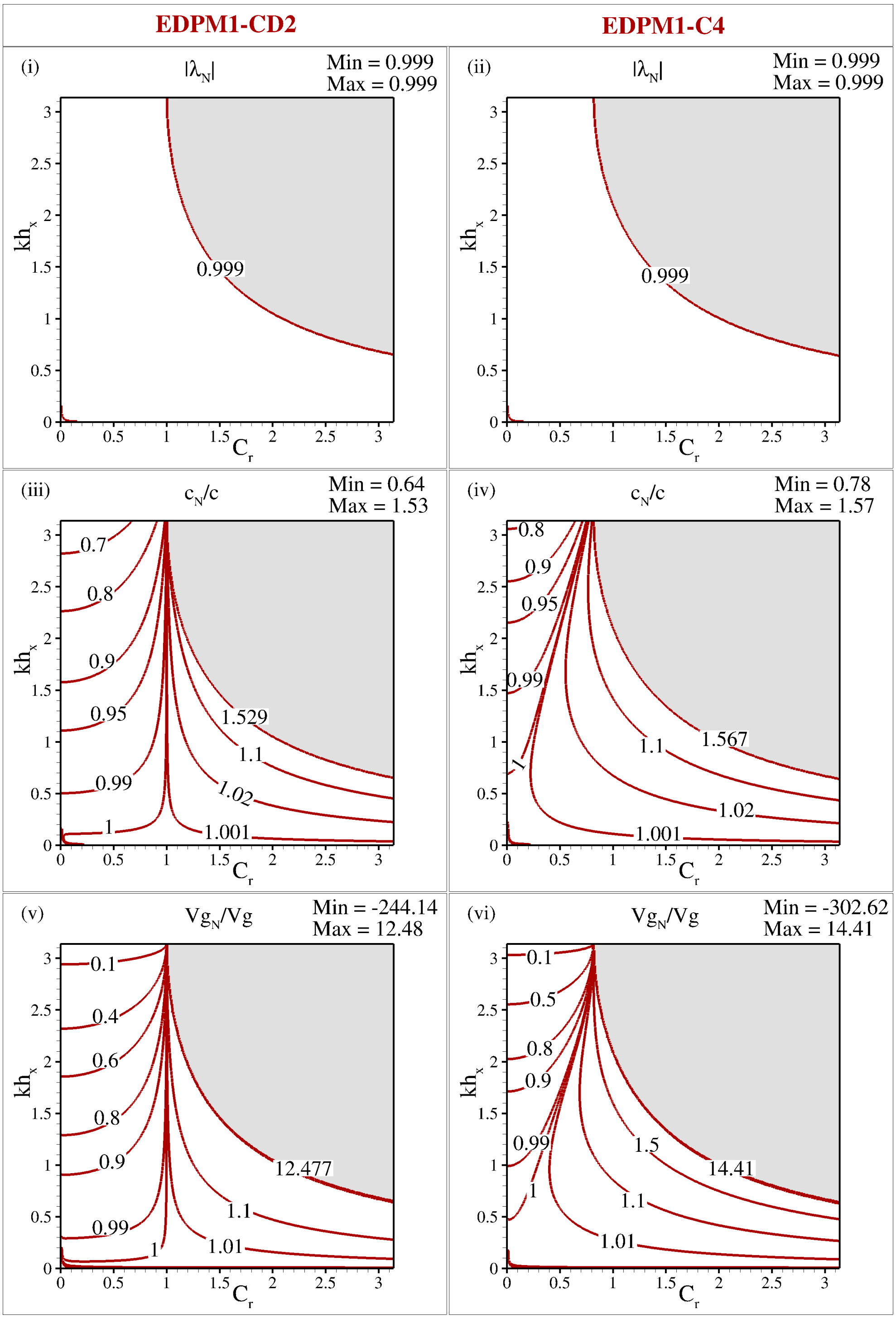

Figure 5.1(b): Contour plots showing $|\lambda_N|$, c_N/c, and V_{gN}/V_g for one-dimensional damped wave equation given in Eq. (5.2.1) with damping coefficient $\tilde{\gamma} = a\Delta t = 0.002$ using indicated schemes. Here, the value of free parameter is chosen as, $\alpha = 0.00015$.

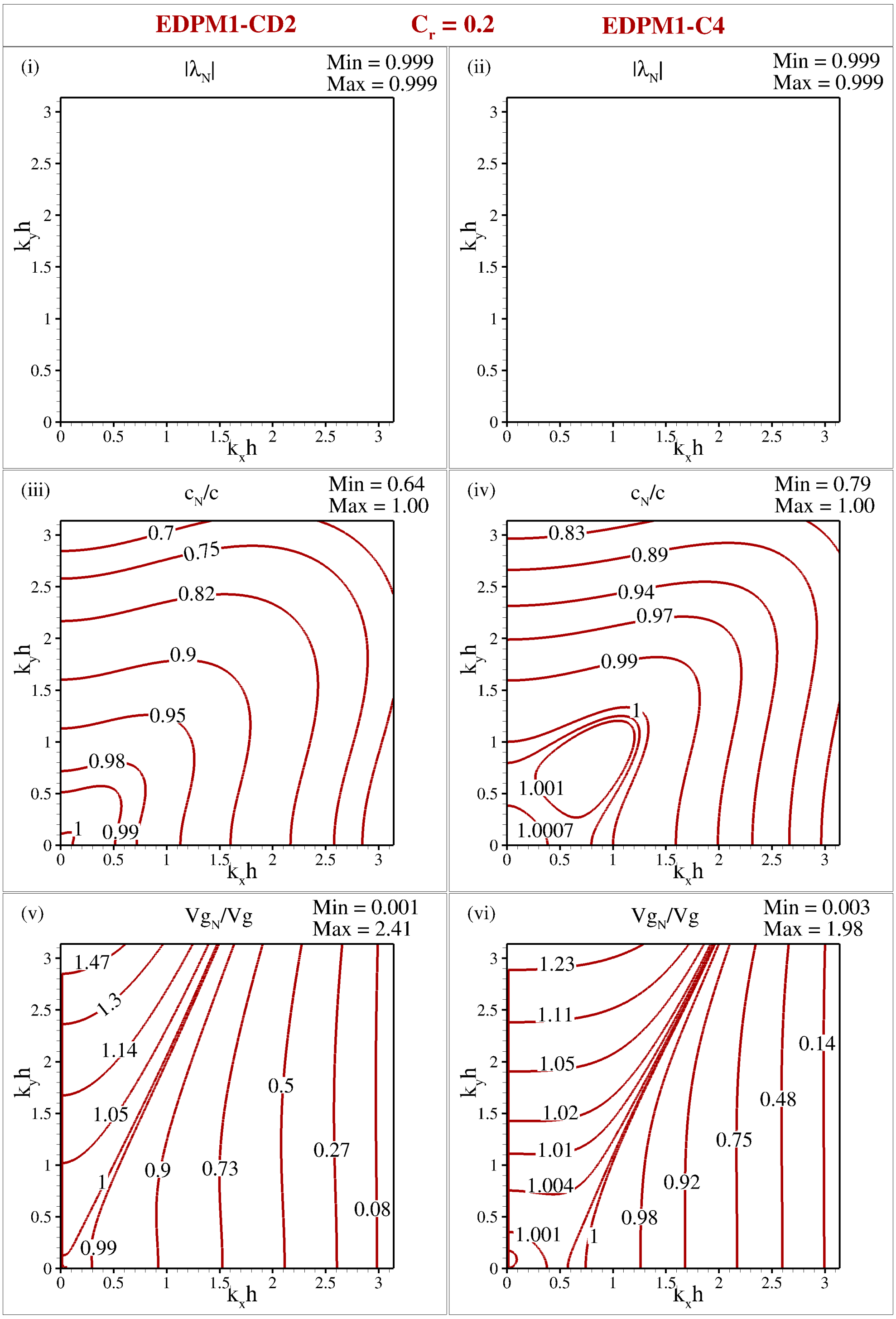

Figure 5.1(c): Contour plots showing $|\lambda_N|$, c_N/c, and V_{gN}/V_g for two-dimensional damped wave equation given in Eq. (5.2.16) with damping coefficient $\tilde{\gamma} = a\Delta t = 0.002$ and $C_r = 0.2$ using indicated schemes. Here, value of free-parameter is chosen as, $\alpha = 0.00015$.

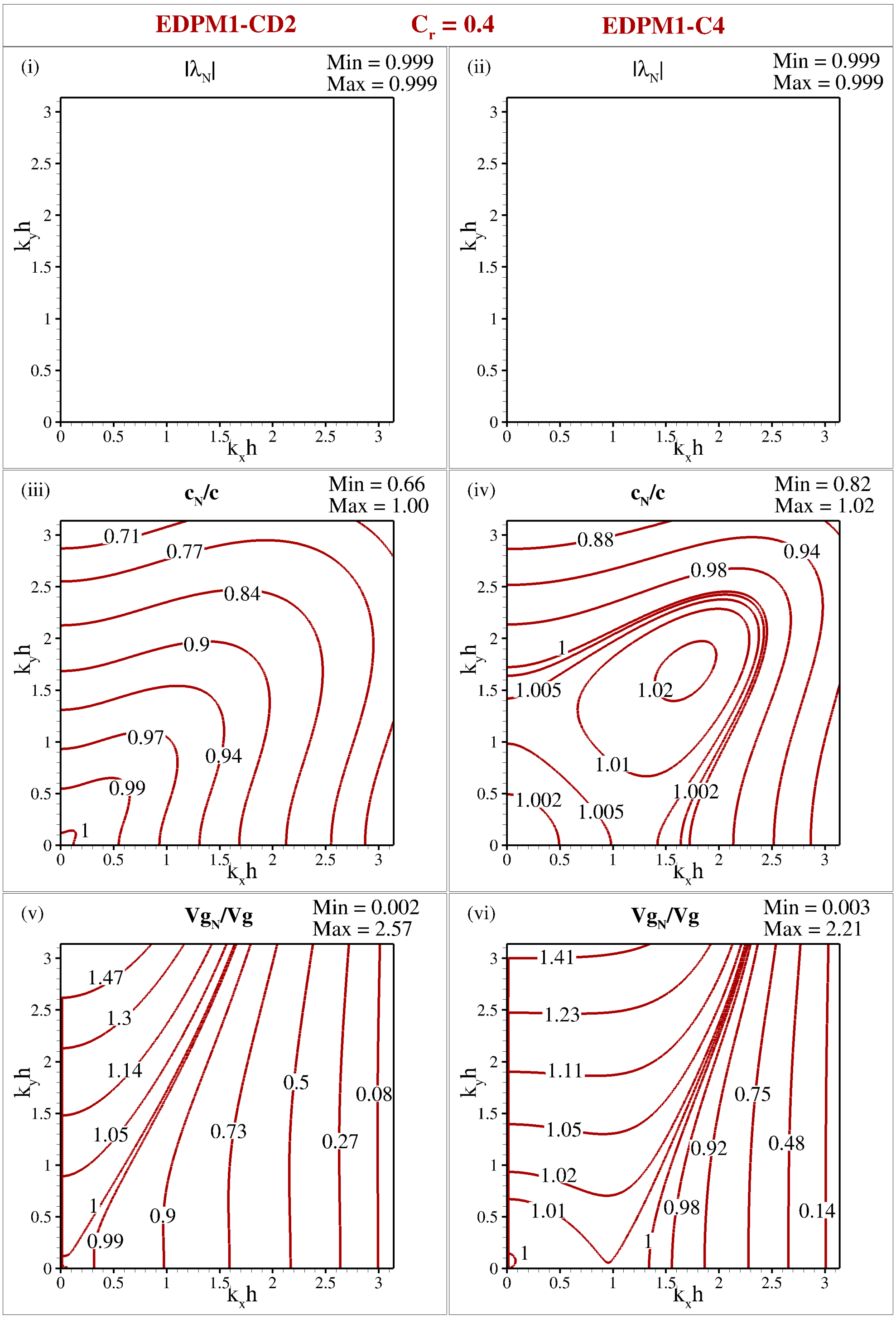

Figure 5.1(d): Contour plots showing $|\lambda_N|$, c_N/c, and V_{gN}/V_g for two-dimensional damped wave equation given in Eq. (5.2.16) with damping coefficient $\tilde{\gamma} = a\Delta t = 0.002$ and $C_r = 0.4$ using indicated schemes. Here, value of free-parameter is chosen as, $\alpha = 0.00015$.

5.2.1 Optimization problem

In order to determine the optimal value of free parameter, an optimization problem [120] is considered. The objective function is chosen as

$$\Psi(\alpha, C_r) = \int_0^{\rho} |\lambda_N - \lambda_{phy}|^2 d(kh) \tag{5.2.25}$$

where λ_N is the numerical amplification factor and $\lambda_{\text{exact}} = e^{iC_r k\Delta x}$ is the exact amplification factor. Constraints are given as,

$$\begin{aligned} \psi_1(\alpha, C_r) &= \int_0^{\rho_1} \Big||\lambda_N| - 1\Big| d(kh) \leq \epsilon_1 \\ \psi_2(\alpha, C_r) &= \int_0^{\rho_2} \left|\left(\frac{V_{g_N}}{c}\right) - 1\right| d(kh) \leq \epsilon_2 \\ \psi_3(\alpha, C_r) &= \int_0^{\rho_3} \left|\left(\frac{c_N}{c}\right) - 1\right| d(kh) \leq \epsilon_3 \end{aligned} \tag{5.2.26}$$

here, ρ_i and ϵ_i are the admissible error tolerances. Following the approach outlined in [134], the values of ϵ_i are chosen. This process systematically explores the parameter space while maintaining C_r fixed at an arbitrary constant. By applying the constraints from Ineq. (5.2.26), the optimization problem, as defined by Eq. (5.2.25) and Ineq. (5.2.26), is converted into a Pareto front optimization problem. As a result, the optimal values of free parameter α for one-dimensional undamped and damped wave equations, are presented in Tables 5.1 and Table 5.2, respectively. Optimal values of free parameter α for two-dimensional damped wave equation are listed in Table 5.3.

5.3 Convergence analysis

Convergence analysis of the discrete system is established following the analysis outlined in [106]. Assume, $\Lambda_h^p = \{U | U = (U_{i,j} | (x_i, y_j) \in \Omega_h^E)\}$ represent the space of periodic mesh functions. For any $W, U \in \Lambda_h^p$ grid functions, the inner-product and discrete norms are given by

$$\begin{gathered} \langle W, U \rangle = \sum_{i=1}^{N_x} \sum_{j=1}^{N_y} \Delta x \Delta y W_{i,j} U_{i,j}, \quad ||W||^2 = \langle W, W \rangle \\ ||\Gamma_x^+ U||^2 = \left\langle \Gamma_x^+ U, \Gamma_x^+ U \right\rangle, \quad ||\Gamma_y^+ U||^2 = \left\langle \Gamma_y^+ U, \Gamma_y^+ U \right\rangle \end{gathered}$$

Table 5.1: Optimal values of free parameter α for the system given in Eq. (5.2.11) for one-dimensional undamped ($a = 0$) wave equation using the EDPM1-CD2 and EDPM1-C4 schemes.

	EDPM1 - CD2				EDPM1 - C4			
α	Min($\lvert\lambda_N\rvert$)	Max($\lvert\lambda_N\rvert$)	$(C_r)_{crit}$	$(C_r)_{max}$	Min($\lvert\lambda_N\rvert$)	Max($\lvert\lambda_N\rvert$)	$(C_r)_{crit}$	$(C_r)_{max}$
0.01000	1.00000	1.02020	1.01010	0.15000	1.00000	1.02020	0.82470	0.12910
0.00100	1.00000	1.00200	1.00100	0.50001	1.00000	1.00200	0.81730	0.40000
0.00015	**1.00000**	**1.00000**	**1.00400**	**1.00400**	**1.00000**	**1.00000**	**0.81660**	**0.81660**
-0.01000	0.98020	1.00000	0.99000	0.99000	0.98020	1.00000	0.80840	0.80840
-0.10000	0.81830	1.00000	0.90890	0.90890	0.81820	1.00000	0.74220	0.74220
-0.25000	0.60010	1.00000	0.79990	0.79990	0.60020	1.00000	0.65310	0.65310

Table 5.2: Optimal values of free parameter α for the system given in Eq. (5.2.11) for one-dimensional damped wave equation using the EDPM1-CD2 and EDPM1-C4 schemes with $\tilde{\gamma} = a\Delta t = 0.002$

	EDPM1 - CD2				EDPM1 - C4			
α	Min($\lvert\lambda_N\rvert$)	Max($\lvert\lambda_N\rvert$)	$(C_r)_{crit}$	$(C_r)_{max}$	Min($\lvert\lambda_N\rvert$)	Max($\lvert\lambda_N\rvert$)	$(C_r)_{crit}$	$(C_r)_{max}$
0.01000	0.99900	1.01920	1.00900	0.27380	0.99900	1.01920	0.82430	0.22350
0.00100	0.99900	1.00100	1.00010	0.86000	0.99900	1.00100	0.81690	0.70710
0.00015	**0.99900**	**0.99900**	**0.99960**	**0.99960**	**0.99900**	**0.99900**	**0.81620**	**0.81620**
-0.01000	0.97920	0.99900	0.98950	0.98950	0.97920	0.99900	0.80800	0.80800
-0.10000	0.81720	0.99900	0.90850	0.90850	0.81730	0.99900	0.74170	0.74170
-0.25000	0.59980	0.99900	0.79890	0.79890	0.59910	0.99900	0.65270	0.65270

Moreover, for symmetric positive definite matrices, P_x and P_y, the discrete norms are defined as

$$||U||_{P_x}^2 = \langle P_x U, U\rangle\,, \quad ||U||_{P_y}^2 = \langle P_y U, U\rangle \tag{5.3.1}$$

Lemma 5.3.1. *Matrices P_x and P_y satisfies the following inequalities*

$$1 \leq ||P_x|| \leq \frac{3}{2}, \quad 1 \leq ||P_y|| \leq \frac{3}{2} \tag{5.3.2}$$

and

Table 5.3: Optimal values of free parameter α for the system given in Eq. (5.2.18) for two-dimensional damped wave equation using the EDPM1-CD2 and EDPM1-C4 schemes with $\tilde{\gamma} = a\Delta t = 0.002$

	EDPM1 - CD2				EDPM1 - C4			
α	Min($\lvert\lambda_N\rvert$)	Max($\lvert\lambda_N\rvert$)	$(C_r)_{crit}$	$(C_r)_{max}$	Min($\lvert\lambda_N\rvert$)	Max($\lvert\lambda_N\rvert$)	$(C_r)_{crit}$	$(C_r)_{max}$
0.01000	0.99900	1.01920	0.71380	0.19360	0.99900	1.01920	0.58280	0.15820
0.00100	0.99900	1.00100	0.70740	0.61230	0.99900	1.00100	0.57760	0.50000
0.00015	**0.99900**	**0.99900**	**0.70680**	**0.70680**	**0.99900**	**0.99900**	**0.57710**	**0.57710**
-0.01000	0.97920	0.99900	0.69970	0.69970	0.97920	0.99900	0.57130	0.57130
-0.10000	0.81720	0.99900	0.64240	0.64240	0.81720	0.99900	0.52450	0.52450
-0.25000	0.59910	0.99900	0.56530	0.56530	0.59920	0.99900	0.46150	0.46150

Table 5.4: Optimal values of free parameter α_1 and α_2 for the system given in Eq. (5.2.11) for one-dimensional damped wave equation using the EDPM2-CD2 and EDPM2-C4 schemes with $\gamma = a\Delta t = 0.002$.

		EDPM2 - CD2				EDPM2 - C4			
α_1	α_2	Min($\lvert\lambda_N\rvert$)	Max($\lvert\lambda_N\rvert$)	$(C_r)_{crit}$	$(C_r)_{max}$	Min($\lvert\lambda_N\rvert$)	Max($\lvert\lambda_N\rvert$)	$(C_r)_{crit}$	$(C_r)_{max}$
0.45000	0.50000	0.81636	0.99900	0.94851	0.94851	0.81642	0.99900	0.77244	0.77244
0.50000	0.50000	0.99800	0.99900	1.00130	1.00136	0.99800	0.99900	0.81206	0.81206
0.51930	0.46000	0.99163	0.99900	1.01897	1.01897	0.99163	0.99900	0.82967	0.82967
0.51930	**0.46370**	**0.99887**	**0.99993**	**1.02337**	**1.02337**	**0.99887**	**0.99993**	**0.82967**	**0.82967**
0.52000	0.46370	0.99894	1.00285	0.76801	1.02337	0.99894	1.00285	0.62716	0.83407
0.51930	0.47000	0.99898	1.01393	0.54351	1.01457	0.99898	1.01393	0.44226	0.82527

$$||U||^2 \leq ||U||^2_{P_x} \leq \frac{3}{2}||U||^2, \quad ||U||^2 \leq ||U||^2_{P_y} \leq \frac{3}{2}||U||^2 \tag{5.3.3}$$

and matrix $\mathcal{A}_x$ satisfy the inequality

$$\frac{2}{3} \leq ||\mathcal{A}_x|| \leq 1 \tag{5.3.4}$$

Proof. Utilizing the properties of circulant matrices, which assert that the eigenvalues of

$\mathcal{A}_x$ have the following form

$$\chi_j = \frac{10}{12} + \frac{1}{12}e^{-2\pi ij/N_x} + \frac{1}{12}e^{2\pi ij/N_x}, \quad j = 0, 1, 2, \ldots, N_x - 1. \tag{5.3.5}$$

Hence, we can obtain $\frac{2}{3} \leq \chi_j \leq 1$. This results in $\frac{2}{3} \leq ||\mathcal{A}_x|| \leq 1$. The eigenvalues of P_x satisfy $1 \leq \mu_i \leq \frac{3}{2}, i = 1, 2, \ldots, N_x \times N_y$, and as a result, $1 \leq ||P_x|| \leq \frac{3}{2}$. Similarly, $1 \leq ||P_y|| \leq \frac{3}{2}$. This is demonstrated by the characteristics of Kronecker product and inverse matrix. Furthermore, it follows that $||U||^2 \leq (P_x U, U) \leq ||P_x|| ||U||^2 \leq \frac{3}{2}||U||^2$. □

Lemma 5.3.2. *Let $W, U \in \Lambda_h^p$ be given mesh-function, then it follows that*

$$(\Gamma_x^+ \Gamma_x^- W, U) = -(\Gamma_x^+ W, \Gamma_x^+ U) \tag{5.3.6}$$

Lemma 5.3.3. *Matrices pairs P_x and Γ_x^+, P_x and Γ_x^-, P_y and Γ_y^+, P_y and Γ_y^- are commutative, i.e.*

$$\begin{aligned} P_x\Gamma_x^+ &= \Gamma_x^+ P_x, \quad P_x\Gamma_x^- = \Gamma_x^- P_x \\ P_y\Gamma_y^+ &= \Gamma_y^+ P_y, \quad P_y\Gamma_y^- = \Gamma_y^- P_y \end{aligned} \tag{5.3.7}$$

Lemma 5.3.4. *For the diagonal matrix C and Q, we have $c_1 \leq ||C|| \leq c_2$ and $\frac{1}{c_2} \leq ||Q|| \leq \frac{1}{c_1}$, where $0 < c_1 = \min_{(x,y)\in\Omega} |c(x, y)|$, $0 < c_2 = \max_{(x,y)\in\Omega} |c(x, y)|$.*

Lemma 5.3.5. *For functions $f_1 \in C^1(\Omega)$ and $f_2 \in C^2(\Omega)$, it holds that*

$$||D_x^+ f_1|| \leq \mathcal{K}, ||D_y^+ f_1|| \leq \mathcal{K}, ||D_x^+ D_x^- f_2|| \leq \mathcal{K}, ||D_y^+ D_y^- f_2|| \leq \mathcal{K}$$

Remark 5.3.1. *The above lemmas are proven in [106].*

Next, we discuss the convergence analysis of the fully discretized system. The equations for the system in Eq. (5.1.12) after full discretization are given by

$$\begin{aligned} \frac{W^{n+1} - W^n}{\Delta t} &= MU^n + Q^2 F_U^n \\ \frac{U^{n+1} - U^n}{\Delta t} &= -aU^n + C^2((1-\alpha)W^{n+1} + \alpha W^n) \end{aligned} \tag{5.3.8}$$

By substituting the exact solutions w and u, Eq. (5.3.8) can be rewritten in terms local truncation errors, as

$$\frac{w^{n+1}-w^n}{\Delta t} = Mu^n + Q^2F_u^n + \mathfrak{R}^{n+1} \tag{5.3.9}$$

$$\frac{u^{n+1}-u^n}{\Delta t} = -au^n + C^2((1-\alpha)w^{n+1} + \alpha w^n) + \tilde{\mathfrak{R}}^{n+1} \tag{5.3.10}$$

where $\mathfrak{R}^{n+1}$ and $\tilde{\mathfrak{R}}^{n+1}$ are the local truncation error vectors.

Lemma 5.3.6. *Let $\{w, v\}$ be the sufficiently smooth solution of Eq. (5.1.3), then we have the following truncation error estimates*

$$||\mathfrak{R}^{n+1}|| \leq \mathcal{K}(\Delta t + \Delta x^4 + \Delta y^4) \tag{5.3.11}$$

$$||\tilde{\mathfrak{R}}^{n+1}|| \leq \mathcal{K}(\Delta t) \tag{5.3.12}$$

Proof. Using Taylor series expansion, it follows that

$$\frac{w^{n+1}-w^n}{\Delta t} = \frac{\partial w}{\partial t} + \frac{\Delta t}{2}\frac{\partial^2 w}{\partial t^2} + \mathcal{O}(\Delta t^2) \tag{5.3.13}$$

And from Eq. (5.1.9), we have

$$Mu^n = \left(\frac{\partial^2 u}{\partial x^2} + \frac{\partial^2 u}{\partial y^2}\right)^n - \mathcal{O}(\Delta y^4 + \Delta y^4) \tag{5.3.14}$$

Thus, Eq. (5.3.9) can be rewritten as

$$\mathfrak{R}^{n+1} = \frac{w^{n+1}-w^n}{\Delta t} - Mu^n - Q^2F_u^n$$

Using Eqs. (5.3.13), (5.3.14) and (5.1.3), it follows that

$$||\mathfrak{R}^{n+1}|| \leq \mathcal{K}(\Delta t + \Delta x^4 + \Delta y^4) \tag{5.3.15}$$

Next, Eq. (5.3.10) gives

$$\tilde{\mathfrak{R}}^{n+1} = \frac{u^{n+1}-u^n}{\Delta t} + au^n - C^2(\alpha w^n + (1-\alpha)w^{n+1})$$

Using Taylor series expansion, it follows that

$$\begin{aligned}\tilde{\mathfrak{R}}^{n+1} &= \frac{\partial u}{\partial t} + \frac{\Delta t}{2}\frac{\partial^2 u}{\partial t^2} + \mathcal{O}(\Delta t^2) + au^n \\ &\quad -C^2\left(\alpha w^n + (1-\alpha)\left(w^n + \Delta t\frac{\partial w}{\partial t} + \frac{\Delta t^2}{2}\frac{\partial^2 w}{\partial t^2} + \mathcal{O}(\Delta t^3)\right)\right)\end{aligned}$$

Using Eq. (5.1.3), we obtain

$$||\tilde{\mathfrak{R}}^{n+1}|| \leq \mathcal{K}(\Delta t) \tag{5.3.16}$$

This completes the proof. □

Theorem 5.3.7. *Let $\{W, U\}$ be the numerical solution of the system described by Eq. (5.1.12) using the EDPM1-C4 scheme, and let $\{w, u\}$ represent the sufficiently smooth closed-form solution of Eq. (5.1.3). Then, there exists a constant $\mathcal{K} > 0$, independent of $\Delta x, \Delta y$, and Δt, which satisfies*

$$||w^n - W^n|| + ||u^n - U^n|| \leq \mathcal{K}(\Delta t + \Delta x^4 + \Delta y^4). \tag{5.3.17}$$

Proof. Let $\varphi^n_{i,j} = w^n_{i,j} - W^n_{i,j}, \zeta^n_{i,j} = u^n_{i,j} - U^n_{i,j}$ denote the solution errors. Subtracting system of equations given in Eq. (5.3.8) from Eqs. (5.3.9) and (5.3.10) give the following error equations, as

$$\frac{\varphi^{n+1} - \varphi^n}{\Delta t} = M\zeta^n + Q^2(F^n_u - F^n_U) + \mathfrak{R}^{n+1} \tag{5.3.18}$$

$$\frac{\zeta^{n+1} - \zeta^n}{\Delta t} = -a\zeta^n + C^2(\alpha\varphi^n + (1-\alpha)\varphi^{n+1}) + \tilde{\mathfrak{R}}^{n+1} \tag{5.3.19}$$

with $\varphi^0 = 0, \zeta^0 = 0$. Applying the inner product to each term of Eq. (5.3.19) with $(\zeta^{n+1} + \zeta^n)$ gives

$$\begin{aligned}\left\langle \frac{\zeta^{n+1} - \zeta^n}{\Delta t}, \zeta^{n+1} + \zeta^n \right\rangle &= \langle -a\zeta^n, \zeta^{n+1} + \zeta^n\rangle + \langle \alpha C^2\varphi^n, \zeta^{n+1} + \zeta^n\rangle \\ &\quad + \langle (1-\alpha)C^2\varphi^{n+1}, \zeta^{n+1} + \zeta^n\rangle + \left\langle \tilde{\mathfrak{R}}^{n+1}, \zeta^{n+1} + \zeta^n\right\rangle \\ &= \mathfrak{S}_1 + \mathfrak{S}_2 + \mathfrak{S}_3 + \mathfrak{S}_4 \end{aligned} \tag{5.3.20}$$

Here

$$\left\langle \frac{\zeta^{n+1} - \zeta^n}{\Delta t}, \zeta^{n+1} + \zeta^n \right\rangle = \frac{1}{\Delta t}(||\zeta^{n+1}||^2 - ||\zeta^n||^2) \tag{5.3.21}$$

$$\mathfrak{S}_1 = \left\langle -a\zeta^n, \zeta^{n+1} + \zeta^n \right\rangle \quad \leq \quad \frac{a^2}{2}||\zeta^n||^2 + ||\zeta^{n+1}||^2 + ||\zeta^n||^2 \tag{5.3.22}$$

$$\mathfrak{S}_2 = \left\langle \alpha C^2\varphi^n, \zeta^{n+1} + \zeta^n \right\rangle \quad \leq \quad \frac{\alpha^2}{2}||C^2\varphi^n||^2 + ||\zeta^{n+1}||^2 + ||\zeta^n||^2 \tag{5.3.23}$$

$$\mathfrak{S}_3 = \left\langle (1-\alpha)C^2\varphi^{n+1}, \zeta^{n+1} + \zeta^n \right\rangle \leq \frac{(1-\alpha)^2}{2}||C^2\varphi^{n+1}||^2 + ||\zeta^{n+1}||^2 + ||\zeta^n||^2 \tag{5.3.24}$$

$$\mathfrak{S}_4 = \left\langle \tilde{\mathfrak{R}}^{n+1}, \zeta^{n+1} + \zeta^n \right\rangle \quad \leq \quad \frac{||\tilde{\mathfrak{R}}^{n+1}||^2}{2} + ||\zeta^{n+1}||^2 + ||\zeta^n||^2 \tag{5.3.25}$$

Using Eq. (5.3.21) and Ineqs. (5.3.22)-(5.3.25), Eq. (5.3.20) gives

$$\begin{aligned}
\frac{1}{\Delta t}(||\zeta^{n+1}||^2 - ||\zeta^n||^2) \quad \leq \quad & \frac{a^2}{2}||\zeta^n||^2 + ||\zeta^{n+1}||^2 + ||\zeta^n||^2 \\
& + \frac{\alpha^2}{2}||C^2\varphi^n||^2 + ||\zeta^{n+1}||^2 + ||\zeta^n||^2 \\
& + \frac{(1-\alpha)^2}{2}||C^2\varphi^{n+1}||^2 + ||\zeta^{n+1}||^2 + ||\zeta^n||^2 \\
& + \frac{1}{2}||\tilde{\mathfrak{R}}^{n+1}||^2 + ||\zeta^{n+1}||^2 + ||\zeta^n||^2
\end{aligned}$$

$$\begin{aligned}
\frac{1}{\Delta t}(||\zeta^{n+1}||^2 - ||\zeta^n||^2) \quad \leq \quad & 4\left(||\zeta^n||^2 + ||\zeta^{n+1}||^2\right) + \frac{\alpha^2}{2}||C^2\varphi^n||^2 + \frac{a^2}{2}||\zeta^n||^2 \\
& + \frac{(1-\alpha)^2}{2}||C^2\varphi^{n+1}||^2 + \frac{1}{2}||\tilde{\mathfrak{R}}^{n+1}||^2
\end{aligned} \tag{5.3.26}$$

Similarly, applying the inner product to each term of Eq. (5.3.18) with $(\varphi^{n+1} + \varphi^n)$ gives

$$\begin{aligned}
\left\langle \frac{\varphi^{n+1} - \varphi^n}{\Delta t}, \varphi^{n+1} + \varphi^n \right\rangle \quad = \quad & \left\langle M\zeta^n, \varphi^{n+1} + \varphi^n \right\rangle + \left\langle \mathfrak{R}^{n+1}, \varphi^{n+1} + \varphi^n \right\rangle \\
& + \left\langle B^2(F_u^n - F_U^n), \varphi^{n+1} + \varphi^n \right\rangle \\
= \quad & \mathfrak{T}_1 + \mathfrak{T}_2 + \mathfrak{T}_3
\end{aligned} \tag{5.3.27}$$

$$\left\langle \frac{\varphi^{n+1} - \varphi^n}{\Delta t}, \varphi^{n+1} + \varphi^n \right\rangle \quad = \quad \frac{1}{\Delta t}(||\varphi^{n+1}||^2 - ||\varphi^n||^2) \tag{5.3.28}$$

$$\mathfrak{T}_1 = \left\langle M\zeta^n, \varphi^{n+1} + \varphi^n \right\rangle \quad \leq \quad \frac{1}{2}||M\zeta^n||^2 + ||\varphi^{n+1}||^2 + ||\varphi^n||^2 \tag{5.3.29}$$

Using the definition of M and Lemmas 5.3.1 - 5.3.2, it follows that

$$\mathfrak{T}_1 \leq \frac{9}{8}(||\Gamma_x^+\Gamma_x^-\zeta^n||^2 + ||\Gamma_y^+\Gamma_y^-\zeta^n||^2) + ||\varphi^{n+1}||^2 + ||\varphi^n||^2 \tag{5.3.30}$$

$$\mathfrak{T}_2 = \left\langle \mathfrak{R}^{n+1}, \varphi^{n+1} + \varphi^n \right\rangle \leq \frac{1}{2}||\mathfrak{R}^{n+1}||^2 + ||\varphi^{n+1}||^2 + ||\varphi^n||^2 \tag{5.3.31}$$

$$\mathfrak{T}_3 = \left\langle Q^2(F_u^n - F_U^n), \varphi^{n+1} + \varphi^n \right\rangle \leq \frac{1}{2}||Q^2\hat{F}^n||^2 + ||\varphi^{n+1}||^2 + ||\varphi^n||^2$$

where $\hat{F}^n = F_u^n - F_U^n$. Using condition given in Ineq. (5.1.2), it follows that

$$\mathfrak{T}_3 \leq \frac{1}{2}||Q^2||^2L^2||\zeta^n||^2 + ||\varphi^{n+1}||^2 + ||\varphi^n||^2 \tag{5.3.32}$$

Combining estimates given in Eq. (5.3.28) and Ineqs. (5.3.29)-(5.3.32), it follows from Eq. (5.3.27) that

$$\begin{aligned}\frac{1}{\Delta t}(||\varphi^{n+1}||^2 - ||\varphi^n||^2) \leq\ & 3(||\varphi^{n+1}||^2 + ||\varphi^n||^2) + \frac{9}{8}(||\Gamma_x^+\Gamma_x^-\zeta^n||^2 + ||\Gamma_y^+\Gamma_y^-\zeta^n||^2) \\ & + \frac{1}{2}||\mathfrak{R}^{n+1}||^2 + \frac{1}{2}||Q^2||^2L^2||\zeta^n||^2\end{aligned} \tag{5.3.33}$$

Adding the estimates given in Ineqs. (5.3.26) and (5.3.33) and using Lemma 5.3.4, it follows that

$$\begin{aligned}\frac{1}{\Delta t}(||\varphi^{n+1}||^2 - ||\varphi^n||^2) + \frac{1}{\Delta t}(||\zeta^{n+1}||^2 - ||\zeta^n||^2) \leq 3(||\varphi^{n+1}||^2 + ||\varphi^n||^2) \\ +4\left(||\zeta^n||^2 + ||\zeta^{n+1}||^2\right) + \frac{9}{8}(||\Gamma_x^+\Gamma_x^-\zeta^n||^2 + ||\Gamma_y^+\Gamma_y^-\zeta^n||^2) + \frac{\alpha^2}{2}c_2^4||\varphi^n||^2 \\ +\frac{1}{2c_1^4}L^2||\zeta^n||^2 + \frac{(1-\alpha)^2}{2}c_2^4||\varphi^{n+1}||^2 + \frac{1}{2}||\tilde{\mathfrak{R}}^{n+1}||^2 + \frac{1}{2}||\mathfrak{R}^{n+1}||^2\end{aligned}$$

$$\begin{aligned}\frac{1}{\Delta t}(||\varphi^{n+1}||^2 - ||\varphi^n||^2 + ||\zeta^{n+1}||^2 - ||\zeta^n||^2) \leq \mathcal{K}(||\varphi^{n+1}||^2 + ||\varphi^n||^2 + ||\zeta^n||^2 + ||\zeta^{n+1}||^2 \\ +||\Gamma_x^+\Gamma_x^-\zeta^n||^2 + ||\Gamma_y^+\Gamma_y^-\zeta^n||^2) + \frac{1}{2}||\tilde{\mathfrak{R}}^{n+1}||^2 + \frac{1}{2}||\mathfrak{R}^{n+1}||^2\end{aligned} \tag{5.3.34}$$

Multiplying Ineq. (5.3.34) by Δt and summing the resulting equation from $n = 0$ to $m-1$ and utilizing with initial conditions $\varphi^0 = 0$ and $\zeta^0 = 0$, it follows that

$$||\varphi^m||^2 + ||\zeta^m||^2 \leq \mathcal{K}\Delta t \sum_{i=1}^{m} (||\varphi^i||^2 + ||\zeta^i||^2 + ||\Gamma_x^+ \Gamma_x^- \zeta^i||^2 + ||\Gamma_y^+ \Gamma_y^- \zeta^i||^2) + \Delta t \sum_{i=0}^{m-1} \left(\frac{1}{2} ||\mathfrak{R}^{i+1}||^2 + \frac{1}{2} ||\tilde{\mathfrak{R}}^{i+1}||^2 \right) \quad (5.3.35)$$

Using Grönwall's inequality, we obtain (5.3.17). □

5.4 Numerical simulations: Linear damped wave equations

Next, we have considered the simulations of the one-dimensional damped wave equation, given as

$$\frac{\partial^2 u}{\partial t^2} + a \frac{\partial u}{\partial t} = c^2 \frac{\partial^2 u}{\partial x^2}, \quad t \in [0, 1],\ x \in [0, \pi] \quad (5.4.1)$$

with initial conditions given as

$$u(x, 0) = \sin(x), \quad \frac{\partial u}{\partial t}(x, 0) = -\sin(x) \quad (5.4.2)$$

The analytic solution for the Eq. (5.4.1) with initial data described by Eq. (5.4.2) is given by $u(x, t) = e^{-t} \sin(x)$. For numerical simulations, we have used the EDPM1-CD2 and EDPM1-C4 schemes with $c^2 = 1$, $a = 2$, and $\Delta x = \pi/6, \pi/12, \pi/24, \pi/48$. The value of the free parameter is taken as $\alpha = 0.00015$. The time-step for the EDPM1-CD2 is chosen as $\Delta t = \Delta x^2$ and for the EDPM1-C4 scheme $\Delta t = \Delta x^4$. Here, boundary conditions are imposed using the exact solution. The L^2-error computed from the numerical solutions and convergence rates in both space and time are presented in Tables 5.5 and 5.6, respectively. The L^2-error computed from the numerical solutions and convergence rates using the developed method EDPM2 with the CD2 and C4 scheme are shown in Table 5.7 and Table 5.8 at $T = 1$, respectively. For the second-order EDPM2 method, the value of the free parameters are taken as $\alpha_1 = 0.51930$ and $\alpha_2 = 0.46370$. Tables 5.7-5.8 validate numerically that the EDPM2 method has second-order rate of convergence in time. The

Table 5.5: L^2-error and rate of convergence for Eq. (5.4.1) using EDPM1-CD2 with initial data specified in Eq. (5.4.2) and damping coefficient $a = 2$.

Δx	Δt	$L^2 - error$	Convergence rate (space)	Convergence rate (time)
$\pi/6$	$(\pi/6)^2$	2.4771×10^{-1}	-	-
$\pi/12$	$(\pi/12)^2$	6.1977×10^{-2}	1.9987	0.9994
$\pi/24$	$(\pi/24)^2$	1.5432×10^{-2}	2.0058	1.0029
$\pi/48$	$(\pi/48)^2$	3.8664×10^{-3}	1.9967	0.9984

Table 5.6: L^2-error and rate of convergence for Eq. (5.4.1) using EDPM1-C4 with initial data specified in Eq. (5.4.2) and damping coefficient $a = 2$.

Δx	Δt	$L^2 - error$	Convergence rate (space)	Convergence rate (time)
$\pi/6$	$(\pi/6)^4$	1.8850×10^{-2}	-	-
$\pi/12$	$(\pi/12)^4$	1.1750×10^{-3}	4.0038	1.0009
$\pi/24$	$(\pi/24)^4$	7.4692×10^{-5}	3.9756	0.9939
$\pi/48$	$(\pi/48)^4$	4.7144×10^{-6}	3.9858	0.9964

relative and absolute energy errors are given in Table 5.9 up to $T = 4$, where T is the final time.

Relative energy error (RE) and absolute errors (AE) are computed using the following formula, given as

$$RE = \left| \frac{E_{exact} - E_N}{E_{exact}} \right|, \quad AE = |E_{exact} - E_N|$$

Table 5.7: L^2-error and rate of convergence for Eq. (5.4.1) - (5.4.2) using EDPM2-CD2 scheme with damping coefficient $a = 2$ at $T = 1$.

Δx	Δt	$L^2 - error$	Convergence rate (space)	Convergence rate (time)
$\pi/6$	$\pi/6$	7.4248×10^{-2}	-	-
$\pi/12$	$\pi/12$	1.3437×10^{-2}	2.4661	2.4661
$\pi/24$	$\pi/24$	2.9063×10^{-3}	2.2090	2.2090
$\pi/48$	$\pi/48$	6.8741×10^{-4}	2.0800	2.0800

Table 5.8: L^2-error and rate of convergence for Eq. (5.4.1) - (5.4.2) using EDPM2-C4 scheme with damping coefficient $a = 2$ at $T = 1$.

Δx	Δt	$L^2 - error$	Convergence rate (space)	Convergence rate (time)
$\pi/6$	$(\pi/6)^2$	1.3342×10^{-2}	-	-
$\pi/12$	$(\pi/12)^2$	6.7917×10^{-4}	4.2960	2.1480
$\pi/24$	$(\pi/24)^2$	4.1146×10^{-5}	4.0450	2.0225
$\pi/48$	$(\pi/48)^2$	2.5572×10^{-6}	4.0081	2.0041

5.4.1 Energy Conservation of linear damped wave equation

Here, we have considered the one-dimensional damped wave equation described in Eq. (5.4.1), using the initial conditions specified in Eq. (5.4.2). In this case, the exact solution is given by $u(x,t) = e^{-t}\sin(x)$. For the numerical computation, we have chosen $N_x = 100$, $\Delta t = 0.001$, and the final time $T = 4$. Energy ($E(u)$) is defined by the following functional, given as

$$E(u) = \frac{1}{2}\int_0^L \left[\left(\frac{\partial u}{\partial t}\right)^2 + \left(\frac{\partial u}{\partial x}\right)^2\right] dx, \quad t \geq 0 \tag{5.4.3}$$

Table 5.9: Relative and absolute energy errors using the EDPM1-C4 for Eq. (5.4.1) with initial conditions given in Eq. (5.4.2). Here, $\Delta x = \pi/48$ and $\Delta t = \Delta x^4$.

Time (T)	Relative Energy Error	Absolute Error
1/4	7.0192×10^{-6}	6.6873×10^{-6}
1/2	1.2917×10^{-5}	7.4639×10^{-6}
1	2.2023×10^{-5}	4.6816×10^{-6}
2	2.9481×10^{-5}	8.4816×10^{-7}
4	1.3805×10^{-6}	7.2746×10^{-10}

Using Eq. (5.4.1), the exact energy of the system is given by $E(u)_{exact} = \frac{\pi e^{-2t}}{2}$. The numerical approximation of the energy $E(u)_N$, is obtained by using the computed solution in Eq. (5.4.1). Figure 5.2(a) shows the variation of exact and approximated energies with respect to time t.

5.4.2 Energy Conservation of linear undamped wave equation

To establish the energy conservation for the undamped wave equation, we have considered one-dimensional linear undamped (with $a = 0$) wave equation with initial conditions given in Eq. (5.4.2). The exact solution is given as, $u(x,t) = \sin(x)(\cos(t) - \sin(t))$. For the numerical computation, we have chosen $N_x = 100$, $\Delta t = 0.001$, and the final time $T = 4$. Figure 5.2(b) shows the variation of exact and approximated energies with respect to time t, calculated using Eq. (5.4.3).

5.5 Numerical simulations: Nonlinear wave equations

This Section deals with numerical simulations of two-dimensional sine-Gordon equation [141]. Numerical solutions are considered for a Josephson junction described by a damped sine-Gordon equation [65], given as

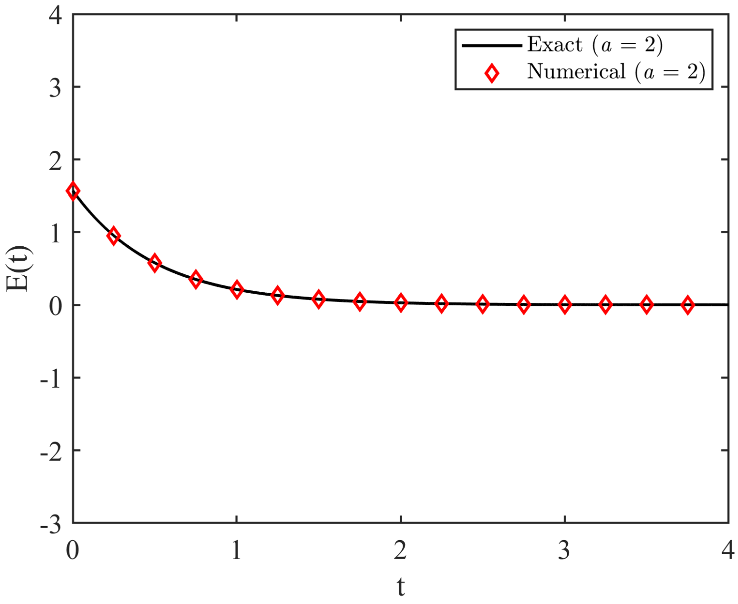

Figure 5.2(a): Variation of energy with time for one-dimensional damped wave equation given in Eq. (5.4.1) with initial conditions given in Eq. (5.4.2). Here, $a = 2$, $\Delta x = 0.03$ and $\Delta t = 0.001$.

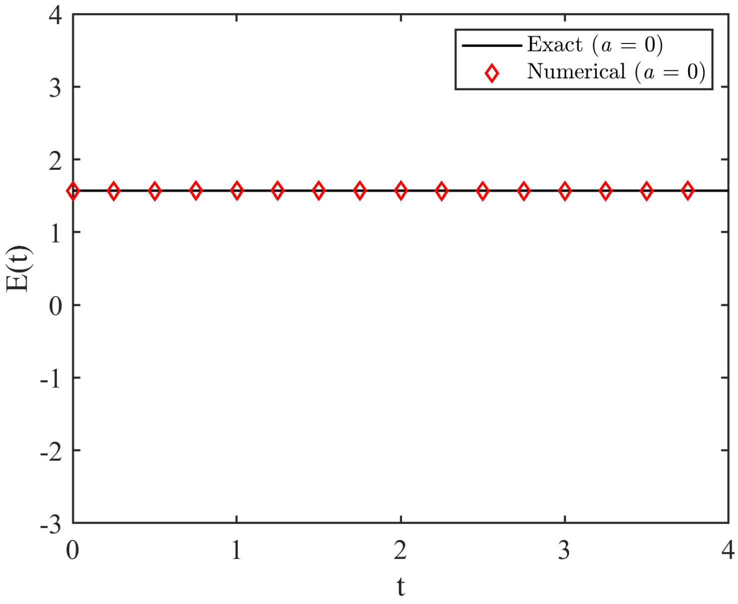

Figure 5.2(b): Variation of energy with time for one-dimensional undamped wave equation given in Eq. (5.4.1) with initial conditions given in Eq. (5.4.2). Here, $a = 0$, $\Delta x = 0.03$ and $\Delta t = 0.001$.

$$\frac{\partial^2 u}{\partial t^2} + a\frac{\partial u}{\partial t} - \frac{\partial^2 u}{\partial x^2} - \frac{\partial^2 u}{\partial y^2} = F(x,y)\sin u, \quad a \geq 0, \tag{5.5.1}$$

For computations, we have selected the computational domain as $\Omega = \{(x,y),\ a_1 < x < b_1,\ a_1 < y < b_1\}$ and $t > 0$, where $a > 0$ is the damping coefficient and the Josephson current density is represented by $F(x,y)$.

5.5.1 Numerical simulations of orthogonal line solitons

The numerical simulations presented here investigate the sine-Gordon equation for the superposition of two orthogonal line solitons. Equation (5.5.1) is simulated using $F(x,y) = -1$ over the computational domain $\Omega = [-6,6]^2$. Initial and and boundary conditions [141] are given by

$$\begin{aligned} u(x,y,0) &= 4\tan^{-1}(e^x) + 4\tan^{-1}(e^y) \\ \frac{\partial u}{\partial t}(x,y,0) &= 0 \end{aligned} \tag{5.5.2}$$

$$\frac{\partial u}{\partial x}(x,y,t)\Big|_{x=-6,6} = 0, \ \ \frac{\partial u}{\partial y}(x,y,t)\Big|_{y=-6,6} = 0 \tag{5.5.3}$$

Simulations are performed with $\Delta t = 0.01$, $\Delta x = \Delta y = 0.25$, and $a = 0.5$ using the EDPM1-C4 scheme. As displayed in Fig. 5.3(a), the line solitons move away from one another along the $y = x$ line. Furthermore, for Eq. (5.5.1), the energy is determined following the conditions for initial solution and boundaries provided in Eqs. (5.5.2) - (5.5.3). For Eq. (5.5.1), the energy is obtained as

$$\frac{\partial E}{\partial t} = -a\int\int_{\Omega}(u_t)^2 dxdy \tag{5.5.4}$$

where

$$E = \frac{1}{2}\int\int_{\Omega}\left(u_x^2 + u_y^2 + u_t^2 + 2(1 - cos(u))\right)dxdy$$

Equation (5.5.4) indicates that energy is conserved when damping is absent ($a = 0$). The energy at the initial time, $E|_{t=0}$ is derived using the conditions specified at $t = 0$ in Eq. (5.5.2). Here, initial energy (E_0) is given by

$$\begin{aligned} E_0 &= 8\left(\frac{b_1\left(e^{a_1}-e^{-a_1}\right)}{e^{a_1}+e^{-a_1}}+\frac{a_1\left(e^{b_1}-e^{-b_1}\right)}{e^{b_1}+e^{-b_1}}\right)+8\left(\frac{1}{1+e^{-2a_1}}-\frac{1}{1+e^{2a_1}}\right)\\ &\times\left(\frac{1}{1+e^{2b_1}}-\frac{1}{1+e^{-2b_1}}+b_1\right)+8\left(\frac{1}{1+e^{-2b_1}}-\frac{1}{1+e^{2b_1}}\right)\\ &\times\left(\frac{1}{1+e^{2a_1}}-\frac{1}{1+e^{-2a_1}}+a_1\right)+4\left(\sin 2(\tan^{-1}(e^{a_1}))-\sin 2(\tan^{-1}(e^{-a_1}))\right)\\ &\times\left(\sin 2(\tan^{-1}(e^{b_1}))-\sin 2(\tan^{-1}(e^{-b_1}))\right) \end{aligned}$$

The temporal variation of energy for the damped ($a = 0.5$) nonlinear wave equation Eq. (5.5.1) is depicted in Fig. 5.3(b). Additionally, the temporal energy variation for the Eq. (5.5.1) without damping ($a = 0$) is presented in Fig. 5.3(c).

5.5.2 Numerical simulations of line solitons

Here, we have performed the numerical simulations of the damped sine-Gordon equation for perturbation of a line soliton in a homogeneous as well as in an inhomogeneous mediums. For homogeneous medium, Eq. (5.5.1) is solved over the computational domain $\Omega = [-7, 7]^2$ with Josephson current density $F(x, y) = -1$, and damping coefficient $a = 0.05$, subject to the prescribed initial and boundary conditions discussed in [141], as

$$\begin{aligned} &u(x,y,0) = 4\tan^{-1}(e^{(x+1-2\mathrm{sech}(y+7)-2\mathrm{sech}(y-7))}),\\ &\frac{\partial u}{\partial t}(x,y,0) = 0 \end{aligned} \tag{5.5.5}$$

$$\frac{\partial u}{\partial x}(x,y,t)\bigg|_{x=-7,7} = 0, \quad \frac{\partial u}{\partial y}(x,y,t)\bigg|_{y=-7,7} = 0 \tag{5.5.6}$$

Simulations are carried out with $\Delta t = 0.1$, $\Delta x = \Delta y = 0.25$, damping coefficient $a = 0.05$, and are presented in the form of $\sin(u/2)$. Numerical solutions for perturbed line solitons at various moments, illustrating two symmetric dents traveling towards each other with the soliton, are displayed in Fig. 5.4(a). The dents collide and the soliton continues to move without any disturbance after the collision.

Furthermore, simulations have also been performed in an inhomogeneous medium to analyze the behavior of a line soliton. To achieve this, we utilized $F(x, y) = -(1 +$

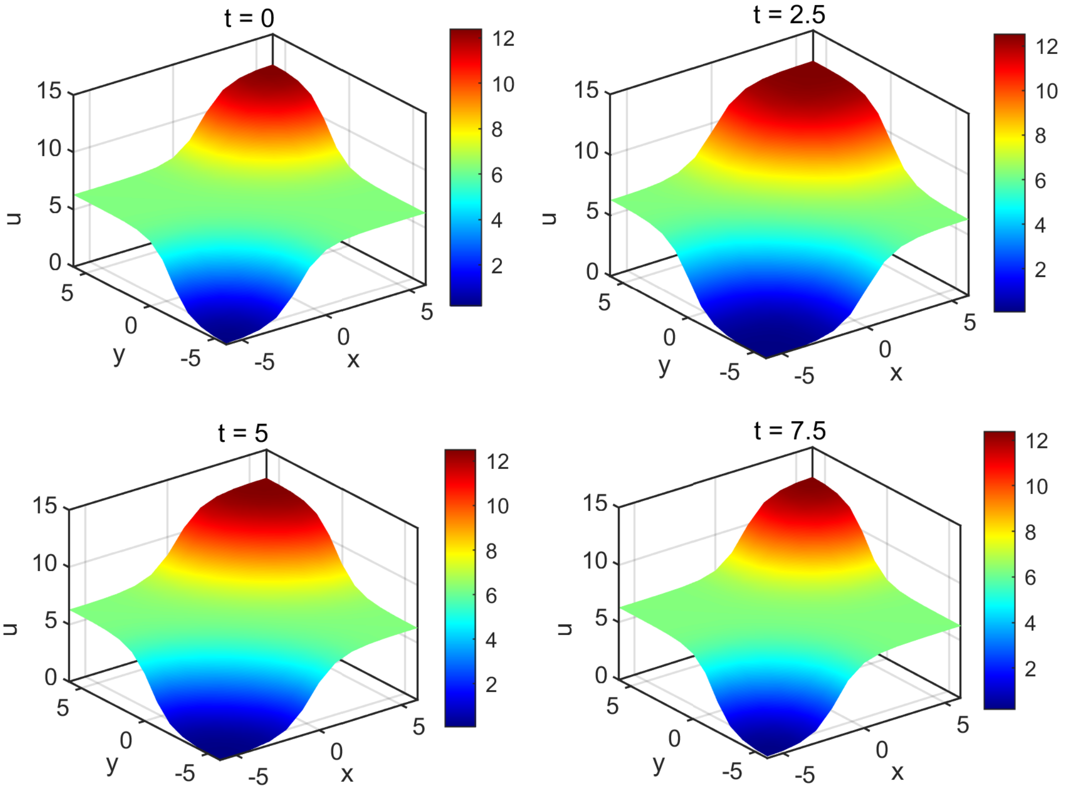

Figure 5.3(a): Numerical simulations for superposition of two orthogonal line solitons following sine-Gordon equation given in Eq. (5.5.1) at indicated instants using the EPM1-C4 with damping coefficient $a = 0.5$. The initial and boundary conditions are given in Eqs. (5.5.2)-(5.5.3).

$\operatorname{sech}^2\sqrt{x^2+y^2}$) over the computational domain $\Omega = [-7,7]^2$, following Eq. (5.5.1) with the data for initial solution and boundaries [141] given by

$$
\begin{aligned}
u(x,y,0) &= 4\tan^{-1}(e^{(x-3.5)/0.954}),\\
\frac{\partial u}{\partial t}(x,y,0) &= 0.629\ \operatorname{sech}((x-3.5)/0.954)
\end{aligned}
\tag{5.5.7}
$$

$$
\frac{\partial u}{\partial x}(x,y,t)\Big|_{x=-7,7} = 0,\quad \frac{\partial u}{\partial y}(x,y,t)\Big|_{y=-7,7} = 0 \tag{5.5.8}
$$

Here, we have chosen $\Delta t = 0.1$, $\Delta x = \Delta y = 0.25$, and $a = 0.05$. Numerical findings are displayed in Fig. 5.4(b) in the form of $\sin(u/2)$. It is evident from Fig. 5.4(b) that the

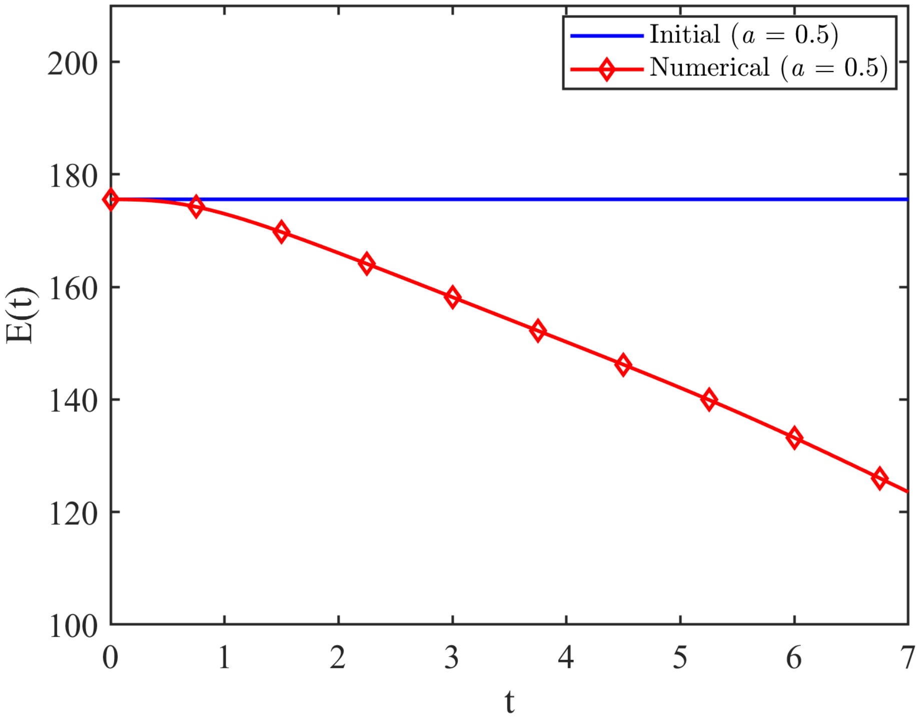

Figure 5.3(b): Variation of the energy with time for superposition of two orthogonal line solitons following the sine-Gordon equation with $a = 0.5$, $\Delta x = \Delta y = 0.25$, and $\Delta t = 0.01$. The initial and boundary conditions are given in Eqs. (5.5.2)-(5.5.3).

line soliton is capable of traversing the inhomogeneous region while encountering a slight deformation. Subsequently, the line soliton begins to straighten again after some time.

5.5.3 Numerical simulations of ring solitons

Finally, simulations of solitons in circular geometries have been performed in an homogeneous medium. Circular ring solitons are simulated with $F(x, y) = -1$ over the computational domain $\Omega = [-7, 7]^2$, following Eq. (5.5.1), using the initial and boundary data [141] given by

$$\begin{aligned} u(x, y, 0) &= 4\tan^{-1}\left(e^{3-\sqrt{x^2+y^2}}\right), \\ \frac{\partial u}{\partial t}(x, y, 0) &= 0 \end{aligned} \tag{5.5.9}$$

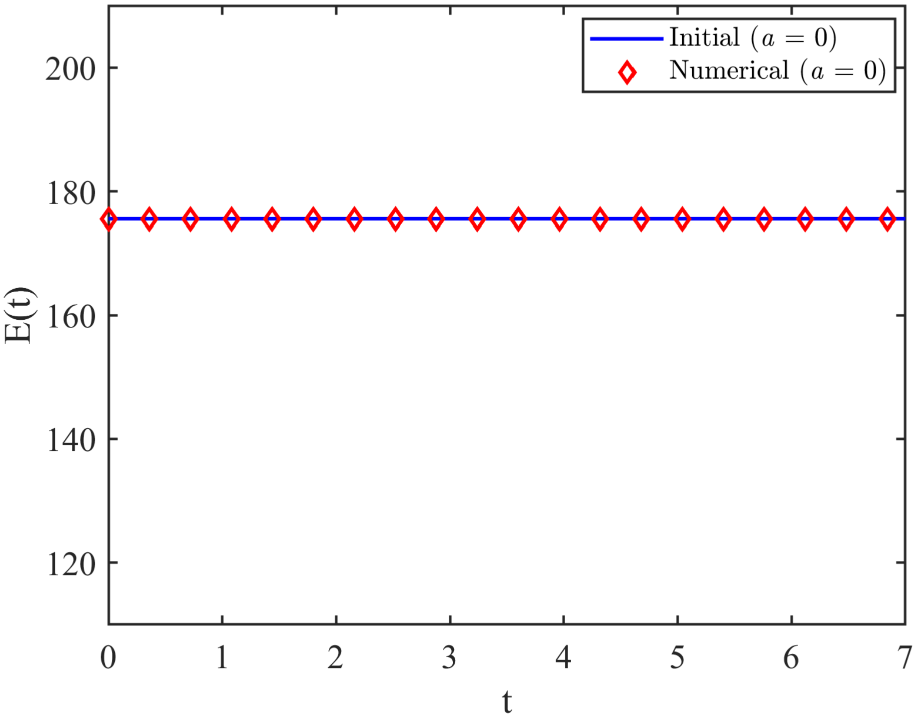

Figure 5.3(c): Variation of the energy with time for superposition of two orthogonal line solitons following the sine-Gordon equation with $a = 0$, $\Delta x = \Delta y = 0.25$, and $\Delta t = 0.01$. The initial and boundary conditions are given in Eqs. (5.5.2)-(5.5.3).

$$\frac{\partial u}{\partial x}(x, y, t)\Big|_{x=-7,7} = 0, \quad \frac{\partial u}{\partial y}(x, y, t)\Big|_{y=-7,7} = 0 \qquad (5.5.10)$$

Figure 5.4(c) presents the computed results in the form of $\sin(u/2)$ with $\Delta t = 0.1$, $\Delta x = \Delta y = 0.25$, and $a = 0.05$. Results shown in Fig. 5.4(c) illustrate that as time lapses, the ring soliton undergoes an initial contraction, followed by the emergence of oscillations and radiations, continuing until $t = 7.8$. Around at $t = 10.4$, the ring soliton started reforming. At larger values of damping coefficient a, the ring soliton exhibits a slow transition from its initial position over a longer duration.

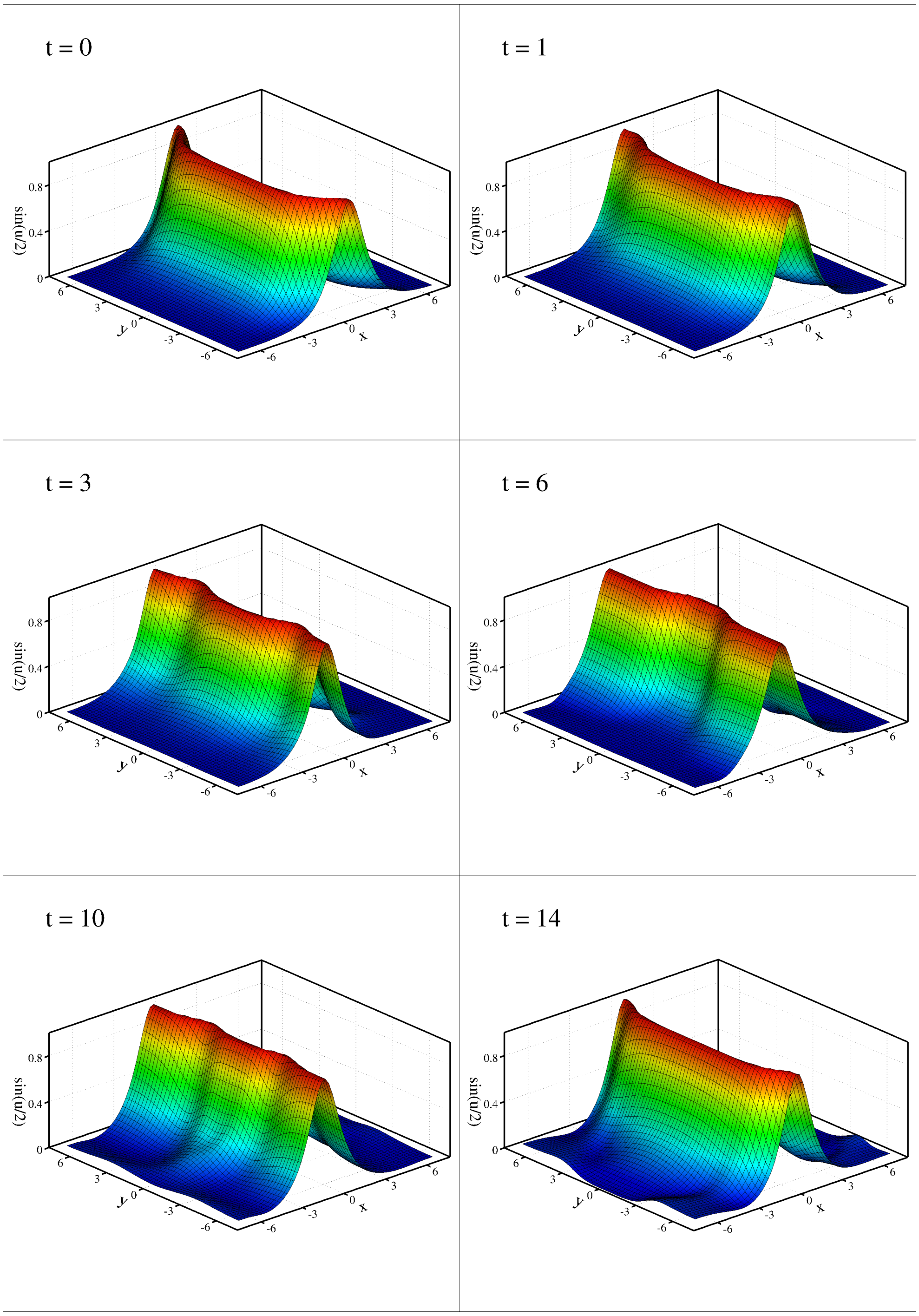

Figure 5.4(a): Propagation of a line soliton (in a homogeneous medium) to a symmetric perturbation following sine-Gordon equation with $a = 0.05$, $F(x, y) = -1$ are shown in terms of $\sin(u/2)$ at indicated instants . The initial and boundary conditions are given in Eqs. (5.5.5) - (5.5.6). Here, $\Delta x = \Delta y = 0.25$ and $\Delta t = 0.1$.

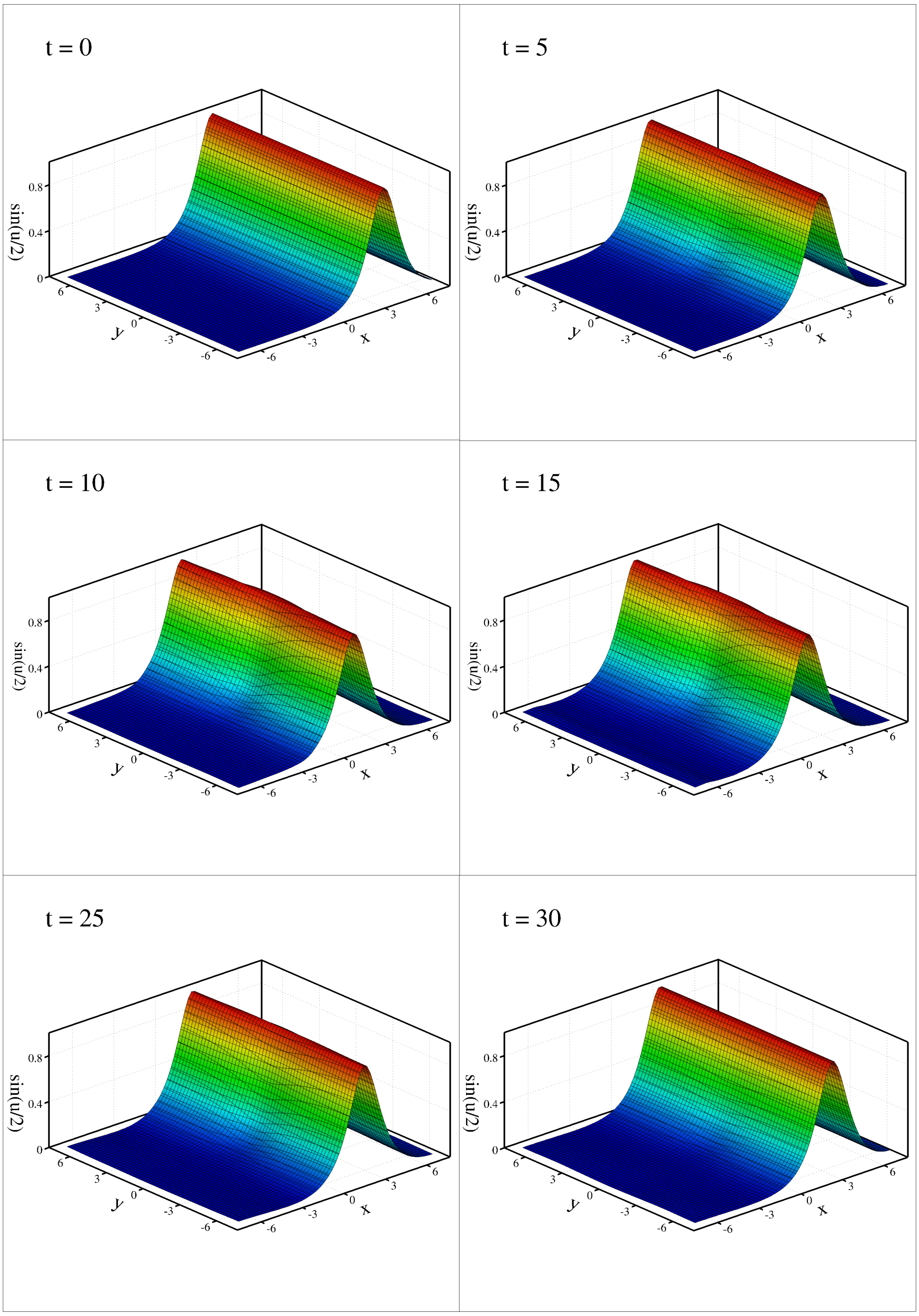

Figure 5.4(b): Transmission of a line soliton across inhomogeneous medium, presented in terms of $\sin(u/2)$ at indicated instants. The initial and boundary conditions are described by Eqs. (5.5.7) - (5.5.8), and using $a = 0.05$, $F(x, y) = -(1+\text{sech}^2\sqrt{x^2+y^2})$, $\Delta x = \Delta y = 0.25$ and $\Delta t = 0.1$.

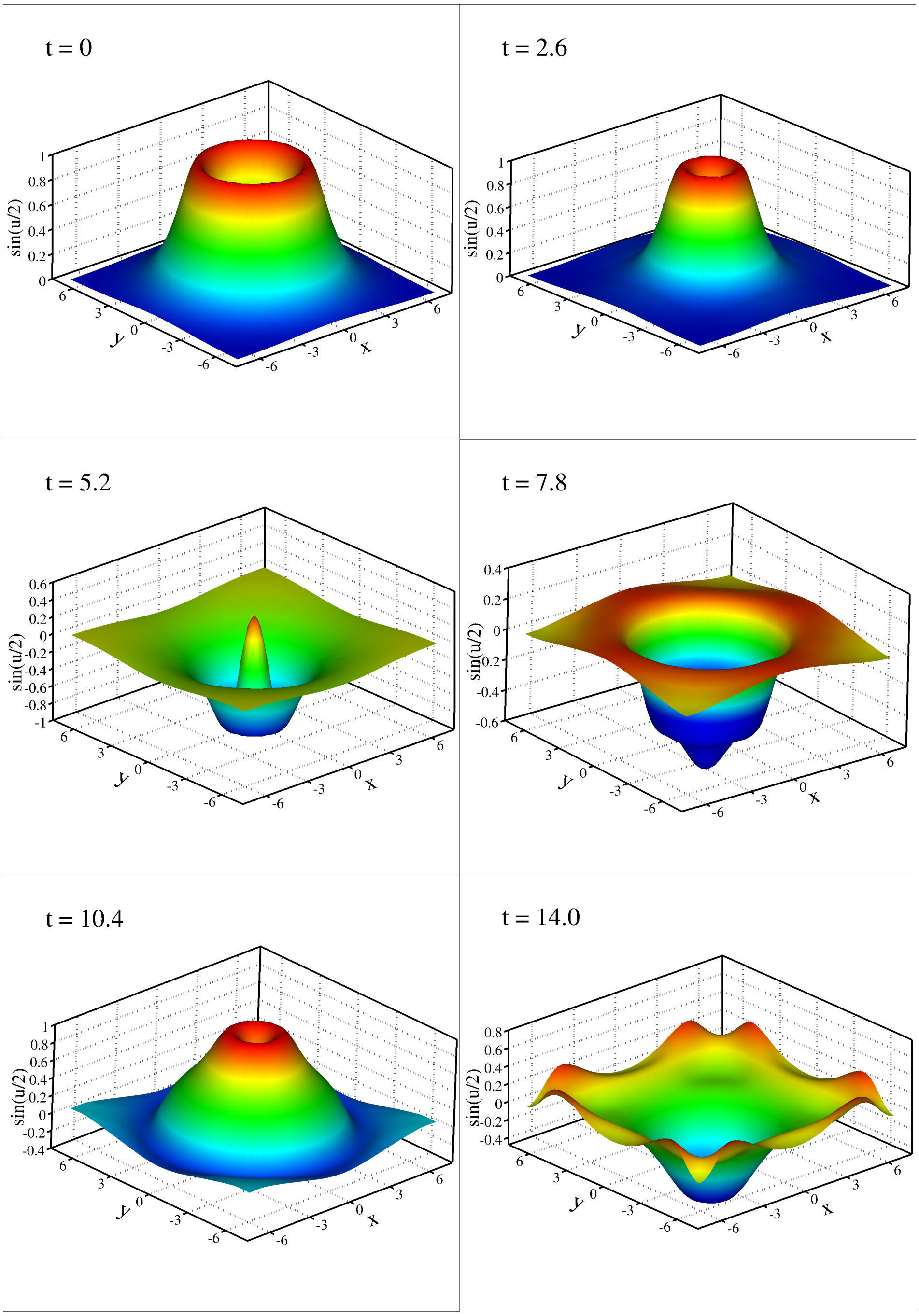

Figure 5.4(c): Numerical simulations of circular ring soliton in a homogeneous medium, presented in terms of $\sin(u/2)$ at specified instant. The initial and boundary conditions are given in Eqs. (5.5.9) - (5.5.10), and using $a = 0.05$, $F(x, y) = -1$, $\Delta x = \Delta y = 0.25$ and $\Delta t = 0.1$.

Chapter 6

Conclusion and Future Scopes

Conclusion

In this thesis, we have developed novel numerical methods for numerical simulation of stiff parabolic systems and nonlinear wave equation with damping. The primary objective was to construct algorithms that not only maintain computational efficiency but also retain high accuracy in resolving localized patterns and multi-scale features. These methods were carefully designed to remain stable in the stiff regimes, and their performance has been validated via a range of benchmark problems. The simulation results confirm that the proposed methods are able to model complex dynamics in both reaction-diffusion and wave propagation systems.

In the first part of this thesis, we have introduced a novel family of computationally explicit two-derivative Runge-Kutta methods, emphasizing positivity and unconditional strong stability preservation. These schemes are constructed based on the backward derivative condition proposed in [37], and their applicability has been demonstrated for stiff reaction-diffusion systems. The proposed method offers a balance between efficiency and stability without resorting to implicit solvers or matrix inversions. The effectiveness of the developed methods is thoroughly evaluated using numerical simulations of classical pattern-forming systems, including the Gray-Scott, Schnakenberg, and Brusselator models both with and without cross-diffusion reported, as discussed in Chapter 2. These simulation results are able to capture the spatial and temporal dynamics accurately, showcasing the ability of the methods to resolve sharp gradients and nonlinear interactions. Moreover, the methods demonstrated consistent accuracy and computational robustness across varying stiffness levels and diffusivity ratios. Beyond their application to reaction-diffusion systems, the developed methods have also the potential for broader use in modeling biological pattern formation, chemical kinetics, and ecological systems governed by stiff PDEs.

Following the successful application of the proposed two-derivative schemes for stiff reaction-diffusion systems, we further extended this approach to develop a class of multi-derivative Runge-Kutta methods suited for unsteady convection-diffusion problems in Chapter 3. These methods have been constructed in accordance with the second derivative condition outlined in [34] for time integration. The proposed schemes are fully explicit, avoiding matrix inversion, and are shown to satisfy strong stability preserving conditions under suitable assumptions. These are particularly effective in capturing the dynamics of convection-diffusion equations, where traditional explicit methods are very restrictive due to stability constraints. Fourier analysis confirms their stability properties. Simulations involving different values of convection and diffusion coefficients validate the accuracy, robustness, and efficiency of the proposed methods, highlighting their capability to model complex transport processes arising in various applications.

In the next part of the thesis, we have introduced time-integration methods for wave propagation. The development of a fully discrete energy-preserving numerical scheme for simulating undamped wave equation is discussed in Chapter 4. The method is designed to ensure long-term stability by conserving the total energy of the system, which is essential for accurately capturing wave dynamics in non-dissipative environments. Fourier analysis is used to examine the stability and dispersion properties of the scheme. Compared to the classical RKN method, the proposed scheme offers enhanced stability properties. To further improve numerical performance, an optimization problem is formulated to determine optimal values for the free parameters. For spatial discretization, fourth-order compact finite difference schemes are employed due to their superior accuracy and efficiency over classical finite difference methods. The smaller stencil size of the compact schemes allow for the accurate incorporation of boundary conditions and better resolution of wave structures.

Theoretical results establishing energy conservation and convergence are rigorously derived and validated through a series of numerical experiments. To assess the effectiveness of the developed methods, simulations were conducted for acoustic wave propagation in homogeneous and layered heterogeneous media, including two- and three-layer configurations. The corner-edge model further added a layer of geometric complexity, testing the robustness of the proposed numerical schemes. The developed scheme demonstrates significantly reduced dispersion errors compared to the classical leapfrog method and aligns more closely with theoretical energy conservation properties. Additionally, the developed method is also used to simulate nonlinear wave equations, such as the sine-Gordon and Klein-Gordon models, in both homogeneous and heterogeneous domains. Computed results confirm the second-order convergence in time and its ability to resolve complex wave phenomena without introducing artificial damping.

Chapter 5 extends the methods developed in Chapter 4 to damped linear and nonlinear wave equations. A space-time discretization scheme is proposed that maintains key dispersive properties along with the effects of damping. Unlike the undamped case, the presence of damping introduces energy dissipation into the system. The proposed scheme is designed to accurately capture both the decay of energy and the wave structure over time. Fourier stability analysis is used to compare the stability and dispersion properties of the developed methods with classical RKN time integration method. For spatial discretization, the C4 scheme is employed.

A series of numerical simulations are carried out to validate the accuracy of the proposed methods for linear and nonlinear damped wave equations, such as the damped sine-Gordon equation. These simulations demonstrate that the developed methods are capable of accurately representing the physical behavior of solitons. Convergence studies based on the L^2-norm of the error validate the theoretical first- and second-order rate of convergence. Computed results using developed methods match well with the theoretical results, providing a reliable and accurate tool for simulating damped wave propagation.

6.1 Recommendations for future work

In this thesis, several directions for future work emerge that could significantly enhance the scope and applicability of the developed numerical methods. A natural extension involves the application of these structure-preserving schemes to three-dimensional problems with unbounded domains and equations with variable coefficients. In three-dimensional settings, the computational cost increases due to the increased number of grid points and the complexity of required calculations. Addressing this will require the integration of parallel computing algorithms and adaptive mesh refinement techniques to maintain computational efficiency without sacrificing accuracy.

Simulating wave propagation in unbounded domains presents additional difficulties, particularly in accurately modeling wave behavior near artificial boundaries. The use of standard boundary conditions can lead to spurious reflections that distort the physical fidelity of the solution. To address this, future research may integrate advanced boundary treatment such as (Sommerfeld) boundary conditions or perfectly matched layers (PMLs), which are specifically designed to suppress non-physical reflections and better approximate open-domain behavior. The developed methods would also able to simulate acoustic, electromagnetic, and seismic waves in bounded or unbounded domains.

Moreover, integration of spatial adaptivity techniques could be particularly beneficial for problems characterized by localized structures, such as solitons, sharp gradients, pattern formation, or evolving interfaces. Coupling the existing schemes with non-uniform grids or adaptive mesh refinement would allow better accurate resolution of fine-scale features while controlling computational cost.

Finally, extending these structure-preserving methods to fluid-structure interaction, biological systems, nonlinear optics, and geophysical flows, would provide meaningful validation of their practical relevance and stimulate interdisciplinary problems. Finally, the developed numerical schemes can also be integrated with machine learning and neural network-based techniques, particularly for accelerating simulations and data-driven insights in reaction-diffusion systems and damped wave equations.

Publications

Thesis Outcomes:

1 **Jyoti Jaglan**, V. Maurya, A. Singh, Vivek S. Yadav, M. K. Rajpoot, *Acoustic and soliton propagation using fully-discrete energy preserving partially implicit scheme in homogeneous and heterogeneous mediums*, Computers and Mathematics with Applications 174 (2024) 379–396.

2 **Jyoti Jaglan**, A. Singh, V. Maurya, Vivek S. Yadav, M. K. Rajpoot, *Strong stability preserving multiderivative time marching methods for stiff reaction–diffusion systems*, Mathematics and Computers in Simulation 225 (2024) 267-282.

3 **Jyoti Jaglan**, A. Singh, M. K. Rajpoot, *Space-time discretizing dispersion relation preserving schemes for inhomogeneous damped wave equations*, under review 2025.

4 **Jyoti Jaglan**, M. K. Rajpoot, *Computationally explicit multiderivative schemes for convection-dominated diffusion problems with strong stability properties*, under review 2025.

List of All Publications:

1 **Jyoti Jaglan**, V. Maurya, A. Singh, Vivek S. Yadav, M. K. Rajpoot, *Acoustic and soliton propagation using fully-discrete energy preserving partially implicit scheme in homogeneous and heterogeneous mediums*, Computers and Mathematics with Applications 174 (2024) 379–396.

2 **Jyoti Jaglan**, A. Singh, V. Maurya, Vivek S. Yadav, M. K. Rajpoot, *Strong stability preserving multiderivative time marching methods for stiff reaction–diffusion systems*, Mathematics and Computers in Simulation 225 (2024) 267-282.

3 Vivek S. Yadav, V. Maurya, M. K. Rajpoot, **Jyoti Jaglan**, *Spatiotemporal pattern formations in stiff reaction-diffusion systems by new time marching methods*, Applied Mathematics and Computations 431 (2022) 127299.

4 M. K. Rajpoot, Vivek S. Yadav, **Jyoti Jaglan**, A. Singh, *Sound and soliton wave propagation in homogeneous and heterogeneous mediums with the new two-derivative implicit explicit Runge-Kutta-Nyström method*, AIP Advances 12 (2022) 075110.

5 **Jyoti Jaglan**, A. Singh, M. K. Rajpoot, *Space-time discretizing dispersion relation preserving schemes for inhomogeneous damped wave equations*, under review 2025.

6 **Jyoti Jaglan**, M. K. Rajpoot, *Computationally explicit multiderivative schemes for convection-dominated diffusion problems with strong stability properties*, under review 2025.

Bibliography

[1] R. J. LeVeque, Finite Difference Methods for Ordinary and Partial Differential Equations, SIAM, Philadelphia, 2007.

[2] W. Hundsdorfer, J. Verwer, Numerical Solution of Time-Dependent Advection-Diffusion-Reaction Equations, Springer Berlin, Heidelberg, 2003.

[3] L. F. Shampine, C. W. Gear, A user's view of solving stiff ordinary differential equations, SIAM Rev. 21 (1979) 1–17.

[4] E. Hairer, G. Wanner, Solving Ordinary Differential Equations II: Stiff and Differential-Algebraic Problems, Springer-Verlag Berlin, Heidelberg, 1996.

[5] D. Garfinkel, C. B. Marbach, N. Z. Shapiro, Stiff differential equations, Ann. Rev. Biophys. Bioeng. 6 (1977) 525–542.

[6] J. D. Murray, Mathematical Biology I: An Introduction, Springer New York, 2002.

[7] J. D. Murray, Mathematical Biology II: Spatial Models and Biomedical Applications, Springer New York, 2003.

[8] J. D. Lambert, Numerical Methods for Ordinary Differential Systems: The Initial Value Problem, John Wiley & Sons, USA, 1991.

[9] U. M. Ascher, L. R. Petzold, Computer Methods for Ordinary Differential Equations and Differential-Algebraic Equations, SIAM, Philadelphia, 1998.

[10] A. M. Turing, The chemical basis of morphogenesis, Phil. Trans. Royal. Soc. Lond. Ser. B, Biol. Sci. 237 (1952) 37–72.

[11] I. Prigogine, R. Lefever, Symmetry breaking instabilities in dissipative systems. II, J. Chem. Phys. 48 (1968) 1695–1700.

[12] J. Schnakenberg, Simple chemical reaction systems with limit cycle behavior, J. Theor. Biol. 81 (1979) 389–400.

[13] S. J. Ruuth, Implicit-explicit methods for reaction-diffusion problems in pattern formation, J. Math. Biol. 34 (1995) 148–176.

[14] S. Kondo, The present and future of Turing models in developmental biology, Development 149 (2022) dev200974.

[15] O. Schmitt, C. Nitzsche, P. Eipert, V. Prathapan, M. T. Hütt, C. C. Hilgetag, Reaction-diffusion models in weighted and directed connectomes, PLoS Comput. Biol. 18 (2022) e1010507.

[16] R. A. McDougal, C. Conte, L. Eggleston, A. J. H. Newton, H. Galijasevic, Efficient simulation of 3D reaction-diffusion in models of neurons and networks, Front. Neuroinform. 16 (2022) 847108.

[17] Y. Luo, Y. Liu, Development of a reaction–diffusion–convection model and its application to NO oxidation in reactors, Ind. Eng. Chem. Res. 63 (2024) 14381–14390.

[18] Y. Fuseya, H. Katsuno, K. Behnia, A. Kapitulnik, Nanoscale Turing patterns in a bismuth monolayer, Nat. Phys. 17 (2021) 1031–1036.

[19] A. Forslund, H. Larsson, Simulation of reaction-diffusion between substrate and coating during vapor deposition processes, Calphad 64 (2019) 278–283.

[20] R. Seenivasan, P. Paul, Turing patterns in exploited predator–prey systems with habitat loss, Eur. Phys. J. B 97 (2024) 174.

[21] N. B. Sharmila, C. Gunasundari, M. Sajid, Spatiotemporal dynamics of a reaction diffusive predator-prey model: A weak nonlinear analysis, Int. J. Diff. Eqns. 2023 (2023) 9190167.

[22] P. Gray, S. K. Scott, Autocatalytic reactions in the isothermal, continuous stirred tank reactor: Oscillations and instabilities in the system $A + 2B \to 3B$; $B \to C$, Chem. Eng. Sci. 39 (1984) 1087–1097.

[23] J. E. Pearson, Complex patterns in a simple system, Science 261 (1993) 189–192.

[24] I. Prigogine, From Being to Becoming: Time and Complexity in the Physical Sciences, W. H. Freeman and Company, San Francisco, 1980.

[25] P. A. Zegeling, H. P. Kok, Adaptive moving mesh computations for reaction-diffusion systems, J. Comput. Appl. Math. 168 (2004) 519–528.

[26] M. Ghergu, V. D. Rădulescu, Nonlinear PDEs: Mathematical Models in Biology, Chemistry and Population Genetics, Springer, Heidelberg, 2012.

[27] P. Liu, J. Shi, Y. Wang, X. Feng, Bifurcation analysis of reaction–diffusion Schnakenberg model, J. Math. Chem. 51 (2013) 2001–2019.

[28] A. K. Omran, M. A. Zaky, A. S. Hendy, V. G. Pimenov, Numerical algorithm for a generalized form of Schnakenberg reaction-diffusion model with gene expression time delay, Appl. Numer. Math. 185 (2023) 295–310.

[29] G. Albi, L. Pareschi, High order semi-implicit multistep methods for time-dependent partial differential equations, Comm. Appl. Math. Comput. 3 (2021) 701–718.

[30] C.-W. Shu, Total-variation-diminishing time discretizations, SIAM J. Sci. Statist. Comput. 9 (1988) 1073–1084.

[31] C.-W. Shu, S. Osher, Efficient implementation of essentially non-oscillatory shock-capturing schemes, J. Comput. Phys. 77 (1988) 439–471.

[32] S. Gottlieb, C.-W. Shu, Total variation diminishing Runge-Kutta schemes, Math. Comp. 67 (1998) 73–85.

[33] D. I. Ketcheson, Step sizes for strong stability preserving with downwind-biased operators, SIAM J. Numer. Anal. 49 (2011) 1649–1660.

[34] A. J. Christlieb, S. Gottlieb, Z. Grant, D. C. Seal, Explicit strong stability preserving multistage two-derivative time-stepping schemes, J. Sci. Comput. 68 (2016) 914–942.

[35] Z. Grant, S. Gottlieb, D. C. Seal, A strong stability preserving analysis for explicit multistage two-derivative time-stepping schemes based on Taylor series conditions, Commun. Appl. Math. Comput. 1 (2019) 21–59.

[36] S. Gottlieb, C.-W. Shu, E. Tadmor, Strong stability-preserving high-order time discretization methods, SIAM Rev. 43 (2001) 89–112.

[37] S. Gottlieb, Z. J. Grant, J. Hu, R. Shu, High order strong stability preserving multiderivative implicit and IMEX Runge-Kutta methods with asymptotic preserving properties, SIAM J. Numer. Anal. 60 (2022) 423–449.

[38] S. Sen, A new family of (5,5) CC-4OC schemes applicable for unsteady Navier–Stokes equations, J. Comput. Phys. 251 (2013) 251–271.

[39] Z. F. Tian, Y. B. Ge, A fourth-order compact ADI method for solving two-dimensional unsteady convection–diffusion problems, J. Comput. Appl. Math. 198 (2007) 268–286.

[40] C. Wang, M. He, P. Sun, A new combined finite element-upwind finite volume method for convection-dominated diffusion problems, Numer. Meth. Partial Differ. Eq. 32 (2016) 799–818.

[41] A. Jaust, J. Schütz, D. C. Seal, Implicit multistage two-derivative discontinuous Galerkin schemes for viscous conservation laws, J. Sci. Comput. 69 (2016) 866–891.

[42] S. Karaa, J. Zhang, High order ADI method for solving unsteady convection–diffusion problems, J. Comput. Phys. 198 (2004) 1–9.

[43] Z. F. Tian, A rational high-order compact ADI method for unsteady convection–diffusion equations, Comput. Phys. Comm. 182 (2011) 649–662.

[44] J. Chen, P. Yu, Z. F. Tian, H. Ouyang, A high-order compact scheme for solving the 2D steady incompressible Navier-Stokes equations in general curvilinear coordinates, Int. J. Numer. Meth. Fluids 92 (2020) 456–477.

[45] M. Ben-Artzi, J. P. Croisille, D. Fishelov, A high order compact scheme for the pure-streamfunction formulation of the Navier-Stokes equations, J. Sci. Comput. 42 (2010) 216–250.

[46] J. H. Adler, C. Cavanaugh, X. Hu, A. Huang, N. Trask, A stable mimetic finite-difference method for convection-dominated diffusion equations, SIAM J. Sci. Comput. 45 (2023) A2973–A3000.

[47] Z. Zhu, J. Chen, Numerical methods for unsteady convection-diffusion problems based on combining compact difference schemes with Runge-Kutta methods, J. Phy. Sci. 33 (2022) 1–15.

[48] D. K. Salkuyeh, On the finite difference approximation to the convection-diffusion equation, Appl. Math. Comput. 179 (2006) 79–86.

[49] B. Wongsaijai, N. Sukantamala, K. Poochinapan, A mass-conservative higher-order ADI method for solving unsteady convection–diffusion equations, Adv. Differ. Eq. 2020 (2020) 513.

[50] K. W. Morton, Numerical Solution of Convection Diffusion Problems, Chapman & Hall, London, 1996.

[51] L. Qian, X. Feng, Y. He, The characteristic finite difference streamline diffusion method for convection-dominated diffusion problems, Appl. Math. Model. 36 (2012) 561–572.

[52] D. Liang, C. Du, H. Wang, A fractional step ELLAM approach to high-dimensional convection–diffusion problems with forward particle tracking, J. Comput. Phys. 221 (2007) 198–225.

[53] J. Jaglan, A. Singh, V. Maurya, V. S. Yadav, M. K. Rajpoot, Strong stability preserving multiderivative time marching methods for stiff reaction–diffusion systems, Math. Comput. Simul. 225 (2024) 267–282.

[54] S. K. Lele, Compact finite difference schemes with spectral-like resolution, J. Comput. Phys. 103 (1992) 16–42.

[55] J. D. Anderson, Computational Fluid Dynamics: The Basics with Applications, McGraw-Hill, 1995.

[56] G. D. Smith, Numerical Solution of Partial Differential Equations: Finite Difference Methods, Oxford University Press, Oxford, 1985.

[57] R. J. Mackinnon, G. F. Carey, Analysis of material interface discontinuities and superconvergent fluxes in finite difference theory, J. Comput. Phys. 75 (1988) 151–167.

[58] W. F. Spotz, G. F. Carey, High-order compact scheme for the steady stream-function vorticity equations, Int. J. Numer. Meth. Eng. 38 (1995) 3497–3512.

[59] A. Balzano, Mosquito: an efficient finite difference scheme for numerical simulation of 2D advection, Int. J. Numer. Meth. Fluids 31 (1999) 481–496.

[60] U. Younas, J. Muhammad, D. K. Almutairi, A. Khan, T. Abdeljawad, Analyzing the neural wave structures in the field of neuroscience, Sci. Rep. 15 (2025) 7181.

[61] P. Singh, K. Senthilnathan, Evolution of a solitary wave: Optical soliton, soliton molecule and soliton crystal, Discov. Appl. Sci. 6 (2024) 464.

[62] J. Cuevas-Maraver, P. G. Kevrekidis, F. Williams, The sine-Gordon Model and its Applications, Springer Cham, 2014.

[63] B. D. Josephson, Supercurrents through barriers, Adv. Phys. 14 (1965) 419–451.

[64] A. G. Bratsos, The solution of the two-dimensional sine-Gordon equation using the method of lines, J. Comput. Appl. Math. 206 (2007) 251 – 277.

[65] B. A. Malomed, Dynamics of quasi-one-dimensional kinks in the two-dimensional sine-Gordon model, Physica D 52 (1991) 157–170.

[66] B. Hou, D. Liang, The energy-preserving time high-order AVF compact finite difference scheme for nonlinear wave equations in two dimensions, Appl. Numer. Math. 170 (2021) 298–320.

[67] M. J. Ablowitz, H. Segur, Solitons and the Inverse Scattering Transform, SIAM, Philadelphia, 1981.

[68] W. Bao, X. Dong, Analysis and comparison of numerical methods for the Klein–Gordon equation in the nonrelativistic limit regime, Numer. Math. 120 (2012) 189–229.

[69] P. Tong, D. Yang, B. Hua, High accuracy wave simulation - Revised derivation, numerical analysis and testing of a nearly analytic integration discrete method for solving acoustic wave equation, Int. J. Solids Struct. 48 (2011) 56–70.

[70] A. Zlotnik, R. Čiegis, On higher-order compact ADI schemes for the variable coefficient wave equation, Appl. Math. Comput. 412 (2022) 126565.

[71] W. Liao, P. Yong, H. Dastour, J. Huang, Efficient and accurate numerical simulation of acoustic wave propagation in a 2D heterogeneous media, Appl. Math. Comput. 321 (2018) 385–400.

[72] K. Li, W. Liao, Y. Lin, A compact high order Alternating Direction Implicit method for three-dimensional acoustic wave equation with variable coefficient, J. Comput. Appl. Math. 361 (2019) 113–129.

[73] H. Hamzehpour, M. Asgari, M. Sahimi, Acoustic wave propagation in heterogeneous two-dimensional fractured porous media, Phys. Rev. E 93 (2016) 063305.

[74] E. Hairer, S. P. Nørsett, G. Wanner, Solving Ordinary Differential Equations I: Nonstiff Problems, Springer Berlin, Heidelberg, 1993.

[75] T. E. Simos, J. Vigo-Aguiar, Exponentially fitted symplectic integrator, Phys. Rev. E 67 (2003) 016701.

[76] J. M. Franco, Exponentially fitted symplectic integrators of RKN type for solving oscillatory problems, Comput. Phys. Comm. 177 (2007) 479–492.

[77] A. Nagy, I. Omle, H. Kareem, E. Kovács, I. F. Barna, G. Bognar, Stable, explicit, leapfrog-hopscotch algorithms for the diffusion equation, Computation 9 (2021) 92.

[78] A. Nagy, M. Saleh, I. Omle, H. Kareem, E. Kovács, New stable, explicit, shifted-hopscotch algorithms for the heat equation, Math. Comput. Appl. 26 (2021) 61.

[79] M. Saleh, E. Kovács, A. Nagy, New stable, explicit, second order hopscotch method for diffusion-type problems, Math. Comput. Simul. 208 (2023) 301–325.

[80] R. Akbari, R. Mokhtari, A new compact finite difference method for solving the generalized long wave equation, Numer. Funct. Anal. Optim. 35 (2014) 133–152.

[81] Y. Luo, X. Li, C. Guo, Fourth-order compact and energy conservative scheme for solving nonlinear Klein-Gordon equation, Numer. Meth. Partial Differ. Eq. 33 (2017) 1283–1304.

[82] T. K. Sengupta, G. Ganeriwal, S. De, Analysis of central and upwind compact schemes, J. Comput. Phys. 192 (2003) 677–694.

[83] T. K. Sengupta, High Accuracy Computing Methods: Fluid Flows and Wave Phenomena, Cambridge Univ. Press, 2013.

[84] R. I. McLachlan, G. R. W. Quispel, N. Robidoux, Geometric integration using discrete gradients, Philos. Trans. R. Soc. A 357 (1999) 1021–1045.

[85] G. R. W. Quispel, D. I. Mclaren, A new class of energy-preserving numerical integration methods, J. Phys. A: Math. Theor. 41 (2008) 045206.

[86] J. L. Cieśliński, Improving the accuracy of the AVF method, J. Comput. Appl. Math. 259 (2014) 233–243.

[87] B. Karasözen, G. Şimşek, Energy preserving integration of bi-Hamiltonian partial differential equations, Appl. Math. Lett. 26 (2013) 1125–1133.

[88] A. S. Hendy, J. E. Macías-Díaz, A. J. Serna-Reyes, On the solution of hyperbolic two-dimensional fractional systems via discrete variational schemes of high order of accuracy, J. Comput. Appl. Math. 354 (2019) 612–622.

[89] A. S. Hendy, J. E. Macías-Díaz, A numerically efficient and conservative model for a Riesz space-fractional Klein-Gordon-Zakharov system, Commun. Nonlinear Sci. Numer. Simulat. 71 (2019) 22–37.

[90] R. Jiwari, S. Pandit, R. C. Mittal, Numerical simulation of two-dimensional sine-Gordon solitons by differential quadrature method, Comput. Phys. Commun. 183 (2012) 600–616.

[91] D. B. Duncan, Symplectic finite difference approximations of the nonlinear Klein-Gordon equation, SIAM J. Numer. Anal. 34 (1997) 1742–1760.

[92] A. G. Bratsos, E. H. Twizell, A family of parametric finite-difference methods for the solution of the sine-Gordon equation, Appl. Math. Comput. 93 (1998) 117–137.

[93] M. Dehghan, A. Mohebbi, Z. Asgari, Fourth-order compact solution of the nonlinear Klein-Gordon equation, Numer. Algorithms 52 (2009) 523–540.

[94] S. R. E. Koumy, E. S. I. Barakat, S. I. Abdelsalam, Hall and porous boundaries effects on peristaltic transport through porous medium of a Maxwell model, Transp. Porous Med. 94 (2012) 643–658.

[95] Y. A. Elmaboud, K. S. Mekheimer, S. I. Abdelsalam, A study of nonlinear variable viscosity in finite-length tube with peristalsis, Appl. Bionics Biomech. 11 (2014) 197–206.

[96] I. M. Eldesoky, S. I. Abdelsalam, W. A. El-Askary, A. M. El-Refaey, M. M. Ahmed, Joint effect of magnetic field and heat transfer on particulate fluid suspension in a catheterized wavy tube, BioNanoScience 9 (2019) 723–739.

[97] S. I. Abdelsalam, M. M. Bhatti, Anomalous reactivity of thermo-bioconvective nanofluid towards oxytactic microorganisms, Appl. Math. Mech. 41 (2020) 711–724.

[98] V. Barbu, N. H. Pavel, Periodic solutions to nonlinear one dimensional wave equation with x-dependent coefficients, Trans. Amer. Math. Soc. 349 (1997) 2035–2048.

[99] S. Gutman, Fréchet differentiability for a damped sine-Gordon equation, J. Math. Anal. Appl. 360 (2009) 503–517.

[100] G. Cohen, P. Joly, Construction and analysis of fourth-order finite difference schemes for the acoustic wave equation in nonhomogeneous media, SIAM J. Numer. Anal. 33 (1996) 1266–1302.

[101] S. Kim, H. Lim, High-order schemes for acoustic waveform simulation, Appl. Numer. Math. 57 (2007) 402–414.

[102] K. Mattsson, J. Nordström, High order finite difference methods for wave propagation in discontinuous media, J. Comput. Phys. 220 (2006) 249–269.

[103] B. Sjögreen, N. A. Petersson, A fourth order accurate finite difference scheme for the elastic wave equation in second order formulation, J. Sci. Comput. 52 (2012) 17–48.

[104] W. Zhang, L. Tong, E. T. Chung, A new high accuracy locally one-dimensional scheme for the wave equation, J. Comput. Appl. Math. 236 (2011) 1343–1353.

[105] B. Hou, D. Liang, H. Zhu, The conservative time high-order AVF compact finite difference schemes for two-dimensional variable coefficient acoustic wave equations, J. Sci. Comput. 80 (2019) 1279–1309.

[106] B. Hou, D. Liang, Energy-preserving time high-order AVF compact finite difference schemes for nonlinear wave equations with variable coefficients, J. Comput. Phys. 421 (2020) 109738.

[107] A. Singh, V. Maurya, M. K. Rajpoot, New two-derivative implicit-explicit Runge-Kutta methods for stiff reaction-diffusion systems, J. Comput. Phys. 471 (2022) 111610.

[108] V. S. Yadav, N. Ganta, B. Mahato, M. K. Rajpoot, Y. G. Bhumkar, New time-marching methods for compressible Navier-Stokes equations with applications to aeroacoustics problems, Appl. Math. Comput. 419 (2022) 126863.

[109] J. Hu, R. Shu, X. Zhang, Asymptotic-preserving and positivity-preserving implicit-explicit schemes for the stiff BGK equation, SIAM J. Numer. Anal. 56 (2018) 942–973.

[110] R. Vichnevetsky, J. B. Bowles, Fourier analysis of numerical approximations of hyperbolic equations, SIAM, Philadelphia, 1982.

[111] F. P. Incropera, D. P. Dewitt, T. L. Bergman, A. S. Lavine, Fundamentals of Heat and Mass Transfer, John Wiley & Sons, USA, 2007.

[112] C. S. Chou, Y. T. Zhang, R. Zhao, Q. Nie, Numerical methods for stiff reaction-diffusion systems, Discrete Contin. Dyn. Syst. Ser. B 7 (2007) 515–525.

[113] E. O. Asante-Asamani, A. Kleefeld, B. A. Wade, A second-order exponential time differencing scheme for non-linear reaction-diffusion systems with dimensional splitting, J. Comput. Phys. 415 (2020) 109490.

[114] E. O. Asante-Asamani, A. Q. M. Khaliq, B. A. Wade, A real distinct poles exponential time differencing scheme for reaction-diffusion systems, J. Comput. Appl. Math. 299 (2016) 24–34.

[115] J. C. Kalita, A dual-purpose high order compact approach for pattern formation using Gray-Scott model, Int. J. Appl. Comput. Math. 3 (2017) 2747–2760.

[116] Z. Lin, R. Ruiz-Baier, C. Tian, Finite volume element approximation of an inhomogeneous Brusselator model with cross-diffusion, J. Comput. Phys. 256 (2014) 806–823.

[117] M. Dehghan, M. Abbaszadeh, Variational multiscale element free Galerkin (VMEFG) and local discontinuous Galerkin (LDG) methods for solving two-dimensional Brusselator reaction-diffusion system with and without cross-diffusion, Comput. Methods Appl. Mech. Eng. 300 (2016) 770–797.

[118] R. Jiwari, S. Singh, A. Kumar, Numerical simulation to capture the pattern formation of coupled reaction-diffusion models, Chaos Solit. Fractals 103 (2017) 422–439.

[119] Y. X. Sun, Z. F. Tian, An efficient fourth-order three-point scheme for solving some nonlinear dispersive wave equations, Commun. Nonlinear Sci. Numer. Simul. Commun. 125 (2023) 107366.

[120] M. K. Rajpoot, T. K. Sengupta, P. K. Dutt, Optimal time advancing dispersion relation preserving schemes, J. Comput. Phys. 229 (2010) 3623–3651.

[121] L. Pareschi, G. Russo, Implicit–explicit Runge–Kutta schemes and applications to hyperbolic systems with relaxation, J. Sci. Comput. 25 (2005) 129–155.

[122] D. Qin, K. Fu, D. Liang, The spatial-temporal fourth-order conservative characteristic Runge-Kutta finite difference method for convection-dominated diffusion equation, Adv. Appl. Math. Mech. 17 (2025) 732–757.

[123] G. Kristensson, Second Order Differential Equations: Special Functions and Their Classification, Springer-Verlag, New York, 2010.

[124] A. D. Pierce, Acoustics: An Introduction to Its Physical Principles and Applications, Springer Cham, 2019.

[125] D. Carolan, Ž. Tuković, N. Murphy, A. Ivanković, Arbitrary crack propagation in multi-phase materials using the finite volume method, Comput. Mater. Sci. 69 (2013) 153–159.

[126] S. Britt, E. Turkel, S. Tsynkov, A high order compact time/space finite difference scheme for the wave equation with variable speed of sound, J. Sci. Comput. 76 (2018) 777–811.

[127] S. Britt, S. Tsynkov, E. Turkel, Numerical solution of the wave equation with variable wave speed on nonconforming domains by high-order difference potentials, J. Comput. Phys. 354 (2018) 26–42.

[128] M. A. Zaky, A. S. Hendy, An efficient dissipation-preserving Legendre-Galerkin spectral method for the Higgs boson equation in the de Sitter spacetime universe, Appl. Numer. Math. 160 (2021) 281–295.

[129] A. Verma, R. Jiwari, S. Kumar, A numerical scheme based on differential quadrature method for numerical simulation of nonlinear Klein-Gordon equation, Int. J. Numer. Meth. Heat Fluid Flow 24 (2014) 1390–1404.

[130] T. Zhang, T. Wang, Optimal error estimates of fourth-order compact finite difference methods for the nonlinear Klein-Gordon equation in nonrelativistic regime, Numer. Meth. Partial Differ. Eq. 37 (2021) 2089–2108.

[131] C. Jiang, W. Cai, Y. Wang, A linearly implicit and local energy-preserving scheme for the sine-Gordon equation based on the invariant energy quadratization approach, J. Sci. Comput. 80 (2019) 1629–1655.

[132] M. Cui, High order compact Alternating Direction Implicit method for the generalized sine-Gordon equation, J. Comput. Appl. Math. 235 (2010) 837–849.

[133] D. Deng, D. Liang, The time fourth-order compact ADI methods for solving two-dimensional nonlinear wave equations, Appl. Math. Comput. 329 (2018) 188–209.

[134] P. K. Maurya, V. S. Yadav, B. Mahato, N. Ganta, M. K. Rajpoot, Y. G. Bhumkar, New optimized implicit-explicit Runge-Kutta methods with applications to the hyperbolic conservation laws, J. Comput. Phys. 446 (2021) 110650.

[135] R. S. Hirsh, Higher order accurate difference solutions of fluid mechanics problems by a compact differencing technique, J. Comput. Phys. 19 (1975) 90–109.

[136] B. V. D. Pol, H. Bremmer, Operational Calculus: Based on the Two-sided Laplace Integral, Cambridge Univ. Press, 2008.

[137] P. K. Maurya, M. K. Rajpoot, V. S. Yadav, Higher-order optimized hybrid Robert-Asselin type time filters, J. Comput. Phys. 399 (2019) 108941.

[138] F. Q. Hu, M. Y. Hussaini, J. L. Manthey, Low-dissipation and low-dispersion Runge-Kutta schemes for computational acoustics, J. Comput. Phys. 124 (1996) 177–191.

[139] J. Ramboer, T. Broeckhoven, S. Smirnov, C. Lacor, Optimization of time integration schemes coupled to spatial discretization for use in CAA applications, J. Comput. Phys. 213 (2006) 777–802.

[140] E. Celledoni, V. Grimm, R. I. McLachlan, D. I. McLaren, D. O'Neale, B. Owren, G. R. W. Quispel, Preserving energy resp. dissipation in numerical PDEs using the "Average Vector Field "method, J. Comput. Phys. 231 (2012) 6770–6789.

[141] K. Djidjeli, W. G. Price, E. H. Twizell, Numerical solutions of a damped sine-Gordon equation in two space variables, J. Eng. Math. 29 (1995) 347–369.

[142] T. K. Sengupta, Y. G. Bhumkar, Computational Aerodynamics and Aeroacoustics, Springer, Singapore, 2020.

[143] N. A. Kampanis, V. A. Dougalis, J. A. Ekaterinaris, Effective Computational Methods for Wave Propagation, Chapman and Hall/CRC, New York, 2008.

[144] G. C. Cohen, Higher-Order Numerical Methods for Transient Wave Equations, Springer Berlin, Heidelberg, 2002.

[145] A. Mulloth, N. Sawant, I. Haider, N. Sharma, T. K. Sengupta, High accuracy solution of bi-directional wave propagation in continuum mechanics, J. Comput. Phys. 298 (2015) 209–236.

[146] P. Sagaut, V. K. Suman, P. Sundaram, M. K. Rajpoot, Y. G. Bhumkar, S. Sengupta, A. Sengupta, T. K. Sengupta, Global spectral analysis: Review of numerical methods, Comput. Fluids 261 (2023) 105915.

[147] T. K. Sengupta, A. Dipankar, P. Sagaut, Error dynamics: Beyond von Neumann analysis, J. Comput. Phys. 226 (2007) 1211–1218.

[148] T. K. Sengupta, A. Bhole, Error dynamics of diffusion equation: Effects of numerical diffusion and dispersive diffusion, J. Comput. Phys. 266 (2014) 240–251.

[149] V. K. Suman, T. K. Sengupta, C. J. D. Prasad, K. S. Mohan, D. Sanwalia, Spectral analysis of finite difference schemes for convection diffusion equation, Comput. Fluids 150 (2017) 95–114.